UNIVERSITY OF LEEDS

Measuring Surface Displacements of Earthquakes and Volcanoes Using C-band Sentinel-1 InSAR Time Series Analysis

Fei Liu

Submitted in accordance with the requirements for the degree of Doctor of Philosophy.

The University of Leeds

School of Earth and Environment

July 2023

Declaration

The candidate confirms that the work submitted is their own, except where explicitly indicated below. The candidate confirms that appropriate credit has been given within the thesis where reference has been made to the work of others.

The work in chapter 3 of this thesis has appeared in publication as follows: **Liu, F.**, Elliott, J. R., Craig, T. J., Hooper, A., & Wright, T. J. (2021). Improving the Resolving Power of InSAR for Earthquakes Using Time Series: A Case Study in Iran. Geophysical Research Letters, 48, e2021GL093043. https://doi.org/10.1029/2021GL093043

The concepts of this study were developed as a collaboration between all the authors. I performed the data processing and analysis, wrote the code and paper, and produced all figures within both the paper and Supporting Information. Broad support and supervision were provided by all co-authors, who provided suggestions and feedback on draft versions of the paper before publication. During the publication process, improvements were also made based on the feedback of two reviewers, T. Wang and R. Jolivet.

The work in chapter 4 is a draft manuscript, and prepare for submission: **Liu, F.**, Craig, T. J., Ebmeier, S. K., & Elliott, J. R. (2023). From Space to Slab: Probing the 112 km Deep M_w 6.8 2020 Intraslab Earthquake, Northern Chile, Using Geodetic & Seismological Observations.

This work is originally from the suggestion of my supervisors T.J. Craig and J.R. Elliott. T.J. Craig studied large intraslab earthquakes using seismology and would like to see if InSAR data could measure the surface deformation from these events. He also calculated the green's function, performed the seismic modelling, and helped me perform geodetic and joint modelling. S.K. Ebmeier provided code and helped me to perform the Independent Component Analysis on InSAR data to retrieve the coseismic signals better. J.R. Elliott provided support and supervision, code for GPS data processing, and valuable comments on draft writing. I performed

the InSAR data processing, including both tropospheric and ionospheric correction, the geodetic and joint inversion of earthquake source modelling, wrote the manuscript, and produced all the figures.

The work in chapter 5 of this thesis has appeared in publication as follows: **Liu, F.**, Elliott, J. R., Ebmeier, S. K., Craig, T. J., Hooper, A., Novoa Lizama, C., & Delgado, F. (2023). First onset of unrest captured at Socompa: A recent geodetic survey at Central Andean volcanoes in Northern Chile. Geophysical Research Letters, 50, e2022GL102480. https://doi.org/10.1029/2022GL102480

The origin of this work is during the discussion of my work in chapter 4, when I, J.R. Elliott, S.K. Ebmeier, and T.J. Craig were analysing the non-tectonic signals on the InSAR deformation map. I processed a large area of InSAR data that covers the Central Andean volcanoes, and performed the modelling. A. Hooper and C. Novoa Lizama later joined the discussion, and provided suggestions on performing and comparing different models. F. Delgado and his colleagues in Chile collected the data of the GPS station near Socompa volcano. All co-authors improved the manuscript through suggested revisions, which were further refined based on the feedback of two reviewers, S. Henderson and M. Pritchard, during the publication process.

Signed

Acknowledgements

The past nearly four years as a PhD student at the University of Leeds have been an amazing journey filled with both joys and challenges. It has been the most fulfilling period of my life so far, and I believe even if the years have passed, the experience of these days seems like yesterday.

First and foremost, I would sincerely say thank you to my supervisors: John Elliott, Tim Crag, Andy Hooper, and Tim Wright. I would like to thank John, thank you for dedicating your precious time providing guidance and help when I most needed. Thanks for your thoughtfulness regular parties, which made it easier for me to fit in with the neighbourhood's culture. I appreciate your consideration and Susi's good wishes when my family was ill, which made us feel warm from the heart. I am extremely thankful to Tim Crag. Thank you for your fantastic enthusiasm and constant encouragement; things would be much harder without you. Thanks also to Andy for being so supportive and for your sense of humour, and Tim W for your mentorship and organizing such a lovely community. I also would like to extend my heartfelt thanks to Susi for your training me on volcanology and guidance on the paper, despite not being my supervisor.

The School of Earth and Environment at the University of Leeds has been a wonderful place to complete a PhD and meet with brilliant minds. Thank you, Jack and Andrew, for always being supportive during the whole PhD time. It is already time to say goodbye, but we made many good memories (COMET meetings, John's BBQ, LPS in Germany, etc.) and wish you all good luck in work and marriage. Big thank you to Qi for the inviting weekend outing, brainstorming discussions throughout the day, and precious friendship. To Ruth, Dehua, Pedro, Victoria, Jess, Scott, John, and Alex, thank you for the daily, or weekly group discussions and feedback; really appreciated. Regarding the COMET-LiCS group, I extend my thanks to Milan, Yasser, Reza, Camila, and Sarabjeet, with whom I had really enjoyed talk and discussion, in both science and

daily life.

My deepest appreciation goes to my parents for their unwavering love, encouragement, and understanding throughout the journey. Words are not enough to express my gratitude, and I just want to let you know that I successfully completed my PhD, and you will see that your hard work and efforts are not in vain. Huge thanks also to my uncles, and Dr Yue Huang (and his family) for your encouragement and valuable suggestions.

Finally, to my beloved wife, Jinyu Yan. You are not only my partner, but also my soulmate. We have known each other for literally over half of our lifetime, and I can say it is the most beautiful and luckiest thing I have ever met. I do not know what challenges are waiting for me in the future, but I am fearless as long as you are with me, and I wish you always happiness. This thesis is dedicated to you.

Abstract

Earthquakes and volcanic eruptions have long been documented and studied due to their devastating effects on human lives. More recently, with the advancement of space geodesy, mainly from Interferometric Synthetic Aperture Radar (InSAR), and the Global Positioning System (GPS), observing the Earth's surface deformation caused by earthquakes and volcanoes has become another important and effective method to study these natural hazards. However, due to the noise level within the InSAR observation, only a certain fraction of earthquakes that are large or shallow enough (usually $M_w > 5.0$ or depth < 10 km) to transmit their energy to the surface is readily observable. It is still unclear whether more advanced InSAR approaches (e.g., time series analysis) could push the limit and improve the resolving power of InSAR for earthquakes. And for volcanic activities, which might be triggered by earthquakes, require frequent estimates of surface displacements to monitor the changes at a long-time scale and detect any potential unrest or eruption, also making InSAR time series analysis essential to study them.

In this thesis, I first perform InSAR time series analysis to improve the detection and modelling of continental earthquakes in the Iran-Iraq border area. I use several shallow moderate magnitude earthquakes (M_w 5.6–6.3, 2018–2019, centroid depth ∼10 km), which are the aftershocks of the major M_w 7.3 Ezgeleh–Sarpolzahab earthquake in 2017, as case studies and process five years of Sentinel-1 InSAR times data spanning Nov 2014 to Sep 2019 over that area. I find that the coseismic displacement signals of these earthquakes, which might not be discernible within single interferograms due to atmospheric noise, are better resolved using the time series approach. Using a time-dependent parameterized model fitted to InSAR time series data, I separate the signals of postseismic deformation from the mainshock and the aftershocks occurring close in time and space, reconstructing the coseismic deformation fields of the case studies. The reconstructed coseismic deformation fields improve the detectability of earthquake signals and the signal-to-noise ratios (SNR), yielding more robust and seismologically consistent earthquake

modelling results when compared to single coseismic interferograms. My work in Iran suggests that a time series approach is an effective way to improve the resolving power of InSAR for shallow earthquake studies, leading to a more refined earthquake catalogue and fault rupture definition.

I then try to apply the time series approach to detect large intraslab earthquakes ($M_w > 6.5$, 40-300 km depth) in subduction zones, given these special events could provide insight into the property of slabs and the Earth's structure, but are rarely the focus of geodetic work. I choose a case study of a 112 km deep M_w 6.8 earthquake that occurred on 3rd June 2020 in Northern Chile, and processed about four years of Sentinel-1 InSAR time series data over the deformation area. After applying both tropospheric and ionospheric noise correction, I successfully retrieve the coseismic deformation field (with peak displacements only ∼6 mm), using the Independent Component Analysis (ICA), a blind source separation approach, on time series data. Combining InSAR and GPS data, I perform the earthquake modelling and get the source parameters, which overall agree well with the independent observations from seismology. I subsequently do a combined geodetic and seismic joint inversion, and achieve well-constrained fault orientation, location, depth, and most importantly the size of the fault (with median value of 7.9 km and 12.8 km for width and length, respectively). This case shows the potential of using InSAR observation to study large intraslab earthquakes, leading to better understanding of their rupture mechanism, the interplay between the sources of stresses, and possible improvements of velocity structure.

Meanwhile, I report the first detection of unrest at Socompa volcano (Chile) and update the volcanic monitoring in the Central Andes for the first time in over ten years, using the same dataset used for the intraslab earthquake study, as numerous active volcanoes are also located in this subduction zone. I find that the Socompa volcano, whilst initially undeforming and with no recorded eruptions for 7.2 kyr, shows a steady uplift (17.5 mm/yr) since ∼2020. Although it might be interesting to assume it is the M_w 6.8 large intraslab earthquake on 3rd June 2020 that triggered this unrest through seismic waves, the independent record by near-field continuous GPS data suggests the onset of uplift dates back to Nov 2019, precluding the possible causal relationship between them. I then test several numeric source models and find the deformation pattern can be fitted with pressure increase in an ellipsoidal source region stretching from 2.1 to 10.5 km, with a volume change rate of $\sim 6.2 \times 10^6$ m^3/yr. The deformation signal I detect

indicates the initiation of unrest at Socompa (Nov 2019), after at least two decades without measurable deformation, and many thousands of years without volcanic activity.

Finally, I conclude my work on the current detect limitation of C-band Sentinel-1 InSAR time series on surface displacements caused by both shallow and deep earthquakes, as well as volcanic activities. I summarise the benefits and implications of applying InSAR time series approaches for studying these events, the remaining challenges regarding data processing, and outline potential research questions for future work.

Contents

List of Figures

List of Tables

Chapter 1

Introduction

1.1 Context and Motivation

Earthquakes and volcanic eruptions are two of the most devastating natural hazards that pose great threats to human daily life and productivity. Throughout human history, the number of casualties caused by earthquakes and volcanoes has been countless, and even cities have been destroyed because of them (Tralli et al., 2005; Stein et al., 2012; White, 2019). To complicate things, earthquakes and volcanic activities are sometimes associated with each other. Volcanic unrest or eruption triggered by earthquakes, and vice versa, seismic activities produced by the volcanic eruptions, are both commonly observed worldwide (Hill et al., 2002; McNutt and Roman, 2015; Seropian et al., 2021). To understand their mechanisms and relationship, and to further respond to these significant natural hazards, a critical starting point is to observe geophysical phenomena associated with events.

Currently, two common main physical phenomena caused by earthquakes and volcanic activities can be measured instrumentally. The first is seismic wavefield generated by earthquakes or seismic activity triggered by a volcanic eruption, which propagates through the Earth and can be recorded by seismometers (globally for large events). From the beginning of the 20^th century to the present, these seismological observations have been the primary tool to provide information about earthquakes (such as the location of hypocentres and fault orientation, Shearer, 2019), and to understand how magma and gases move towards the surface for volcanic study (Zobin, 2017). Another type of phenomenon observable is the static displacement of the Earth's surface, due to the sudden slip across the fault surface resulting in permanent elastic deformation caused

by earthquakes (e.g., Massonnet et al., 1993; Johanson et al., 2006), or the accumulation and ascent of magma under volcanoes (e.g., Hooper et al., 2004; Pritchard and Simons, 2004a; Poland et al., 2006). With the rapid advancement of geodetic observations in recent decades, here mainly refers to the data from Interferometric Synthetic Aperture Radar (InSAR, Figure 1.1) and Global Positioning System (GPS, and other global navigation satellite system as well), such displacements can be accurately measured over global landmasses (Rott, 2009; Bock and Melgar, 2016; Pepe and Calò, 2017). Geodetic data offer measurements independent from seismology to obtain the properties of the deformation source (including location, orientation, and geometry), significantly improving our ability to observe active tectonic and volcanic activities (Rucci et al., 2012; Di Traglia et al., 2014; Elliott et al., 2016). Since geodetic and seismological measurements are independent and can complement each other, they can be used together to achieve more comprehensive results of the temporal evolution of rupture and spatial distribution of faulting, or history of pressure change in a magma reservoir (e.g., Fernández et al., 2012; Elliott et al., 2010; Grandin et al., 2017; etc.).

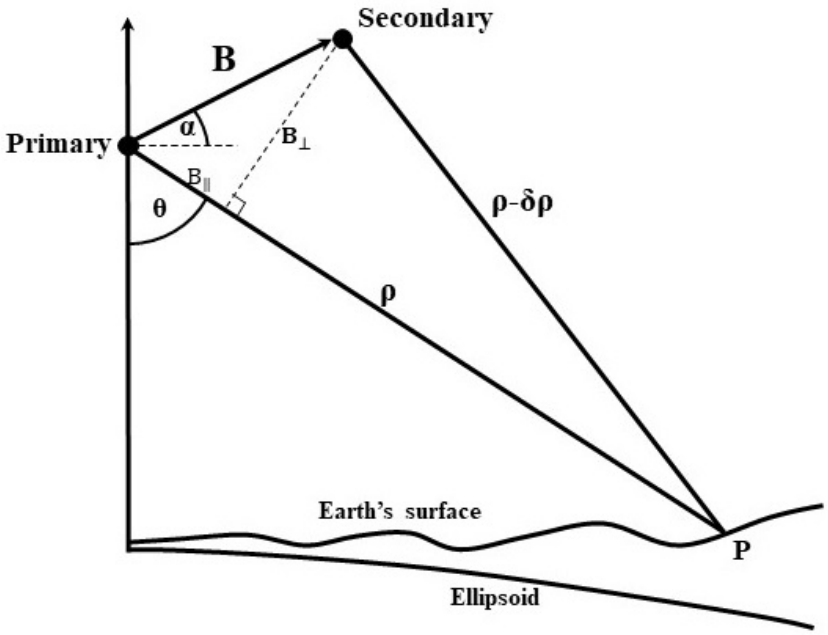

Figure 1.1: Schematic diagram showing the basic principle of InSAR measurements. The primary and secondary represent the locations of the SAR satellite at different acquisition times, and their spatial distance of baseline $\mathbf{B}$. The path difference $\boldsymbol{\delta\rho}$ between the satellites to the ground target $\mathbf{P}$ determines the phase value on the interferogram, which contains the topography information of the Earth's surface, and any changes on the ground in the line-of-sight direction (LOS, defined by look angle $\boldsymbol{\theta}$ and flight direction during the revisit time). The geometry of the baseline, including the perpendicular baseline $\mathbf{B}_\perp$, parallel baseline $\mathbf{B}_\parallel$, and angle $\boldsymbol{\alpha}$, affects the coherence, sensitivity, and the error from certain sources of the observation.

However, such observations are not always feasible or accurate enough due to the limitations of each dataset. The noise within the InSAR data, such as decorrelation and atmospheric delay (Zebker et al., 1997; Agram and Simons, 2015), result in only certain earthquakes and volcanoes whose deformation signals at the surface are large enough to be observed (e.g., Funning and Garcia, 2019, Figure 1.2). Yet we are still unclear about the detectability limits of current InSAR data, and what magnitude of signals can be robustly observed. While GPS could provide more precise measurements, the sparse spatial distribution of GPS stations prevents the capture of full deformation patterns caused by earthquakes, and not all active volcanoes are monitored by a nearby GPS stations (Bock and Melgar, 2016). On the other hand, the constraints of precise fault location by seismological observations are restricted in regions of low instrumentation, and are also affected by the processing approaches and used velocity model of the subsurface (Kagan, 2003; Husen and Hardebeck, 2010; Karasözen and Karasözen, 2020). In addition, earthquakes generated by volcanic activity generally have a small magnitude (generally $M_w < 5.0$) and often require dense local seismic networks to capture their signals, which is not available everywhere worldwide (Traversa and Grasso, 2010; McNutt and Roman, 2015).

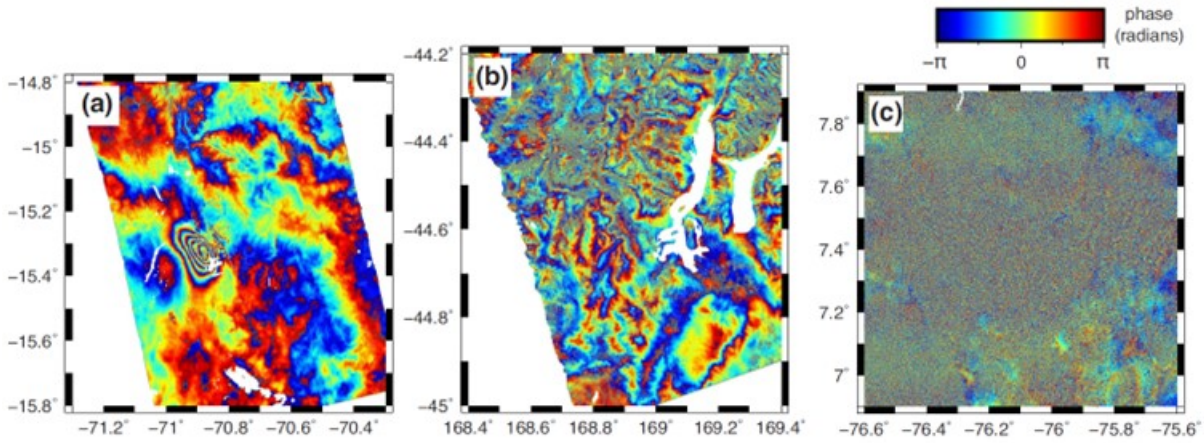

Figure 1.2: Examples of atmospheric and decorrelation noise within a single interferogram that impede robust earthquake detection. a) Detected case where apparent coseismic deformation is captured by a single interferogram; b) Ambiguous case due to atmospheric noise; c) Undetected case where no clear signal could be identified due to strong decorrelation noise. In all three cases, the epicentre is near the centre of the map. Reproduced from Funning and Garcia, 2019.

In this thesis, I will mainly focus on using InSAR observations to measure the static displacements caused by earthquakes or volcanic activities, although GPS and seismological data will also be used for providing ground truth, comparison, and joint inversion. I will try to answer the question of how small surface deformation caused by earthquakes and volcanic activities,

mainly coseismic deformation and linear deformation which contains in part the interseismic deformation, can be robustly captured by current InSAR observations, and push the measurement limits of InSAR using advanced time series approaches. I choose the C-band Sentinel-1 constellation as the test dataset, given it is one of the latest InSAR missions, which has good orbit control (spatial baseline usually ¡ 150 m), advanced imaging mode(Terrain Observation with Progressive Scans, TOPS), and short revisit time (6-24 days)(Geudtner et al., 2014). More importantly, Sentinel-1 by far is the most widely used InSAR dataset in geophysics as it provides global coverage and is open to use (Li et al., 2016), making it especially beneficial to study the characteristics of the data systematically (Figure 1.3).

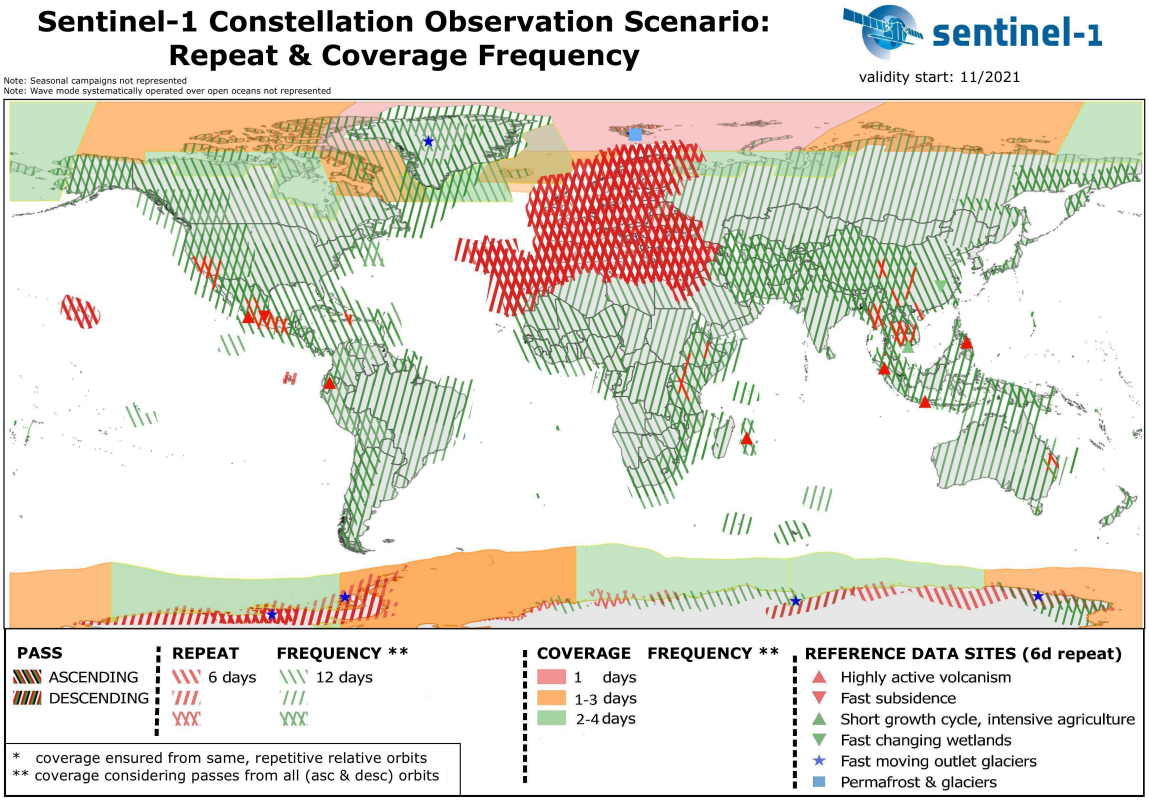

Figure 1.3: Global coverage and repeat time of the Sentinel-1 missions (map based on when Sentinel-1A and Sentinel-1B both were working). Reproduced from the European Space Agency ("Sentinel-1 Observation Scenario", 2023).

For InSAR earthquake study, in general, larger magnitude and shallower depth earthquakes show more significant surface displacement near the epicentre as the released energy is more likely to be transmitted to the surface. Therefore, two types of earthquakes that I am particularly interested to see if they are detectable by InSAR, namely shallow continental earthquakes (M_w 5.0-6.5, 0-40 km depth) in fault zones of plate boundaries, and large intraslab earthquakes

(M_w > 6.5, 40-300 km depth) at subduction zones. Surface deformations of these two types of earthquakes are relatively small and could be the ideal targets for testing the measurement limits of InSAR. Considering the different physical properties of these earthquakes and volcanic activities, I will introduce the motivation of my work individually for each type of event.

1.1.1 Shallow Continental Earthquakes (M_w 5.0-6.5, 0-40 km depth)

There are several advantages of studying shallow continental earthquakes using InSAR. Firstly, in contrast to subduction zones where the location of seismic events is predominantly controlled by the subduction zone and a single major fault interface, deformation for continental zones is very widely distributed, and thus so are the earthquakes that may occur relatively far from the known fault(Jackson, 2001; Hayes et al., 2018). Accordingly, we often do not know the location of active faults that well before the seismic events for continental interiors. InSAR can provide the precise location of these small earthquakes, which could help us better identify and define the (hidden) fault ruptures that are potentially capable of proclaiming larger earthquakes. This is particularly important in the region where seismology provides poor constraints on the fault location due to the lack of dense seismic instrumentation coverage. Secondly, the depth estimation from seismology regarding the shallow continental earthquakes sometimes contains large uncertainty, and even cannot give a reliable value thus fixed depth is given (such as 10 km depth from the United States Geological Survey, USGS, catalogue). While InSAR could provide depth measurements with more realistic uncertainties, potentially giving us important information about the Earth's structure by observing multiple events (Weston et al., 2012) and the tectonic setting of the local region. Finally, the number of small magnitude earthquakes are much bigger than that of large ones. We can draw inferences from small earthquakes to better understand the occurrence and even mechanism of major events by increasing the sensitivity of our observations, if we assume their behaviour are similar (Ide, 2019).

1.1.2 Large Intraslab Earthquakes (M_w > 6.5, 40-300 km depth)

Although simply deeper and larger, the detection of large intraslab earthquakes at Earth's surface by InSAR is significantly different from the shallow continental ones when taken the velocity structure into account. The velocity structure of the subsurface, which makes a massive difference to the source parameters derived from seismology (Kagan, 2003; Karasözen and Karasözen, 2020), also decides the rigidity value (or shear modulus). And since the fault plane

of large intraslab earthquake dipping deep into the mantle, the change of rigidity value with the increase of depth must be considered. For the earthquake moment (M_0) calculation, we have

$$M_0 = \mu LWu, \tag{1.1}$$

where μ is the rigidity, W and L are the width and length respectively that define the rupture size, and u is the average slip value on rupture area. We can see that, for a given moment value, the value of LWu is proportional to the inverse of the rigidity value, suggesting a larger value of LWu (or equivalent surface displacement) can be achieved if a smaller rigidity value is provided. The empirical rigidity value we commonly used is 32 GPa for shallow continental earthquakes occurring in the crust, and 75 GPa is used for large intraslab earthquakes occurring in the mantle in comparison (all values from USGS). However, these empirical may be wrong from the truth, especially for the intraslab events, and we may need to calculate the rigidity value for individual case if velocity structure is given in that specific area.

The velocity structure brings in another question that we may need to consider, which is the impact of using layered space when doing earthquake modelling. When modelling shallow earthquakes using InSAR observation, we often assume a uniform elastic half-space to retrieve the source parameters. Although it is not the case in real world, the impact of using a uniform half-space for InSAR data is relatively small (e.g., Lohman et al., 2002; Lohman and Simons, 2005a; Lohman and Simons, 2005b; Weston et al., 2012) given their shallow depth. However, it is still unclear how large it will affect the surface displacement observations and source modelling by InSAR for large intraslab earthquakes. If the impact is still relatively small for large intraslab earthquakes, it will allow us to obtain closer to real-world uncertainties regarding the constraints on fault location. Conversely, if the impact could not be neglected, it would also provide a great chance to refine the current velocity model, which would be more significant at a long-term scale. In either case, it would be a great chance to explore the velocity structure using InSAR data, thus worth investigating.

Additional difficulties are also aroused for the detection of large intraslab earthquakes regarding the InSAR data processing. The larger magnitude also leads to a larger area of the surface deformation pattern, which makes it harder to distinguish earthquake signals from other long-wavelength noise on interferograms (e.g., orbit error, Fattahi and Amelung, 2014) and significantly increases the data processing volume.

However, the rewards of measuring the surface displacement caused by large intraslab earthquakes using InSAR could also be exceptionally high, considering our understanding of the rupture mechanism of these events is still poor. Large intraslab earthquakes have commonly been observed to divide into two layers within the subducting slab, which are so-called Double Seismic Zones (DSZ, e.g., Kawakatsu, 1985; Dorbath et al., 2008; Wei et al., 2017). These two layers are separated by a 10-40 km width aseismic region, with the upper seismicity layer (USL) of the DSZ located in the oceanic crust, and the lower seismicity layer (LSL) in the lithospheric mantle (Sippl et al., 2018). For the events that occurred in the USL, it is generally thought that the dehydration embrittlement (Hacker et al., 2003), which involves releasing free fluid into the slab and causing overpressures, explains the rupture mechanism. However, the mechanism for the LSL events remains controversial. The thermal runaway model (e.g., Schmidt and Poli, 1998; Karato et al., 2001; John et al., 2009), which relies on the internal generation of heat in the deforming material through shear heating, could also be the answer to explain the occurrence of LSL events. To understand the rupture mechanism of large intraslab earthquakes, one of the most critical problems here is the determination of the hypocentre (Florez and Prieto, 2019; Zhan, 2020). In addition, the location of the hypocentre and focal mechanism of the intraslab events provide essential information regarding the geometry and stress orientation within slabs, providing insight into the interplay between the sources of stress and even the properties of slabs such as temperature, hydrous state, and phase changes (Frohlich, 2006; Thielmann et al., 2015; Hasegawa and Nakajima, 2017; Hosseinzadehsabeti et al., 2021).

Currently, the location of large intraslab earthquakes heavily relies on seismology. However, achieving accurate, bias-free earthquake locations from seismology for these events remains to be challenging tasks for several reasons: 1) phase picking errors (Billings et al., 1994; Shearer, 1997; Richards-Dinger and Shearer, 2000); 2) the inaccuracy contained in the used average 1-D velocity structures, which is especially in subduction zones where lateral velocity variations can be significant (Engdahl et al., 1998); 3) the processing approaches from the linear to non-linear inversion (e.g., Pavlis et al., 2004; Lin and Shearer, 2006; Lomax et al., 2009), grid search to probabilistic algorithms (e.g., Rodi, 2006; Myers et al., 2007; Myers et al., 2009), etc. will also affect the result. Overall, it would enormously enrich our dataset and lead to a better understanding of large intraslab earthquakes and slabs if InSAR could observe the surface deformation from these events, and provide additional constraints on the fault location and geometry.

1.1.3 Volcanic Activities

The majority of the volcanoes are located above active subduction zones, and additionally it is also the place where large intraslab earthquakes occur (McGuire, 1996). This is not simply a coincidence, and the interactions between volcanic activities and earthquakes have been widely observed (e.g., Hill et al., 2002; Lemarchand and Grasso, 2007; Eggert and Walter, 2009; Seropian et al., 2021). However, such interactions tend to involve either megathrust earthquakes ($M_w \geq 7.0$) or shallow moderate earthquakes (M_w 5.0-6.5, 0-30 km depth) very close to the volcanoes in the brittle crust (e.g., Ebmeier, 2016; Nishimura, 2017; Prejean and Hill, 2018). Large intraslab earthquakes have not generally been linked to volcanic unrest or deformation. In addition, when using InSAR to measure the surface displacement by large intraslab earthquakes, it requires processing a large area as mentioned above, which will inevitably cover many Holocene volcanoes near the epicentre. Exploring the potential connections between intraslab earthquakes and nearby volcanic activities, and evaluating the impact of volcanic activities on seismic deformation, is one of the main reasons why I am monitoring volcanic activities in this thesis.

For volcanic monitoring, due to the remote location and high topography, only a small portion of the Holocene volcanoes are currently actively monitored using ground-based instrumentation (e.g., Chien et al., 2020; Di Traglia et al., 2021; Aguilera et al., 2022). Since InSAR provides remote measurements of the surface displacement at the millimetre level, it has increased the number of volcanoes where deformation has been studied by order of magnitude (e.g., Biggs et al., 2014; Poland and Zebker, 2022). The main difference in using InSAR observations between volcanoes and earthquakes is that the location of volcanoes is already known, but they require constant observations to monitor the change of behaviours, making InSAR time series analysis a perfect tool for studying them (e.g., Ofeigsson et al., 2011; Henderson and Pritchard, 2013; Pritchard et al., 2018; Wang et al., 2018). This is also the point of pushing the accuracy of InSAR measurements on volcanoes. The surface deformation rate associated with volcanic activity generally is non-linear at a long-time scale (> 10 years, Biggs and Pritchard, 2017). Precisely detecting and measuring the change of deformation rate could help us better calculate and understand the volume and pressure change, and the movement of magma, and inform us of the possibility of chamber wall failure and eventually eruption, which are all critical for hazard assessment (Paton et al., 2008; Wilson et al., 2014).

1.2 Previous InSAR Studies

Despite a large amount of InSAR-based earthquake studies, most studied earthquakes are shallow events ($M_w > 4.0$, 0-40 km depth, Merryman Boncori, 2019). In addition, single interferograms are used in the first instance to capture the coseismic deformation in most cases. However, recent studies suggest that the overall detectability of earthquakes by this approach is inconsistent and non-robust, and subject to extremely high failure rates even using the latest SAR missions (49% failure for Sentinel-1 and 23% failure for ALOS-2, Funning and Garcia, 2019; Morishita, 2019). This mainly due to the decorrelation and atmospheric noise, and some other factors such as snow coverage (e.g., Kumar and Venkataraman, 2011) and seasonal effects (e.g., Tomás et al., 2016), while ALOS-2 is less affected by decorrelation noise and has lower failure detection rate because of using L-band microwave. The circumstance is even worse for shallow continental earthquakes (M_w 5.0-6.5, 0-40 km depth) due to their relatively weak signals. On the other hand, large intraslab earthquakes ($M_w > 6.5$, 40-300 km depth) are rarely the focus of InSAR work, and the coseismic deformation of only two large events have been recorded (Khash, Iran, M_w 7.7, 80 km depth, Barnhart et al., 2014; Navarro, Peru, M_w 8.0, 112 km depth, Vallée et al., 2023), therefore it is unknown whether events at such depth are as readily observable as shallow events, and additional efforts are required to distinguish their surface deformation from noise.

The volcanic studies using InSAR data are numerous. Since the location of volcanoes is readily known, the main issue here for InSAR-based volcanic study is not the accuracy of the observation, but rather the lack of monitoring (Pritchard et al., 2018). Further discussion regarding global volcanic data processing is beyond the scope of this thesis, and I will focus on how we can improve the quality of InSAR data on volcanic monitoring, and the triggering of volcanic unrest or eruption by nearby earthquakes. Recent research using statistical approaches or case studies suggests that, according to the magnitude of earthquakes, there are mainly two classic scenarios for earthquake-volcano interaction (Seropian et al., 2021). The first one is volcanic activities triggered by large megathrust earthquakes ($M_w \geq 7.0$), mostly in subduction zones. These earthquakes emit large amounts of seismic energy and cause pressure changes, and volcanoes within hundred kilometres can be triggered. Either by static stress changes, dynamic seismic waves, or both, depending on the distance from the volcano to the epicentre (e.g., Pritchard et al., 2013; Takada and Fukushima, 2013). Another category is related to moderate earthquakes

(M_w 5.0-6.5), and these earthquakes need to be very close to the volcanoes (within 0-50 km) to trigger them by mainly static stress changes (e.g., Nishimura, 2018; Gregg et al., 2018). Overall, in both cases, the earthquakes occurred first and then triggered volcanic activities. Therefore, for exploring the interaction between large intraslab earthquakes and nearby volcanic activities, one of the most important things is the determination of the onset time of volcanic unrest and eruption, which requires high temporal resolution InSAR (or even GPS) data (Figure 1.4).

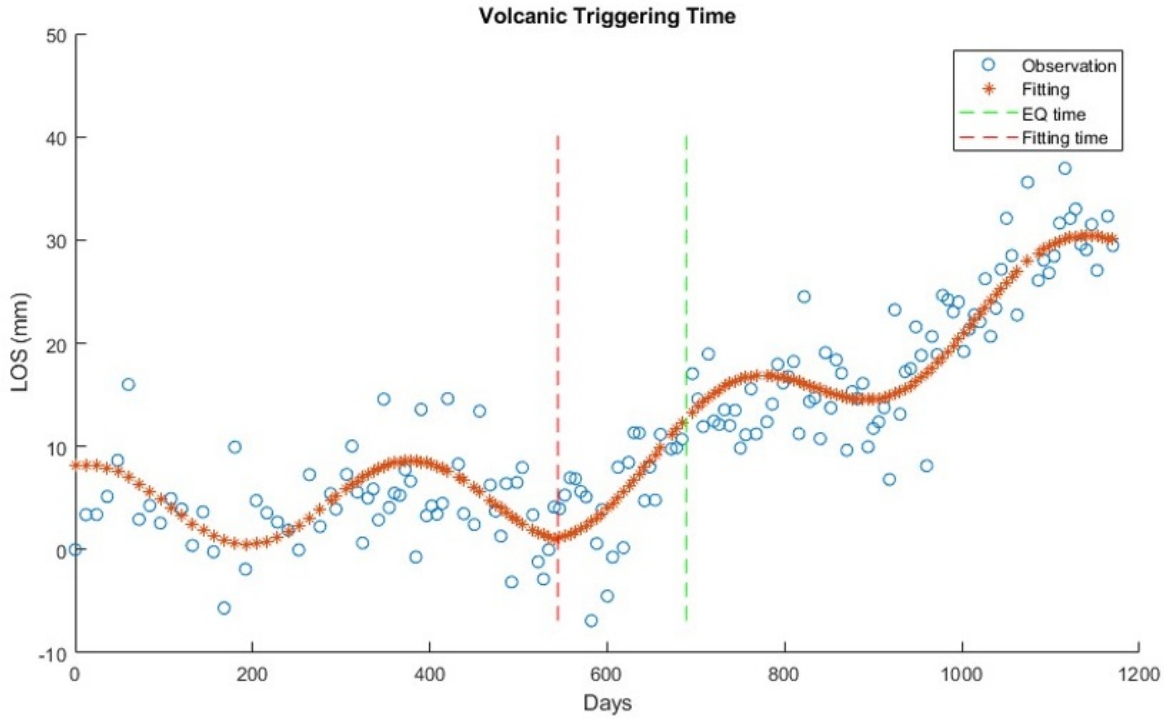

Figure 1.4: An example of applying InSAR time series data to determine the onset time of volcanic unrest and compare it to the earthquake event time. The InSAR time series data is fitted by two different linear velocities separated by the onset time (the 'Fitting time' indicated by the red dashed vertical line), with additional annual terms. Data is from chapter 5, using descending track pixels that close the deformation source.

InSAR time series analysis has been proposed (Hooper et al., 2012; Jolivet et al., 2012; Crosetto et al., 2016; Osmanoğlu et al., 2016), to obtain the frequent estimation of surface displacements, achieving more accurate and robust measurements by repeated observations and systematic error removal. For earthquake study, InSAR time series can be used to measure long-time deformation signals, such as interseismic strain rate or postseismic deformation (Hilley et al., 2004; Fialko, 2006; Ryder et al., 2007). The better noise resilience of time series data also suggests a potential way for enhancing earthquake detection using InSAR (e.g., Fielding et al., 2017; Grandin et al., 2017). More details of InSAR data processing and time series analysis will

be introduced in chapter 2.

1.3 Surface Deformation Models

To better understand the physical process behind earthquakes and volcanic activities using InSAR time series data, we need appropriate deformation models to explain the evolution of surface displacements through time. Although they share some common characteristics, the different mechanisms of the earthquake and volcanic activities illustrate specific deformation patterns, and I will discuss them separately here.

1.3.1 The Seismic Cycle

The observation of earthquake events in time can be divided into three repeated periods, namely coseismic, postseismic, and interseismic, which is also called the seismic cycle. The coseismic period, caused by the sudden stress release along a fault rupture, normally occurs very quickly (on the order of several seconds to minutes) and represents an abrupt surface displacement in time series data. The postseismic period (vary from seconds to decades) describes the subsequent viscoelastic and poroelastic relaxation after the mainshock, and usually indicate a logarithm decay in time (Ingleby and Wright, 2017). The interseismic deformation is a slow stress accumulation process (decades to centuries) and generally represents a linear deformation in time. Overall, the surface displacements $\Theta(t)$ associated with the seismic cycle can be decomposed as follows:

$$\Theta(t) = H(t - t_0)[C + A \ln (1 + \frac{t}{\tau})] + Vt + b, \tag{1.2}$$

where $H(t - t_0)$ is the step function at the earthquake event time t_0 (it equals zero when $t < t_0$, and one when $t > t_0$), C represents the coseismic deformation, A and τ are the parameters in the logarithm function, which represents the postseismic deformation (Ingleby and Wright, 2017), V is the linear deformation rate which represents the longer-term interseismic deformation, and b stands for the constant reference offset in observations.

For InSAR coseismic measurements, in addition to the detectability, another main issue here is the latency of SAR observations (0-24 days for Sentinel-1 data), and the diversity of deformation associated with the postseismic period, which will cause part of the postseismic deformation

to be contained within the single coseismic interferograms(Figure 1.5), causing the earthquake magnitudes modelled by InSAR being biased to larger values than that constrained by seismological observations (e.g., Weston et al., 2012; Floyd et al., 2016). Furthermore, many shallow continental earthquakes are actually the aftershocks of nearby much larger mainshocks ($M_w >$ 7.0), and the postseismic signal from the mainshock might be the dominant signal that mixed with the coseismic signals in the InSAR data, which also requires consideration in the model.

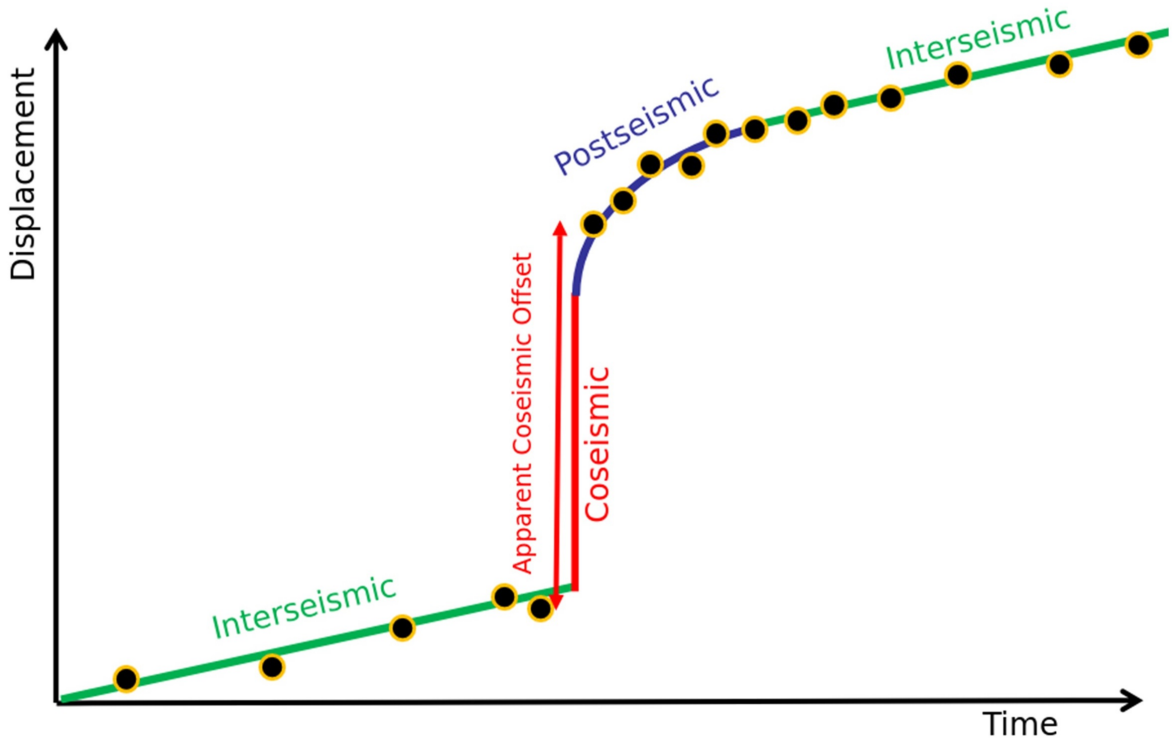

Figure 1.5: The conceptive view of the deformation in the seismic cycle when measured by InSAR observation. Since the earthquake happened between two SAR image acquisitions, a single interferogram usually contains both coseismic and part of early postseismic deformation (the 'Apparent Coseismic Offset').

Resolving the postseismic deformation is also not easy because the movement is non-linear and affected by the property of that surface material near the epicentre. The postseismic decay time of parameter τ varies case by case, and might be different across the area even for the same event (e.g., Hearn, 2003; Perfettini and Avouac, 2004; Gonzalez-Ortega et al., 2014; Gratier et al., 2014). In addition, we also need to consider the magnitude of the postseismic signals, especially for the shallow continental and deep intraslab earthquakes I studied here. The postseismic deformation from these events could be very difficult for InSAR observations to capture due to their weak signal. And in many cases, we might simply ignore the insignificant postseismic

deformations due to the difficulty of robustly measuring them by InSAR data. While on the other hand, in the scenario when significant displacements of aftershocks are observed, we might need to determine if deformations of multiple postseismic deformation processes could be incorporated into the model.

Lastly, the measurement of interseismic deformation contained in the long-term linear deformation rate observed by InSAR also faces some challenges. The primary issue is the non-tectonic linear deformation in InSAR measurements, such as subsidence, landslide, soil moisture change (e.g., Osmanoğlu et al., 2011; Scott et al., 2017; Solari et al., 2020), etc. It usually requires additional information, for example, optical images or field data, regarding the property of the surface to identify the deformation mechanisms (e.g., Gutiérrez et al., 2011; Zhao and Lu, 2018). In addition, it is also challenging to separate interseismic deformation from these non-tectonic signals, especially when they have a similar magnitude of deformation rate (e.g., Lin et al., 2015; Xu et al., 2021). And one interesting question we also need to consider here is the change of interseismic rate itself after an earthquake, which might be the case after large events ($M_w >$ 7.0, e.g., Melnick et al., 2017). Another problem is that due to the decorrelation noise within InSAR data, we may lose some or even a wide area of coverage, leaving blanks in our datasets (Wei and Sandwell, 2010; Ahmed et al., 2011; Malinverni et al., 2014). The same problem also exists for the measurement of coseismic and postseismic deformation, however not as impactful as the interseismic rate if the deformation area is large enough to preserve the main deformation features.

1.3.2 Volcanic Activities

The classical model of the 'volcanic deformation cycle' describes a process in which magma gradually inflates a chamber directly beneath the volcano that uplifts the surface, and then erupts until the pressure threshold is reached, accompanied by rapid subsidence. However, volcanic activity and their corresponding surface deformations are much more complicated in the real world, and this oversimplified model does not apply to many volcanoes (Biggs and Pritchard, 2017). The surface deformation of a specific volcano depends on the physical process occurring. For example, a dyke instruction, cooling lava flow, or pressure increase of a magma chamber all have distinct deformation patterns (e.g., Yun et al., 2006; Morishita et al., 2016; Wittmann et al., 2017). Therefore, I will focus more on the behaviour changes of volcanic surface deformation, explore the causal relationship between such changes and nearby earthquakes, and

explain the physical processes accordingly.

1.4 Thesis Outline

1.4.1 Aims and Objectives

I aim to explore the full potential of using C-band Sentinel-1 InSAR time series analysis to detect and measure the small coseismic deformation on Earth's surface caused by shallow continental earthquakes (M_w 5.0-6.5, $>$ 40 km depth) or large intraslab earthquakes ($M_w > 6.5$, 40-300 km depth), and combine these with seismological observations to improve our understanding of the nature of these seismic events. In addition, I also aim to explore the potential relationship between volcanic activities and large intraslab earthquakes in the subduction zones. My specific objectives are as follows:

1. Processing long-time, large-scale, Sentinel-1 InSAR time series data to measure surface deformation associated with shallow continental or large intraslab earthquakes over the active tectonic region (such as Iran or Chile), and improving the quality of data using state-of-the-art InSAR processing approaches and atmospheric corrections.

2. Using a time-dependent model of surface displacements during the seismic cycle to fit InSAR time series data, or other methods, such as blind source separation, to improve the SNR and better retrieve the coseismic deformation fields.

3. Using InSAR alone or with other datasets (GPS or seismic waveforms) to obtain earthquake source parameters by numeric modelling, and evaluating the contribution of InSAR to studying these events.

4. Updating the volcanic monitoring in subduction zone, and exploring the potential causal relationship between volcanic activities and intraslab earthquakes.

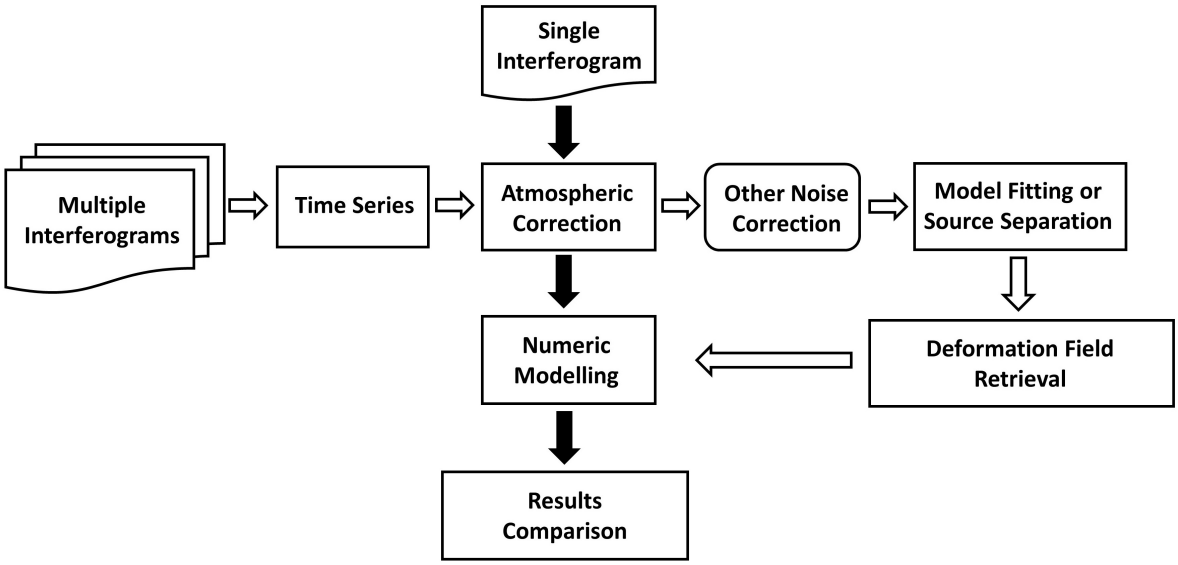

Figure 1.6: Different workflow between single interferograms and InSAR time series approaches. The InSAR time series approaches have more acquisitions to remove the systematic errors within the data (including atmospheric noise, DEM and orbit errors, etc.), and more importantly can better retrieve the deformation signals and improve the subsequent modelling.

1.4.2 Outline of Work

This thesis is structured as follows: In chapter 2, I introduce the methodology of InSAR time series analysis, including the noise source characteristics and how time series data can be applied to better measure the surface displacements associated with earthquakes and volcanic activities. In chapter 3, I apply the InSAR time series approach to measure the shallow continental earthquake in Iran, which extracts higher SNR coseismic deformation fields, and achieves better-constrained source parameters. In chapter 4, I study a 112 km depth, M_w 6.8 intraslab earthquake in Northern Chile, combing datasets from InSAR time series, GPS, and seismology. I perform joint inversion of multiple datasets to better determine the fault location and geometry, providing insights into the rupture mechanism of intraslab events. In chapter 5, I update the volcanic monitoring in Northern Chile, and report the first detection of unrest at Socompa volcano. I test and find that it is unlikely that the Socompa unrest is triggered by the M_w 6.8 earthquake described in chapter 4. And finally in chapter 6, I summarize my research findings and outline the possible future work directions for the field.

Chapter 2

InSAR Time Series Analysis

2.1 Introduction

A single interferogram, generated by two Single Look Complex (SLC) images at different acquisition times (or called two epochs), with a suitably large perpendicular baseline, is initially used to generate the Digital Elevation Model of the coverage area (e.g., Ferretti et al., 1999; Crosetto, 2002; Gao et al., 2017). Moreover, if the DEM of the coverage area is provided from additional sources, we could also obtain the surface displacements during this period by differencing the DEM derived from InSAR and that from additional sources. This technique is called Differential InSAR (DInSAR, e.g., Stramondo et al., 2005; Lanari et al., 2007; Ishwar and Kumar, 2017) and can also be applied by using three or four epochs without additional DEM to obtain surface displacements during a certain period.

InSAR time series analysis is an extension of the DInSAR technique, by using multiple epochs rather than just three or four, to obtain frequent estimates of surface displacements across years or decades (Osmanoğlu et al., 2016; Xue et al., 2020; Li et al., 2022). For current InSAR time series processing, we use additional DEM (for example, the most commonly used is DEM from the Shuttle Radar Topography Mission, or SRTM (van Zyl, 2001)) to assist coregistration during the interferogram generation and remove the topography-related phases to focus on the deformation signals of interest (e.g., Bürgmann, 2002; Zebker et al., 2010; Das et al., 2014). It is natural that time series analysis is more appealing for long-term observations regarding the displacements associated with the seismic loading cycle or volcanic activity. With the launch of the Sentinel-1 mission in 2014, it became possible to observe the tectonic or volcanic movements

regularly (every 6-24 days depends on the region, 1.3) at a global scale (onshore), making time series analysis more applicable for long-time, large-scale displacements monitoring (Geudtner et al., 2014; Potin et al., 2018).

Since I only use Sentinel-1 InSAR data in my thesis, in this chapter, I will focus on the analysis and application of C-band Sentinel-1 data, although different satellites share many common characteristics and processing difficulties.

2.2 Phase Composition and Noise Sources

After removing the topography-related signals in an interferogram, the unwrapped phase contains several terms which can be expressed by the following formula (Agram and Simons, 2015):

$$\psi = \psi_{defo} + \psi_{dcoh} + \psi_{atm} + \psi_{other} + 2k\pi \tag{2.1}$$

where ψ_{defo}, ψ_{doch}, and ψ_{atm} are the displacement in the Line of Sight (LOS) direction, the decorrelation signal, and the atmospheric delay, respectively. ψ_{other} represents all the other terms, including plate motion, solid earth tide, other noise sources (e.g., DEM and orbit errors, thermal noise of the radar sensor), etc. $2k\pi$ is the phase ambiguity that may include Phase Unwrapping (PU) errors (Yu et al., 2019). For the following part, I will go through each term in Equation (2.1) and explain how it affects the results of InSAR measurement.

2.2.1 Decorrelation Signal

Coherence expresses the similarity of the radar reflection between two epochs, and it is the most important factor in InSAR measurement (Bamler and Hartl, 1998; Moreira et al., 2013). The loss of coherence, or decorrelation, will introduce errors into the data, severely affecting the reliability of the measured phase values. In the extreme case, when the data are totally decorrelated, the whole interferogram will be overwhelmed by the noise and we cannot obtain any useful information. Maintaining coherence is crucial, and several factors control the magnitude of the decorrelation signals.

1. The observed objects. It greatly depends on the scattering characteristics of the object's surface to determine the level of coherence. Usually, man-made structure or bare soil can keep its surface property unchanged for quite a long time and therefore have high

coherence (Sousa et al., 2011; Crosetto et al., 2016). In contrast, other objects like water or vegetation change rapidly and can hardly keep coherence after several days.

2. Satellite geometry and revisit time. The change of look angle and the length of revisit time also have a large impact on the coherence (Pepe and Calò, 2017). The shorter the perpendicular baseline and revisit time, the higher the coherence. Sentinel-1 has a revisit time of 6, 12, or 24 days depending on the location (also acquisition time due to the failure of Sentinel-1B in 2021), and the length of perpendicular baselines is usually less than 150 m, making it feasible to maintain coherence in most cases (Potin et al., 2018).

3. The wavelength of the radar. The wavelength of the microwave determines its penetration, and how severe the signal is affected by vegetation (Pepe and Calò, 2017). Therefore, the L-band (wavelength of 24 cm) instrument overall can achieve higher coherence than that C-band and X-band (wavelength of 5.6 cm and 3 cm, respectively) due to better penetration (Rignot et al., 2001).

Since the decorrelation signal is more related to the imaging condition and hardware, this can hardly be overcome after the interferogram formation. The practical way to deal with this issue is simply discarding the decorrelated pixels, which will inevitably cause the loss of coverage.

2.2.2 Atmospheric Delay

Atmospheric delay refers to the refraction of the signal as it transits the atmosphere, resulting in a change in the trajectory of the radar waves and introducing extra noise in the interferogram. It can be further divided into tropospheric and ionospheric delays with different properties and should be treated differently (Ding et al., 2008).

The tropospheric delay contains two components: the one determined by the pressure and temperature, called the dry component and affected by topography, and the wet component expressed by a function of the partial pressure of water vapour (Jolivet et al., 2011; Bekaert et al., 2015; Zebker, 2021). The magnitude of tropospheric delay highly depends on the weather conditions and varies case by case, and generally show displacements of the order of a few centimetres in the interferogram (Bekaert et al., 2015). Its impact therefore depends on the relative strength between the deformation signal and the tropospheric delay.

The ionospheric delay is determined by the LOS vertical Total Electron Content (TEC) in the

ionosphere (Wegmuller et al., 2006; Jung et al., 2012). Unlike tropospheric delay, which is almost independent of radar wavelength, ionospheric noise is typically considered to be small at the shorter-wavelength C-band (only one-sixteenth of those of the L-band, considering the typical wavelength ratio of four between them, Ishimaru et al., 1999; Belcher and Rogers, 2009). In addition, since TEC is directly linked to the sun's activities, the acquisition time (dust or dawn) and latitude also play important roles here (Pi, 2015). For Sentinel-1 data, lower latitude regions have a higher delay as they are closer to the sun, and the ascending track generally suffers more ionospheric delay due to the acquisition at ∼6 pm, compared to ∼6 am of descending (all local time, Hobbs et al., 2014, Figure 2.1, Figure 2.2). The ionospheric delay on the Sentinel-1 interferogram shows long-wavelength deformation signals and generally can be ignored except for the ascending track data in the low magnitude region (like Northern Chile, e.g., Liang et al., 2019; Zhang et al., 2021).

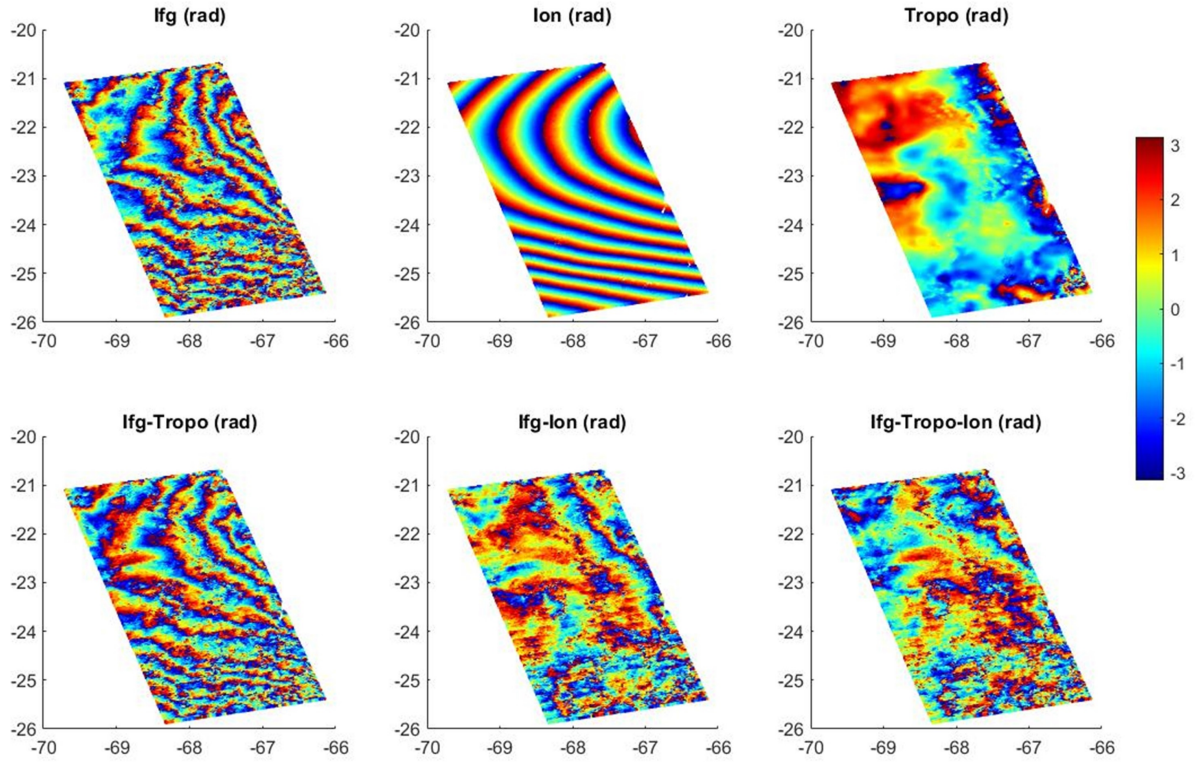

Figure 2.1: An example of applying tropospheric and ionospheric correction of a single interferogram on ascending track. It shows the original interferogram (Ifg), the ionospheric delay (Ion, estimated by split spectrum method), the tropospheric delay (Tropo, provided by GACOS), and the corresponding removals. The SNR of the interferogram significantly improved after both corrections, especially the removal of dominant longwave signals from the ionospheric delay. Data from a single interferogram with particularly strong ionospheric delay in chapter 4.

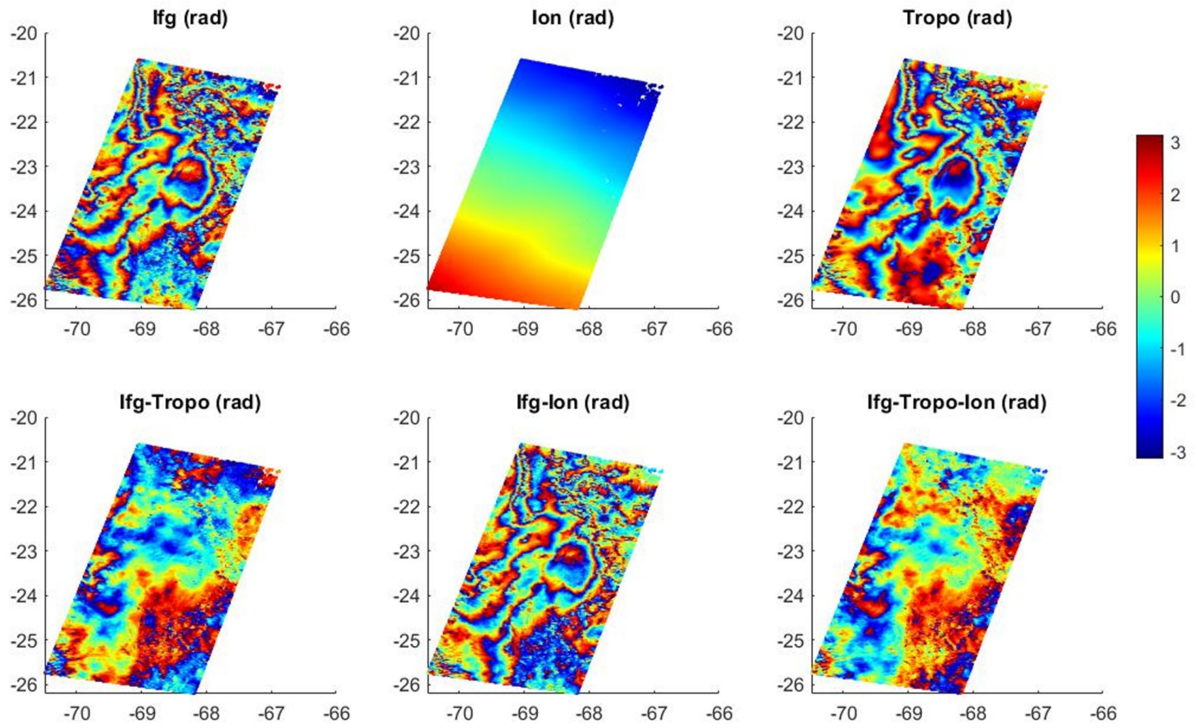

Figure 2.2: Same as Figure 2.1 but for descending track data. The ionospheric delay is significantly smaller than that from the ascending track, mainly due to the different acquisition times. The tropospheric delay is the primary noise source and has been well corrected by GACOS.

The correction methods for atmospheric delay can be broadly divided into two categories. The first category uses information in the data to perform the correction, for example, the power-law method (e.g., Bekaert et al., 2015; Zhu et al., 2017) for tropospheric correction and the split-spectrum method for ionospheric correction (e.g., Gomba et al., 2016; Fattahi et al., 2017; Liang et al., 2019; Luo et al., 2019). While another one is more atmosphere model-based, and usually needs data from additional sources to know the key parameters in the model and then perform the correction (e.g., GACOS correction for the tropospheric delay, Yu et al., 2018).

For Sentinel-1 InSAR time series analysis, although frequent estimations could alleviate the situation, it is always recommended to perform the tropospheric corrections to reduce the uncertainties of estimated linear velocity or coseismic deformations given the substantial noise level. However, the magnitude of ionospheric delay depends on the latitude of the experimental area and the acquisition time, which affects sun activity and the TEC, and therefore is more worth doing in low latitude region on ascending track data (Figure 2.3, 2.4, 2.5).

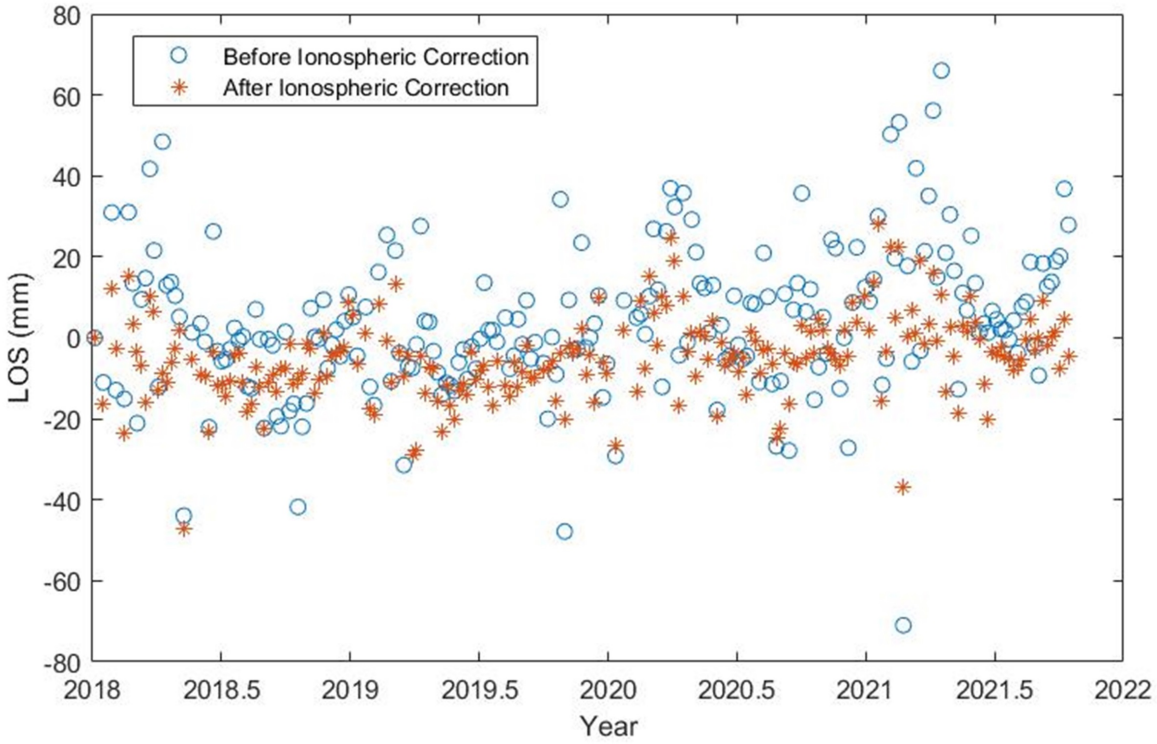

Figure 2.3: An example of applying ionospheric corrections on ascending time series data. The data shows the standard deviation reduction after ionospheric corrections, and becoming more feasible to fit the seasonal term. Data from chapter 4 with tropospheric correction (by GACOS) already been applied.

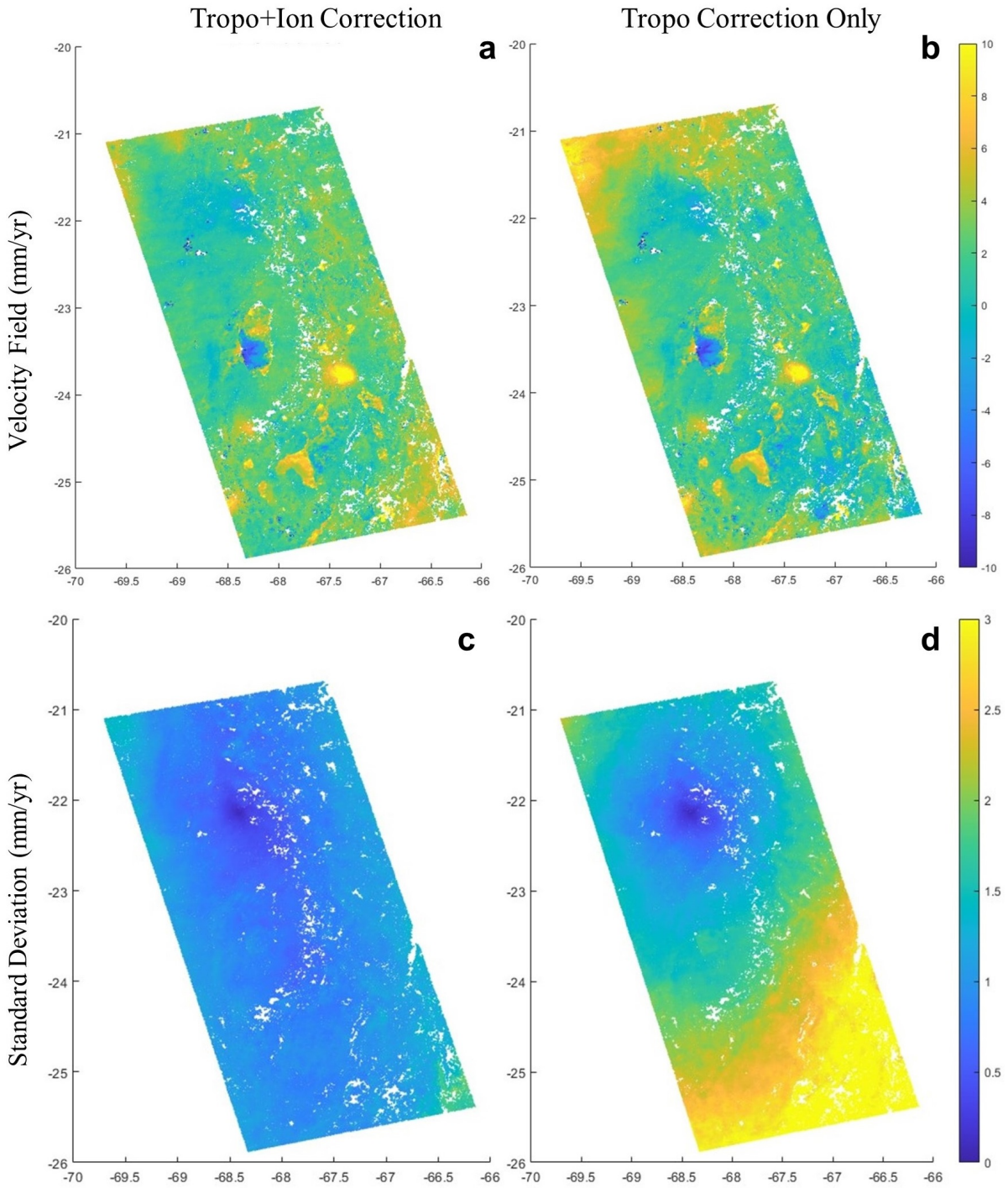

Figure 2.4: The impact of the ionospheric correction on the velocity field estimation. It shows although ionospheric correction has only a minor effect on absolute values of the velocity field (panel a,b), the standard deviations of the estimated value are significantly reduced (panel c,d). The low standard deviation values in the north indicate the location of the reference point on the tropospheric correction only panel, as errors will become smaller when get closer to the reference point. While on the contrary, the noise level remains low across the whole map after the ionospheric correction. Data from the ascending track in chapter 4

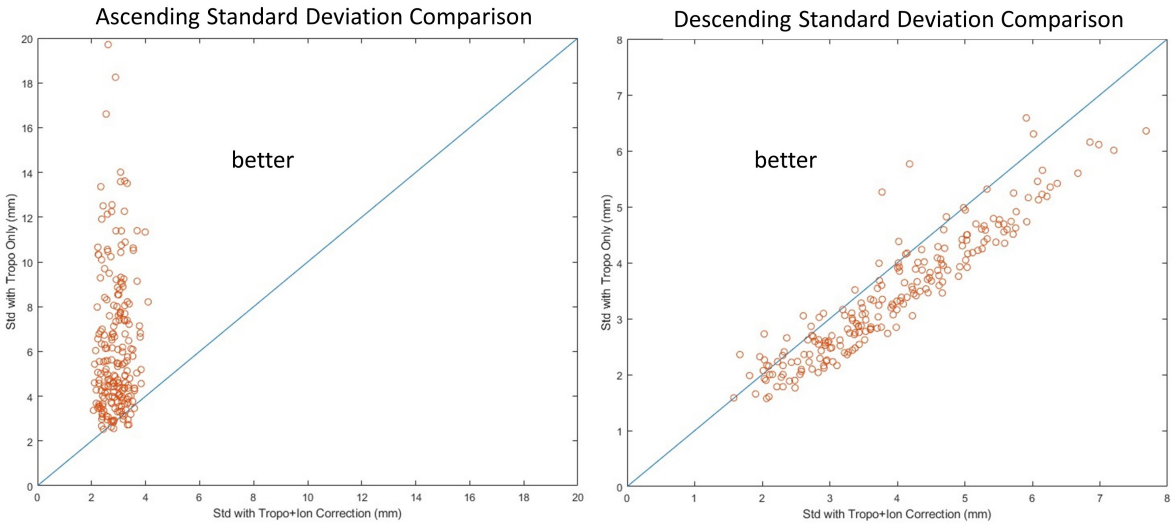

Figure 2.5: The comparison between ascending and descending ionospheric correction, using data from chapter 4 It shows the standard deviation comparison of individual interferograms after ionospheric correction, in addition to the tropospheric correction. It shows that although ascending track data is much improved after applying the ionospheric correction, the descending track data get worse. This is mainly due to the relatively small magnitude of the ionospheric delay on descending track data, the sensitivity and the introduced noise of the split spectrum method.

2.2.3 Phase Unwrapping Errors

Phase Unwrapping (PU) is another major error source for InSAR data processing. The PU error will add or subtract additional modulo 2π to the phase value of pixels, causing misinterpretation of at least half of the wavelength (for one 2π), or 28 mm for C-band InSAR data. PU errors could occur on individual pixels, but more often affect a broad area of pixels due to the integrating nature of the PU process (Goldstein et al., 1988). Similarly, since the InSAR time series represents cumulative deformation, the PU errors on the time series will propagate from where they occurred and affect all subsequent acquisitions, making it an even more pressing issue (Hooper et al., 2007; Osmanoğlu et al., 2011).

Unfortunately, currently, there is no ideal solution for correcting PU errors. Checking the phase consistency by adding up the unwrapped phase values in a phase closure could sometimes help identify or even correct the PU errors (e.g., Yunjun et al., 2019). However, this approach requires an epoch to present in multiple phase closures to identify whether the errors come from it. In addition, phase consistency is only the necessary, but not sufficient condition for correct PU solutions, and therefore cannot solve the problem entirely (Liu and Pan, 2019). While visually detecting and correcting PU errors manually could work, it requires experience and is

too time-consuming for large datasets. Overall, since the quality of PU is directly related to the coherence, obtaining high coherence or masking out low coherence pixels is still the primary way to guarantee the quality of phase unwrapping results.

2.2.4 Other Noise Sources

There are also some other error sources contained in the interferograms, including orbit error, DEM error, plate motion, phase closure residual, etc.

The orbit error will affect the perpendicular baseline estimation, which is typically small given the precision of the Sentinel-1 orbit, and will cause a long wavelength ramp on the interferogram that can be removed by polynomial fitting (e.g., Shirzaei and Walter, 2011; Fattahi and Amelung, 2014).

The DEM error comes from the inaccuracy of the DEM from external sources, and the look angle change due to the difference between the geometric and signal centroid of a pixel (Hooper, 2008). It is proportional to the length of the perpendicular baseline, and can be estimated and then removed when generating the velocity map (e.g., Ducret et al., 2013; Fattahi and Amelung, 2013).

The plate motion will cause a long wavelength signal on the InSAR velocity map, and it could be estimated and corrected by projecting the speed of local plate motion into the LOS direction (Figure 2.6, 2.7; Stephenson et al., 2022).

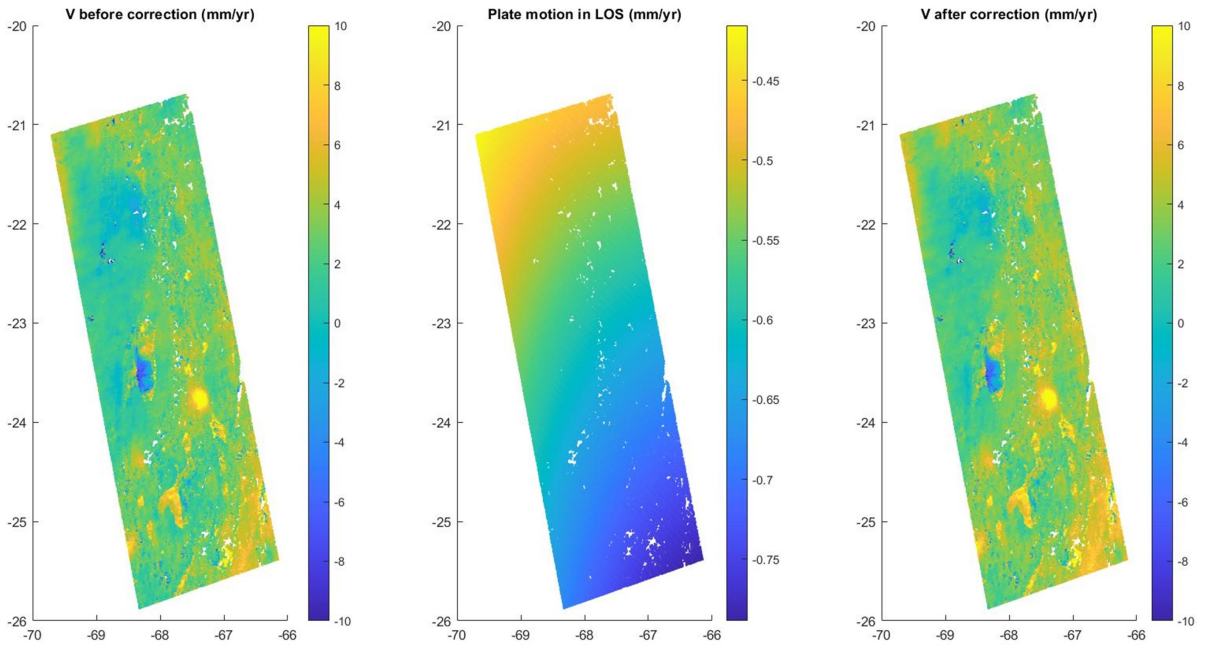

Figure 2.6: The plate motion correction on the velocity field. It shows the small magnitude of plate motion in the LOS direction due to the movement being mainly in the north-south direction which Sentinel-1 is less sensitive. Data from the ascending track in chapter 4.

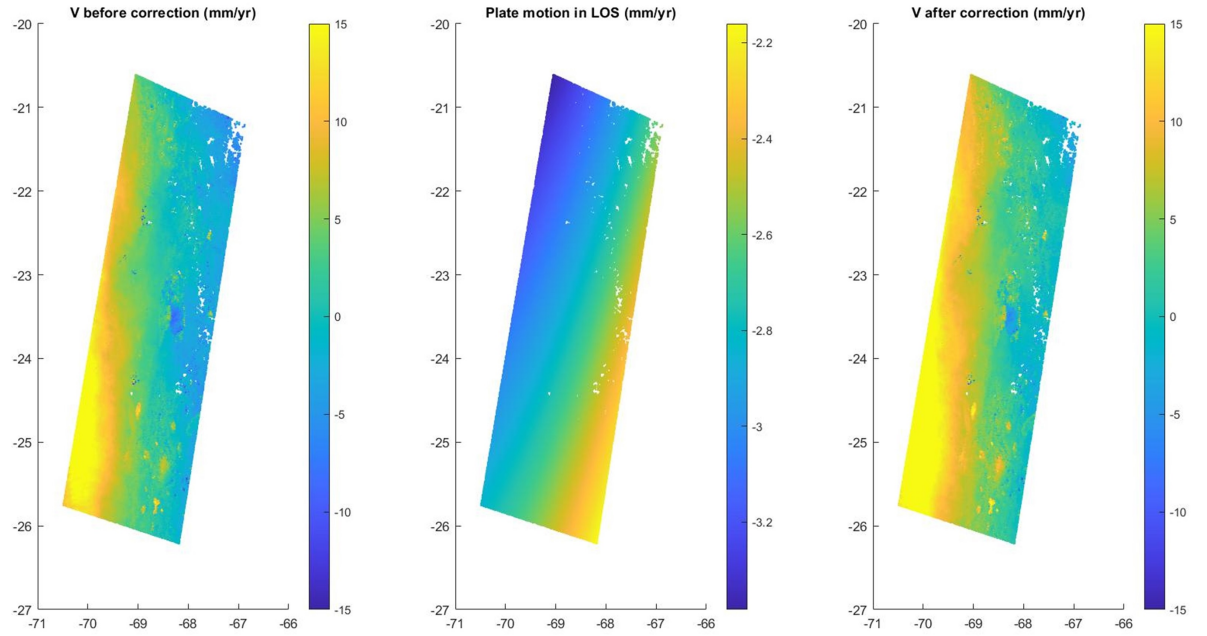

Figure 2.7: Same as Figure 2.6 but for the descending track data. The velocity in the southwest direction is faster due to the smaller angle of plate motion and LOS.

The phase closure residual refers to the non-modulo 2π residual of the sum of phases around a loop of three or more interferograms (De Zan et al., 2015; Zheng et al., 2022). It is caused by multilooking and non-linear filtering during the interferogram generation, and therefore should

be zero for non-filtered full-resolution interferogram (Liu and Pan, 2019). Recent studies suggest that this residual may cause the bias of velocity estimation, and could be associated with soil moisture (De Zan and Gomba, 2018). It is still not fully understood how the phase closure residual works, but it shows a clear connection to the quality of the pixel (or coherence) and should not have a large impact on the time series analysis of high coherence region (Maghsoudi et al., 2022).

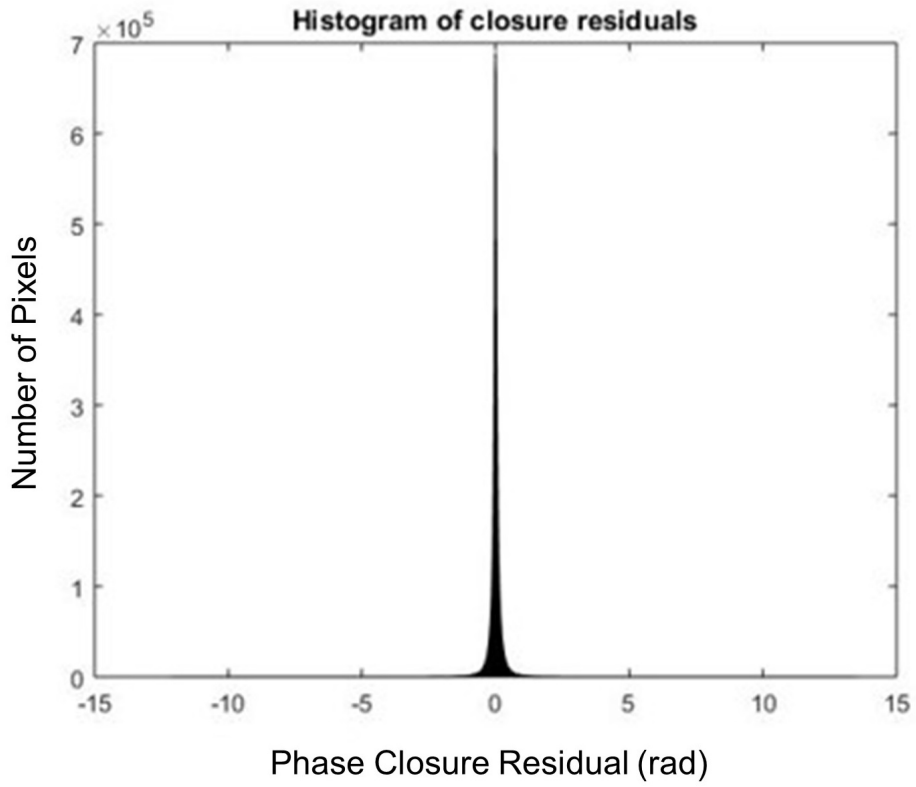

Figure 2.8: Phase closure residual due to multilooking or phase filtering. It shows the histogram of the non-zero sum of unwrapped phases on phase closures. When the data quality is good enough, these values should be concentrated on zero (which means that they all are unwrapped correctly). Data from the ascending track in chapter 3.

There are also other terms like solid earth tide or thermal noise (Agram and Simons, 2015; Xu and Sandwell, 2019; Wu et al., 2020), I simply ignore them due to the small magnitude of these signals and minor impacts on the results.

2.3 Time-Dependent Parameterized Fitting

For earthquake studies, InSAR time series analysis can obtain frequent estimations of the surface displacement thus provide better noise resilience. In addition, if I assume a time-dependent

deformation model appropriate for displacements caused by earthquakes, and fit it to the InSAR time series data, I can separate these signals and reconstruct the deformation (or velocity) fields for each of them. Considering deformation associated with the seismic cycle in Equation 1.2 and other non-tectonic signals within InSAR time series data, I assume that surface deformation at time t following a major earthquake at a time t_1 can be decomposed as follows:

$$\psi(t) = V_1 t + H(t-t_1)[C_1 + A_1 \ln(1+\frac{t}{\tau}) + V_2 t] + \sum_{i=2}^{n} H(t-t_i)C_i + A_2 \sin 2\pi t + A_3 \cos 2\pi t + b, \tag{2.2}$$

where V_1 is the long-term linear deformation rate through the whole time period which contains in part the interseismic displacement, A_1 and τ are the parameters for a logarithmic function representing the postseismic deformation (Ingleby and Wright, 2017; Liu and Xu, 2019), C_1 represents the coseismic displacement from the mainshock, V_2 is the potential linear deformation rate change after the earthquake event time, t_i and C_i represent the event time and the amplitude of aftershocks sorted by time, and A_2 and A_3 represent amplitude of the seasonal terms given the unit of t is year.

The deformation terms in the model may vary under different circumstances, depending on the magnitude and depth of the earthquake, the existence of aftershocks, and the noise level within the InSAR data. For large earthquakes occurring in the crust ($M_w > 7.0$) that can produce centimetre or even higher levels of displacements on Earth's surface, the coseismic and postseismic deformation signals are both significant and can be well captured if the coherence of InSAR data is good enough. I then can disentangle coseismic signals from the postseismic signal that occurred before the first post-acquisition due to the latency of SAR acquisition, and reconstruct less noisy coseismic and postseismic deformation fields, which is useful for the analysis of both coseismic and postseismic deformations and avoiding any possible systematic bias. Meanwhile, I can split up complex sequences of aftershocks by counting the coseismic deformations of these events into the model and solving them jointly with the mainshock. While for shallow small (M_w ~5.0, depth < 10 km), or large deep ($M_w > 6.5$, depth > 40 km) earthquakes, whose coseismic deformations on Earth's surface are barely observed, not to mention the postseismic signals, the model could be simplified by removing the postseismic deformation, the potential linear velocity changes, and all the aftershocks after the event. Then

the primary use of the time series fitting approach in this case is to improve the earthquake detectability and refine the deformation signal of earthquakes with low SNR. As for the seasonal terms, it usually depends on the magnitude of atmospheric noise (or how well they are corrected) and also the length of time series data, and I find that it is more feasible to fit the seasonal terms after better atmospheric noise removal.

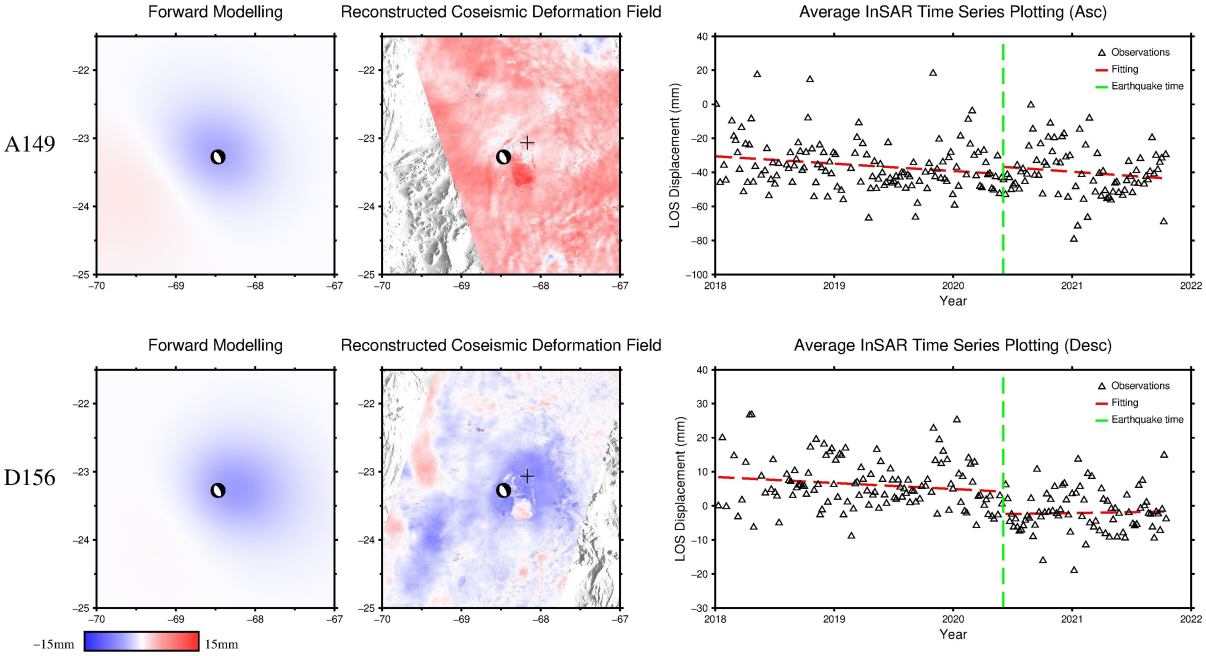

Figure 2.9: Example of the reconstruction of the coseismic deformation fields affected by ionospheric noise (the M_w 6.8 earthquake in chapter 4) when corrections are not applied. From left to right, the forward modelling from the USGS solution (strike: 332°, Dip: 59°, Rake: -94°, centroid depth: 112 km, Moment: 2.29×10^{19} N-m), the reconstructed coseismic deformation field, and the average InSAR time series of peak displacement pixels. The data does not include ionospheric correction so we cannot see clear coseismic signals on the ascending track. For the forward modelling, I assume a uniform dislocation embedded in an isotropic elastic half-space, faults are equal in width and length, the slip-to-length ratio is set to 1.5×10^{-5} for this interplate earthquake (Scholz, 2002), and an empirical rigidity value of 75 GPa (from USGS) is used here for moment calculation. The epicentre of the earthquake and the location of peak displacement pixel are indicated by the black focal mechanism, and the plus symbols. The red patch close to the southeastern point of the epicentre marked (which is observed on both tracks) indicates the shape of Salar de Atacama, and has different behaviour in the time series. In all figures, positive values mean movements towards the satellite.

Equation 2.2 can become a linear equation if the value of postseismic time τ is determined or assumed, which is important for performing least square inversion and evaluating the uncertainties of each solved parameter. This can be achieved by solving a few pixels near the field using a non-linear method like the Bayesian approach, and using their solution of τ for all the other pixels for quick parameterised fitting.

Similar models can also be used to simulate the surface displacements caused by volcanic activities on the InSAR time series. The sudden offsets on time series now can be explained by the volcanic eruption instead of the coseismic deformation, and the linear velocity change might be triggered by volcanic unrest. Taking the Socompa volcano unrest in chapter 5 for example, I observed the linear velocity change after the onset time of the unrest, and use the following model to fit the time series data:

$$\psi(t) = V_1 t + H(t - t_0)V_2 t + b, \tag{2.3}$$

where t_0 indicates the onset time of the volcanic unrest. In this scenario, I did not need to fit any deformations that related to earthquakes in Equation 2.2, and the seasonal terms due to the noise level.

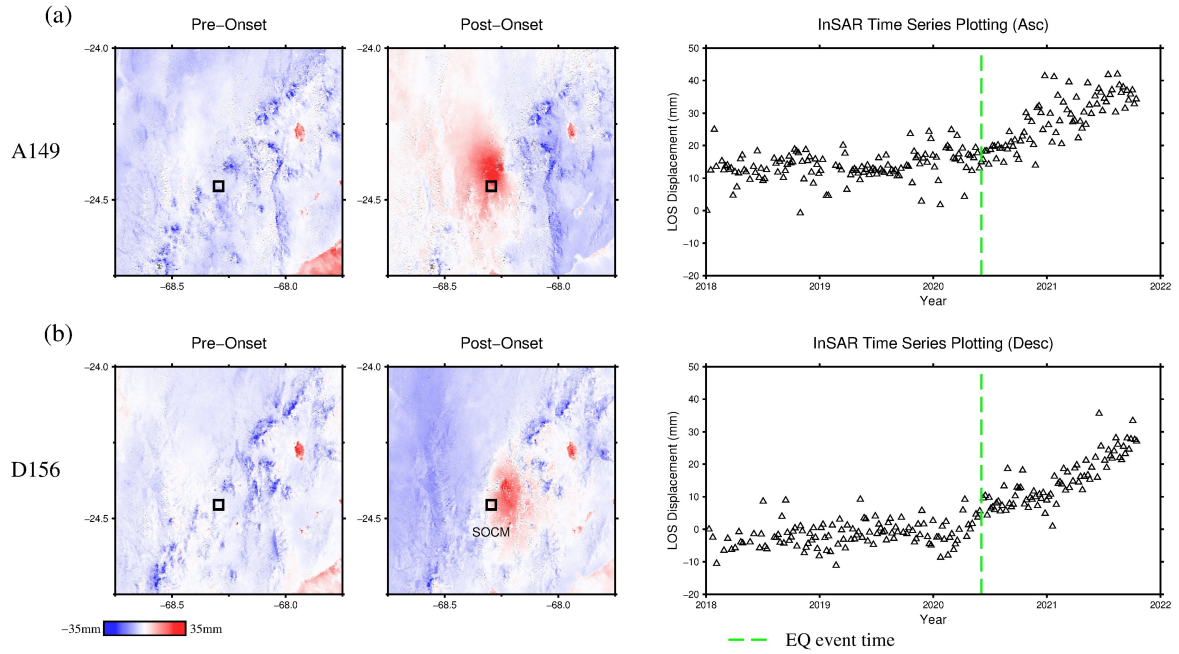

Figure 2.10: The example of the change of velocity after the Socompa unrest onset time. (a) The cumulative displacements pre- and post-onset time on ascending track data, and the time series data of the peak displacement pixels, using data from chapter 5 The green dashed vertical line indicates the event time of the nearby M_w 6.8 earthquake. (b) Same as (a) but for the descending track data.

Naturally, the processes of volcanic activities and earthquakes differ, and their displacement on Earth's surface in time varies case by case. Still, suppose a proper time-dependent model could be applied, and the InSAR time series data is well processed; in that case, we can perform the parameterised fitting and solve each deformation component for subsequent analysis and

modelling.

2.4 Independent Component Analysis (ICA)

Although parameterised fitting can retrieve different components, and reconstruct the deformation field or velocity maps from InSAR time series data, the noise level within the InSAR data could not always give robust solutions. In addition, parameterised fitting might suffer from the overfitting issue, especially when taking multiple aftershocks into account while the pixels are away from the earthquake or volcanic deformation source. The displacement signals of these far field pixels should be minor or neglectable, while the parameterised fitting will still provide a solution which might be unreasonable and far from the truth. A straightforward solution to this overfitting issue is trying to use different models based on the uncertainty of the solution, or the spatial distance to the deformation source (e.g., do not solve the coseismic offsets for the pixels at a given distance from the epicentre and set their values to zero), which however will produce inhomogeneous deformation field and might misinterpret some signals.

ICA is another frequently used approach to extract desired signals from various noises, which allows decomposing a mixed signal into a set of linear, additive components (Hyvärinen and Oja, 1997). A typical example of ICA is to identify one person's speech in a noisy room, which is based on the assumption that all the subcomponents are statistically independent of each other, and at most, one is Gaussian (Hyvärinen and Oja, 2000).

The deformation sources on InSAR time series data are either temporally or spatially independent of each other (Hetland et al., 2012), making it ideal for performing ICA approaches to extract earthquake or volcanic signals of interest (e.g., Ebmeier, 2016; Gaddes et al., 2018; Maubant et al., 2020). Generally, when we use multiple interferograms or InSAR time series data as input, ICA is capable to separate the data into several independent sources sources, including but not limited to linear deformation rate, topographic related signal, earthquake or volcanic signals, and random noise that contains in part the atmospheric delay, that all have the same dimension of a single interferogram. Since ICA is performed based on multiple images rather than pixels by pixels, it does not have the overfitting issue like the parameterised fitting and supposes to achieve less noisy deformation pattern of earthquake and volcanic signals (especially on the far field).

Depends on the temporal and spatial properties of deformation signals, and the size of input dataset, there are several different approaches to performing ICA on the same dataset (e.g., Cohen-Waeber et al., 2018; Zhu et al., 2022): 1) Using the time series data (cumulative displacements) and assuming the components are independent in space to perform spatial ICA (sICA). 2) Same as 1) but assuming components are independent in time to perform temporal ICA (tICA). 3) Using individual interferograms that span the deformation period to perform sICA or tICA. In this thesis, I apply ICA to retrieve the coseismic deformation of the M_w 6.8 intraslab earthquake in Northern Chile from 4 years InSAR observations as a case study. Due to the coseismic deformation is spatially independent to other sources and its relatively weak signal, sICA on the time series data shows superior performance over other ICA approaches using my dataset and successfully retrieve the coseismic signals (see more in chapter 4).

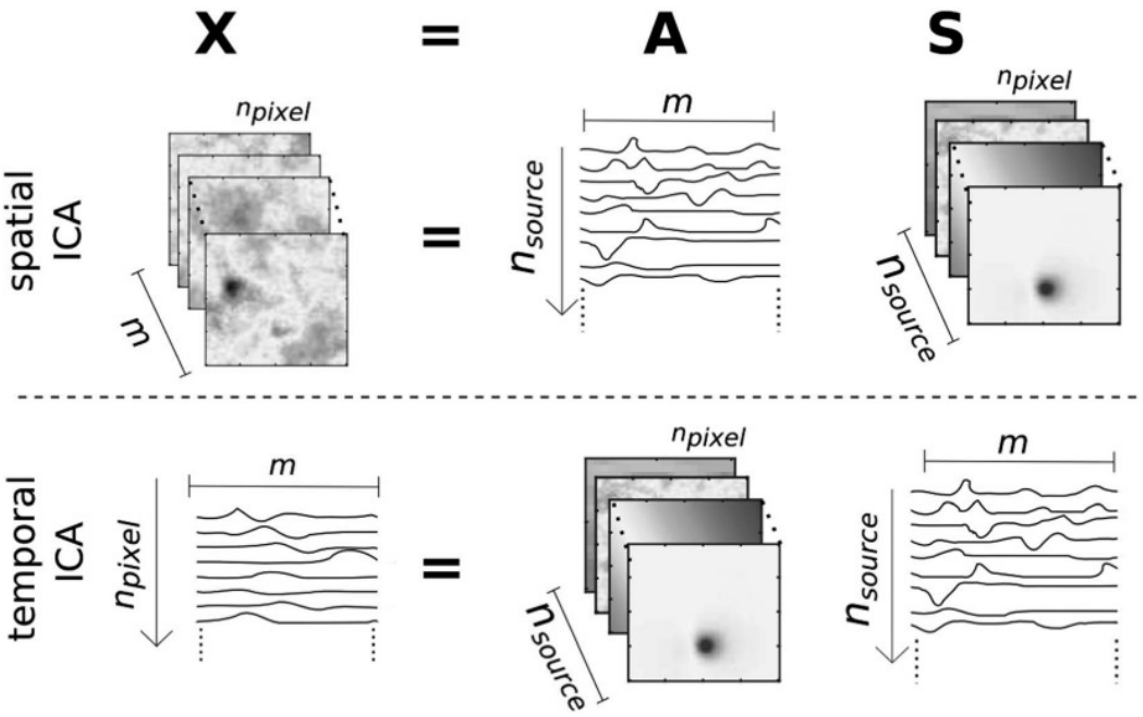

Figure 2.11: Cartoon illustrating the geometry of decomposition for InSAR time series data **X**, with **m** interferograms, each made up of n_{pixel} pixels. For sICA, rows of the mixing matrix, **A**, capture the relative contribution of each independent spatial component (rows of **S**). For tICA, spatial patterns are retrieved in the rows of **A**, while independent temporal components are retrieved in rows of **S**. Figure reproduced from Ebmeier, 2016

In my case study, when applying sICA for the InSAR time series dataset (matrix **X**, size of $n_{epoch} \times n_{pixel}$, where n_{epoch} and n_{pixel} are the number of epochs and pixels in each epoch, respectively), it can be decomposed into statistically independent components (matrix **S**, size

of $n_{ncomp} \times n_{pixel}$, where n_{ncomp} is the number of components that you would like the dataset to be decomposed), and the mixing matrix $\mathbf{A}$ (size of $n_{epoch} \times n_{ncomp}$) which describes the strength of each independent spatial component at each time step to restore the input datasets ($\mathbf{X}=\mathbf{A}\cdot\mathbf{S}$, Figure 2.11). Given the coseismic signal is spatially independent of other sources, I can apply sICA to extract the coseismic deformation pattern as an independent component from the input time series of cumulative displacements. More importantly, since the permanent coseismic spatial deformation pattern will remain on the time series data (the cumulative displacements) after the earthquake, we see a "coseismic offset" in the corresponding column of the mixing matrix, at the epoch near the earthquake event time. I then can solve for this "coseismic offset" using Equation 2.2 and use it to scale the deformation pattern retrieved in the corresponding independent component to estimate the coseismic deformation field.

However, despite ICA is a powerful tool to extract independent deformation signals from InSAR data, one major concern is how to determine the number of independent components. We would over-decompose the signal of interest into more local features and miss the complete signal if the number is too large, and the other hand, the data would be not fully decomposed the signal of interest would be covered by other more dominant components if the number is too small. The key factor here is the relative strength of signal of interest compared to other independent sources, and the random noise level within the input dataset (e.g., Gualandi and Liu, 2021; Peng et al., 2022). If the signal of interest is relatively strong, such as the linear deformation in InSAR data, then a small number of input components should work (e.g., less than 5) and probably no extra noise corrections are required. Otherwise, for very weak signal like the intraslab earthquake in my case, the number of components should be relatively high (e.g., larger than 10) to fully decompose the data and retrieve the signal of interest, and some corrections might have to be done to reduce the random noise level within the data before applying the ICA. Therefore, for the real world application, we need to know the spatiotemporal characteristics of the main deformation sources, which includes the relative magnitude of signal of interest, and also the random noise level (mainly from atmospheric delay for InSAR data). However, such information may know or not before applying the ICA, and normally multiple iterates and adjustments are required to test the robustness of the algorithm performance before determining the optimal number of components (e.g., Gaddes et al., 2019), which however sometime could be subjective (Hyvärinen, 2013).

In my case study in chapter 4, since the coseismic signal is very weak and long wavelength from InSAR perspective, I do the atmospheric correction (both troposphere and ionosphere) before ICA is applied, which greatly reduce the level of random noise within InSAR data that otherwise ICA may fail to retrieve the coseismic signal. In addition, I also mask out some areas that show different behaviours in response to the earthquake, or still have strong remaining atmospheric turbulence near the coast, that may impede the robustness and effectiveness of the algorithm performance. Then I apply the sICA on time series data, and manually adjust the number of components until robust coseismic signals can be retrieved (obtaining the same results by running multiple times). Finally, nine components in ascending and ten components in descending are selected, respectively, to perform sICA and retrieve the coseismic deformation field using the method mentioned above.

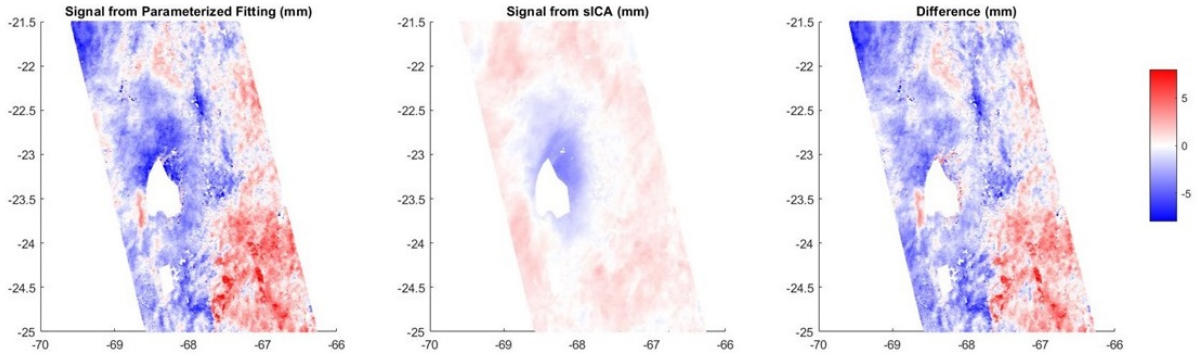

Figure 2.12: A comparison between parameterized fitting and sICA using InSAR time series data. It shows the retrieved coseismic deformation fields of the M_w 6.8 earthquake using different approaches on ascending track data (both tropospheric and ionospheric delays are corrected). It shows that sICA achieves higher SNR signals compared to that from the parameterized fitting. More details are described in chapter 4.

2.5 Conclusion

Overall, InSAR time series analysis utilises multiple observations to provides frequent estimation of surface displacement through time, improving our ability to measure the seismic cycle and monitor volcanic activities. It also boosts the accuracy and robustness of measurements by mitigating some systematic errors within the InSAR data (for example, atmospheric delay, DEM errors, etc). Furthermore, by applying the time-dependent parameterised fitting or blind source separation approaches like ICA to the time series data, it is possible to better retrieve the deformation field and improve the SNR and subsequent modelling results.Although some challenging issues like PU or quality control remain to be difficult to deal with, the performance

of InSAR time series have been improving with developed algorithms and new SAR missions (e.g., forthcoming NISAR, Kellogg et al., 2020), leading to fully automated processing flow in the future (Feng et al., 2016).

Chapter 3

Improving the Resolving Power of InSAR for Earthquakes Using Time Series: A Case Study in Iran

F. Liu[1], J. R. Elliott[1], T. J. Craig[1], A. Hooper[1], and T. J. Wright[1]

[1]COMET, School of Earth and Environment, University of Leeds, UK

Citation: Liu, F., Elliott, J. R., Craig, T. J., Hooper, A., & Wright, T. J. (2021). Improving the Resolving Power of InSAR for Earthquakes Using Time Series: A Case Study in Iran. Geophysical Research Letters, 48, e2021GL093043. https://doi.org/10.1029/2021GL093043

Key Points

- Using time series analysis, we can detect small coseismic displacements that are not readily visible or ambiguous in single interferograms
- Earthquakes occurring close in time and space can be separated by a time-dependent parameterized model fitted to InSAR time series analysis
- We can achieve more robust and seismologically consistent earthquake modelling results by using a time series approach

3.1 Abstract

Interferometric Synthetic Aperture Radar (InSAR) is an established method to measure earthquake surface displacements. However, due to decorrelation and atmospheric noise, only a certain fraction of earthquakes is readily observable with single interferograms. To enhance the potential of retrieving InSAR earthquake observations, we apply InSAR time series analysis and use several recent earthquakes (M_w 5.6-6.3, 2018-2019) in Iran as case studies. We find that the coseismic displacement signals of these earthquakes, which might not be discernible within single interferograms, are better resolved using our approach. We reconstruct the coseismic deformation fields by fitting surface displacements using a time-series approach. We find that the reconstructed coseismic deformation fields yield more robust and seismologically consistent earthquake modelling results when compared to single coseismic interferograms. Our work suggests that a time-series approach is an effective way to improve the resolving power of InSAR for earthquake studies.

Plain Language Summary

Earthquakes cause the ground to temporarily shake, but also result in permanent movement of the surface of the Earth. This surface displacement can be detected using sensitive radar echoes from satellites when it is large enough. By differencing phases of radar images from before and after the earthquake (a technique known as interferometry), it is possible to detect where an earthquake has happened and determine its source parameters. However, the atmosphere and different imaging conditions cause noise in individual interferogram images, masking the earthquake movement. Here, we use a method involving a time series of multiple images before and after the earthquake to improve the picture of the earthquake by observing how the estimates of ground movement change through time. We therefore improve measurement of the distribution and amount of ground movement, allowing the detection of smaller earthquakes than before. Using a sequence of recent earthquakes in Iran as a test case, our method improves the assessment of the type and the location of detected earthquakes compared with single image interferogram data (average 36% uncertainty reduction), with the validation from seismic data. Our work demonstrates the enhancement of this time series approach and its potential in future earthquake studies.

3.2 Introduction

With the advancement of Synthetic Aperture Radar (SAR) satellite missions, Interferometric SAR (InSAR) has become an established method to measure the Earth's surface deformation caused by earthquakes, greatly improving our ability to observe active tectonic processes (Massonnet et al., 1993; Peltzer and Rosen, 1995; Salvi et al., 2012; Elliott et al., 2016). InSAR offers an alternative approach, other than seismology, to provide independent measures of fault location, depth and orientation (e.g., Pedersen et al., 2003; Lohman and Simons, 2005a). Unfortunately, due to the dominant error sources within InSAR data of decorrelation and atmospheric noise (Zebker et al., 1997; Agram and Simons, 2015), only earthquakes above a certain size or that are shallow enough can be observed. Recent studies exploit the potential of the latest SAR satellites using single interferograms to detect earthquakes in the first instance (e.g., Funning and Garcia, 2019; Morishita, 2019), but the overall detectability of earthquakes by this approach is inconsistent and non-robust, and subject to extremely high failure rates (49% failure for Sentinel-1 and 23% failure for ALOS-2).

This circumstance makes using InSAR for earthquake studies challenging, especially for small earthquakes (M_w 5.0-6.5, from a geodetic point of view) due to their weak signals, despite in some cases still causing fatalities when close to population centres (England and Jackson, 2011). However, there is merit in trying to increase the sensitivity of our observations, as we can draw inferences from a huge number of small earthquakes assuming their behavior scales similarly with large ones (Ide, 2019). Additionally, by precisely locating these small earthquakes, it may be possible to link seismic activity directly with active fault structures that are capable of larger earthquakes.

To achieve more accurate and robust measurements, InSAR time series analysis has previously been proposed (Hooper et al., 2012; Jolivet et al., 2012; Crosetto et al., 2016; Osmanoğlu et al., 2016). Phase-stable or high-coherence pixels are identified to reduce the decorrelation noise (e.g., Ferretti et al., 2011; Samiei-Esfahany et al., 2016), and spatiotemporal filtering is applied with the optional implementation of a tropospheric correction to lower the impact of atmospheric noise (e.g., Goldstein et al., 1988; Li et al., 2005; Doin et al., 2009; Pepe et al., 2015; Dalaison and Jolivet, 2020). Some recent cases show that InSAR time series analysis, which has been used to measure small amplitude, long duration ground displacements associated with interseismic strain accumulation, postseismic deformation, and shallow creep (Hilley et al., 2004;

Fialko, 2006; Ryder et al., 2007), has the capability to extract coseismic signals from various sources of noise (Fielding et al., 2017; Grandin et al., 2017), suggesting a promising way for enhancing earthquake detection using InSAR.

To fully exploit the potential of InSAR in earthquake detection and modelling, we perform InSAR time series analysis of Sentinel-1 data and focus on three recent earthquakes (M_w 5.6-6.3, ~10 km depth) in south-western Iran as case studies. The Arabia-Eurasia collision causes numerous large earthquakes that have been recorded in history (Ambraseys, 2001) and long-lived postseismic afterslip from more recent observed events in this broad deformation zone (Copley and Reynolds, 2014; Copley et al., 2015). On 12 November 2017, the large M_w 7.3 Ezgeleh-Sarpolzahab earthquake struck this region, triggering many aftershocks and long-lived post-seismic deformation in the area surrounding the mainshock (Feng et al., 2018; Barnhart et al., 2018; Nissen et al., 2019). We focus on three notable late aftershocks as examples (M_w 6.0, M_w 6.3, and M_w 5.6 earthquakes, which happened on 25 August 2018, 25 November 2018, and 6 January 2019 respectively). We process five years of Sentinel-1 observations over this area, from November 2014 to September 2019 to ensure enough data is available to constrain potential secular and annual deformation (Figure 3.1), and reconstruct the enhanced coseismic deformation field using a parameterized function describing surface displacement to time series data. We use independent seismological observations and a recent geodetic solution (Fathian et al., 2021) to validate our approach. We find that our deformation fields better constrain the source models and are more consistent with seismological data compared to those using single interferograms.

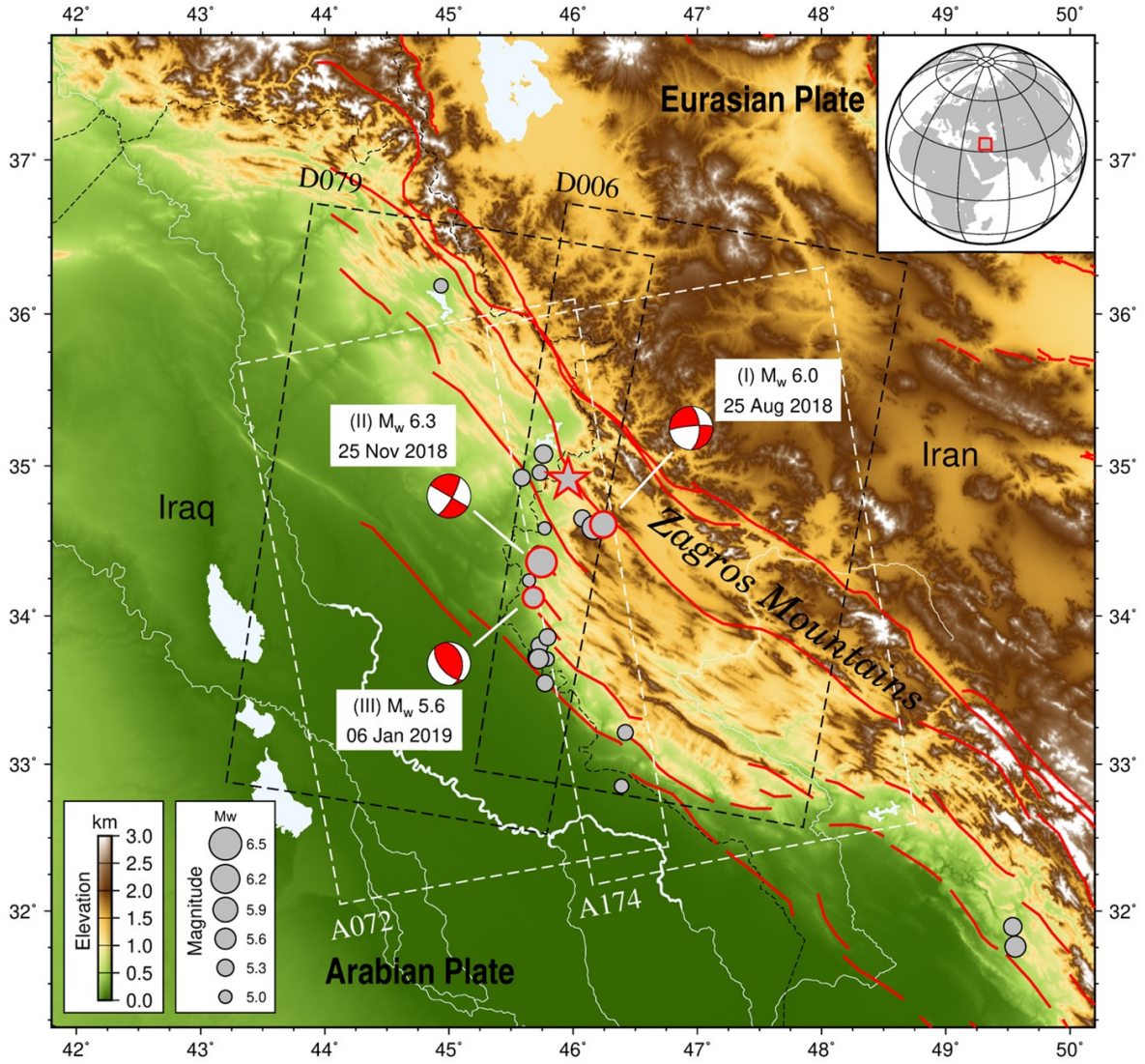

Figure 3.1: Topographic map of the Iran-Iraq border area. The epicentre of the large M_w 7.3 earthquake from 12 November 2017 is shown by the red star, the three study cases are indicated by focal mechanisms, and all other $M_w \geq 5.0$ earthquakes from the United States Geological Survey (USGS) catalog are represented by gray circles (spanning Nov 2014 to Sep 2019). The white and black dashed rectangle boxes show the area of processed Sentinel-1 data from two ascending tracks (A072 and A174) and two descending tracks (D079 and D006). Red lines show major active faults (Styron and Pagani, 2020).

3.3 Methodology

Using Sentinel-1 Single Look Complex (SLC) images we form interferograms with multilooking (4 in azimuth and 20 in range yielding a pixel size of ~50×60 m^2) and spatial filtering using the LiCSAR processor chain (Lazeckỳ et al., 2020). The DEM used during the processing is Shuttle Radar Topography Mission (SRTM) 3 sec. We form interferogram networks by connecting each image to three subsequent acquisitions and use the StaMPS software (Hooper et al., 2007) to

perform time series analysis, including GACOS corrections for tropospheric artefacts using the TRAIN software (Bekaert et al., 2015; Yu et al., 2018).

For earthquake studies, InSAR time series analysis leads to frequent estimates of surface displacement through time, providing better noise resilience. Compared to single interferograms, we can improve earthquake detection and the quality of coseismic surface deformation measurements in time series, especially when the deformation signals are obscured by decorrelation or atmospheric noise. Additionally, we can separate multiple earthquakes which occur close in time and space (e.g., the M_w 6.3 and M_w 5.6 earthquakes are separated by only 42 days and 30 km) through data fitting to time series (Figure 3.2).

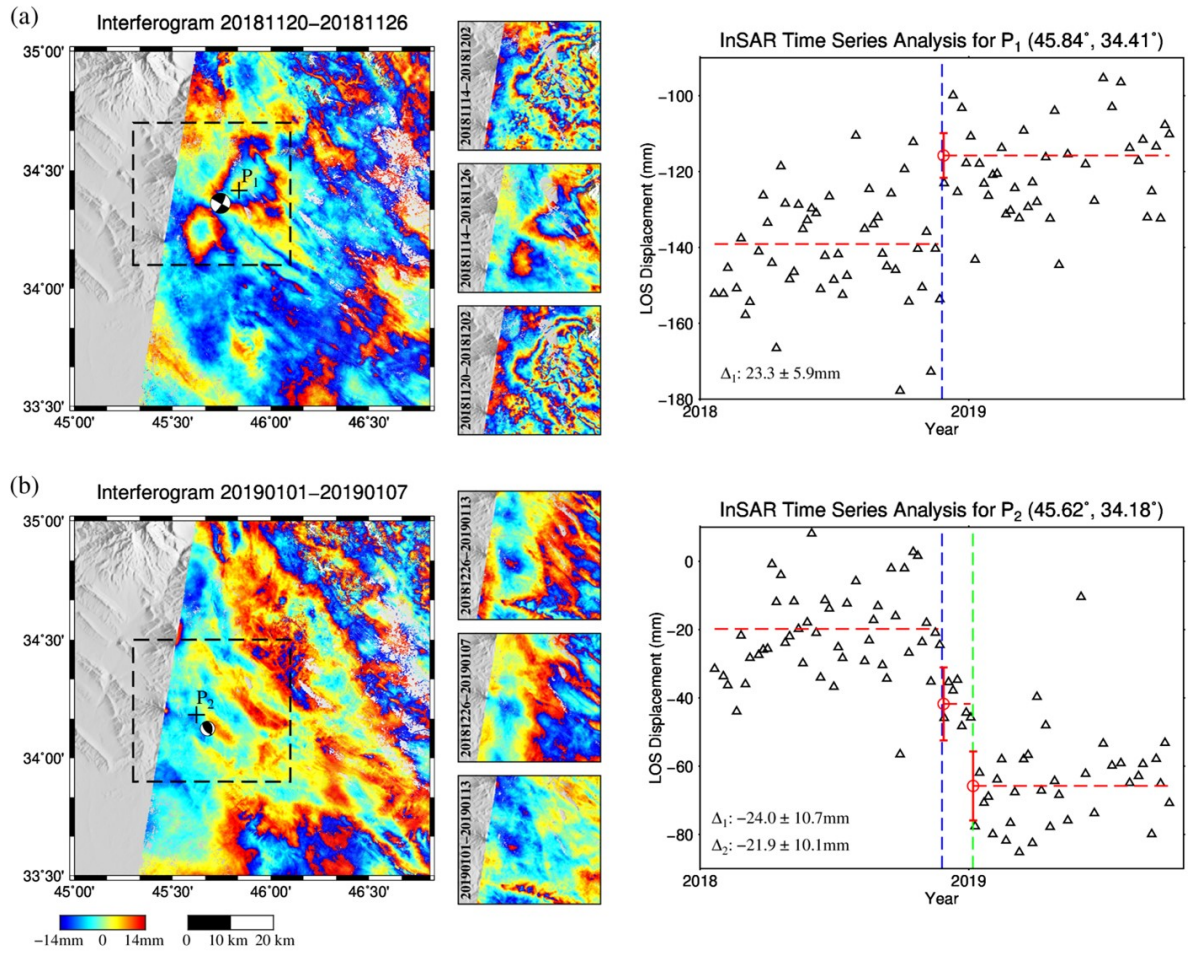

Figure 3.2: InSAR time series analysis improvements to earthquake detection, using the M_w 6.3 and M_w 5.6 earthquakes on track D006 as examples. The tropospheric noise has been corrected using GACOS. (a) Left: the shortest (6 days) interferogram covering the M_w 6.3 earthquake, and three longer interferograms (acquisition dates are indicated by the title) of the area covering the earthquake deformation marked by the dashed rectangle. Right: time series analysis for a representative peak displacement pixel P_1. Blue vertical dashed line represents the event time of the M_w 6.3 earthquake. Red horizontal dashed lines show a simple step function fitting of the data, and the values of the offsets (Δ) and error bars are shown at the lower-left corner. (b) Same as (a) but for the M_w 5.6 earthquake and pixel P_2, green vertical dashed line represents the event time of the M_w 5.6 earthquake.

Having established that a coseismic signal is discernable in time series, further improvements can be made if we assume a deformation model appropriate for displacements due to the seismic cycle. We can reconstruct the coseismic deformation field via a time series approach similar to that used in GNSS (Tobita, 2016; Heflin et al., 2020). Considering deformation associated with the seismic loading cycle, we assume that surface deformation at time t following an earthquake

at time t_0 can be decomposed as follows:

$$\Theta(t) = H(t - t_0)[C + A\ln(1 + \frac{t}{\tau})] + Vt + b, \tag{3.1}$$

where $H(t - t_0)$ is a Heaviside step function, C represents the coseismic displacement, A and τ are the parameters for a logarithmic function representing the postseismic deformation (Ingleby and Wright, 2017; Liu and Xu, 2019), V is the long-term linear deformation rate which contains in part the interseismic displacement, and b is a constant reference offset in observations.

Whilst postseismic deformation may occur following all earthquakes, we only consider the dominant postseismic deformation of the M_w 7.3 mainshock, as the three aftershocks we focus on are either relatively small in magnitude or occurred too close in time or space, impeding for robust postseismic fitting. Although this simplification will lead to the inclusion of some early post-seismic motion into the reconstructed coseismic deformation fields, the InSAR derived magnitude and moment from our approach (Table A.1) is consistent with seismological observations, illustrating this effect is limited in these cases. Other smaller events occurred close to our study cases but cannot be distinguished in time series either because they are too small or too close to other larger-magnitude earthquakes. Additionally, since the deformation signals of the three study cases are coincident in time (Figure 3.2b), we fit all three aftershocks in one equation. The model we used in this study is then:

$$\psi(t) = H(t - t_1)[C_1 + A\ln(1 + \frac{t}{\tau})] + \sum_{i=2}^{n} H(t - t_i)C_i + Vt + b, \tag{3.2}$$

where t_i and C_i represent the event time and the coseismic deformation of each earthquake sorted by time ($n = 4$ in this study, with first event at t_1 denoting the mainshock).

We first use maximum likelihood approach to determine the postseismic time τ and find it can be a constant value ($\sim$ 6 days) in our study (Figure A.1). We then reduce the fitting of Equation 3.2 to a linear inverse problem and evaluate the other parameters and their uncertainties (Figures A.2-A.4).

3.4 Results

3.4.1 Coseismic Deformation Reconstruction

Our reconstructed coseismic deformation fields improve the detectability of earthquakes (Figure 3.3 and A.5), and obtain higher signal-to-noise ratios (SNR) as indicated by the reduced noise observed in the semi-variogram fitting (Figure A.6). The coseismic deformation signals are clearer and more easily recognizable after reconstruction, especially on the ascending track. Here we take the most challenging M_w 5.6 earthquake (given its small magnitude) as an example. On both ascending and descending tracks, the deformation signals in the interferograms are masked by strong atmospheric noise, but are not quite weak enough to be completely invisible upon examination of multiple interferograms (Figure 3.2b). After reconstruction, we successfully make the earthquake signal more readily apparent for identification, resolving the ambiguity of whether it is associated with an earthquake deformation signal or solely atmospheric noise. Additionally, we can see that the deformation pattern in the reconstructed signal becomes more similar to the expected deformation, shown in the forward modelling (based upon the seismological catalog focal plane solution), implying a more seismologically consistent earthquake model.

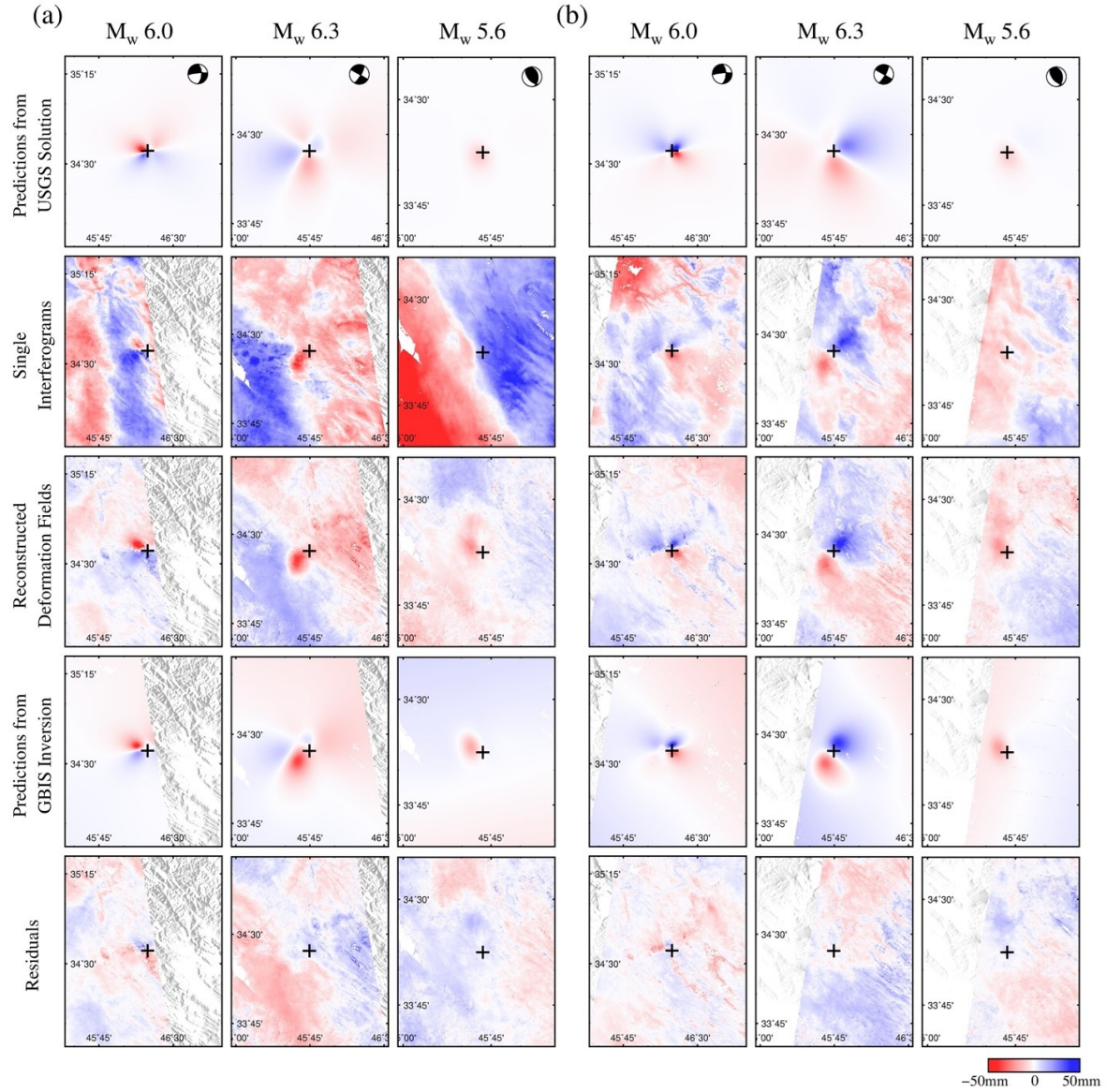

Figure 3.3: Comparison between the shortest interferograms and the reconstructed deformation fields. For the prediction from USGS solution, we assume a uniform dislocation embedded in an isotropic elastic half-space (Okada, 1985), faults are equal in width and length, and the slip-to-length ratio is set to 6×10^{-5} for these intraplate earthquakes (Scholz, 2002). The plus symbols indicate the epicentre of the focal mechanism from USGS solution. (a) Data from track A072. From top to bottom, the rows represent the predictions from USGS solution, the single interferograms, the reconstructed deformation fields, predictions from GBIS inversion (Bagnardi and Hooper, 2018), and the residuals between the reconstructed deformation fields and the predictions from GBIS inversion, respectively. (b) Same as for (a) but for track D006.

3.4.2 Earthquake Modelling

We first downsample the data, reducing the number of pixels to ~ 500, with a greater pixel density in the nearfield (Figure A.7). Then we use the GBIS software (Bagnardi and Hooper, 2018) to provide a uniform fault plane slip solution with uncertainties to ascertain the improvement

gain in constraining fault parameters from our reconstructed deformation fields, and compared to independent seismological observations and a recent InSAR solution (Fathian et al., 2021). A common issue when modelling small or buried earthquakes that do not rupture up to the surface, is that a focal plane ambiguity remains in InSAR solutions (as it does in seismologically determined solutions). Here we try to model both focal planes and select the one which provides a normally distributed output of strike values (M_w 6.0 and M_w 6.3) or more seismologically consistent solution (M_w 5.6).

The geodetic solutions from our data (Figure 3.4 and Table A.1) show that although there are some discrepancies (e.g., rake value for the M_w 6.0 earthquake), they agree well with the seismological observations, and the modelling results from our time series approach are more seismologically consistent (average 18% vs 22% relative changes). More importantly, reconstructed deformation fields provide better-constrained solutions, with an average of 36% narrower confidence interval (CI) for all three earthquake parameters. The M_w 6.0 earthquake achieved the most obvious gains (average 56% CI reduction) as the deformation signals are more distinct after reconstruction. The M_w 6.3 earthquake, whose signals are already clear before reconstruction, has the least difference modelling results (1% relative change) while our approach gives significant CI reduction (average 26%). Conversely, the solution of the M_w 5.6 earthquake, whose signals have been greatly enhanced following our approach, is still relatively poorly constrained. With only one elliptical lobe being clearly observed, it becomes difficult to constrain the fault geometry well (large uncertainties for strike and rake values). This reemphasizes the limitation of surface displacements in constraining geometry and resolving the focal plane rupture ambiguity when the rupture is buried and does not break the surface, even with improved SNR (Biggs et al., 2006; Elliott et al., 2010). Additionally, our approach achieves similar fault parameters and uncertainties as that from Fathian et al., 2021 for the already visible M_w 6.3 earthquake, whilst also providing significant improvements for the M_w 6.0 earthquake (Table A.1).

The better constrained result from depth and location measurements shows the advantage of InSAR observations (especially for time series, Figure A.8). Routine depth measurements for shallow continental earthquakes from the seismological observations contain values probably fixed a priori (such as 10 km depth for the M_w 6.0 earthquake from USGS catalog). Although the true values cannot be known without additional near-field constraints such as a dense aftershock survey, our approach provides better-constrained locations, and more informative

depth measurements with uncertainties for shallow events.

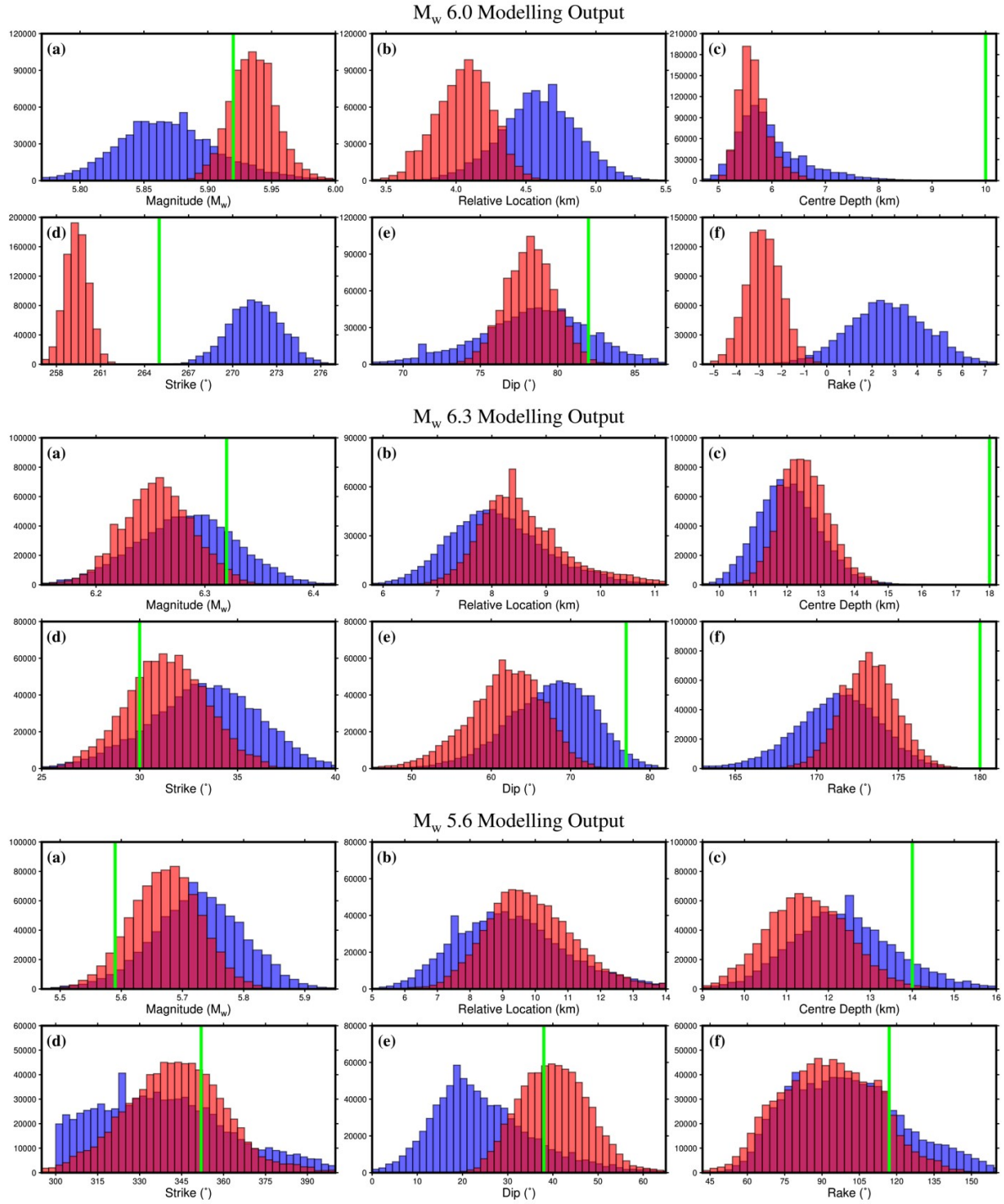

Figure 3.4: Modelling outputs for selected fault parameters. Red and blue bins represent the distributions from the reconstructed deformation fields and the shortest interferograms respectively. Green lines are the USGS solutions (note the rake value for the M_w 6.0 event is -31^o). (a) Earthquake moment magnitude. (b) Relative location, the horizontal distance between the InSAR derived source location and the epicentre of USGS (not indicated by green lines as zero reference value). (c-f) Fault plane centre depth, Strike, Dip and Rake values.

3.4.3 Comparison with Stacking

Stacking is another method to improve the SNR of InSAR data, which can also be helpful in extracting the coseismic deformation of small earthquakes (e.g., Qian et al., 2019; Luo et al., 2019; Luo et al., 2021). We perform stacking using all reconstructed pairs of pre- and post-event acquisitions to derive the coseismic deformation (Text S1), and compare it to our approach (Figure A.9, A.10).

Overall, stacking achieves a similar SNR to our reconstructed deformation fields, while our approach provides more robust earthquake modelling (average 17% CI reduction). Noticeably, the magnitude of the M_w 6.0 earthquake from stacking is biased larger than our approach, compared to the results of the other two earthquakes. We think this is because the post-seismic deformation of the mainshock is contained in the stacked results (Figure A.11), although we use observations six months later than the mainshock to perform stacking. This shows the larger impact from the post-seismic deformation of the mainshock than the early post-seismic motions of the aftershock in our model, and highlights a significant advantage of our approach that such bias can be reduced when modelling the aftershocks.

3.5 Discussion

3.5.1 Post-observation Numbers and Atmospheric Correction

As the reconstruction requires multiple observations either side of the event time, it is important to know how many acquisitions are required to achieve a reliable estimation of coseismic offset within uncertainty. Given the large archive of Sentinel-1 data that is being amassed, the required pre-observations can be flexible (depending on the noise characteristic, or the time series fitting model used) and may vary for different scenarios and study purposes. What we consider here is the number of post-earthquake observations required for a stable earthquake solution. Due to the long revisit time ($\geq$ 6 days now), it would be of little value if we needed to wait many months or even years to collect enough images to obtain a high SNR reconstruction. A key factor here is the magnitude of atmospheric noise, as it is one of the main error sources of InSAR. To determine the relationship between the quality of reconstruction, the post-observations numbers, and the level of atmospheric noise, we calculate the change of standard errors (SEs) of the fitted coseismic displacements as we increase the use of post-observations during fitting for both tracks,

with and without applying GACOS corrections first.

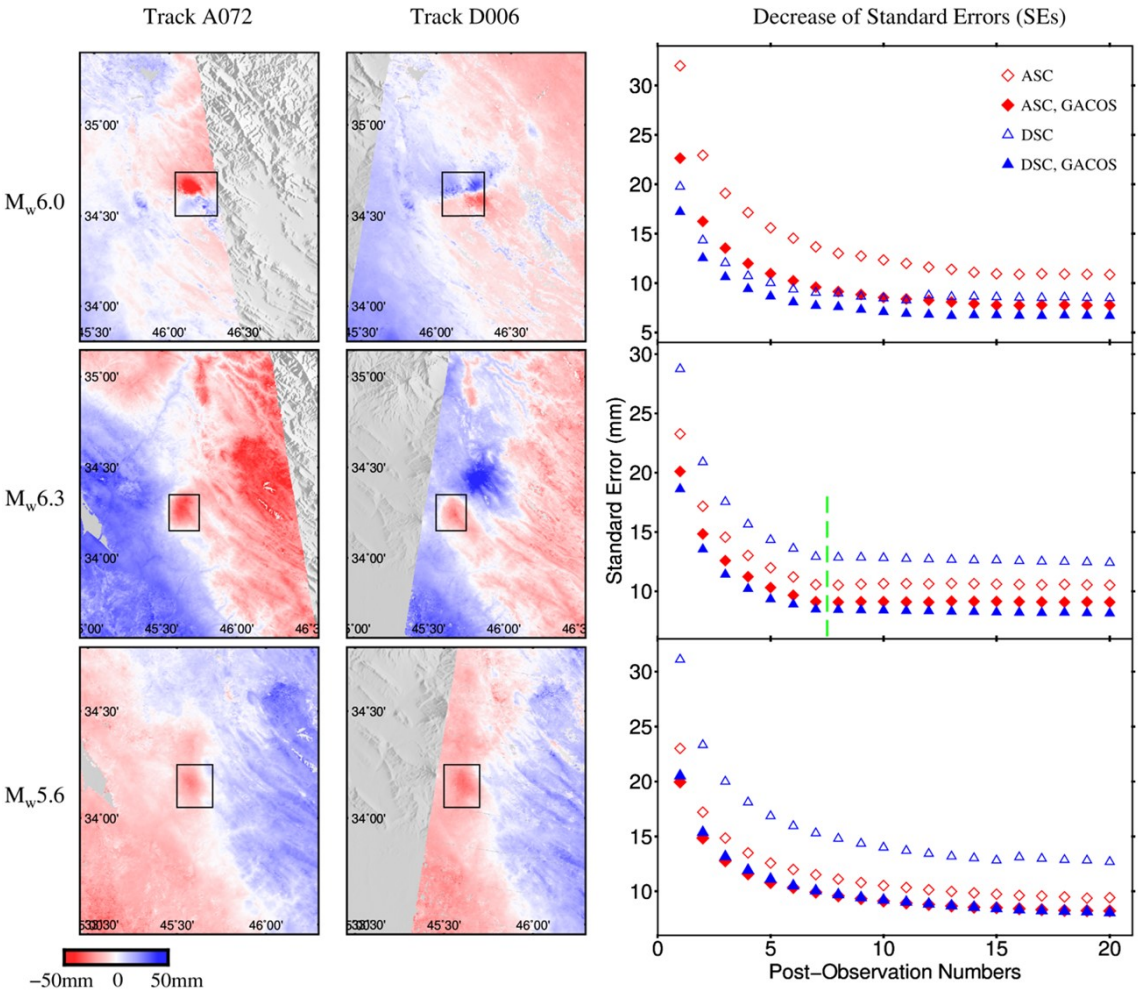

Figure 3.5: The impact of the number of post-observations used in time series and application of GACOS corrections on the quality of coseismic displacement reconstruction. For each row we show the optimal reconstructed deformation fields (using all our data) from two tracks without GACOS correction, and the corresponding decrease (proportional to $1/\sqrt{N}$) of the SEs as the post-observation numbers increase (using all pre-observations, $\sim$ 100 images). We show the mean SE values of all pixels within the black rectangle that cover the peak displacements.

The quality of reconstruction improves both with the application of GACOS corrections (average 24.1% SEs reduction) and the increase of post-observation numbers used (Figure 3.5). The M_w 6.3 earthquake is a special case as subsequent data are also used to fit the M_w 5.6 earthquake from the seventh post-observation onwards (the green dash line on Figure 3.5), causing its SEs to be fixed from that point forward. The low SEs at that point indicates the good quality of the reconstruction and also explains why these two earthquakes can be separated, although they are close in time and space. We determine the average number of post-observations for reaching

a threshold, where the SE is 10% above its minimum value, is 14 acquisitions. This suggests our approach will achieve a stable output after around 3 months from the event time (assuming the revisit time is 6 days) in our study area. The number of acquisitions for other areas, with different noise characteristics, may vary somewhat.

3.5.2 Long-term Linear Deformation Rate

For most of the pixels, the obtained long-term linear deformation rates are less than 10 mm/year (Figure A.12). However, considering InSAR can only acquire relative displacements to the reference point, the long-term deformation rates we measured are noticeably above the level of interseismic deformation rate expected from the recent strain-rate map of our study area derived from GNSS data (Khorrami et al., 2019). One of the main reasons for this difference may come from using a constant linear rate in Equation 3.2. The linear deformation rate may be markedly changed after the mainshock according to time series, which potentially biases the estimation of the interseismic deformation rate and consequently the coseismic offset. Additionally, the long-term rates may be associated with several other sources. Firstly, non-tectonic deformation, such as that from hydrologically-driven subsidence within basins is likely in this region. Secondly, topographically correlated atmosphere can map in as we do not include a seasonal term in the fitting. Thirdly, a cumulated bias for linear rate estimation in time series may be expected from the use of short period interferograms (Ansari et al., 2020). Lastly, discontinuities from phase unwrapping errors or any observation gap can have a significant impact on linear rate evaluation.

3.5.3 Implications of Our Approach

The primary use of our approach is to improve the InSAR detectability such that very small earthquakes ($M_w < 5.0$) may be observed when they reach to the surface (e.g., Qian et al., 2019; Lohman and Simons, 2005a), and refine the deformation signal of earthquakes with low SNR. Due to the poor constraints of precise fault location by seismological observations in regions of low instrumentation (Husen and Hardebeck, 2010), this will be useful for improving the identification of active faults within continental areas lacking dense seismic coverage.

Our approach can also be used to enhance the complex signals of large earthquakes ($M_w \geq 6.5$), reducing extra noise as we have done with smaller earthquakes. Additionally, it can disentangle coseismic signals from the postseismic signal that occurred before the first post-acquisition due

to the latency of SAR acquisition (Zinke et al., 2014; Floyd et al., 2016; Twardzik et al., 2019), useful for the analysis of both coseismic and postseismic deformations and avoiding any possible systematic bias in subsequent earthquake modelling (Weston et al., 2012).

Further applications of our approach include splitting up complex sequences of earthquakes (especially aftershock sequences as we have done here), and possibly studying small-amplitude signals from large, deep earthquakes within subduction zones (Barnhart et al., 2014).

3.6 Conclusion

We demonstrate the use of InSAR time series analysis for detecting and modelling aftershocks in the presence of the postseismic signal following a major earthquake that otherwise might go undetected within single interferograms. We develop an approach using reconstructed coseismic deformation fields to enhance the surface displacement signals and subsequently to better constrain the earthquake modelling, in particular location and depth. We show that our time series approach improves on noise reduction using additional acquisitions following an earthquake, and achieves a stable result with 14 post-observations in this study area. We conclude that a time series approach is effective for enhancing the InSAR resolving power for earthquake studies, and outline its possible applications for the future.

Acknowledgement

This work is supported by the UK Natural Environment Research Council (NERC) through the Centre for the Observation and Modelling of Earthquakes, Volcanoes and Tectonics (COMET, http://comet. nerc.ac.uk), and the Continents from Space (LiCS) large Grant (NE/K010867/1). Figures are made using the Generic Mapping Tools (GMT) (Wessel et al., 2013). The Sentinel-1 SAR data are copyrighted by the European Space Agency, and are additionally distributed by the Alaska Satellite Facility Distributed Active Archive Center (https://earthdata.nasa.gov/eosdis/daacs/asf). The processed InSAR interferograms used in this work are available at COMET-LiCS Sentinel-1 InSAR portal (https://comet.nerc.ac.uk/COMET-LiCS-portal/). John Elliott acknowledges support from the Royal Society through a University Research Fellowship (UF150282). Tim Craig thanks the Royal Society for support through URF180088.

Chapter 4

From Space to Slab: Probing the 112 km Deep M_w 6.8 2020 Intraslab Earthquake, Northern Chile, Using Geodetic & Seismological Observations

F. Liu[1], T. J. Craig[1], S. K. Ebmeier[1], and J. R. Elliott[1]

[1]COMET, School of Earth and Environment, University of Leeds, UK

4.1 Abstract

The driving factors behind large intraslab earthquakes ($M_w > 6.5$, 40-300 km depth), along with their potential seismic hazards, are poorly understood due to limited observational data of such events. Here, we present a case study of a 112 km deep M_w 6.8 earthquake on 3rd June 2020 under Northern Chile, supplementing seismological data with additional constraints from space geodesy. We retrieve the sub-centimetre coseismic deformation field (with peak surface displacements $\sim$ 6 mm) from four years of Sentinel-1 Interferometric Synthetic Aperture Radar (InSAR) time series analysis with atmospheric corrections, pushing the detectability limits of the technique for such deep events. Modelling this with combined Global Positioning System (GPS) and seismic data, we obtain a well-constrained fault plane and high average rupture speed (3.5 km/s rupture speed on 12.8 km length). Our work demonstrates the potential of using geodetic data to measure intraslab events, and the insights such data can add into the rupture mechanism and geodynamics of intraslab events.

4.2 Introduction

Large intermediate depth earthquakes ($M_w > 6.5$, 40-300 km depth) occurring within subducting slabs (hereafter referred to as intraslab events), are relatively infrequent ($\sim$ 500 events worldwide since 1976) and comprise only a small portion of the total moment release at subduction zones (Frohlich, 2006). However, they can be particularly devastating as they typically occur beneath coastal onshore areas, often with large population centres and have caused significant casualties in the past (e.g., Beck et al., 1998; Nakajima and Hasegawa, 2010; Singh et al., 2018). In the example case of South America, intraslab events comprise only $\sim$ 5% of the total moment release since 1918, which however are responsible for $\sim$80% of all earthquake-derived fatalities over the same period (Di Giacomo et al., 2018), predominantly in two catastrophic intraslab events in 1939 (Chillán, Chile, Astiz et al., 1988) and 1970 (Ancash, Peru, Abe, 1972). Due to the low frequency of intraslab earthquakes occurrence, we only have a short incomplete catalogue of the potential for these events to occur (e.g., Astiz et al., 1988), making it challenging to anticipate where and how large further earthquakes will be. Furthermore, the high topography of the volcanic arcs below which intraslab events mainly occur, is dominated by steep slopes and rapid erosion, leading to a higher probability of triggering secondary hazards (particularly landslides, Keefer, 2002), which themselves make the hazard assessment of

intraslab seismicity even more challenging.

Our understanding of intraslab earthquakes remains narrow in part due to a relative paucity of observational data, which heavily relies on seismology. With limited observations, it is difficult to grasp the physical process behind the occurrence of intraslab earthquakes. Since the brittle failure of intraslab events cannot be explained by a simple frictional model (Frohlich, 2006), different assumptions are raised regarding the additional processes, commonly inferred to be either through fluid overpressure linked to dehydration reactions (dehydration embrittlement, e.g., Hacker et al., 2003), or a rheological weakening of the fault zone (thermal runaway, e.g., Schmidt and Poli, 1998; Karato et al., 2001). These two hypotheses are still being debated, given the resolution of observational data and the accuracy of comparable models for the downdip evolution of the slab (such as thermal structure). In addition, the location of the hypocentre and focal mechanism of the intraslab events provide essential information regarding the geometry and stress orientation within slabs, which provide insight into the interplay between the sources of stress and even the properties of slabs such as temperature, hydrous state, and phase changes (Zhan, 2020; Hosseinzadehsabeti et al., 2021). However, this information is not always accurate and hard to evaluate from seismology, due to the quality of data, different processing approaches, and inherent uncertainty within the velocity model, particularly for the hypocentre depth due to the lack of vertical resolution (Engdahl et al., 1998). Overall, innovative ways are needed to explore and extract additional information from existing global multi-source observations, for a physics-based characterisation of the seismic potential of subducted slabs.

The development of space geodetic observations, mainly from Interferometric Synthetic Aperture Radar (InSAR), allows us to measure at a large scale the Earth's land surface deformation at the millimetre level, significantly improving our ability to observe and study active tectonic processes (Fielding et al., 2013; Hu et al., 2014; Elliott et al., 2016). InSAR offers measurements independent from seismology to obtain the properties of the source rupture (including location, orientation, and even geometry), yielding a potential for use in intraslab earthquake studies. Currently, the majority of earthquakes measured with InSAR are shallow events (depth < 40 km, e.g., Weston et al., 2012; Funning and Garcia, 2019) whose surface displacement signals are relatively large (centimetre level or higher) and easy to capture, even for smaller magnitude (M_w ~5.0) when these are very shallow (e.g., Békési et al., 2021). Conversely, intraslab earthquakes are rarely the focus of geodetic work, and only a few of the largest events have

been studied (Khash, Iran, M_w 7.7, 80 km depth, Barnhart et al., 2014; Navarro, Peru, M_w 8.0, 112 km depth, Vallée et al., 2023), due to the efforts required to distinguish ground deformation from noise. Global Positioning System (GPS) observations also provide high-precision surface displacement measurements, which are used to capture the signal of intraslab events (e.g., Wiseman et al., 2012; Steblov et al., 2014; Alif et al., 2021; etc.). Still, their sparse spatial distribution prevents the detection of the full extent of deformation patterns, and instead, they are commonly used as control points providing ground truth for InSAR (e.g., Del Soldato et al., 2021).

To demonstrate the potential of geodetic observations in intraslab earthquake studies, we focus on the 112 km deep M_w 6.8 earthquake that occurred on 3rd June 2020 in Northern Chile as a case study, using the geodetic data from both InSAR and GPS (Figure 4.1). We process $\sim$ 4 years of Sentinel-1 radar data to perform InSAR time series analysis (spanning Jan 2018 to Nov 2021) over the potential deformation area to better resolve the coseismic deformation that may otherwise be masked by atmospheric noise in individual interferograms (Methods 4.5.2). After correcting for both ionospheric and tropospheric noise, we successfully retrieve the coseismic deformation field (with peak displacements of $\sim$ 6 mm), and compare the difference in estimated surface displacements retrieved by using Independent Component Analysis (ICA) and model-based parameterised fitting approaches to the time series (Liu et al., 2021). Combined with the independent observations from several GPS stations in the near-field region and global seismology, we obtain a well-constrained subsurface fault plane (7.9 km and 12.8 km for median width and length, respectively), with high rupture speed (median value of 3.5 km/s) and centroid depth value of 110 km, using numeric models (e.g., Hutchings, 1994). We discuss the source characterisation and possible rupture mechanism of this event, and finally the potential contribution of geodesy, especially InSAR, for future study of intraslab events.

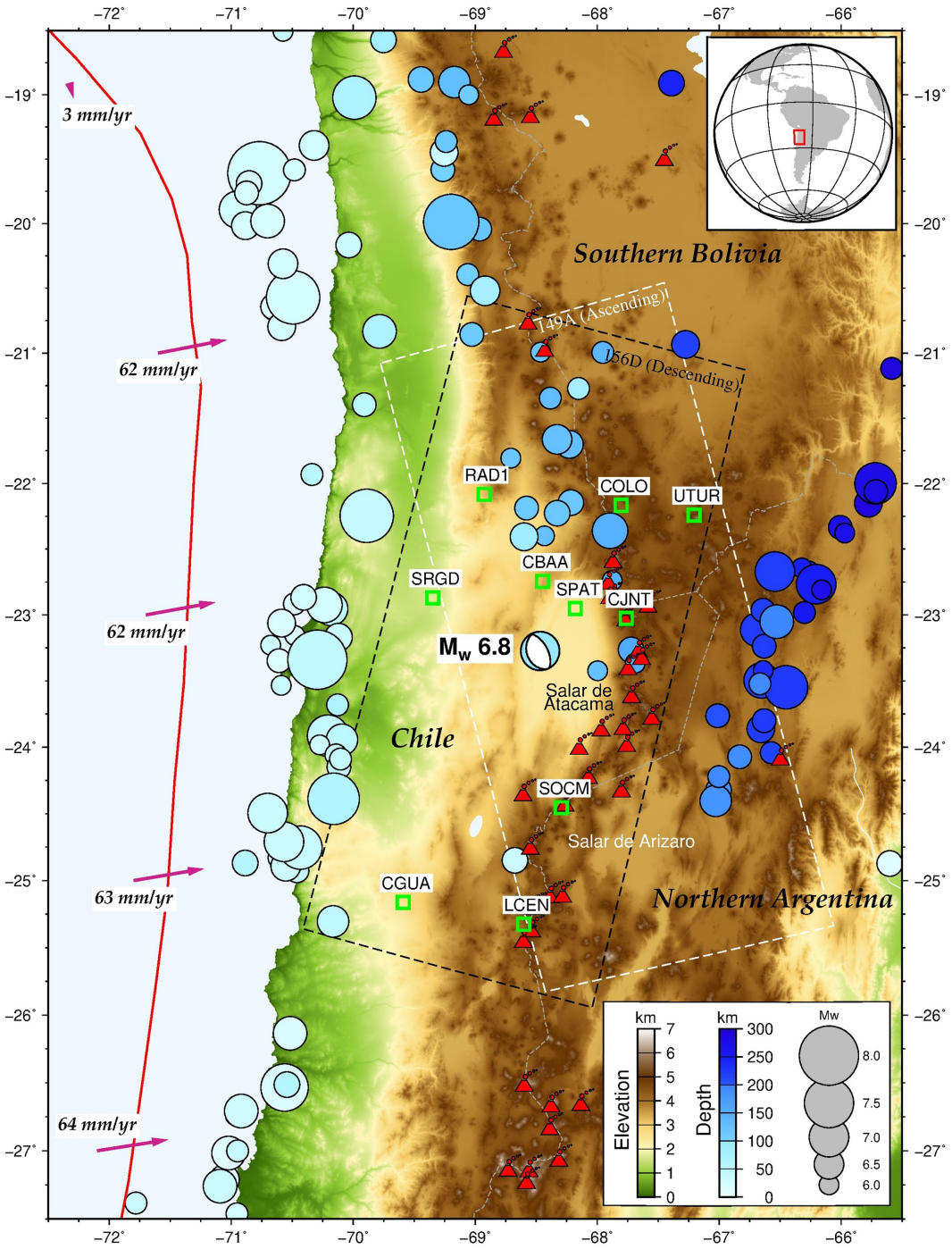

Figure 4.1: Seismotectonic setting of the epicentral region, Northern Chile. The M_w 6.8 earthquake epicentre (3rd Jun 2020 with a 112 km centroid depth) is marked by the focal mechanism, while all the $M_w > 6.0$ historical earthquakes since 1976 (where a precise global seismic network was established) in this region are shown by circles coloured by centroid depth (records from the United States Geological Survey, USGS). White and black dashed rectangle boxes show the Sentinel-1 data coverage from two tracks (149 ascending and 156 descending, spanning Jan 2018 to Oct 2021). Green boxes are the GPS stations used in our study (Blewitt et al., 2018), and their names are labelled. The background topographic map comes from Shuttle Radar Topography Mission (SRTM). The red line presents the plate boundary (Bird, 2003), and the red arrows indicate the relative velocities of Pacific plate motion with respect to South America. All Holocene volcanoes in this region are also marked by red triangles (Aguilera et al., 2022).

4.3 Results

4.3.1 Coseismic Deformation Field Captured from InSAR Time Series Analysis

Even after atmospheric corrections, signal-to-noise ratio (SNR) within single coseismic interferograms remains low given the magnitude of the expected deformation signals. We therefore apply two different approaches to recover the coseismic deformation from the InSAR time series: (1) spatial ICA (sICA) and (2) parametrised fitting (Figure 4.2).

The parametrised fitting uses a time-dependent model appropriate for expected surface displacements due to the seismic cycle, and fits the InSAR time series data pixel by pixel to reconstruct the coseismic deformation field (Liu et al., 2021). Contrastingly sICA is a blind source separation based on maximising signal independence (Hyvärinen and Oja, 1997; Hyvärinen and Oja, 2000), and here we apply it to identify the coseismic spatial component, using contributions to the corresponding column in the mixing matrix to identify and scale the appropriate component (e.g., Ebmeier, 2016).

Although both methods successfully retrieve the sub-centimetre coseismic deformation signals over a spatial scale of 100 km, sICA provides a much cleaner deformation pattern in both the near and far field, after masking out some non-tectonic signals (Salars/salt pans, volcanoes, remaining atmospheric artefacts, etc.). The derived deformation pattern from InSAR is in general similar to the predicted deformation pattern from forward modelling using the USGS bodywave solution, suggesting the consistency between these independent observations.

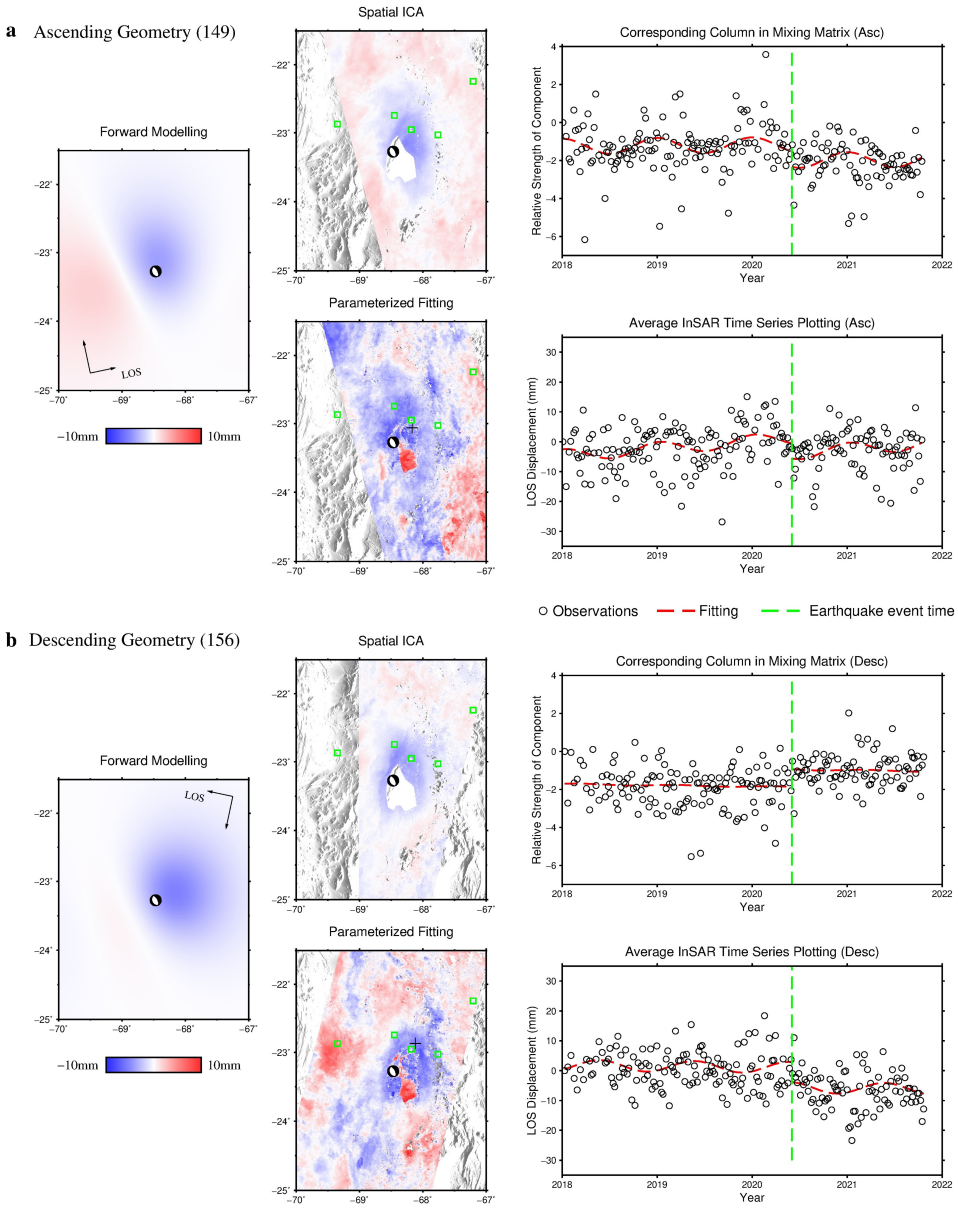

Figure 4.2: Spatiotemporal evolution of deformation from InSAR observations of the M_w 6.8 earthquake. (a) Ascending track data (track 149). The deformation panels on the left-hand side show the coseismic deformation fields from the forward modelling using the USGS bodywave solution (strike: 335°, dip: 67°, rake: -96°, centroid depth: 112 km, Moment: 2.1410^{1}9 N-m), the time-dependent parameterised fitting, and the sICA, respectively. While the time series panels on the right-hand side show one of the columns in the mixing matrix corresponding to the coseismic component when using sICA, and the average time series plot of the peak displacement pixels in line of sight (LOS) direction. (b) Same as (a) but for descending track data (track 156). Earthquake is indicated by the black focal mechanism, and the location of plotted peak InSAR displacement pixels and the GPS stations are marked by a black plus symbol and green rectangles, respectively. For the forward modelling, we assume a dislocation embedded in an isotropic elastic layered half-space, faults are equal in width and length, the slip-to-length ratio is set to 1.510^{-5} for this interplate earthquake, and then calculate these parameters using a rigidity value of 75 GPa. The Salar de Atacama and the Socompa volcano, shown as red patches close to the epicentre and further south on parameterised fitting results, have different behaviour in the time series (Liu et al., 2023), and thus are masked out when using sICA. In all figures, positive values mean movements towards the satellite.

4.3.2 Independent Observations from GPS and Seismology

We also extract the coseismic deformation offsets recorded from five GPS stations near the epicentre (e.g., SPTA station shown in Figure 4.3) using a trajectory model fitting (e.g., Heflin et al., 2020). Although there are just a few GPS stations and not all of them have captured significant coseismic deformation, it is critical in our study to incorporate these datasets for the following two reasons: 1) It is a strong validation of InSAR observations and helps constrain where the deformation occurred (near field) and where not (far field). 2) It provides accurate three-dimensional measurements, especially in the North-South direction where InSAR is less sensitive due to the sub-polar orbits of the Sentinel-1 constellation, which is important for the constraint of some fault parameters during the modelling.

Lastly, the seismological observations provide essential information on the location of hypocentres and focal mechanisms extracted from seismic waveforms, measuring intraslab earthquakes from another angle. We use the bodywave data from seismic stations near the epicentre of this M_w 6.8 earthquake (from 3, 300 to 10, 000 km) downloaded from the international Federation of Digital Seismograph Networks (FDSN). For modelling, we use Greens functions calculated using a locally-constrained 1-D velocity model under Northern Chile (Husen et al., 1999), merged into the global velocity model ak135 below 200 km depth.

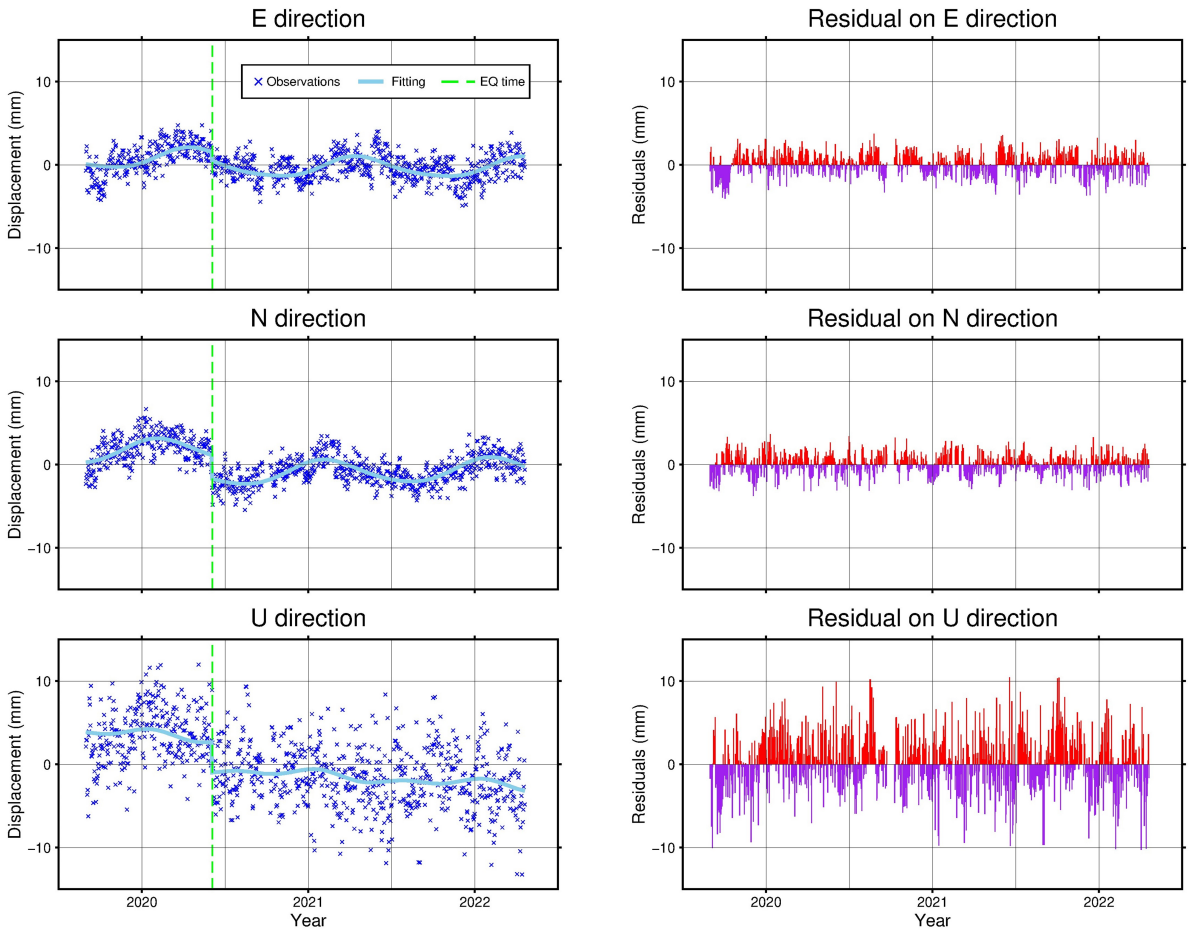

Figure 4.3: GPS time series fitting of the SPAT station. This station is closest to the epicentre ($\sim$ 45 km) and captures the most significant coseismic deformation (total displacement of 5.4 mm). It plots the daily GPS time series on three components, parameterised fitting curves, and corresponding residuals. We only use partial datasets to perform fitting to minimise the impact from steps caused by other nearby earthquakes or equipment changes, and the data have been detrended using the Median Interannual Difference Adjusted for Skewness (MIDAS) algorithm before fitting (Blewitt et al., 2016).

4.3.3 Numerical Modelling

We use the Bayesian Earthquake Analysis Tool (BEAT, Vasyura-Bathke et al., 2020) to perform earthquake source modelling, which allows the inversion of multiple datasets and provides the posterior probability density functions of fault rupture source parameters. We have run various inversions using different datasets and settings, to test the factors that affect the modelling output.

We initially perform a seismic inversion (using data from seismological stations only, Figure B.1-B.6) to evaluate the quality of input seismological data and compare the model outputs to publicly available earthquake catalogues. We find that it provides confident solutions and

achieves high consistency with source parameters from routine global catalogues (the USGS, GCMT, etc.; Table B.1) that use similar datasets.

We then run a geodetic inversion, using InSAR (derived from sICA) and GPS data, using a layered elastic model based on the same velocity structure as that employed for the seismic inversion (Figure B.7-B.22). We achieve a relatively wide posterior distribution of some source parameters (98 $\pm$ 8 km depth, a margin of error $< 5^{\circ}$ for strike, dip, and rake) compared to seismic inversion, and poor constraints on length, width, and slip due to the trade-off between these parameters (Figure B.17). We find that the modelling outputs from geodetic inversion generally agree well with those from seismic inversion, despite some discrepancies (e.g., rake values and slightly shallower depth). The relatively large displacements of 2.8 $\pm$ 0.1 mm observed by GPS in the North direction (Figure 4.3) contribute a higher rake value (-137° compared to -96° from seismic inversion), implying a significant strike-slip motion. In addition, we also test the impact of using a uniform elastic half-space, with parameters based on averaging the properties between the earthquake source and the surface. We find that using layered half-space achieves smaller values (though differences $< 10\%$) of moment but deeper depth, and the source parameters are also slightly better constrained and more seismologically consistent than those from uniform half-space (Figure B.21).

Finally, we perform a joint inversion combining all three datasets that complement each other, and show the modelling results and the trade-off between some selected source parameters (Figure 4.4, 4.5, and B.23-B.25). We find that parameters in the joint inversion are better constrained, in terms of narrower posterior distributions and reduced trade-offs, compared to employing each dataset separately. Overall, the model fits the observations well for all datasets, and only marginal differences are found between the solved parameters and those of seismic inversion. The main adjustment here compared to the geodetic inversion is the change in the hypocentre location. With the additional constraints from seismological data, the model adjusts the location of the epicentre and the depth to compensate for the north displacements captured by GPS and the higher rake value in geodetic inversion.

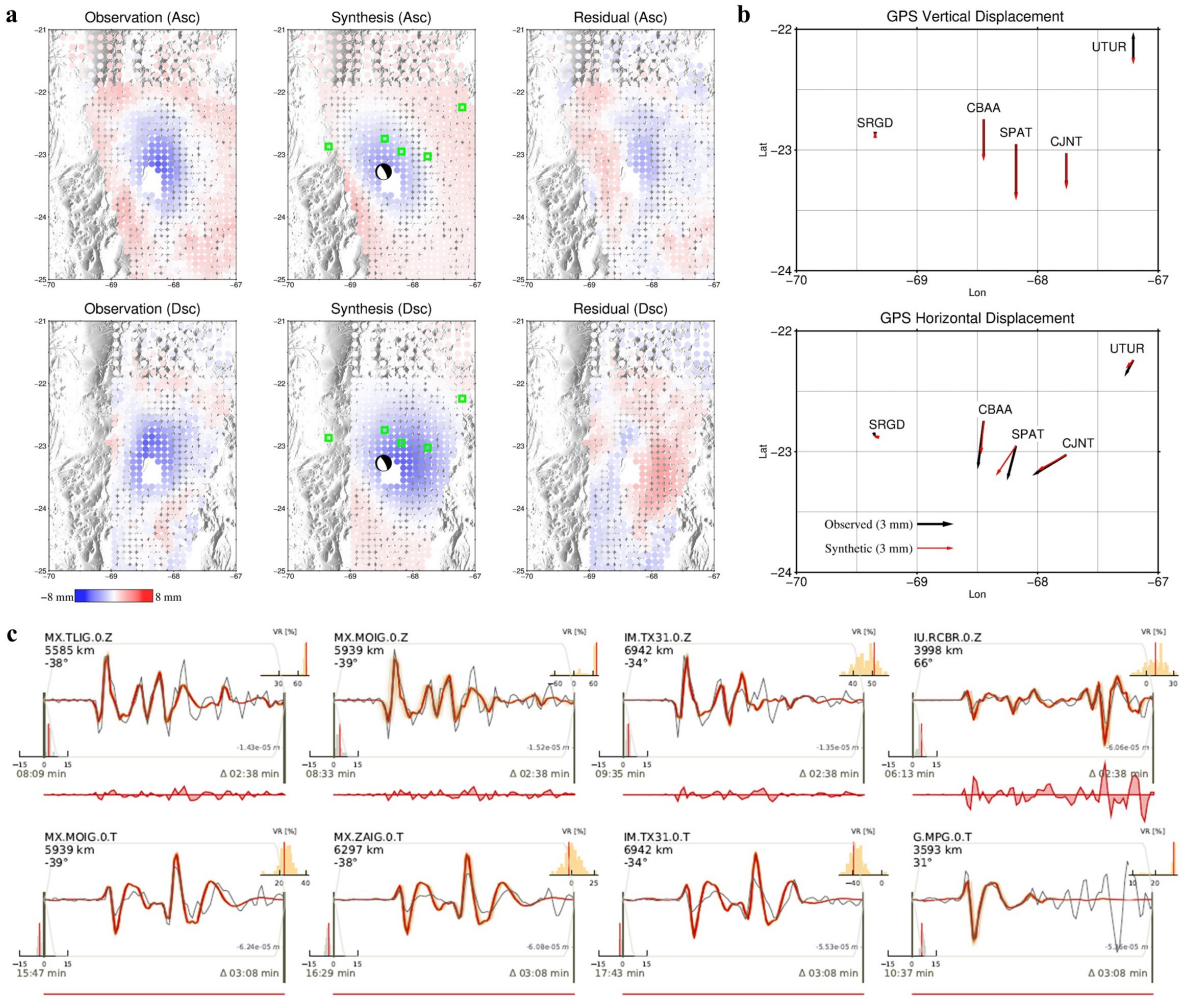

Figure 4.4: Modelling results from joint inversion. (a) Modelling results of the InSAR coseismic displacement field (derived from sICA), which shows the observation, synthesis, and the residual between them on downsampled ascending (746 points) and descending tracks data (576 points), respectively. The best-fit solution from joint inversion is marked by the focal mechanisms, and the green boxes on the synthetic panels represent the locations of GPS stations. (b) GPS modelling results, labelled by their ID, in vertical and horizontal directions, respectively. (c) Seismic waveform, and their fitting (including time shift and cross-correlation panels) of some best fit stations from vertical (Z) and (transverse) T components.

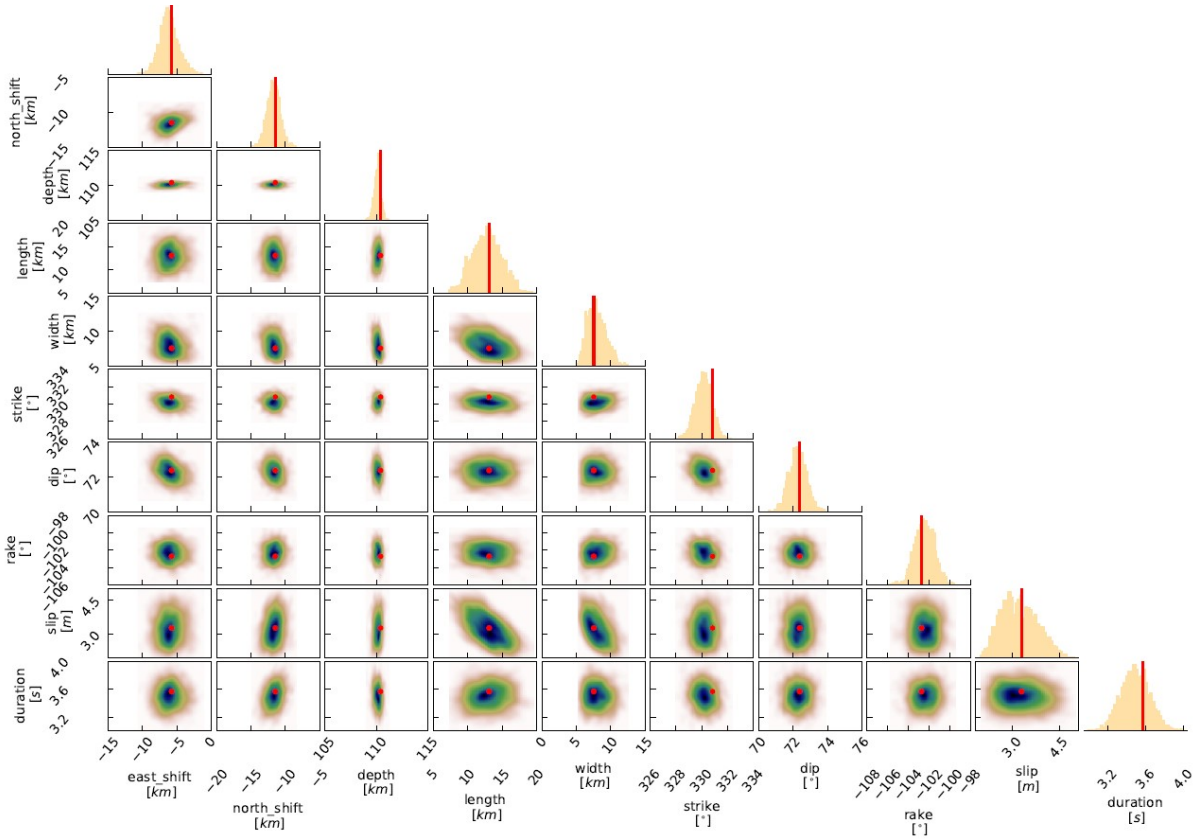

Figure 4.5: Fault parameter trade-offs and uncertainties. Correlation histogram of some selected source parameters derived from the joint modelling results using InSAR displacements (derived from sICA), GPS, and seismology, which shows the posterior distributions and trade-offs between different parameters during the inversion (red dot and line depict the maximum likelihood solution).

4.4 Discussion

4.4.1 Source Characterisation

Although the coseismic surface deformation signal of the study case is close to the limit of what can be detected by either InSAR or GPS, as a result of its moderate magnitude and intermediate depth, the contribution from geodetic data is significant as it provides supplementary constraints on fault geometry and, importantly, the spatial extent of the rupture.

We find that despite the length, width, and slip of the fault being poorly constrained in the geodetic-only inversion due to their large trade-offs against other parameters, and that the seismic-only inversion struggles to provide any information regarding these parameters at the frequencies used, they instead exhibit a relatively narrow Gaussian posterior distribution when we perform the joint inversion. The median values of the width and length of the fault from

joint inversion are 7.9 km and 12.8 km, respectively, which suggests an aspect ratio of ~ 1.6. This width value, and the resulting rupture area, are relatively small compared to the empirical source-scaling values (width > 10 km for the same magnitude, Strasser et al., 2010; Thingbaijam et al., 2017), implying different rupture mechanisms of this intraslab event.

In addition, the posterior distributions of the centroid depth and fault orientation are also very narrow (110.1 ± 0.6 km depth, a margin of error $< 3°$ for strike, dip, and rake). Note that the depth variation is a formal uncertainty from the inversion scheme and does not consider, for example, the bias contained in the choice of velocity model of the subsurface. However, it still provides more refined information regarding the fault location and further helps us to better understand its rupture mechanism.

4.4.2 Implications for Understanding the Mechanism of Intraslab Events

Intraslab earthquakes, including the events in Northern Chile, have commonly been observed to divide into two layers within the subducting slab, which are so-called Double Seismic Zones (DSZ, e.g., Kawakatsu, 1985; Dorbath et al., 2008; Wei et al., 2017). These two layers are separated by a 10-40 km width aseismic region, with the upper seismicity layer (USL) of the DSZ located in the oceanic crust, and the lower one in the lithospheric mantle (Sippl et al., 2018).

The centroid depth of this study event, considering all the modelling outputs and uncertainties, and the already well-known DSZ geometry in Northern Chile (e.g., Lu et al., 2021) indicate that rupture is more likely to occur in the lower seismicity layer (LSL). For the events that occurred in the USL, it is generally thought that the dehydration embrittlement, which involves releasing free fluid into the slab and causing overpressures, is the explanation for the rupture mechanism. However, the mechanism for the LSL events remains controversial due to the relatively dry conditions indicated by the small b values observed in earthquake populations (Florez and Prieto, 2019). Previous work from the laboratory and the field suggests that dehydration-driven stress transfer mechanism could trigger rupture without a highly hydrated lithospheric mantle (e.g., Ferrand et al., 2017). Although the thermal runaway model, which relies on the internal generation of heat in the deforming material through shear heating (e.g., John et al., 2009), could also be the answer to explain the occurrence of LSL events.

For the triggering of this M_w 6.8 earthquake, we prefer the dehydration-driven stress transfer

mechanism for mainly two reasons. Firstly, the width range of the fault plane, from the posterior distribution, is only 6-10 km. This unusually narrow width is consistent with the idea of a clear boundary existing between hydrous and anhydrous peridotite at LSL, which is explained by the depth of hydration of the incoming slab due to penetration (Ranero et al., 2003). In addition, the recent 3-D tomographic model of this event (Herrera et al., 2022) also indicates the potential occurrence of massive dehydration reactions at this depth. Secondly, although the thermal runaway model is thought to be at least part of the intraslab earthquake rupture process, it generally expects low rupture speed and radiation efficiency (Kanamori et al., 1998), while here we obtain a short duration time (median value of 3.5s) that indicates high rupture speed (median value of 3.6 km/s).

4.4.3 Prospects and Future Work

Here, we present an example of using space geodesy to measure the static displacements at the Earth's surface caused by a 112 km deep M_w 6.8 intraslab earthquake. By applying sICA or parameterised fitting with atmospheric corrections, we show that a large scale ($>$ 100 km) coseismic deformation pattern caused by intraslab on the order of a few millimetres could be precisely retrieved from InSAR time series data.

Using this case example, we show approximate the minimum magnitude and maximum depth of intraslab earthquakes to be detectable by InSAR. By forward modelling, we find that in addition to the magnitude and depth of the earthquakes, the velocity structure (and the value of shear modulus) of the subsurface also plays important roles in deciding the anticipated coseismic deformation signals on the surface (Figure 4.6). For real-world observations, more complicated circumstances need to be considered. For example, the quality of InSAR data (coherence, atmospheric noise, etc), only onshore observations, and the material property of the surface (e.g., the Salars shown here) will also significantly affect the observed signals. Nevertheless, we demonstrate the capability of existing, and presumably better of the forthcoming (e.g., NISAR), InSAR observations for measuring intraslab earthquakes, making InSAR data more viable when measuring stronger signals, greatly enriching the data sources for studying these events.

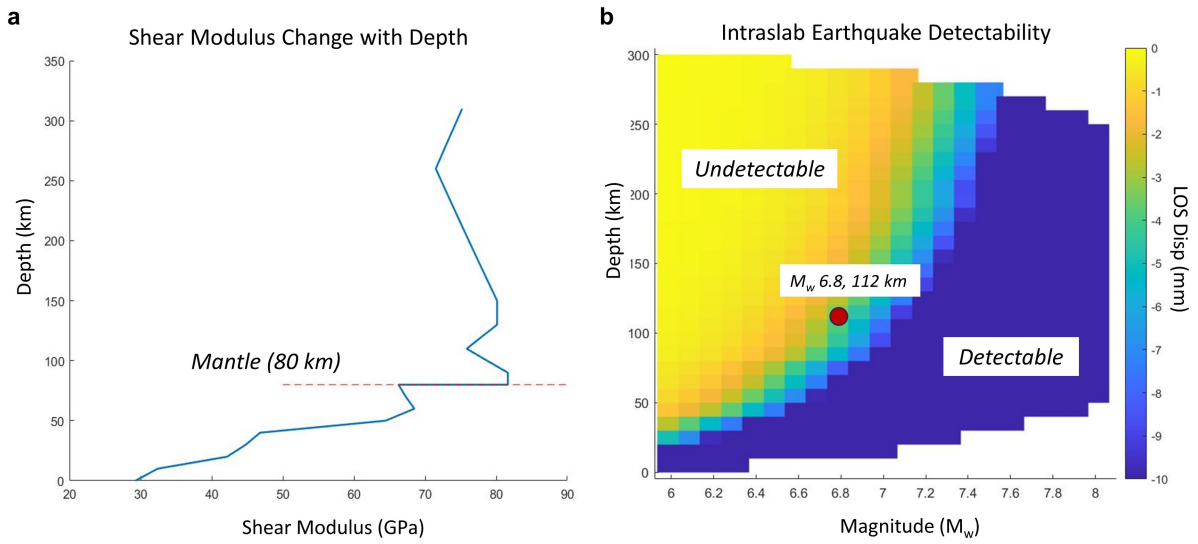

Figure 4.6: Impact of velocity structure on intraslab earthquake detectability. a) Shear modulus (rigidity value) change with the increase of depth, using the 1-D velocity structure under Northern Chile (Husen et al., 1999). b) Peak surface displacements in the LOS direction of ascending track (incident angle 39°) for a range of magnitudes and centroid depths in Northern Chile, simulated by forward modelling (negative values mean movements away from the satellite). We use the same focal mechanism of the M_w 6.8 from the USGS bodywave solution (strike: 335°, dip: 67°, rake: -96°), assume faults are equal in width and length, and the slip-to-length ratio is set to 1.5×10^{-5}.

More importantly, we show that the additional constraints from InSAR data, combined with those from GPS and seismological data, could help us better determine the source of intraslab earthquakes, including depth, focal mechanisms, fault geometry, etc., leading to a better understanding of the rupture mechanism and the properties of slabs. In addition, the surface deformation observed by geodesy, which is associated with the velocity model and rigidity values, could also in turn provide insight into the better resolving of them. Although more data processing and systematic analysis are required, this could make huge impact on the accuracy of seismological modelling (e.g., Craig et al., 2023), and further improving our understanding of Earth's structure in the long term.

4.5 Method

4.5.1 GPS Processing

There are several GPS stations near the epicentre whose observation periods cover the earthquake event time and capture the coseismic deformation. To calculate the coseismic deformation recorded by these stations and later to tie the velocity field with InSAR, we use a time series

with average daily positions processed by the Nevada Geodetic Laboratory in a South American Plate reference frame (Blewitt et al., 2018) to do a time-dependent parameterised fitting, using a trajectory model that is appropriate for the anticipated types of displacements due to the seismic cycle:

$$\psi(t) = H(t - t_0)C + Vt + A_1 \sin 2\pi t + A_2 \cos 2\pi t + A_3 \sin 4\pi t + A_4 \cos 4\pi t + b, \tag{4.1}$$

where the unit of time t is year, $H(*)$ is a Heaviside step function, C represents the coseismic deformation at the earthquake event time t_0, V is the background long-term linear deformation rate which contains in part the interseismic displacement, A_1, A_2 and A_3, A_4 represent the annual and semi-annual terms, respectively, and b is a constant reference offset in observations. We do not model the post-seismic deformation here as the observed surface deformation of the earthquake is relatively weak (< 5 mm), and no clear post-seismic signals are captured by visual checks.

4.5.2 InSAR Time Series Analysis

Using the European Space Agency (ESA) Sentinel-1 Interferometric Wide (IW) swath mode Single Look Complex (SLC) images, we form interferograms with multilooking (10 in azimuth and 40 in range, yielding a pixel size of $\sim$ 140 m $\times$ 93 m) but no spatial filtering using the InSAR Scientific Computing Environment (ISCE) software (Rosen et al., 2012). We use the Copernicus Digital Elevation Model (DEM) with global coverage at 30 m resolution (GLO-30) during the processing. We form interferogram networks by connecting each image to 10 subsequent acquisitions (6-60 days temporal interferogram, assuming a revisit time of 6 days for combined Sentinel-1A and 1B acquisitions). Meanwhile, the ionospheric phase variation across the acquisition area for each epoch is also obtained and later removed from time series data using the range split-spectrum method (Liang et al., 2019).

We then use the Stanford Method for Persistent Scatterers (StaMPS) software (Hooper et al., 2007) to perform time series analysis, which includes a) resampling pixels to 500 m resolution to reduce data volume, b) unwrapping all the interferograms iteratively to reduce unwrapping errors by checking for phase consistency (Hussain et al., 2016), c) application of Generic Atmospheric Correction Online Service (GACOS, Yu et al., 2018) for tropospheric artefacts using the Toolbox for Reducing Atmospheric InSAR Noise (TRAIN) software (Bekaert et al., 2015), and

further refine this correction using a spatially varying scaling method (Shen et al., 2019), and finally d) using only longer temporal interferograms (48-60 days) to do small baseline subset inversion to reduce the potential impact of the fading signal (Ansari et al., 2020).

4.5.3 Noise within InSAR data

As the vast majority of Northern Chile lacks vegetation, the coherence in our experimental area is very high, which significantly lowers the impact of unwrapping errors and fading signals (Agram and Simons, 2015; Ansari et al., 2020). The main source of uncertainty in our InSAR data comes from atmospheric noise, including both tropospheric and ionospheric components.

We evaluate the improvements in the quality of data after the tropospheric (GACOS, Yu et al., 2018) and ionospheric (split spectrum method, Liang et al., 2019) correction, by checking the reduction of the standard deviation of interferograms, the SNR of interferograms, or the root mean square error of parameterised fitting of InSAR time series (Table B.2). Due to the high vertical Total Electron Content (TEC) in Northern Chile at the acquisition time of the ascending track (Fattahi et al., 2017), we find that for the ascending track, the GACOS correction alone did not work very well, but quality of data is significantly improved after incorporating the ionospheric correction, showing the complementarity between these corrections. While for the descending track, the GACOS alone reduces the noise level a lot. However, little refinements are observed after ionospheric correction since the ionospheric delay is less significant than that of the ascending track, and the split spectrum method is not sensitive enough to work well. As a result, the noise level within the ascending track data is lower than that of descending track data after all these atmospheric corrections.

4.5.4 Parameterised Fitting and Independent Component Analysis (ICA)

Compared to single interferograms, InSAR time series analysis provides frequent estimates of surface displacement through time, providing better noise resilience. Furthermore, if we assume a deformation model appropriate for displacements due to the seismic cycle as is the case for GPS, we can reconstruct the coseismic deformation field via a time-dependent parameterized model fitted to InSAR time series data (Liu et al., 2021). We use the same model as (1) except removing the semi-annual term to avoid over-fitting, given the high noise level within the InSAR

data:

$$\psi(t) = H(t - t_0)C + Vt + A_1 \sin 2\pi t + A_2 \cos 2\pi t + b, \tag{4.2}$$

We can fit the InSAR time series data using Equation 4.2 pixel by pixel, and obtain the reconstructed coseismic deformation field using the values of solved coseismic deformation (Figure 4.2).

ICA is another frequently used approach to extract independent signals from mixtures of variables, which allows the decomposition of a mixed signal into a set of linear, additive components. Since the signals within InSAR data (individual interferograms or time series) are either spatially or temporally independent, ICA has been applied to extract deformation signals from various noise sources (e.g., Ebmeier, 2016; Cohen-Waeber et al., 2018). For example, when applying spatial ICA (sICA) for a given InSAR time series dataset (matrix $\mathbf{X}$, size of $n_{epoch} \times n_{pixel}$, where n_{epoch} and n_{pixel} are the number of epochs and pixels in each epoch, respectively), it can be decomposed into statistically independent components (matrix $\mathbf{S}$, size of $n_{ncomp} \times n_{pixel}$, where n_{ncomp} is the number of components that you would like the dataset to be decomposed), and the mixing matrix $\mathbf{A}$ (size of $n_{epoch} \times n_{ncomp}$) which describes the strength of each independent spatial component at each time step to restore the input datasets ($\mathbf{X}$=$\mathbf{A}$·$\mathbf{S}$). Given the coseismic signal is spatially independent of other sources (e.g., interseismic deformation related to the Chilean subduction megathrust, topographic-related signal, residual atmospheric noise, etc), we can apply sICA to extract the coseismic deformation pattern as an independent component from the input time series of cumulative displacements. More importantly, since the permanent coseismic spatial deformation pattern will remain on the time series data (the cumulative displacements) after the earthquake, we see a "coseismic offset" in the corresponding column of the mixing matrix, at the epoch near the earthquake event time. We then can solve for this "coseismic offset" using Equation 4.2 and use it to scale the deformation pattern retrieved in the corresponding independent component to estimate the coseismic deformation field (Figure 4.2).

We apply sICA using the InSAR time series data, with tropospheric and ionospheric noise already corrected, on both tracks. We first whiten and reduce the number of dimensions of the data using principal component analysis, and then manually adjust the number of independent components to test the performance, and find that nine and ten are the most suitable number of

components (too many or too few will cause the coseismic deformation to be either dismantled or buried by other signals or noise), for ascending and descending track data, respectively. We masked out the Salar de Atacama due to different time series behaviours that might be related to lithium mining and groundwater movements, and Socompa volcanic unrest that caused velocity changes since Nov 2019 (Liu et al., 2023). We also mask out some coverage on the west of descending track data due to still strong remaining atmospheric turbulence near the coast. All these strong signals in these regions impede the robustness and effectiveness of retrieving the coseismic deformation pattern from the algorithm.

4.5.5 Seismological Observations

We downloaded the bodywave data from the international Federation of Digital Seismograph Networks (FDSN), using the command implemented in BEAT software (69 stations for Z component, and 37 for T component, aiming to achieve good azimuth and epicentral coverage, note the deficiency due to the Pacific and Atlantic Ocean). We choose the seismic stations near the epicentre of this Mw 6.8 earthquake (from 3, 300 to 10, 000 km). We manually identify and remove some low-quality data from P and S waves, respectively, to improve the subsequent modelling outputs. When perform inversion, we use a filter range of 0.025-0.25 Hz, with a window from 20s before to 130s after the P-wave onset with 20s taper either end, and a window from 20s before and 150s after S-wave onset with the same taper as the P-wave. The optimization is done in the T (S waves window) and Z (P waves window) rotated coordinate system, with alignment allows 15s for synthetic and observed seismic wave by cross correlation.

4.5.6 Modelling Settings

We calculate Green's function based on the velocities of P and S waves under Northern Chile (Husen et al., 1999) and global model $ak135$ (below 200 km depth), to set up the layered (for both geodetic and seismic inversions) elastic half-space, and later the uniform one (for geodetic inversion only) using parameters based on averaging the properties between the earthquake source and the surface.

For geodetic inversion, we use a nested uniform downsampling of the coseismic deformation fields (derived from parameterised fitting or sICA), with a greater pixel density in the near field, and mask out the regions of Salar de Atacama and Socompa volcano due to different behaviours in response to the earthquake (Liu et al., 2023). We use a rectangular source, solve

for depth, length, width, slip, strike, dip, rake, east shift and north shift, and run 200 chains and 500 steps. For seismic inversion, we use a double couple point source with no CLVD or isotropic component, solve for magnitude, depth, strike, dip, rake, time, duration, east shift, and north shift, and run 1000 chains and 300 steps. For joint inversion, we use a rectangular source, additional solve for duration, time, nucleation parameters in length and width direction of the fault plane compared to geodetic inversion, and run 1000 chains and 300 steps.

For all inversion, we use uniform priors for all parameters (initial value are from the USGS or empirical numbers, with meaningful and wide enough boundaries). We also solve for several hierarchical parameters, including ramp estimations for the InSAR data, and time shifts for each seismic station to compensate for along-path variations in velocity structure. We do not do noise scaling, but use four hyperparameters (one for GPS, one for InSAR, one for P waves, and one for S waves) when multiple datasets are used, to adjust the relative weight between different datasets automatically. However, when performing the inversion with GPS data, since there are only five GPS stations so the GPS hyperparameter cannot be well constrained, we fix its value to zero to avoid any overweighted or underweighted of the GPS dataset.

Open Research

The Sentinel-1 SAR data are copyrighted by the European Space Agency and additionally distributed by the Alaska Satellite Facility Distributed Active Archive Centre (https://earthdata.nasa.gov/eosdis/daacs/asf). The Copernicus DEM datasets (GLO-30) used in our study are available with a free license and can be found here: https://doi.org/10.5270/ESA-c5d3d65. The daily GPS time series data we used are processed by the Nevada Geodetic Laboratory (http://geodesy.unr.edu), which are based on services provided by the GAGE Facility, operated by UNAVCO, Inc., with support from the National Science Foundation, the National Aeronautics and Space Administration, and the U.S. Geological Survey under NSF Cooperative Agreement EAR-1724794.

Acknowledgement

This work is supported by the UK Natural Environment Research Council (NERC) through the Centre for the Observation and Modelling of Earthquakes, Volcanoes and Tectonics (COMET,

http://comet.nerc.ac.uk), and the Looking into the Continents from Space (LiCS) large Grant (NE/K010867/1). Figures were made using the Generic Mapping Tools (GMT) (Wessel et al., 2013). This work was undertaken on ARC4, part of the High-Performance Computing facilities at the University of Leeds, UK. FL acknowledges support from the Great Britain-China Educational Trust. JE acknowledges support from the Royal Society through a University Research Fellowships (UF150282 and URF\R\211006). SE is funded by a NERC Independent Research Fellowship (NE/R015546/1). TC thanks the Royal Society for support through URF\R1\180088.

Competing interests

The authors declare no competing interests.

Chapter 5

First onset of unrest captured at Socompa: A Recent Geodetic Survey at Central Andean volcanoes in Northern Chile

F. Liu[1], J. R. Elliott[1], S. K. Ebmeier[1], T. J. Craig[1], A. Hooper[1], C. Novoa Lizama[1], and F. Delgado[2]

[1]COMET, School of Earth and Environment, University of Leeds, UK

[1]Department of Geology and Centro de Excelencia en Geotermia Andina, Universidad de Chile, Santiago, Chile

Citation: Liu, F., Elliott, J. R., Ebmeier, S. K., Craig, T. J., Hooper, A., Novoa Lizama, C., Delgado, F. (2023). First onset of unrest captured at Socompa: A recent geodetic survey at Central Andean volcanoes in Northern Chile. Geophysical Research Letters, 50, e2022GL102480. https://doi.org/10.1029/2022GL102480

Key Points

- We combine InSAR and GPS data to survey the Central Andean volcanoes, some of which have been updated for the first time in over 10 years

- We show the first detection of unrest at Socompa volcano with steady uplift up to 17.5 mm/yr since Nov 2019
- Deformation patterns are consistent with an ellipsoidal source, stretching from 2.1 to 10.5 km and with a volume change of 6.2×10^6 m^3/yr

5.1 Abstract

We report the first detection of unrest at Socompa volcano during our recent survey of Central Andean volcanos in Northern Chile using Interferometric Synthetic Aperture Radar (InSAR) measurements spanning Jan 2018 to Oct 2021. We find that Socompa volcano, whilst initially undeforming and no recorded eruptions for 7.2 kyr, shows a steady uplift (17.5 mm/yr) from Nov 2019, independently recorded by near-field continuous Global Positioning System (GPS) data. The deformation pattern can be fitted with pressure increase in an ellipsoidal source region stretching from 2.1 to 10.5 km, with a volume change rate of $\sim6.2\times10^6$ m^3/yr. Our observations of the onset of uplift suggest it is unlikely that a nearby M_w 6.8 deep intraslab earthquake on 3rd June 2020 triggered the unrest. The deformation signal we detect indicates the initiation of unrest at Socompa, after at least two decades without measurable deformation, and many thousands of years without volcanic activity.

Plain Language Summary

Here we report the first observation of unrest of the Socompa volcano, Northern Chile, which is thought to have last erupted thousands of years ago. Using radar interferometry technique and differencing radar images from two dates, it is possible to retrieve millimetre-level surface displacements during this period. Here, we use a time series of multiple images spanning Jan 2018 to Jan 2023, over the Central Andean volcanoes in Northern Chile, to estimate the change in ground movement through time. Combined with GPS data, we find Socompa volcano started to uplift in Nov 2019 at a relatively stable speed (of 17.5 mm/yr) without any trace of slowing down up to Dec 2021. Our analysis suggests that this volcanic deformation is unlikely to have been triggered by a nearby 112 km depth, M_w 6.8 earthquake, which occurred in June 2020, and was thus after the onset time. Deformation at Socompa has similarities with other volcanoes in the Central Andes, where low rates of magmatic uplift have been detected at other apparently quiescent volcanoes. Such large-scale monitoring efforts using remote sensing data

are important, as we can better understand the deformation style of these volcanoes in areas that are poorly instrumented.

5.2 Introduction

Satellite Interferometric Synthetic Aperture Radar (InSAR) measures the Earth's surface deformation at the millimetre-level and has increased the number of volcanoes where deformation has been studied by an order of magnitude (e.g., Biggs et al., 2014; Ebmeier et al., 2018; Poland and Zebker, 2022). InSAR can capture deformation caused by the movement of magma through the Earth's crust (e.g., Reath et al., 2019), by pressure changes within a zone of magma storage (e.g., Chaussard and Amelung, 2012) or overlying hydrothermal system (e.g., Yunjun et al., 2021). In Northern Chile (17.5-27°S), where only 10 of the region's 42 Holocene volcanoes are currently actively monitored using ground-based instrumentation (Aguilera et al., 2022), the systematic displacement measurements possible with InSAR can provide the best record of timings of recent unrest and magmatic activity at Central Andean volcanoes (e.g., Pritchard and Simons, 2004a; Henderson and Pritchard, 2013).

Survey-mode InSAR first detected magmatic deformation in the Central Andes at Uturuncu, Lazufre, Cerro Blanco and Sabancaya-Hualca Hualca in the 1990s (Pritchard and Simons, 2002; MacQueen et al., 2020). Uturuncu has been the subject of numerous subsequent studies (e.g., Fialko and Pearse, 2012; Hickey et al., 2013; Henderson and Pritchard, 2013; Henderson and Pritchard, 2013; Henderson et al., 2017; Barone et al., 2019), showing a reservoir depth of 15-30 km and deformation potentially related to deeper magma movement associated with the Altiplano-Puna Magma Body (APMB, Ward et al., 2014). The deformation signal near Cerro Overo, which has no ground-based monitoring, is intriguing as it transitioned from subsidence to uplift in ∼2003-2005, which involves fluid accumulation and loss within the crust at ∼10 km depth (Henderson and Pritchard, 2013). The deformation pattern of uplift at Lazufre (Lastarria and Azufre) has been interpreted to represent magma accumulation in the mid-upper crust with source depth < 10 km (Ruch and Walter, 2010; Pearse and Lundgren, 2013; Remy et al., 2014; Díaz et al., 2015; Henderson et al., 2017), in addition to a source ~ 1 km under the Lastarria summit observed between 2003 and 2005 (Froger et al., 2007). Other deformation, for example during the 2010 unrest at Lascar (which erupted in 2015-2017 without deformation, Gaete et al., 2020, and most recently in Dec 2022) can be linked to crater evolution

processes such as gravitational slumping or piston-like subsidence (Richter et al., 2018). Putana and Sillajhuay showed short-lived, low-magnitude uplift in 2009 and 2007-2010, respectively, related to hydrothermal or seismic activity (Henderson and Pritchard, 2013; Stebel et al., 2014; Pritchard et al., 2014).

The triggers for episodes of magmatic uplift (or subsidence) in the Central Andes are obscure but could potentially include (1) variations in flux from lower crustal bodies of melt (e.g., the APMB) or (2) changes within shallow reservoirs such as crystal mushor degassing as inferred in other settings (Pritchard et al., 2019). These processes cause pressure changes within reservoirs, thus controlling the initiation and cessation of inflation and deflation (or even possible episodic inflation and deflation as shown at Cerro Overo and Uturuncu, Walter and Motagh, 2014). The initiation of deformation may be linked to external events like earthquakes. For example, large subduction earthquakes in the Southern Andes and Japan caused stress field changes that triggered episodes of subsidence at multiple volcanoes (Pritchard et al., 2013; Takada and Fukushima, 2013), and regional earthquakes are also thought to have triggered delayed uplift through surface waves (e.g., Lupi et al., 2017).

Here, we analyse $\sim$ 4 years of Sentinel-1 InSAR time series data, spanning Jan 2018 to Oct 2021, in the region of Antofagasta, Chile (Figure 5.1). Similarly to those previously reported, we observe uplift at Uturuncu, and Cerro Overo and Azufre. However, we also find a previously unreported deformation signal centred on the Socompa volcano, where no deformation has previously been observed from regional InSAR studies (1992-2010, Henderson and Pritchard, 2013). We measure a steady linear uplift (rate of 17.5 $\pm$ 3.7 mm/yr) starting from Nov 2019, which continues through the rest of our InSAR observation time (until Oct 2021).

Socompa is a large stratovolcano (peak elevation 6,031 m) and is the site of a trainline and manned border control between Chile and Argentina. It is known for the failure of the north-western flank that produced a 600 km^2 debris-avalanche deposit and triggered post-collapse eruptions $\sim$7, 200 years ago (Wadge et al., 1995). As a result of its remote location and presumed quiescence, it lacks targeted ground monitoring, although it was selected as the site of a single Global Positioning System (GPS) station (SOCM) installed in 2011 as part of the NSF PLUTONS network (Pritchard et al., 2018) due to its location halfway between Lazufre and Uturuncu and previously used as a far-field non-deforming reference station. A small lake at the foot, and several warmspots near the summit of the volcano form a complex microbial

ecosystem (Halloy, 1991; Costello et al., 2009; Farías et al., 2013) where both water and CO_2 degassing have been observed during field studies (but not from a satellite IR survey; Jay et al., 2013), implying the presence of active hydrothermal and therefore magmatic systems.

We determine the precise onset time of uplift at Socompa using a time-dependent parameterized model fitting the GPS time series from SOCM, and investigate the temporal relationship between the onset of Socompa uplift and nearby earthquakes to explore the potential trigger mechanisms. We reconstruct the cumulative deformation fields using an InSAR time series approach (Liu et al., 2021), and combine both InSAR and GPS data as inputs to assess several potential geodetic source models to explain the Socompa deformation. Finally, we discuss the sudden onset of uplift at Socompa in the context of the long timescales of unrest as observed with InSAR in the Central Andean volcanoes since the 1990s.

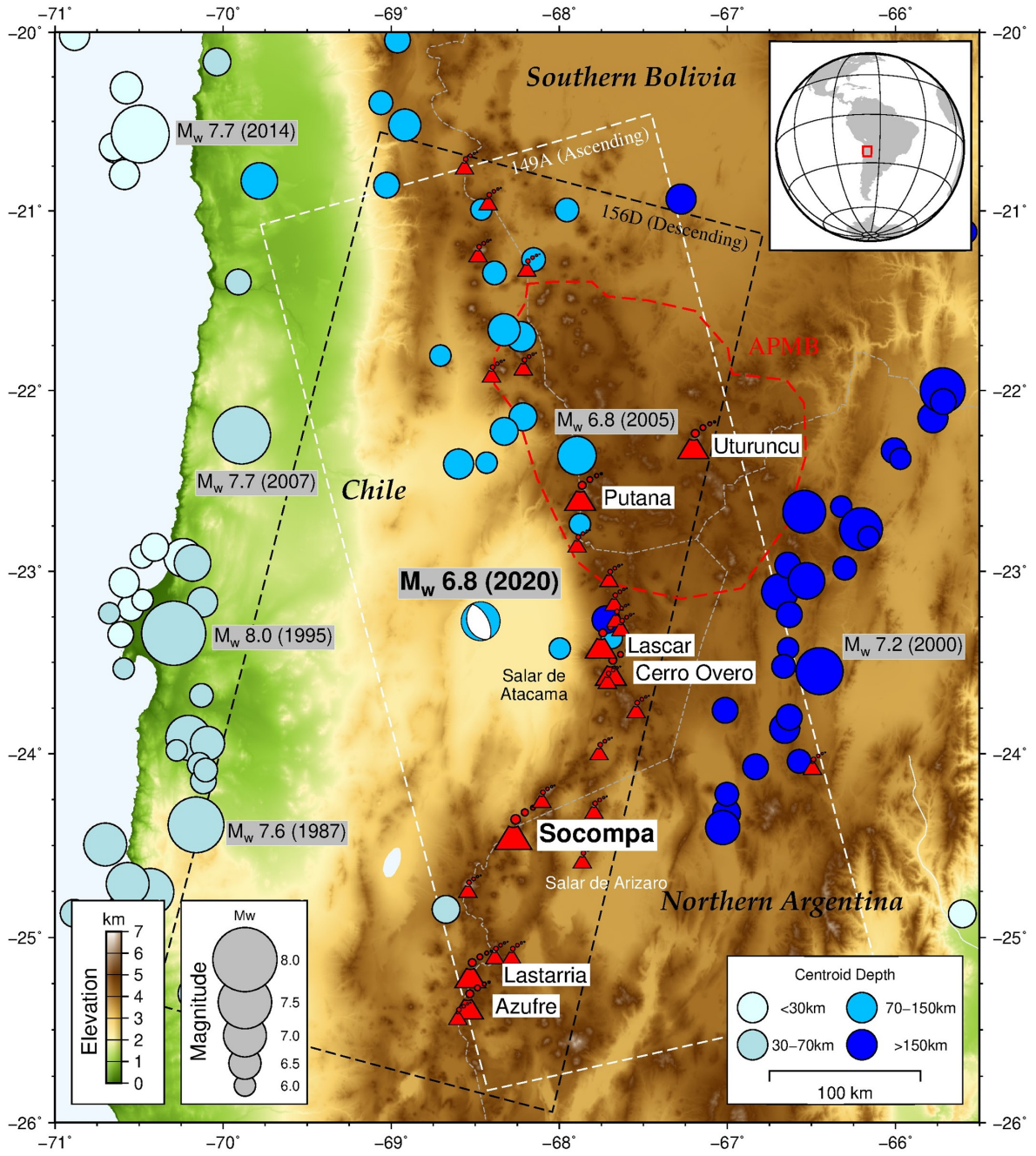

Figure 5.1: Topographic map of Northern Chile from Shuttle Radar Topography Mission (SRTM). White and black dashed rectangle boxes show the Sentinel-1 data coverage from two tracks (149A Ascending and 156D Descending, spanning Jan 2018 to Oct 2021). All Holocene volcanoes are marked and some active volcanoes with larger icons are labelled by their name. The red dashed line roughly defines the extent of the APMB (Perkins et al., 2016). The M_w 6.8 earthquake epicentre (3rd Jun 2020 with a 112 km centroid depth), is marked by the focal mechanism, while all the $M_w > 6.0$ historical earthquakes since 1976 (where a precise global seismic network was established) in this region are shown by blue circles coloured by centroid depth (records from the United States Geological Survey, USGS).

5.3 InSAR Time Series Analysis

Here we process Sentinel-1 InSAR time series using the LiCSAR processing chain (Lazecký et al., 2020) and StaMPS software (Hooper et al., 2007, processing details in Text S1). Compared to single interferograms, InSAR time series analysis provides frequent estimates of surface displacement through time (every 6 or 12 days for Sentinel-1), reducing measurement uncertainties from noise (Osmanoğlu et al., 2016). In addition, if we assume a deformation model appropriate for displacements due to Socompa unrest, we can reconstruct the post-onset cumulative deformation field via a time-dependent parameterized model fitted to the InSAR time series. As the observed velocity change at Socompa is approximately linear, we assume that surface displacement at time t following the onset time t_0 can be decomposed as follows:

$$\psi(t) = V_1 t + H(t - t_0) V_2 t + b, \tag{5.1}$$

where $H(*)$ is a Heaviside step function, V_1 is the background long-term linear deformation rate, V_2 is the linear velocity change after the onset time, and b is a constant reference offset in observations. We do not fit the seasonal signals because the already-applied GACOS correction should suppress the seasonality, and it is also difficult to model it accurately considering the noise level within the InSAR data in this region (particularly from ionospheric delay, Liang et al., 2019). After fitting the data, we reconstruct the cumulative pre- and post-onset deformation field in the line of sight (LOS) direction via the difference between the points at both ends of the fitting lines (Figure 5.2).

As the Central Andes predominately lacks vegetation, coherence is very high, significantly lowering the impact of unwrapping errors and fading signals (Agram and Simons, 2015). The main InSAR error sources arise from atmospheric noise, including both tropospheric and ionospheric components. Although the applied GACOS corrections (Yu et al., 2018) improve the data quality (with average standard error reductions of 16.9% and 45.7% for ascending and descending interferograms, respectively, Figure C.1), the ionospheric noise is very strong and could not be ignored, especially on ascending track. We therefore remove a linear ramp that spans the whole interferogram to reduce ionospheric noise, and other long wavelength signals associated with orbit errors and plate motion. Overall, the noise level in the ascending data is much higher than for descending, and noticeable atmospheric artefacts remain in high topography areas.

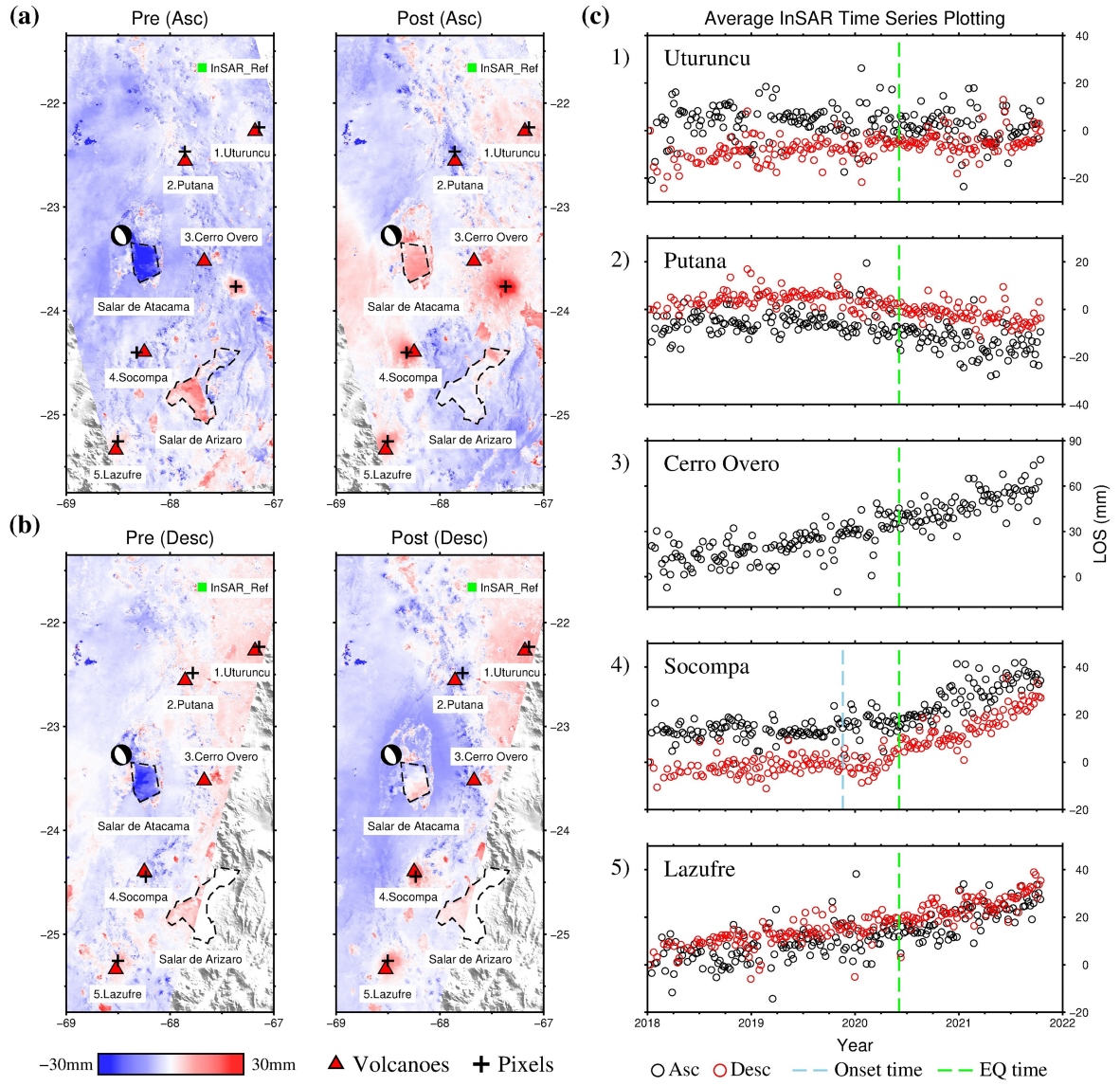

Figure 5.2: Reconstructed pre- and post-onset cumulative deformation fields and corresponding InSAR time series plots. (a) The pre- and post-onset cumulative deformation fields using ascending track data. The focal mechanism, black dashed polygon, and green square represent the epicentre of the M_w 6.8 earthquake, the approximate boundaries of the salar (salt pan) regions (Text S2), and the InSAR reference points, respectively. The InSAR time series plots of some peak displacement pixels near the volcanoes are shown in (c). (b) Same as (a) but for descending track data. In all figures, positive values mean movement towards the satellite. Note the displacement signal associated with Cerro Overo is ∼40 km southeast of the volcano and falls outside of the data coverage on the descending frame.

5.4 Socompa Uplift

5.4.1 Onset Time Implications

Determining the onset time for Socompa uplift is important not only for reconstructing the cumulative deformation field, but also for investigating potential causes for initiating unrest at Socompa. Due to historically lower temporal resolution satellite imagery and the typically long duration of unrest, it has not previously been possible to determine precisely the initiation time of deformation at a Central Andean volcano. For example, while uplift at Sabancaya is known to have started in 2013, the distribution of SAR acquisitions means that it could have taken place at any point over several months (MacQueen et al., 2020). Here we investigate potential triggering mechanisms from earthquakes in this region by exploring all major historical events ($M_w > 6.0$ since 1976, see Figure 5.1). We find the closest event in space and time is a M_w 6.8 intraslab earthquake with a 112 km centroid depth, which occurred on 3rd Jun 2020, and whose epicentre is 120 km northwest of Socompa (Figure C.2). Initial visual inspection of the deformation signal pointed to the potential for a causal relationship given the close correlation in time, but the InSAR time series are noisy and contain seasonal signals that overprint changes in long-term trends.

5.4.2 Onset Time Determination

To determine the exact onset time, we collect data from a previously installed GPS station (SOCM, Henderson et al., 2017), which is located ~8 km southwest of the Socompa volcano and captures the deformation signal (Figure 5.3c). We use a time series with average daily positions processed by the Nevada Geodetic Laboratory in a South American Plate reference frame (Blewitt et al., 2018) to do a time-dependent parameterized fitting, using the trajectory model:

$$\begin{aligned}\delta(t) = V_1 t + H(t - t_0)V_2 t + A_1 \sin(2\pi t + \varphi_1) \\ + A_2 \sin(4\pi t + \varphi_2) + \sum H(t - t_{eq(i)})C_i + b,\end{aligned} \tag{5.2}$$

where the unit of time t is year, A_1, A_2 and φ_1, φ_2 are the amplitudes and phases of annual and semi-annual terms respectively, $t_{eq(i)}$ and C_i are historical earthquake event times and corresponding coseismic offsets that are close to the station (based on the database of the

Nevada Geodetic Laboratory). We use a Markov Chain Monte Carlo approach to determine that the optimal onset time t_0 is 19th Nov 2019 (197 $\pm$ 12 days ahead of the earthquake event time, Text S3), using all three components of GPS time series data and weighting them by the noise level within each component (Figure 5.3a).

Such analysis highlights strong seasonal effects in the GPS time series, especially in the North direction, leaving some uncertainty about the onset time in the data fitting. To reduce the influence of seasonal signals, we further use a novel method of vector decomposition, transforming the East-North vectors into another orthogonal coordinate system, aligned along the movements parallel and perpendicular to the direction of seasonal motion (Text S4). The decomposition results (Figure 5.3b) clearly show an onset time half a year ahead of the earthquake, suggesting that unrest at Socompa was unlikely dynamically triggered by seismic waves induced by this earthquake.

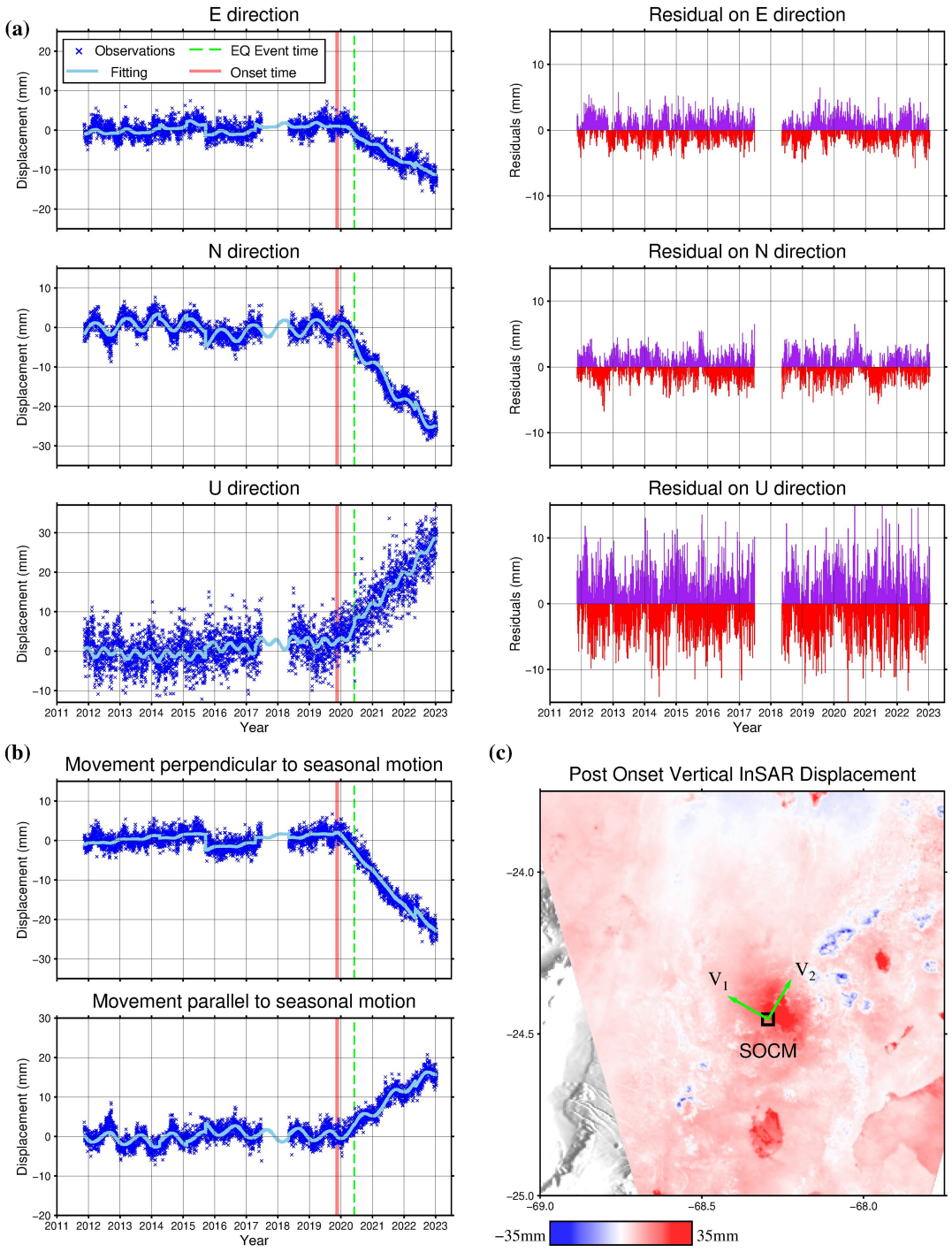

Figure 5.3: GPS time series parameter fitting to determine the deformation onset at Socompa volcano. (a) Daily GPS time series and parameterized fitting using Equation 5.2, and corresponding residuals. The thick red vertical line shows the 95% confidence interval of the onset time. The data have been detrended using the MIDAS algorithm before fitting (Blewitt et al., 2016). (b) Decomposition of East and North directions of GPS data into movement perpendicular and parallel to the direction of seasonal motion. (c) The relative location of this SOCM GPS station, using the vertical post onset time cumulative deformation field decomposed from ascending and descending as the background image. The green arrows indicate the rough direction of movement perpendicular (V_1) and parallel (V_2) to the seasonal motion used in (b).

5.4.3 Volcanic Geodetic Source Modelling

As we detect unrest at Socompa for the first time, we explore several source models to explain the observed deformation, including a point pressure source (Mogi, 1958), prolate spheroid (Yang et al., 1988), dipping dike with uniform opening (Okada, 1985), and a point Compound Dislocation Model (pCDM, Nikkhoo et al., 2017; Lundgren et al., 2017). We use the reconstructed post-onset cumulative deformation fields from the InSAR time series (Nov 2019 to Oct 2021), and cumulative GPS deformation at SOCM station that has the same time scale as InSAR data, as it improves the signal-to-noise ratio (SNR) of input data and subsequently provides more robust modelling results.

We first use a nested uniform downsampling of the reconstructed post-onset cumulative deformation fields, with a greater pixel density in the deformation area (Figure C.3). Then we use the GBIS software (Bagnardi and Hooper, 2018), a Bayesian approach for the inversion of multiple geodetic data sets that provides the posterior probability density functions of source model parameters, to invert the model parameters. We embed the code of pCDM (Nikkhoo et al., 2017) into the GBIS software so that all models run in the same environment, and use the data uncertainty within the InSAR and GPS observations to weight them during the inversion (Figure C.4).

To obtain the equivalent volume change of pCDM, we further use the point Ellipsoidal Cavity Model (pECM, Nikkhoo et al., 2017), a special case of pCDM that is constrained to represent a pressurized ellipsoidal cavity, to perform the inversion using the inferred source location and orientation from pCDM. Our modelling results show the Yang and pCDM (pECM) fits the observations best (Figure 5.4, C.5-C.9, and Table C.1, the values of reduced chi-squared, Text S5 are 0.42, 0.43, 0.48, and 0.65 for pCDM, Yang, Okada, and Mogi, respectively), and these two models give similar source depth (6.3 and 7.3 km for pCDM and Yang, respectively), geometry, and volume change ($\sim 1.1 \times 10^7$ m^3 for both models).

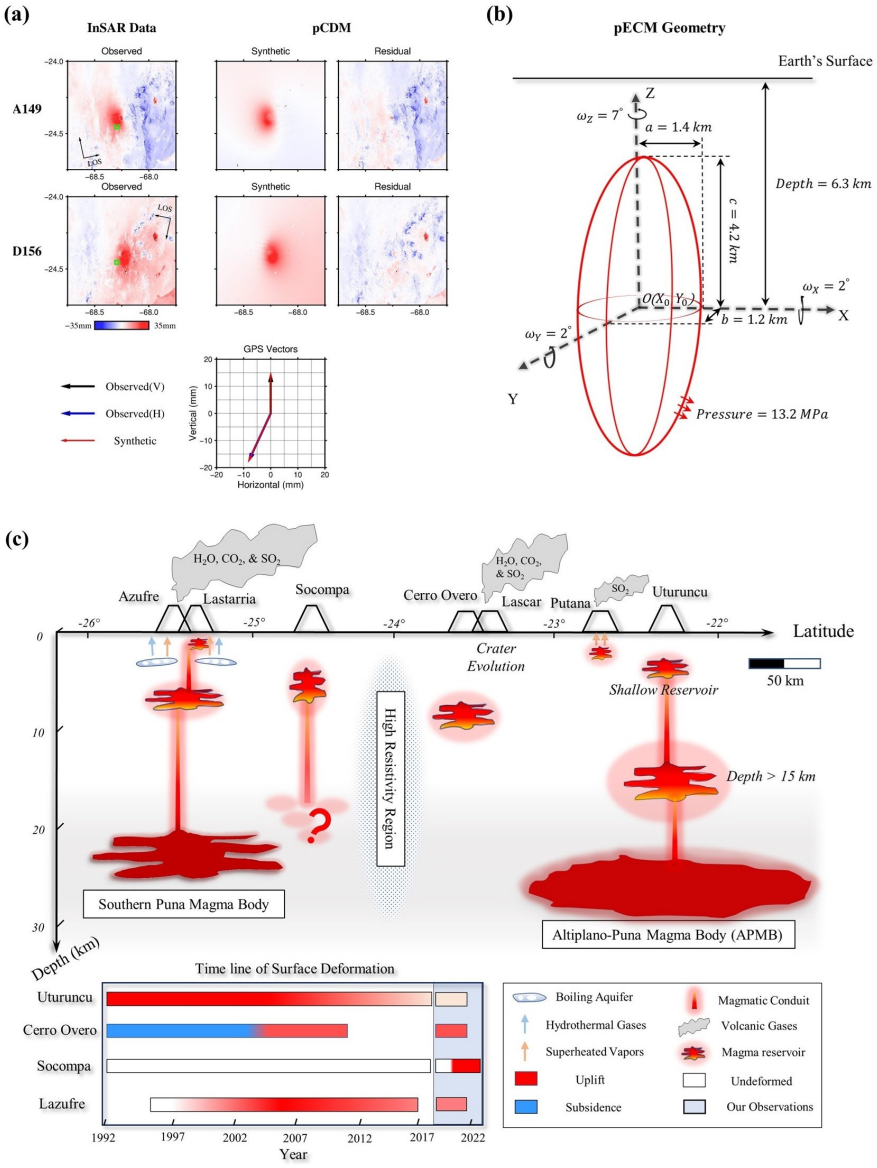

Figure 5.4: (a) Volcanic source model of Socompa cumulative uplift (Nov 2019 – Oct 2021) using pCDM. It shows the modelling results of InSAR and GPS observations. The green box in InSAR observations indicates the location of the SOCM station. In the GPS panel, the black vertical vector represents the up-component deformation (∼15 mm), while the blue vector signifies the horizontal deformation in the east (∼-10 mm) and north (∼-20 mm) directions. (b) Source geometry derived from pECM, which is defined by the source location (X_0,Y_0,Depth), the rotation angles around three axes (ω_X,ω_Y,ω_Z), the semi-axes along three axes (a,b,c), and the pressure on the cavity walls. Poisson's ratio is 0.25 and shear modulus is 32GPa here. (c) Cartoon depicting the magmatic systems in this region (approximate representation of relative locations), and those timelines of surface deformations from 1992-2023 measured by InSAR and GPS. Note the source depths vary based on different models and observation periods (e.g., Uturuncu 15-30 km, Lazufre < 10 km), and here we only plot the approximate depth of the magma reservoir, including the shallow reservoirs reported at Lastarria and Uturuncu (Froger et al., 2007; Lau et al., 2018; Gottsmann et al., 2022). We plot the rough depth of the Southern Puna Magma Body under Lazufre from Stechern et al., 2017, the shape and depth of APMB from Ward et al., 2014, and the extent of the high resistivity region from Ślezak et al., 2021. Depth at 0 km means the earth's surface at the local topography (summit elevations: 5, 706 m at Lazufre, 6, 031 m at Socompa, ∼5, 000 m at Cerro Overo, and 6, 008 m at Uturuncu).

5.5 Other Volcanic Deformations

Several volcanoes have been reported to be deforming in the past few decades (Figure 5.2) and we tie our InSAR observation to the GPS network in this region (Text S6 and Figure C.10) to compare our results to these earlier studies. Starting in the north, Uturuncu previously showed a deformation rate of ∼15 mm/yr in the 1990s (Fialko and Pearse, 2012; Henderson and Pritchard, 2013), but this gradually slowed in the 2010s (Gottsmann et al., 2017) to a rate of 3-5 mm/yr in ∼2017 (Lau et al., 2018) and ∼3 mm/yr in ∼2020 (Eiden et al., 2023). In agreement with previous studies, we observe an uplift rate of 2.5 ± 1.8 mm/yr on Uturuncu (2018-2021, Figure C.11a). Putana displayed short-lived uplift totaling 40 mm displacement in 2009-2010 (Henderson and Pritchard, 2013), whilst we find potential subsidence of -3.9 ± 2.1 mm/yr (Nov 2019-Oct 2021), with an onset which seems coincident with the deformation at Socompa (Figure C.11b). The deformation signal close to the Cerro Overo, which previously changed from subsidence of -4 mm/yr (1992-2003) to uplift of 5 mm/yr through 2010 on descending track (Henderson and Pritchard, 2013), continues to uplift at a rate of 3.8 ± 2.6 mm/yr (ascending LOS velocity, 2018-2021). Lazufre volcano shows uplift rates of 11.2 ± 1.7 mm/yr (2018-2021, Figure C.11c), consistent with the trend of surface deformation slowing at this volcano (Henderson and Pritchard, 2013; Remy et al., 2014; Henderson et al., 2017).

5.6 Discussion

Since uplift at Socompa started months before the M_w 6.8 intraslab earthquake, we instead consider a plausible explanation for the sudden uplift to be the ascent of magmatic fluids from a deeper melt source into a shallower reservoir. A magnetotelluric study (Ślezak et al., 2021) in the Atacama region found a high conductivity zone at Socompa (∼5 km west of the volcano and spanning 2 km to over 30 km depth), although there is significant uncertainty on the existence of the high conductivity zone as it is constrained by only one measurement point at Socompa, whereas the high resistivity region suggests that Socompa is unlikely connected to APMB (Figure 5.4c). The crust beneath Socompa and Cerro Overo has not been subject to the same level of study as Uturuncu and the APMB (e.g., Comeau et al., 2016). Deformation at Socompa has some first order similarities to that at Lazufre (∼90 km to the South): they have similar source depth (< 10 km) and rate of volume change in order of 10^6 m^3/yr (Remy et al., 2014; Henderson et al., 2017). The shallow reservoir and hydrothermal system beneath

Lazufre have been suggested to be linked to the Southern Puna Magma Body (Budach et al., 2013; Stechern et al., 2017; Ward et al., 2017), but there is no independent evidence for this at Socompa.

An interesting question here is whether the initiation of uplift at Socompa will maintain a linear rate, decrease exponentially like at Lazufre or whether it will gradually slow and eventually cease. The current geodetic observations show no trace of deceleration, which in a purely elastic system would imply a constant pressure increase. Alternatively, it may be too early to detect any decrease in magnitude of a hydraulic connection to a deeper magma supply. Note that the current pressure we obtain from the model is ∼13.2 MPa, which is far less than the overpressure required for chamber wall failure (Gerbault et al., 2018).

Deformation at Socompa is very consistent with other observations of unrest in the Central Andes (e.g., **Pritchard:2004**; Henderson and Pritchard, 2013). The deformation rate is low (usually < 30 mm/yr), and uplift started after an apparently very long period of quiescence (like Lazufre), consistent with deformation taking place on much longer timescales that other parts of the Andes (inter-eruptive and co-eruptive deformation rates are much higher in both the Northern and Southern Andes, e.g., Pritchard and Simons, 2004b; Fournier et al., 2010; Morales Rivera et al., 2016). This means that Holocene activity is not necessarily a good basis for assessing whether Central Andean volcanoes have active magmatic systems or are likely to enter a phase of unrest. InSAR measurements of deformation are therefore critical for the detection of volcanic unrest. However, volcano deformation in the Central Andes is generally not associated with eruption (except at Sabancaya and Lascar), reflecting lower rates of reservoir pressurization and therefore lower rates of magma flux that are more conducive to intrusion growth than brittle failure, dyke propagation and magma ascent (Biggs and Pritchard, 2017).

5.7 Conclusion

Our observations update the volcanic monitoring at Central Andean volcanoes in Northern Chile. We first detected unrest at Socompa volcano, contribute to a picture of low-rate, episodic deformation in this region, indicative of magmatic processes that take place on very long time scales of decades. We determine the onset time of Socompa uplift in Nov 2019, with a linear rate of 17.5 mm/yr up to Jan 2023, using InSAR and GPS observations. We test several geodetic source models, finding the best-fit for an ellipsoidal source located at a depth of ∼6.3 km and

volume change of $\sim 6.2 \times 10^6$ m^3/yr. We capture the onset of deformation at a Central Andean volcano for the first time at high temporal resolution, which suggests earthquake triggering is unlikely in this case. This provides a potentially important dataset for assessing the temporal development and therefore origin of such deformation.

Acknowledgement

This work is supported by the UK Natural Environment Research Council (NERC) through the Centre for the Observation and Modelling of Earthquakes, Volcanoes and Tectonics (COMET, http://comet.nerc.ac.uk), and the Looking into the Continents from Space (LiCS) large Grant (NE/K010867/1). Figures were made using the Generic Mapping Tools (GMT) (Wessel et al., 2013).

FL acknowledges support from the Great Britain-China Educational Trust. JE and TC acknowledge support from the Royal Society through University Research Fellowships (UF150282 and URF\R1\180088). SE is funded by a NERC Independent Research Fellowship (NE/R015546/1). AH and CNL acknowledge support from the European Research Council (ERC) through the EU Horizon 2020 project DEEPVOLC (grant number 866085). FD thanks FONDECYT Iniciacion 11220513 research grant for funding.

We acknowledge Kristina Butler, Catherine Gagnon, Joaquín Castillo, Sofía Parra, Milton Quinteros, and Gabriela Herrera for collecting the GPS data of the SOCM station. We thank Scott Henderson, Julie Elliott, and especially Matthew Pritchard (for installing the SOCM station) for their help in retrieving and processing the data.

Open Research

The Sentinel-1 SAR data are copyrighted by the European Space Agency and additionally distributed by the Alaska Satellite Facility Distributed Active Archive Center (https://earthdata.nasa.gov/eosdis/daacs/asf). All the GPS data we use, including SOCM (https://doi.org/10.7283/T5TT4P27), is processed by the Nevada Geodetic Laboratory (http://geodesy.unr.edu), which are based on services provided by the GAGE Facility, operated by UNAVCO, Inc., with support from the National Science Foundation, the National Aeronautics and Space Administration, and the U.S. Geological Survey under NSF Cooperative

Agreement EAR-1724794. The InSAR time series fitting and geodetic modelling results are available on Zenodo (https://doi.org/10.5281/zenodo.7688945).

Chapter 6

Conclusion

6.1 Summary of Research Outcomes

In this thesis, I have applied InSAR time series approaches to detect and measure the surface deformation of three shallow continental earthquakes (M_w 5.6-6.3, 0-20 km depth) in Iran, and a large intraslab earthquake (M_w 6.8, 112 km depth), as well as the nearby volcanic activities, in Northern Chile.

In chapter 3, I choose three shallow moderate magnitude earthquakes (M_w 6.0, 5 km depth, Aug 2018; M_w 6.3, 12 km depth, Nov 2018; and M_w 5.6, 11 km depth, Jan 2019) following the M_w 7.3 mainshock occurring in Nov 2017, Iran-Iraq border, as case studies to test the capability of InSAR for shallow continental earthquakes. I perform (five years of Sentinel-1 data) InSAR time series analysis to improve the detectability of these events that otherwise might go undetected within single interferograms. I reconstruct the coseismic deformation fields of three study cases, and remove the impact of the postseismic signals of the mainshock, using a time-dependent parameterized model fitted to time series data. The reconstructed coseismic deformation fields provide higher SNR and better signal identification, achieving more robust and seismologically consistent source modelling results than single interferograms. My work in Iran proves the better resolving power of InSAR time series approaches on shallow continental earthquakes.

In chapter 4, I further push the detectability limits of InSAR data on large intraslab earthquakes. I select a M_w 6.8, 112 km depth that occurred in Jun 2020, Northern Chile, as the case study, and perform four years of Sentinel-1 InSAR time series analysis spanning the earthquake event time.

I correct the ionospheric and tropospheric delay using split-spectrum and GACOS, respectively, which significantly improves the quality of time series data and makes it possible to retrieve the coseismic signals on both ascending and descending tracks. Due to the reconstructed coseismic deformation field derived from parameterized fitting still being noisy, especially in the far field, I use a blind source separation method, ICA, and successfully obtain an even 'cleaner' coseismic deformation field (with peak displacement of only ∼6 mm). I then perform earthquake source modelling using a combination of different datasets, including InSAR, GPS, and seismology. I find that InSAR provides a key contribution regarding the determination of the width and length of the fault, and a well-constrained fault plane can be achieved (7.9 km and 12.8 km for median width and length, respectively) when using all the datasets. This is by far the deepest and smallest earthquake observed by InSAR, which demonstrates the capability of using InSAR to study large intraslab earthquakes, providing new tools to help us better understand the rupture mechanisms of these events, and insights into the Earth's structure and properties of slabs.

In chapter 5, I use the same dataset as chapter 4 to monitor the volcanic activities in Central Andes. I report the first detection of unrest at Socompa, a volcano with no historical eruptions or previous observations of unrest. Since the location of Socompa is very close to the epicentre of the M_w 6.8 earthquake (∼120 km southeast), and the onset time of unrest is also close to the earthquake event time (Jun 2020) by visual check of InSAR time series data, I suspect that this deep intraslab event might trigger the Socompa unrest. I later use the continuous GPS observations from the nearby SOCM site, and precisely determine the onset time in Nov 2019, which suggests that the earthquake unlikely triggered the Socompa unrest. After determining the onset time, I calculate a steady uplift rate of 17.5 ± 3.7 mm/yr from Nov 2019 up to our observation end time. I then test several source models and find the deformation pattern can be best fitted with pressure increase in an ellipsoidal source region stretching from 2.1 to 10.5 km, with a volume change rate of 6.2×10^6 m^3/yr. My work updates Central Andean volcanoes' geodesy survey and explores their potential connections to intraslab earthquakes in this region.

6.2 Observational Limit of Sentinel-1 InSAR Observation

Back to the primary question in the introduction: how small surface deformation caused by earthquakes/volcanic activities, can be robustly captured by current InSAR observations? My short answer to this question is, for Sentinel-1 data, if time series approaches are applied, and

atmospheric noise is properly corrected, then ideally, the observation of ∼5 mm abrupt offsets (e.g., coseismic deformation) and linear velocity with an accuracy of standard deviation ∼1 mm/yr can be robustly achieved.

However, the actual situation is complicated, and it is very hard to tell how small signals could be identified before processing the data. Here, I summarise some of the most important factors that control the precision of Sentinel-1 InSAR time series measurements on earthquakes and volcanic activities:

1. Good coherence. As mentioned in chapter 2, the direct impact of low coherence is the loss of coverage, which seems not to affect the accurate measurements of the reserved area. However, even for the pixels with relatively high coherence, the non-zero phase closure residuals which are generally associated with the coherence (Michaelides et al., 2019; Maghsoudi et al., 2022), will still cause phase bias and affect the velocity estimation and its uncertainty (Ansari et al., 2020). While for estimating coseismic offsets, the loss of coherence may affect the phase unwrapping results, eventually impeding the robust estimation.

2. Atmospheric correction. The accuracy of InSAR measurements heavily depends on atmospheric noise removal. In addition, the impact of ionospheric delay is increasing because we are moving towards the next solar maximum, which is predicted to begin in 2025 (compared to the solar minimum in 2020). Considering the Chile case in chapter 4, I suggest that more attention should be paid to the correction of ionospheric delay, especially in the low-latitude region. Since atmospheric noise is generally thought to be random in time (Agram and Simons, 2015), it should not affect the optimal linear velocity values estimated from InSAR, but the uncertainty of these values might increase significantly, causing low SNR and making the coseismic deformation estimation more difficult.

3. Phase unwrapping. Since InSAR time series data is cumulative deformation, the main problem of phase unwrapping is that it will propagate throughout the time series from where it occurred. Therefore, it will severely bias the estimation of linear velocity, since each 2π error will cause a 28 mm offset (act like coseismic offsets) on the time series. To make things even worse, the small baseline subset inversion will use least square inversion to further 'optimise' this error, making it even harder to be identified and corrected as it no longer a 28 mm offset. This is also why many existing time series packages check the phase

closure residuals, and even try to use it to correct some unwrapping errors (e.g., MintPy, Yunjun et al., 2019; LiCSBAS, Morishita et al., 2020). However, as I have suggested in chapter 2, this does not entirely solve the problem. As for the extraction of coseismic offsets, phase unwrapping errors will be more about the misfit of the time series data due to the unwrapping errors that will cause the miscalculation of the coseismic deformation. In addition, the similar behaviour of coseismic deformation and phase unwrapping errors might cause errors in visual and automatic interpretation.

In conclusion, my work suggests that time series approaches could be applied to overall improve the quality of Sentinel-1 InSAR observation on surface deformation caused by earthquakes and volcanic activities. However, it still depends on the specific application scenarios and the quality of InSAR processing to determine the accuracy of the results.

6.3 Future Work

6.3.1 Application of InSAR Time Series Approaches

Given InSAR time series approaches can better retrieve coseismic deformation field, disentangle early postseismic deformation, split up complex sequences of earthquakes, estimate the change caused by volcanic unrest, etc. I make the following recommendations for the application of InSAR time series observations to the measurements related to earthquakes or volcanic activities:

1. Applying InSAR time series approaches (including parameterised fitting, ICA, etc.) to extract the surface deformation signals associated with the seismic cycle, especially for low SNR areas. More earthquake studies could be conducted in tectonically active region (such as Turkey, Japan, etc.) to validate and improve the overall performance of time series approaches. In addition, more cases of improved source parameters derived from InSAR would help to systematically evaluate the difference between InSAR and seismology. Determining any systematic, potentially region-specific biases, generic catalogue uncertainties, and finally exploring possible ways to calibrate such biases and reduce uncertainties.

2. Specifically, studying the intraslab earthquakes to better understand their rupture mechanisms and subsequent properties of slabs (Hosseinzadehsabeti et al., 2021). In addition, systematically evaluating how the change of the velocity structure of the subsurface can

affect InSAR observations, and exploring innovative approaches to use InSAR data to retrieve the velocity structure (Weston et al., 2012) will improve the seismological observations and help us reveal the Earth's structure.

3. Improving the state of the art of existing approaches (e.g., ICA), or deep learning methods to achieve automatic detection of the surface deformation caused by earthquakes and volcanoes (e.g., Malfante et al., 2018). This could be achieved if we had better characterisation of the deformation patterns of these events, and the rapid growth of data on earthquake and volcanic deformation using InSAR data is making this progress a reality.

6.3.2 Further InSAR Advancement

There are several major issues for the current InSAR time series data processing, which I think could potentially be the future work for better InSAR measurement:

1. Ionospheric correction approaches. Although the impact from ionospheric delay for C-band data is not particularly strong compared to L-band data, my work in Chile suggests that it still could greatly impact the accuracy of time series. In addition, considering the current ionospheric correction approaches still have their limitations (for example, the coherence issue and phase unwrapping errors for the split spectrum method) and the upcoming L-band data of the NISAR mission (Kellogg et al., 2020), it will be worth the effort to improve current existing approaches or develop new algorithms in the long run.

2. Phase bias caused by phase closure. It has been found that the combination of short (6-24 days) and long ($>$ 6 months) temporal baseline interferograms could potentially alleviate the effect of phase bias on linear velocity estimation (Purcell et al., 2022). However, such a strategy can hardly be the final solution for this problem considering the decorrelation noise and the large data volume required to be processed. Contrary to the idea of compensating for this error (e.g., Maghsoudi et al., 2022), I recommend re-checking the InSAR processing chain from the beginning, and re-evaluating if the current commonly used multilooking strategy is the best way to improve the SNR of the interferograms. I believe the proposal of new multilooking or filtering strategies could potentially be the answer to solve the phase bias issue.

3. Phase unwrapping algorithm. Although challenging, the reward is potentially huge given how severely current InSAR time series analysis suffers from this issue. Possible solutions

include utilizing phase closure during the unwrapping to directly output phase consistency results (Liu and Pan, 2019), machine learning approaches to better estimate the phase gradients (Zhou et al., 2021), or combining both.

References

Abe, K. (1972). Mechanics and tectonic implications of the 1966 and 1970 Peru earthquakes. *Physics of the Earth and Planetary Interiors*, *5*, 367–379. https://doi.org/10.1016/0031-9201(72)90108-2

Agram, P. S., & Simons, M. (2015). A noise model for InSAR time series. *Journal of Geophysical Research: Solid Earth*, *120*(4), 2752–2771. https://doi.org/10.1002/2014JB011271

Aguilera, F., Apaza, F., Del Carpio, J., Grosse, P., Jiménez, N., Ureta, G., Inostroza, M., Báez, W., Layana, S., Gonzalez, C., Rivera, M., Ortega, M., Gonzalez, R., & Iriarte, R. (2022). Advances in scientific understanding of the Central Volcanic Zone of the Andes: A review of contributing factors. *Bulletin of Volcanology*, *84*(3), 1–8. https://doi.org/10.1007/s00445-022-01526-y

Ahmed, R., Siqueira, P., Hensley, S., Chapman, B., & Bergen, K. (2011). A survey of temporal decorrelation from spaceborne L-Band repeat-pass InSAR. *Remote Sensing of Environment*, *115*(11), 2887–2896. https://doi.org/10.1016/j.rse.2010.03.017

Alif, S. M., Fattah, E. I., Kholil, M., & Anggara, O. (2021). Source of the 2019 Mw6. 9 Banten Intraslab earthquake modelled with GPS data inversion. *Geodesy and Geodynamics*, *12*(4), 308–314. https://doi.org/10.1016/j.geog.2021.06.001

Ambraseys, N. N. (2001). Reassessment of earthquakes, 1900-1999, in the Eastern Mediterranean and the Middle East. *Geophysical Journal International*, *145*(2), 471–485. https://doi.org/10.1046/j.0956-540x.2001.01396.x

Ansari, H., De Zan, F., & Parizzi, A. (2020). Study of systematic bias in measuring surface deformation with SAR interferometry. *IEEE Transactions on Geoscience and Remote Sensing*, *59*(2), 1285–1301. https://doi.org/10.1109/TGRS.2020.3003421

Astiz, L., Lay, T., & Kanamori, H. (1988). Large intermediate-depth earthquakes and the subduction process. *Physics of the Earth and Planetary interiors*, *53*(1-2), 80–166. https://doi.org/10.1016/0031-9201(88)90138-0

Bagnardi, M., & Hooper, A. (2018). Inversion of Surface Deformation Data for Rapid Estimates of Source Parameters and Uncertainties: A Bayesian Approach. *Geochemistry, Geophysics, Geosystems*, *19*(7), 2194–2211. https://doi.org/10.1029/2018GC007585

Bamler, R., & Hartl, P. (1998). Synthetic Aperture Radar interferometry. *Inverse Problems*, *14*(4). https://doi.org/10.1088/0266-5611/14/4/001

Barnhart, W. D., Brengman, C. M. J., Li, S., & Peterson, K. E. (2018). Ramp-flat basement structures of the Zagros Mountains inferred from co-seismic slip and afterslip of the 2017 Mw7.3 Darbandikhan, Iran/Iraq earthquake. *Earth and Planetary Science Letters*, *496*, 96–107. https://doi.org/10.1016/j.epsl.2018.05.036

Barnhart, W. D., Hayes, G. P., Samsonov, S. V., Fielding, E. J., & Seidman, L. E. (2014). Breaking the oceanic lithosphere of a subducting slab: The 2013 Khash, Iran earthquake. *Geophysical Research Letters*, *41*(1), 32–36. https://doi.org/10.1002/2013GL058096

Barone, A., Fedi, M., Tizzani, P., & Castaldo, R. (2019). Multiscale analysis of DInSAR measurements for multi-source investigation at uturuncu volcano (Bolivia). *Remote Sensing*, *11*(6), 703. https://doi.org/10.3390/rs11060703

Beck, S., Barrientos, S., Kausel, E., & Reyes, M. (1998). Source characteristics of historic earthquakes along the central Chile subduction Askew et Alzone. *Journal of South American Earth Sciences*, *11*(2), 115–129. https://doi.org/10.1016/S0895-9811(98)00005-4

Bekaert, D. P. S., Hooper, A., & Wright, T. J. (2015). A spatially variable power law tropospheric correction technique for InSAR Data. *Journal of Geophysical Research: Solid Earth*, *120*(2), 1345–1356. https://doi.org/10.1002/2014jb011558

Békési, E., Fokker, P. A., Martins, J. E., Norini, G., & van Wees, J. D. (2021). Source parameters of the 8 February 2016, Mw=4.2 Los Humeros earthquake by the inversion of InSAR-based ground deformation. *Geothermics*, *94*, 102133. https://doi.org/10.1016/j.geothermics.2021.102133

Belcher, D. P., & Rogers, N. C. (2009). Theory and simulation of ionospheric effects on Synthetic Aperture Radar. *IET Radar, Sonar and Navigation*, *3*(5), 541–551. https://doi.org/10.1049/iet-rsn.2008.0205

Biggs, J., Bergman, E., Emmerson, B., Funning, G. J., Jackson, J., Parsons, B., & Wright, T. J. (2006). Fault identification for buried strike-slip earthquakes using InSAR: The 1994 and 2004 Al Hoceima, Morocco earthquakes. *Geophysical Journal International*, *166*(3), 1347–1362. https://doi.org/10.1111/j.1365-246x.2006.03071.x

Biggs, J., Ebmeier, S. K., Aspinall, W. P., Lu, Z., Pritchard, M. E., Sparks, R. S. J., & Mather, T. A. (2014). Global link between deformation and volcanic eruption quantified by satellite imagery. *Nature Communications*, *5*(1), 3471. https://doi.org/10.1038/ncomms4471

Biggs, J., & Pritchard, M. E. (2017). Global volcano monitoring: what does it mean when volcanoes deform? *Elements*, *13*(1), 17–22. https://doi.org/10.2113/gselements.13.1.17

Billings, S. D., Sambridge, M. S., & Kennett, B. L. (1994). Errors in hypocenter location: Picking, model, and magnitude dependence. *Bulletin of the Seismological Society of America*, *84*(6), 1978–1990. https://doi.org/10.1785/bssa0840061978

Bird, P. (2003). An updated digital model of plate boundaries. *Geochemistry, Geophysics, Geosystems*, *4*(3). https://doi.org/10.1029/2001gc000252

Blewitt, G., Hammond, W., & Kreemer, C. (2018). Harnessing the GPS data explosion for interdisciplinary science. *Eos*, *99*. https://doi.org/10.1029/2018eo104623

Blewitt, G., Kreemer, C., Hammond, W. C., & Gazeaux, J. (2016). Midas robust trend estimator for accurate GPS station velocities without step detection. *Journal of Geophysical Research: Solid Earth*, *121*(3), 2054–2068. https://doi.org/10.1002/2015jb012552

Bock, Y., & Melgar, D. (2016). Physical applications of GPS geodesy: A Review. *Reports on Progress in Physics*, *79*(10), 106801. https://doi.org/10.1088/0034-4885/79/10/106801

Budach, I., Brasse, H., & Díaz, D. (2013). Crustal-scale electrical conductivity anomaly beneath inflating Lazufre volcanic complex, Central Andes. *Journal of South American Earth Sciences*, *42*, 144–149. https://doi.org/10.1016/j.jsames.2012.11.002

Bürgmann, R. (2002). Deformation during the 12 November 1999 Duzce, Turkey, earthquake, from GPS and InSAR Data. *Bulletin of the Seismological Society of America*, *92*(1), 161–171. https://doi.org/10.1785/0120000834

Chaussard, E., & Amelung, F. (2012). Precursory inflation of shallow magma reservoirs at West Sunda Volcanoes detected by InSAR. *Geophysical Research Letters*, *39*(21), 6–11. https://doi.org/10.1029/2012GL053817

Chien, S. A., Davies, A. G., Doubleday, J., Tran, D. Q., Mclaren, D., Chi, W., & Maillard, A. (2020). Automated Volcano Monitoring using multiple space and ground sensors. *Journal of Aerospace Information Systems*, *17*(4), 214–228. https://doi.org/10.2514/1.i010798

Cohen-Waeber, J., Bürgmann, R., Chaussard, E., Giannico, C., & Ferretti, A. (2018). Spatiotemporal patterns of precipitation-modulated landslide deformation from independent component analysis of InSAR Time Series. *Geophysical Research Letters*, *45*(4), 1878–1887. https://doi.org/10.1002/2017gl075950

Comeau, M. J., Unsworth, M. J., & Cordell, D. (2016). New constraints on the magma distribution and composition beneath Volcan Uturuncu and the southern Bolivian Altiplano from magnetotelluric data. *Geosphere*, *12*(5), 1391–1421. https://doi.org/10.1130/GES01277.1

Copley, A., Karasozen, E., Oveisi, B., Elliott, J. R., Samsonov, S., & Nissen, E. (2015). Seismogenic faulting of the sedimentary sequence and laterally variable material properties in the Zagros Mountains (Iran) revealed by the August 2014 murmuri (E. Dehloran) earthquake sequence. *Geophysical Journal International*, *203*(2), 1436–1459. https://doi.org/10.1093/gji/ggv365

Copley, A., & Reynolds, K. (2014). Imaging topographic growth by long-lived postseismic afterslip at Sefidabeh, East Iran. *Tectonics*, *33*(3), 330–345. https://doi.org/10.1002/2013tc003462

Costello, E. K., Halloy, S. R., Reed, S. C., Sowell, P., & Schmidt, S. K. (2009). Fumarole-supported islands of biodiversity within a hyperarid, high-elevation landscape on Socompa volcano, Puna de Atacama, Andes. *Applied and Environmental Microbiology*, *75*(3), 735–747. https://doi.org/10.1128/aem.01469-08

Craig, T. J., Jackson, J., Priestley, K., & Ekström, G. (2023). A cautionary tale: Examples of the mis-location of small earthquakes beneath the Tibetan Plateau by routine approaches. *Geophysical Journal International*, *233*(3), 2021–2038. https://doi.org/10.1093/gji/ggad025

Crosetto, M. (2002). Calibration and validation of SAR interferometry for DEM generation. *ISPRS Journal of Photogrammetry and Remote Sensing*, *57*(3), 213–227. https://doi.org/10.1016/s0924-2716(02)00107-7

Crosetto, M., Monserrat, O., Cuevas-González, M., Devanthéry, N., & Crippa, B. (2016). Persistent Scatterer Interferometry: A review. *ISPRS Journal of Photogrammetry and Remote Sensing*, *115*, 78–89. https://doi.org/10.1016/j.isprsjprs.2015.10.011

Dalaison, M., & Jolivet, R. (2020). A Kalman filter time series analysis method for InSAR. *Journal of Geophysical Research: Solid Earth*, *125*(7). https://doi.org/10.1029/2019jb019150

Das, A., Agrawal, R., & Mohan, S. (2014). Topographic correction of ALOS-PALSAR images using InSAR-derived DEM. *Geocarto International*, *30*(2), 145–153. https://doi.org/10.1080/10106049.2014.883436

De Zan, F., & Gomba, G. (2018). Vegetation and soil moisture inversion from SAR closure phases: First experiments and results. *Remote Sensing of Environment*, *217*, 562–572. https://doi.org/10.1016/j.rse.2018.08.034

De Zan, F., Zonno, M., & Lopez-Dekker, P. (2015). Phase inconsistencies and multiple scattering in SAR interferometry. *IEEE Transactions on Geoscience and Remote Sensing*, *53*(12), 6608–6616. https://doi.org/10.1109/tgrs.2015.2444431

Del Soldato, M., Confuorto, P., Bianchini, S., Sbarra, P., & Casagli, N. (2021). Review of works combining GNSS and InSAR in Europe. *Remote Sensing*, *13*(9), 1684. https://doi.org/10.3390/rs13091684

Di Giacomo, D., Engdahl, E. R., & Storchak, D. A. (2018). The ISC-GEM Earthquake Catalogue (1904-2014): Status after the Extension Project. *Earth System Science Data*, *10*(4), 1877–1899. https://doi.org/10.5194/essd-10-1877-2018

Di Traglia, F., De Luca, C., Manzo, M., Nolesini, T., Casagli, N., Lanari, R., & Casu, F. (2021). Joint exploitation of space-borne and ground-based multitemporal insar measurements for Volcano Monitoring: The Stromboli Volcano Case Study. *Remote Sensing of Environment*, *260*, 112441. https://doi.org/10.1016/j.rse.2021.112441

Di Traglia, F., Nolesini, T., Intrieri, E., Mugnai, F., Leva, D., Rosi, M., & Casagli, N. (2014). Review of ten years of volcano deformations recorded by the ground-based InSAR Monitoring System at stromboli volcano: A tool to mitigate volcano flank dynamics and intense volcanic activity. *Earth-Science Reviews*, *139*, 317–335. https://doi.org/10.1016/j.earscirev.2014.09.011

Díaz, D., Heise, W., & Zamudio, F. (2015). Three-dimensional resistivity image of the magmatic system beneath Lastarria Volcano and evidence for magmatic intrusion in the Back Arc

(Northern Chile). *Geophysical Research Letters*, *42*(13), 5212–5218. https://doi.org/10.1002/2015gl064426

Ding, X. L., Li, Z. W., Zhu, J. J., Feng, G. C., & Long, J. P. (2008). Atmospheric effects on InSAR measurements and their mitigation. *Sensors*, *8*(9), 5426–5448. https://doi.org/10.3390/s8095426

Doin, M. P., Lasserre, C., Peltzer, G., Cavalié, O., & Doubre, C. (2009). Corrections of stratified tropospheric delays in SAR interferometry: Validation with global atmospheric models. *Journal of Applied Geophysics*, *69*(1), 35–50. https://doi.org/10.1016/j.jappgeo.2009.03.010

Dorbath, C., Gerbault, M., Carlier, G., & Guiraud, M. (2008). Double seismic zone of the Nazca plate in northern Chile: High-resolution velocity structure, petrological implications, and thermomechanical modeling. *Geochemistry, Geophysics, Geosystems*, *9*(7). https://doi.org/10.1029/2008GC002020

Ducret, G., Doin, M. P., Grandin, R., Lasserre, C., & Guillaso, S. (2013). DEM corrections before unwrapping in a small baseline strategy for InSAR time series analysis. *IEEE Geoscience and Remote Sensing Letters*, *11*(3), 696–700. https://doi.org/10.1109/lgrs.2013.2276040

Ebmeier, S. K. (2016). Application of independent component analysis to multitemporal InSAR data with volcanic case studies. *Journal of Geophysical Research: Solid Earth*, *121*(12), 8970–8986. https://doi.org/10.1002/2016JB013765

Ebmeier, S. K., Andrews, B. J., Araya, M. C., Arnold, D. W., Biggs, J., Cooper, C., Cottrell, E., Furtney, M., Hickey, J., Jay, J., Lloyd, R., Parker, A. L., Pritchard, M. E., Robertson, E., Venzke, E., & Williamson, J. L. (2018). Synthesis of global satellite observations of magmatic and volcanic deformation: Implications for volcano monitoring the lateral extent of magmatic domains. *Journal of Applied Volcanology*, *7*(1). https://doi.org/10.1186/s13617-018-0071-3

Eggert, S., & Walter, T. R. (2009). Volcanic activity before and after large tectonic earthquakes: Observations and statistical significance. *Tectonophysics*, *471*(1–2), 14–26. https://doi.org/10.1016/j.tecto.2008.10.003

Eiden, E., MacQueen, P., Henderson, S., & Pritchard, M. (2023). Multiple spatial and temporal scales of deformation from geodetic monitoring point to active transcrustal magma

system at Uturuncu Volcano, Bolivia. *Geosphere*, *19*(2), 370–382. https://doi.org/10.1130/ges02520.1

Elliott, J. R., Walters, R. J., England, P. C., Jackson, J. A., Li, Z., & Parsons, B. (2010). Extension on the Tibetan Plateau: Recent normal faulting measured by InSAR and body wave seismology. *Geophysical Journal International*, *183*(2), 503–535. https://doi.org/10.1111/j.1365-246x.2010.04754.x

Elliott, J. R., Walters, R. J., & Wright, T. J. (2016). The role of space-based observation in understanding and responding to active tectonics and earthquakes. *Nature Communications*, *7*(1), 1–16. https://doi.org/10.1038/ncomms13844

Engdahl, E. R., van der Hilst, R., & Buland, R. (1998). Global teleseismic earthquake relocation with improved travel times and procedures for depth determination. *Bulletin of the Seismological Society of America*, *88*(3), 722–743. https://doi.org/10.1785/BSSA0880030722

England, P., & Jackson, J. (2011). Uncharted seismic risk. *Nature Geoscience*, *4*(6), 348–349. https://doi.org/10.1038/ngeo1168

Farías, M. E., Rascovan, N., Toneatti, D. M., Albarracín, V. H., Flores, M. R., Poiré, D. G., Collavino, M. M., Aguilar, O. M., Vazquez, M. P., & Polerecky, L. (2013). The Discovery of Stromatolites Developing at 3570 m above Sea Level in a High-Altitude Volcanic Lake Socompa, Argentinean Andes. *PLoS ONE*, *8*(1). https://doi.org/10.1371/journal.pone.0053497

Fathian, A., Atzori, S., Nazari, H., Reicherter, K., Salvi, S., Svigkas, N., Tatar, M., Tolomei, C., & Yaminifard, F. (2021). Complex co- and postseismic faulting of the 2017–2018 seismic sequence in western Iran revealed by InSAR and Seismic Data. *Remote Sensing of Environment*, *253*, 112224. https://doi.org/10.1016/j.rse.2020.112224

Fattahi, H., & Amelung, F. (2013). Dem error correction in InSAR Time Series. *IEEE Transactions on Geoscience and Remote Sensing*, *51*(7), 4249–4259. https://doi.org/10.1109/tgrs.2012.2227761

Fattahi, H., & Amelung, F. (2014). InSAR uncertainty due to orbital errors. *Geophysical Journal International*, *199*(1), 549–560. https://doi.org/10.1093/gji/ggu276

Fattahi, H., Simons, M., & Agram, P. (2017). InSAR time-series estimation of the ionospheric phase delay: An extension of the split range-spectrum technique. *IEEE Transactions on*

Geoscience and Remote Sensing, *55*(10), 5984–5996. https://doi.org/10.1109/TGRS.2017.2718566

Feng, W., Omari, K., & Samsonov, S. V. (2016). An automated InSAR Processing System: Potentials and challenges. *2016 IEEE International Geoscience and Remote Sensing Symposium (IGARSS)*, 3209–3210. https://doi.org/10.1109/IGARSS.2016.7729830

Feng, W., Samsonov, S., Almeida, R., Yassaghi, A., Li, J., Qiu, Q., Li, P., & Zheng, W. (2018). Geodetic constraints of the 2017 Mw7.3 Sarpol Zahab, Iran earthquake, and its implications on the structure and mechanics of the northwest Zagros thrust-fold belt. *Geophysical Research Letters*, *45*(14), 6853–6861. https://doi.org/10.1029/2018gl078577

Fernández, J., Romero, R., Carrasco, D., Luzón, F., & Araña, V. (2012). InSAR volcano and seismic monitoring in Spain. Results for the period 1992–2000 and possible interpretations. *Optics and Lasers in Engineering*, *37*(2-3), 285–297. https://doi.org/10.1029/2011jb008732

Ferrand, T. P., Hilairet, N., Incel, S., Deldicque, D., Labrousse, L., Gasc, J., Renner, J., Wang, Y., Green II, H. W., & Schubnel, A. (2017). Dehydration-driven stress transfer triggers intermediate-depth earthquakes. *Nature Communications*, *8*(1), 15247. https://doi.org/10.1038/ncomms15247

Ferretti, A., Fumagalli, A., Novali, F., Prati, C., Rocca, F., & Rucci, A. (2011). A new algorithm for processing interferometric data-stacks: SqueeSAR. *IEEE Transactions on Geoscience and Remote Sensing*, *49*(9), 3460–3470. https://doi.org/10.1109/TGRS.2011.2124465

Ferretti, A., Prati, C., & Rocca, F. (1999). Multibaseline InSAR DEM Reconstruction: The wavelet approach. *IEEE Transactions on Geoscience and Remote Sensing*, *37*(2), 705–715. https://doi.org/10.1109/36.752187

Fialko, Y. (2006). Interseismic strain accumulation and the earthquake potential on the southern San Andreas Fault System. *Nature*, *441*(7096), 968–971. https://doi.org/10.1038/nature04797

Fialko, Y., & Pearse, J. (2012). Sombrero uplift above the Altiplano-Puna magma body: Evidence of a ballooning mid-crustal diapir. *Science*, *338*(6104), 250–252. https://doi.org/10.1126/science.1226358

Fielding, E. J., Lundgren, P. R., Taymaz, T., Yolsal-Çevikbilen, S., & Owen, S. E. (2013). Fault-slip source models for the 2011 M 7.1 Van earthquake in Turkey from SAR in-

terferometry, pixel offset tracking, GPS, and seismic waveform analysis. *Seismological Research Letters*, *84*(4), 579–593. https://doi.org/10.1785/0220120164

Fielding, E. J., Sangha, S. S., Bekaert, D. P. S., Samsonov, S. V., & Chang, J. C. (2017). Surface deformation of North-Central Oklahoma related to the 2016 Mw 5.8 Pawnee earthquake from SAR interferometry time series. *Seismological Research Letters*, *88*(4), 971–982. https://doi.org/10.1785/0220170010

Florez, M. A., & Prieto, G. A. (2019). Controlling factors of seismicity and geometry in double seismic zones. *Geophysical Research Letters*, *46*(8), 4174–4181. https://doi.org/10.1029/2018GL081168

Floyd, M. A., Walters, R. J., Elliott, J. R., Funning, G. J., Svarc, J. L., Murray, J. R., Hooper, A. J., Larsen, Y., Marinkovic, P., Bürgmann, R., Johanson, I. A., & Wright, T. J. (2016). Spatial variations in fault friction related to lithology from rupture and Afterslip of the 2014 South Napa, California, earthquake. *Geophysical Research Letters*, *43*(13), 6808–6816. https://doi.org/10.1002/2016gl069428

Fournier, T. J., Pritchard, M. E., & Riddick, S. N. (2010). Duration, magnitude, and frequency of subaerial volcano deformation events: New results from Latin America using InSAR and a global synthesis. *Geochemistry, Geophysics, Geosystems*, *11*(1). https://doi.org/10.1029/2009GC002558

Froger, J. L., Remy, D., Bonvalot, S., & Legrand, D. (2007). Two scales of inflation at Lastarria-Cordon del Azufre volcanic complex, central Andes, revealed from ASAR-ENVISAT interferometric data. *Earth and Planetary Science Letters*, *255*(1–2), 148–163. https://doi.org/10.1016/j.epsl.2006.12.012

Frohlich, C. (2006). *Deep earthquakes*. Cambridge University Press. https://doi.org/10.1017/CBO9781107297562

Funning, G. J., & Garcia, A. (2019). A systematic study of earthquake detectability using Sentinel-1 Interferometric Wide-Swath data. *Geophysical Journal International*, *216*(1), 332–349. https://doi.org/10.1093/gji/ggy426

Gaddes, M. E., Hooper, A., & Bagnardi, M. (2019). Using machine learning to automatically detect volcanic unrest in a time series of interferograms. *Journal of Geophysical Research: Solid Earth*, *124*(12), 304–322. https://doi.org/10.1029/2019JB017519

Gaddes, M. E., Hooper, A., Bagnardi, M., Inman, H., & Albino, F. (2018). Blind Signal Separation Methods for Insar: The potential to automatically detect and monitor signals of volcanic deformation. *Journal of Geophysical Research: Solid Earth*, *123*(11), 10–226. https://doi.org/10.1029/2018jb016210

Gaete, A., Walter, T. R., Bredemeyer, S., Zimmer, M., Kujawa, C., Franco Marin, L., San Martin, J., & Bucarey Parra, C. (2020). Processes culminating in the 2015 phreatic explosion at Lascar volcano, Chile, evidenced by multiparametric data. *Natural Hazards and Earth System Sciences*, *20*(2), 377–397. https://doi.org/10.5194/nhess-20-377-2020

Gao, X., Liu, Y., Li, T., & Wu, D. (2017). High precision dem generation algorithm based on Insar Multi-look iteration. *Remote Sensing*, *9*(7), 741. https://doi.org/10.3390/rs9070741

Gerbault, M., Hassani, R., Novoa Lizama, C., & Souche, A. (2018). Three-Dimensional Failure Patterns Around an Inflating Magmatic Chamber. *Geochemistry, Geophysics, Geosystems*, *19*(3), 749–771. https://doi.org/10.1002/2017GC007174

Geudtner, D., Torres, R., Snoeij, P., Davidson, M., & Rommen, B. (2014). Sentinel-1 system capabilities and applications. *2014 IEEE Geoscience and Remote Sensing Symposium*. https://doi.org/10.1109/igarss.2014.6946711

Goldstein, R. M., Zebker, H. A., & Werner, C. L. (1988). Satellite radar interferometry: Two-dimensional phase unwrapping. *Radio Science*, *23*(4), 713–720. https://doi.org/10.1029/rs023i004p00713

Gomba, G., A., P., F., D. Z., M., E., & Bamler, R. (2016). Toward Operational Compensation of Ionospheric Effects in SAR Interferograms: The Split-Spectrum Method. *IEEE Transactions on Geoscience and Remote Sensing*, *54*(3), 1446–1461. https://doi.org/10.1109/TGRS.2015.2481079

Gonzalez-Ortega, A., Fialko, Y., Sandwell, D., Alejandro Nava-Pichardo, F., Fletcher, J., Gonzalez-Garcia, J., Lipovsky, B., Floyd, M., & Funning, G. (2014). El Mayor-Cucapah (Mw 7.2) earthquake: Early near-field postseismic deformation from InSAR and GPS observations. *Journal of Geophysical Research: Solid Earth*, *119*(2), 1482–1497. https://doi.org/10.1002/2013jb010193

Gottsmann, J., Blundy, J., Henderson, S., Pritchard, M. E., & Sparks, R. S. J. (2017). Thermomechanical modeling of the altiplano-puna deformation anomaly: Multiparameter

insights into magma mush reorganization. *Geosphere*, *13*(4), 1042–1045. https://doi.org/10.1130/GES01420.1

Gottsmann, J., Eiden, E., & Pritchard, M. E. (2022). Transcrustal Compressible Fluid Flow Explains the Altiplano-Puna Gravity and Deformation Anomalies. *Geophysical Research Letters*, *49*(16), 1–11. https://doi.org/10.1029/2022GL099487

Grandin, R., Vallée, M., & Lacassin, R. (2017). Rupture process of the Mw 5.8 Pawnee, Oklahoma, Earthquake from Sentinel-1 InSAR and Seismological Data. *Seismological Research Letters*, *88*(4), 994–1004. https://doi.org/10.1785/0220160226

Gratier, J. P., Renard, F., & Vial, B. (2014). Postseismic pressure solution creep: Evidence and time-dependent change from dynamic indenting experiments. *Journal of Geophysical Research: Solid Earth*, *119*(4), 2764–2779. https://doi.org/10.1002/2013jb010768

Gregg, P. M., Le Mével, H., Zhan, Y., Dufek, J., Geist, D., & Chadwick Jr, W. W. (2018). Stress triggering of the 2005 eruption of Sierra Negra Volcano, Galápagos. *Geophysical Research Letters*, *45*(24), 13–288. https://doi.org/10.1029/2018gl080393

Gualandi, A., & Liu, Z. (2021). Variational Bayesian Independent Component Analysis for InSAR Displacement Time-series with application to Central California, USA. *Journal of Geophysical Research: Solid Earth*, *126*(4). https://doi.org/10.1029/2020jb020845

Gutiérrez, F., Galve, J. P., Lucha, P., Castañeda, C., Bonachea, J., & Guerrero, J. (2011). Integrating geomorphological mapping, trenching, Insar and GPR for the identification and characterization of sinkholes: A review and application in the mantled evaporite karst of the Ebro Valley (Ne Spain). *Geomorphology*, *134*(1–2), 144–156. https://doi.org/10.1016/j.geomorph.2011.01.018

Hacker, B. R., Peacock, S. M., Abers, G. A., & Holloway, S. D. (2003). Subduction factory 2. Are intermediate-depth earthquakes in subducting slabs linked to metamorphic dehydration reactions? *Journal of Geophysical Research: Solid Earth*, *108*(B1). https://doi.org/10.1029/2001jb001129

Halloy, S. (1991). Islands of life at 6000 M Altitude: The Environment of the Highest Autotrophic Communities on Earth (Socompa Volcano, Andes). *Arctic and Alpine Research*, *23*(3), 247–262. https://doi.org/10.1080/00040851.1991.12002843

Hasegawa, A., & Nakajima, J. (2017). Seismic imaging of slab metamorphism and genesis of intermediate-depth intraslab earthquakes. *Progress in Earth and Planetary Science*, *4*(1), 12. https://doi.org/10.1186/s40645-017-0126-9

Hayes, G. P., Moore, G. L., Portner, D. E., Hearne, M., Flamme, H., Furtney, M., & Smoczyk, G. M. (2018). Slab2, a comprehensive subduction zone geometry model. *Science*, *362*(6410), 58–61. https://doi.org/10.1126/science.aat4723

Hearn, E. H. (2003). What can GPS data tell us about the dynamics of post-seismic deformation? *Geophysical Journal International*, *155*(3), 753–777. https://doi.org/10.1111/j.1365-246x.2003.02030.x

Heflin, M., Donnellan, A., Parker, J., Lyzenga, G., Moore, A., Ludwig, L. G., Rundle, J., Wang, J., & Pierce, M. (2020). Automated Estimation and Tools to Extract Positions, Velocities, Breaks, and Seasonal Terms From Daily GNSS Measurements: Illuminating Nonlinear Salton Trough Deformation. *Earth and Space Science*, *7*(7). https://doi.org/10.1029/2019ea000644

Henderson, S. T., Delgado, F., Elliott, J., Pritchard, M. E., & Lundgren, P. R. (2017). Decelerating uplift at Lazufre Volcanic Center, Central Andes, from A.D. 2010 to 2016, and Implications for Geodetic models. *Geosphere*, *13*(5), 1489–1505. https://doi.org/10.1130/ges01441.1

Henderson, S. T., & Pritchard, M. E. (2013). Decadal volcanic deformation in the Central Andes Volcanic Zone revealed by InSAR Time Series. *Geochemistry, Geophysics, Geosystems*, *14*(5), 1358–1374. https://doi.org/10.1002/ggge.20074

Herrera, C., Pastén-Araya, F., Cabrera, L., Potin, B., Rivera, E., Ruiz, S., Madariaga, R., & Contreras-Reyes, E. (2022). Rupture properties of the 2020 Mw 6.8 Calama (Northern Chile) intraslab earthquake. Comparison with similar intraslab events in the region. *Geophysical Journal International*, *232*(3), 2070–2079. https://doi.org/10.1093/gji/ggac434

Hetland, E. A., Musé, P., Simons, M., Lin, Y., Agram, P. S., & DiCaprio, C. J. (2012). Multiscale InSAR time series (MInTS) analysis of surface deformation. *Journal of Geophysical Research: Solid Earth*, *117*(B2). https://doi.org/10.1029/2011jb008731

Hickey, J., Gottsmann, J., & Del Potro, R. (2013). The large-scale surface uplift in the Altiplano-Puna region of Bolivia: A parametric study of source characteristics and crustal rheology

using finite element analysis. *Geochemistry, Geophysics, Geosystems*, *14*(3), 540–555. https://doi.org/10.1002/ggge.20057

Hill, D. P., Pollitz, F., & Newhall, C. (2002). Earthquake–volcano interactions. *Physics Today*, *55*(11), 41–47. https://doi.org/10.1063/1.1535006

Hilley, G. E., Bürgmann, R., Ferretti, A., Novali, F., & Rocca, F. (2004). Dynamics of slow-moving landslides from permanent scatterer analysis. *Science*, *304*(5679), 1952–1955. https://doi.org/10.1126/science.1098821

Hobbs, S., Mitchell, C., Forte, B., Holley, R., Snapir, B., & Whittaker, P. (2014). System design for Geosynchronous Synthetic Aperture Radar Missions. *IEEE Transactions on Geoscience and Remote Sensing*, *52*(12), 7750–7763. https://doi.org/10.1109/tgrs.2014.2318171

Hooper, A. (2008). A multi-temporal InSAR method incorporating both persistent scatterer and small baseline approaches. *Geophysical Research Letters*, *35*(16). https://doi.org/10.1029/2008gl034654

Hooper, A., Bekaert, D., Spaans, K., & Arıkan, M. (2012). Recent advances in SAR interferometry time series analysis for measuring crustal deformation. *Tectonophysics*, *514–517*, 1–13. https://doi.org/10.1016/j.tecto.2011.10.013

Hooper, A., Segall, P., & Zebker, H. (2007). Persistent scatterer interferometric synthetic aperture radar for crustal deformation analysis, with application to Volcán Alcedo, Galápagos. *Journal of Geophysical Research: Solid Earth*, *112*(7), 1–21. https://doi.org/10.1029/2006JB004763

Hooper, A., Zebker, H., Segall, P., & Kampes, B. (2004). A new method for measuring deformation on volcanoes and other natural terrains using InSAR persistent scatterers. *Geophysical Research Letters*, *31*(23). https://doi.org/10.1029/2004gl021737

Hosseinzadehsabeti, E., Ferré, E. C., Persaud, P., Fabbri, O., & Geissman, J. W. (2021). The rupture mechanisms of intraslab earthquakes: A multiscale review and re-evaluation. *Earth-Science Reviews*, *221*, 103782. https://doi.org/10.1016/j.earscirev.2021.103782

Hu, J., Li, Z. W., Ding, X. L., Zhu, J. J., Zhang, L., & Sun, Q. (2014). Resolving three-dimensional surface displacements from InSAR measurements: A review. *Earth-Science Reviews*, *133*, 1–17. https://doi.org/10.1016/j.earscirev.2014.02.005

Husen, S., & Hardebeck, J. L. (2010). *Theme iv - understanding seismicity catalogs and their problems: Earthquake location accuracy*. Community Online Resource for Statistical Seismicity Analysis. https://doi.org/10.5078/corssa-55815573

Husen, S., Kissling, E., Flueh, E., & Asch, G. (1999). Accurate hypocentre determination in the seismogenic zone of the subducting Nazca Plate in Northern Chile using a combined on-/offshore Network. *Geophysical Journal International*, *138*(3), 687–701. https://doi.org/10.1046/j.1365-246x.1999.00893.x

Hussain, E., Hooper, A., Wright, T. J., Walters, R. J., & Bekaert, D. P. (2016). Interseismic strain accumulation across the central North Anatolian Fault from iteratively unwrapped InSAR measurements. *Journal of Geophysical Research: Solid Earth*, *121*(12), 9000–9019. https://doi.org/10.1002/2016jb013108

Hutchings, L. (1994). Kinematic earthquake models and synthesized ground motion using empirical Green's functions. *Bulletin of the Seismological Society of America*, *84*(4), 1028–1050. https://doi.org/10.1785/BSSA0840041028

Hyvärinen, A. (2013). Independent component analysis: recent advances. *Philosophical Transactions of the Royal Society A: Mathematical, Physical and Engineering Sciences*, *371*(1984), 75–82. https://doi.org/10.1098/rsta.2011.0534

Hyvärinen, A., & Oja, E. (1997). A fast fixed-point algorithm for ICA. *Neural Comput*, *9*(7), 1483–1492. https://doi.org/10.1162/neco.1997.9.7.1483

Hyvärinen, A., & Oja, E. (2000). Independent component analysis: Algorithms and applications. *Neural Networks*, *13*(4), 411–430. https://doi.org/10.1016/S0893-6080(00)00026-5

Ide, S. (2019). Frequent observations of identical onsets of large and small earthquakes. *Nature*, *573*(7772), 112–116. https://doi.org/10.1038/s41586-019-1508-5

Ingleby, T., & Wright, T. J. (2017). Omori-like decay of postseismic velocities following continental earthquakes. *Geophysical Research Letters*, *44*(7), 3119–3130. https://doi.org/10.1002/2017gl072865

Ishimaru, A., Kuga, Y., Liu, J., Kim, Y., & Freeman, T. (1999). Ionospheric effects on Synthetic Aperture Radar at 100 MHz to 2 GHz. *Radio Science*, *34*(1), 257–268. https://doi.org/10.1029/1998rs900021

Ishwar, S. G., & Kumar, D. (2017). Application of DInSAR in mine surface subsidence monitoring and prediction. *Current Science*, *112*(1), 46–51. https://doi.org/10.18520/cs/v112/i01/46-51

Jackson, J. (2001). Living with earthquakes: Know your faults. *Journal of Earthquake Engineering*, *5*(sup001), 5–123. https://doi.org/10.1080/13632460109350530

Jay, J. A., Welch, M., Pritchard, M. E., Mares, P. J., Mnich, M. E., Melkonian, A. K., Aguilera, F., Naranjo, J. A., Sunagua, M., & Clavero, J. (2013). Volcanic hotspots of the central and southern andes as seen from space by ASTER and MODVOLC between the years 2000 and 2010. *Geological Society Special Publication*, *380*(1), 161–185. https://doi.org/10.1144/SP380.1

Johanson, I. A., Fielding, E. J., Rolandone, F., & Bürgmann, R. (2006). Coseismic and postseismic slip of the 2004 Parkfield earthquake from space-geodetic data. *Bulletin of the Seismological Society of America*, *96*(4B), S269–S282. https://doi.org/10.1785/0120050818

John, T., Medvedev, S., Rüpke, L. H., Andersen, T. B., Podladchikov, Y. Y., & Austrheim, H. (2009). Generation of intermediate-depth earthquakes by self-localizing thermal runaway. *Nature Geoscience*, *2*(2), 137–140. https://doi.org/10.1038/ngeo419

Jolivet, R., Grandin, R., Lasserre, C., Doin, M. P., & Peltzer, G. (2011). Systematic InSAR tropospheric phase delay corrections from global meteorological reanalysis data. *Geophysical Research Letters*, *38*(17),) https://doi.org/10.1029/2011gl048757

Jolivet, R., Lasserre, C., Doin, M. P., Guillaso, S., Peltzer, G., Dailu, R., Sun, J., Shen, Z. K., & Xu, X. (2012). Shallow creep on the Haiyuan Fault (Gansu, China) revealed by SAR Interferometry. *Journal of Geophysical Research: Solid Earth*, *117*(B6). https://doi.org/10.1029/2011jb008732

Jung, H. S., Lee, D. T., Lu, Z., & Won, J. S. (2012). Ionospheric correction of SAR Interferograms by multiple-aperture interferometry. *IEEE Transactions on Geoscience and Remote Sensing*, *51*(5), 3191–3199. https://doi.org/10.1109/tgrs.2012.2218660

Kagan, Y. Y. (2003). Accuracy of modern global earthquake catalogs. *Physics of the Earth and Planetary Interiors*, *135*(2–3), 173–209. https://doi.org/10.1016/s00319201(02)00214-5

Kanamori, H., Anderson, D. L., & Heaton, T. H. (1998). Frictional melting during the rupture of the 1994 Bolivian earthquake. *Science*, *279*(5352), 839–842. https://doi.org/10.1126/science.279.5352.839

Karasözen, E., & Karasözen, B. (2020). Earthquake location methods. *GEM - International Journal on Geomathematics*, *11*(1), 1–28. https://doi.org/10.1007/s13137-020-00149-9

Karato, S., Riedel, M. R., & Yuen, D. A. (2001). Rheological structure and deformation of subducted slabs in the mantle transition zone: Implications for mantle circulation and deep earthquakes. *Physics of the Earth and Planetary Interiors*, *127*(1–4), 83–108. https://doi.org/10.1016/s0031-9201(01)00223-0

Kawakatsu, H. (1985). Double seismic zone in Tonga. *Nature*, *316*(6023), 53–55. https://doi.org/10.1038/316053a0

Keefer, D. K. (2002). Investigating landslides caused by earthquakes–A historical review. *Surveys in Geophysics*, *23*(6), 473–510. https://doi.org/10.1023/a:1021274710840

Kellogg, K., Hoffman, P., Standley, S., Shaffer, S., Rosen, P., Edelstein, W., Dunn, C., Baker, C., Barela, P., Shen, Y., Guerrero, A. M., Xaypraseuth, P., Sagi, V. R., Sreekantha, C. V., Harinath, N., Kumar, R., Bhan, R., & Sarma, C. V. (2020). NASA-ISRO Synthetic Aperture Radar (NISAR) mission. *2020 IEEE Aerospace Conference*, 1–21. https://doi.org/10.1109/aero47225.2020.9172638

Khorrami, F., Vernant, P., Masson, F., Nilfouroushan, F., Mousavi, Z., Nankali, H., Saadat, S. A., Walpersdorf, A., Hosseini, S., Tavakoli, P., Aghamohammadi, A., & Alijanzade, M. (2019). An up-to-date crustal deformation map of Iran using integrated campaign-mode and permanent GPS velocities. *Geophysical Journal International*, *217*(2), 832–843. https://doi.org/10.1093/gji/ggz045

Kumar, V., & Venkataraman, G. (2011). SAR interferometric coherence analysis for snow cover mapping in the Western Himalayan region. *International Journal of Digital Earth*, *4*(1), 78–90. https://doi.org/10.1080/17538940903521591

Lanari, R., Casu, F., Manzo, M., Zeni, G., Berardino, P., Manunta, M., & Pepe, A. (2007). An overview of the small baseline subset algorithm: A DInSAR technique for surface deformation analysis. *Deformation and Gravity Change: Indicators of Isostasy, Tectonics, Volcanism, and Climate Change*, 637–661. https://doi.org/10.1007/978-3-7643-8417-3_2

Lau, N., Tymofyeyeva, E., & Fialko, Y. (2018). Variations in the long-term uplift rate due to the Altiplano–Puna magma body observed with Sentinel-1 interferometry. *Earth and Planetary Science Letters*, *491*, 43–47. https://doi.org/10.1016/j.epsl.2018.03.026

Lazeckỳ, M., Spaans, K., González, P. J., Maghsoudi, Y., Morishita, Y., Albino, F., Elliott, J., Greenall, N., Hatton, E., Hooper, A., Juncu, D., McDougall, A., Walters, R., Watson, C. S., Weiss, J. R., & Wright, T. J. (2020). LiCSAR: An automatic InSAR tool for measuring and monitoring tectonic and volcanic activity. *Remote Sensing*, *12*(15), 2430. https://doi.org/10.3390/RS12152430

Lemarchand, N., & Grasso, J. R. (2007). Interactions between earthquakes and volcano activity. *Geophysical Research Letters*, *34*(24). https://doi.org/10.1029/2007gl031438

Li, S., Xu, W., & Li, Z. (2022). Review of the SBAS InSAR Time-series algorithms, applications, and challenges. *Geodesy and Geodynamics*, *13*(2), 114–126. https://doi.org/10.1016/j.geog.2021.09.007

Li, Z., Muller, J. P., Cross, P., & Fielding, E. J. (2005). Interferometric synthetic aperture radar (InSAR) atmospheric correction: GPS, Moderate Resolution Imaging Spectroradiometer (MODIS), and InSAR integration. *Geophysical Research Letters*, *110*, B03410. https://doi.org/10.1029/2004JB003446

Li, Z., Wright, T., Hooper, A., Crippa, P., Gonzalez, P., Walters, R., Elliott, J., Ebmeier, S., Hatton, E., & Parsons, B. (2016). Towards InSAR everywhere, all the time, with sentinel-1. *ISPRS - International Archives of the Photogrammetry, Remote Sensing and Spatial Information Sciences*, *XLI-B4*, 763–766. https://doi.org/10.5194/isprsarchives-xli-b4-763-2016

Liang, C., Agram, P., Simons, M., & Fielding, E. J. (2019). Ionospheric correction of InSAR time series analysis of C-band sentinel-1 TOPS data. *IEEE Transactions on Geoscience and Remote Sensing*, *57*(9), 6755–6773. https://doi.org/10.1109/TGRS.2019.2908494

Lin, G., & Shearer, P. (2006). The COMPLOC earthquake location package. *Seismological Research Letters*, *77*(4), 440–444. https://doi.org/10.1785/gssrl.77.4.440

Lin, Y. N., Jolivet, R., Simons, M., Agram, P. S., Martens, H. R., Li, Z., & Lodi, S. H. (2015). High interseismic coupling in the Eastern Makran (Pakistan) subduction zone. *Earth and Planetary Science Letters*, *420*, 116–126. https://doi.org/10.1016/j.epsl.2015.03.037

Liu, F., Elliott, J. R., Craig, T. J., Hooper, A., & Wright, T. J. (2021). Improving the Resolving Power of InSAR for Earthquakes Using Time Series: A Case Study in Iran. *Geophysical Research Letters*, *48*, e2021GL093043. https://doi.org/10.1029/2021GL093043

Liu, F., Elliott, J. R., Ebmeier, S. K., Craig, T. J., Hooper, A., Novoa Lizama, C., & Delgado, F. (2023). First onset of unrest captured at Socompa: A recent geodetic survey at Central Andean volcanoes in Northern Chile. *Geophysical Research Letters*, *50*, e2022GL102480. https://doi.org/10.1029/2022GL102480

Liu, F., & Pan, B. (2019). A new 3-D minimum cost flow phase unwrapping algorithm based on closure phase. *IEEE Transactions on Geoscience and Remote Sensing*, *58*(3), 1857–1867. https://doi.org/10.1109/tgrs.2019.2949926

Liu, W., Agusdinata, D. B., & Myint, S. W. (2019). Spatiotemporal patterns of lithium mining and environmental degradation in the Atacama Salt Flat, Chile. *International Journal of Applied Earth Observation and Geoinformation*, *80*, 145–156. https://doi.org/10.1016/j.jag.2019.04.016

Liu, X., & Xu, W. (2019). Logarithmic Model Joint Inversion Method for Coseismic and Postseismic Slip: Application to the 2017 Mw 7.3 Sarpol Zahāb Earthquake, Iran. *Journal of Geophysical Research: Solid Earth*, *124*(11), 12034–12052. https://doi.org/10.1029/2019JB017953

Lohman, R. B., & Simons, M. (2005a). Locations of selected small earthquakes in the Zagros mountains. *Geochemistry, Geophysics, Geosystems*, *6*(3). https://doi.org/10.1029/2004GC000849

Lohman, R. B., & Simons, M. (2005b). Some thoughts on the use of InSAR data to constrain models of surface deformation: Noise structure and data downsampling. *Geochemistry, Geophysics, Geosystems*, *6*(1). https://doi.org/10.1029/2004gc000841

Lohman, R. B., Simons, M., & Savage, B. (2002). Location and mechanism of the Little Skull Mountain earthquake as constrained by satellite radar interferometry and seismic waveform modeling. *Journal of Geophysical Research: Solid Earth*, *107*(B6), ETG–7. https://doi.org/10.1029/2001jb000627

Lomax, A., Michelini, A., Curtis, A., & Meyers, R. A. (2009). Earthquake location, direct, global-search methods. *Encyclopedia of complexity and systems science*, *5*, 2449–2473. https://doi.org/10.1007/978-0-387-30440-3_150

Lu, P., Zhang, H., Gao, L., & Comte, D. (2021). Seismic imaging of the double seismic zone in the subducting slab in Northern Chile. *Earthquake Research Advances*, *1*(1), 100003. https://doi.org/10.1016/j.eqrea.2021.100003

Lundgren, P., Nikkhoo, M., Samsonov, S. V., Milillo, P., Gil-Cruz, F., & Lazo, J. (2017). Source model for the Copahue volcano magma plumbing system constrained by InSAR surface deformation observations. *Journal of Geophysical Research: Solid Earth*, *122*(7), 5729–5747. https://doi.org/10.1002/2017JB014368

Luo, H., Li, Z., Chen, J., Pearson, C., Wang, M., Lv, W., & Ding, H. (2019). Integration of Range Split Spectrum Interferometry and conventional InSAR to monitor large gradient surface displacements. *International Journal of Applied Earth Observation and Geoinformation*, *74*, 130–137. https://doi.org/10.1016/j.jag.2018.09.004

Luo, H., Wang, T., Wei, S., Liao, M., & Gong, J. (2021). Deriving Centimeter-Level Coseismic Deformation and Fault Geometries of Small-To-Moderate Earthquakes From Time-Series Sentinel-1 SAR Images. *Frontiers in Earth Science*, *9*, 1–13. https://doi.org/10.3389/feart.2021.636398

Lupi, M., Frehner, M., Weis, P., Skelton, A., Saenger, E. H., Tisato, N., Geiger, S., Chiodini, G., & Driesner, T. (2017). Regional earthquakes followed by delayed ground uplifts at Campi Flegrei Caldera, Italy: Arguments for a causal link. *Earth and Planetary Science Letters*, *474*, 436–446. https://doi.org/10.1016/j.epsl.2017.07.006

MacQueen, P., Delgado, F., Reath, K., Pritchard, M. E., Bagnardi, M., Milillo, P., Lundgren, P., Macedo, O., Aguilar, V., Ortega, M., Anccasi, R., Lazarte Zerpa, I. A., & Miranda, R. (2020). Volcano-tectonic interactions at Sabancaya Volcano, Peru: Eruptions, magmatic inflation, moderate earthquakes, and fault creep. *Journal of Geophysical Research: Solid Earth*, *125*(5), e2019JB019281. https://doi.org/10.1029/2019jb019281

Maghsoudi, Y., Hooper, A. J., Wright, T. J., Lazecky, M., & Ansari, H. (2022). Characterizing and correcting phase biases in short-term, multilooked interferograms. *Remote Sensing of Environment*, *275*, 113022. https://doi.org/10.1016/j.rse.2022.113022

Malfante, M., Dalla Mura, M., Metaxian, J. P., Mars, J. I., Macedo, O., & Inza, A. (2018). Machine learning for volcano-seismic signals: Challenges and perspectives. *IEEE Signal Processing Magazine*, *35*(2), 20–30. https://doi.org/10.1109/msp.2017.2779166

Malinverni, E. S., Sandwell, D. T., Tassetti, A. N., & Cappelletti, L. (2014). InSAR decorrelation to assess and prevent volcanic risk. *European Journal of Remote Sensing*, *47*(1), 537–556. https://doi.org/10.5721/eujrs20144730

Massonnet, D., Rossi, M., Carmona, C., Adragna, F., Peltzer, G., Feigl, K., & Rabaute, T. (1993). The displacement field of the Landers earthquake mapped by radar interferometry. *Nature*, *364*, 138–142. https://doi.org/10.1038/364138a0

Maubant, L., Pathier, E., Daout, S., Radiguet, M., Doin, M. P., Kazachkina, E., Kostoglodov, V., Cotte, N., & Walpersdorf, A. (2020). Independent component analysis and parametric approach for source separation in InSAR time series at regional scale: application to the 2017–2018 Slow Slip Event in Guerrero (Mexico). *Journal of Geophysical Research: Solid Earth*, *125*(3), e2019JB018187. https://doi.org/10.1029/2019jb018187

McGuire, W. J. (1996). Volcano instability: A review of contemporary themes. *Geological Society, London, Special Publications*, *110*(1), 1–23. https://doi.org/10.1144/gsl.sp.1996.110.01.01

McNutt, S. R., & Roman, D. C. (2015). Volcanic seismicity. *The Encyclopedia of Volcanoes*, 1011–1034. https://doi.org/10.1016/b978-0-12-385938-9.00059-6

Melnick, D., Moreno, M., Quinteros, J., Baez, J. C., Deng, Z., Li, S., & Oncken, O. (2017). The super-interseismic phase of the Megathrust earthquake cycle in Chile. *Geophysical Research Letters*, *44*(2), 784–791. https://doi.org/10.1002/2016gl071845

Merryman Boncori, J. P. (2019). Measuring coseismic deformation with Spaceborne Synthetic Aperture Radar: A Review. *Frontiers in Earth Science*, *7*, 16. https://doi.org/10.3389/feart.2019.00016

Michaelides, R. J., Zebker, H. A., & Zheng, Y. (2019). An algorithm for estimating and correcting decorrelation phase from InSAR data using closure phase triplets. *IEEE Transactions on Geoscience and Remote Sensing*, *57*(12), 10390–10397. https://doi.org/10.1109/tgrs.2019.2934362

Mogi, K. (1958). Relations between the eruptions of various volcanoes and the deformations of the ground surfaces around them. *Bulletin of Earthquake Research Institute*, *36*, 99–134.

Morales Rivera, A. M., Amelung, F., & Mothes, P. (2016). Volcano deformation survey over the Northern and Central Andes with ALOS InSAR time series. *Geochemistry, Geophysics, Geosystems*, *17*(7), 2869–2883. https://doi.org/10.1002/2016gc006393

Moreira, A., Prats-Iraola, P., Younis, M., Krieger, G., Hajnsek, I., & Papathanassiou, K. P. (2013). A tutorial on Synthetic Aperture Radar. *IEEE Geoscience and Remote Sensing Magazine*, *1*(1), 6–43. https://doi.org/10.1109/mgrs.2013.2248301

Morishita, Y. (2019). A Systematic Study of Synthetic Aperture Radar Interferograms Produced From ALOS-2 Data for Large Global Earthquakes From 2014 to 2016. *IEEE Journal of Selected Topics in Applied Earth Observations and Remote Sensing*, *12*(7), 2397–2408. https://doi.org/10.1109/jstars.2019.2921664

Morishita, Y., Kobayashi, T., & Yarai, H. (2016). Three-dimensional deformation mapping of a dike intrusion event in Sakurajima in 2015 by exploiting the right- and left-looking ALOS-2 InSAR. *Geophysical Research Letters*, *43*(9), 4197–4204. https://doi.org/10.1002/2016gl068293

Morishita, Y., Lazecky, M., Wright, T. J., Weiss, J. R., Elliott, J. R., & Hooper, A. (2020). LiCSBAS: An open-source InSAR time series analysis package integrated with the LiCSAR automated Sentinel-1 InSAR processor. *Remote Sensing*, *12*(3), 424. https://doi.org/10.3390/rs12030424

Myers, S. C., Johannesson, G., & Hanley, W. (2007). A Bayesian hierarchical method for multiple-event seismic location. *Geophysical Journal International*, *171*(3), 1049–1063. https://doi.org/10.1111/j.1365-246x.2007.03555.x

Myers, S. C., Johannesson, G., & Hanley, W. (2009). Incorporation of probabilistic seismic phase labels into a Bayesian multiple-event seismic locator. *Geophysical Journal International*, *177*(1), 193–204. https://doi.org/10.1111/j.1365-246x.2008.04070.x

Nakajima, J., & Hasegawa, A. (2010). Cause of M 7 intraslab earthquakes beneath the Tokyo metropolitan area, Japan: Possible evidence for a vertical tear at the easternmost portion of the Philippine Sea slab. *Journal of Geophysical Research: Solid Earth*, *115*(B4). https://doi.org/10.1029/2009JB006863

Nikkhoo, M., Walter, T. R., Lundgren, P. R., & Prats-Iraola, P. (2017). Compound dislocation models (CDMs) for Volcano Deformation Analyses. *Geophysical Journal International*, *208*(2), 877–894. https://doi.org/10.1093/gji/ggw427

Nishimura, T. (2017). Triggering of volcanic eruptions by large earthquakes. *Geophysical Research Letters*, *44*(15), 7750–7756. https://doi.org/10.1002/2017gl074579

Nishimura, T. (2018). Interaction between moderate earthquakes and volcanic eruptions: Analyses of Global Data Catalog. *Geophysical Research Letters*, *45*(16), 8199–8204. https://doi.org/10.1029/2018gl079060

Nissen, E., Ghods, A., Karasözen, E., Elliott, J. R., Barnhart, W. D., Bergman, E. A., Hayes, G. P., Jamal-Reyhani, M., Nemati, M., Tan, F., Abdulnaby, W., Benz, H. M., Shahvar, M. P., Talebian, M., & Chen, L. (2019). The 12 November 2017 Mw 7.3 Ezgeleh-Sarpolzahab (Iran) earthquake and active tectonics of the Lurestan Arc. *Journal of Geophysical Research: Solid Earth*, *124*(2), 2124–2152. https://doi.org/10.1029/2018JB016221

Ofeigsson, B. G., Hooper, A., Sigmundsson, F., Sturkell, E., & Grapenthin, R. (2011). Deep magma storage at Hekla Volcano, Iceland, revealed by InSAR Time Series analysis. *Journal of Geophysical Research*, *116*(B5). https://doi.org/10.1029/2010jb007576

Okada, Y. (1985). Surface deformation due to shear and tensile faults in a half-space. *Bulletin of the Seismological Society of America*, *75*(4), 1135–1154. https://doi.org/10.1785/bssa0750041135

Osmanoğlu, B., Dixon, T. H., Wdowinski, S., Cabral-Cano, E., & Jiang, Y. (2011). Mexico City subsidence observed with persistent Scatterer InSAR. *International Journal of Applied Earth Observation and Geoinformation*, *13*(1), 1–12. https://doi.org/10.1016/j.jag.2010.05.009

Osmanoğlu, B., Sunar, F., Wdowinski, S., & Cabral-Cano, E. (2016). Time series analysis of InSAR data: Methods and trends. *ISPRS Journal of Photogrammetry and Remote Sensing*, *115*, 90–102. https://doi.org/10.1016/j.isprsjprs.2015.10.003

Paton, D., Smith, L., Daly, M., & Johnston, D. (2008). Risk perception and volcanic hazard mitigation: Individual and Social Perspectives. *Journal of Volcanology and Geothermal Research*, *172*(3–4), 179–188. https://doi.org/10.1016/j.jvolgeores.2007.12.026

Pavlis, G. L., Vernon, F., Harvey, D., & Quinlan, D. (2004). The generalized earthquake-location (GENLOC) package: An earthquake-location library. *Computers and Geosciences*, *30*(9–10), 1079–1091. https://doi.org/10.1016/j.cageo.2004.06.010

Pearse, J., & Lundgren, P. (2013). Source model of deformation at Lazufre Volcanic Center, Central Andes, constrained by Insar Time Series. *Geophysical Research Letters*, *40*(6), 1059–1064. https://doi.org/10.1002/grl.50276

Pedersen, R., Jónsson, S., Árnadóttir, T., Sigmundsson, F., & Feigl, K. L. (2003). Fault slip distribution of two June 2000 m w 6.5 earthquakes in South Iceland estimated from

joint inversion of InSAR and GPS measurements. *Earth and Planetary Science Letters*, *213*(3–4), 487–502. https://doi.org/10.1016/s0012-821x(03)00302-9

Peltzer, G., & Rosen, P. (1995). Surface displacement of the 17 May 1993 Eureka Valley, California, earthquake observed by SAR interferometry. *Science*, *268*(5215), 1333–1336. https://doi.org/10.1126/science.268.5215.1333

Peng, M., Lu, Z., Zhao, C., Motagh, M., Bai, L., Conway, B. D., & Chen, H. (2022). Mapping land subsidence and aquifer system properties of the Willcox Basin, Arizona, from InSAR Observations and independent component analysis. *Remote Sensing of Environment*, *271*, 112894. https://doi.org/10.1016/j.rse.2022.112894

Pepe, A., & Calò, F. (2017). A review of interferometric synthetic aperture RADAR (InSAR) multi-track approaches for the retrieval of Earth's surface displacements. *Applied Sciences*, *7*(12), 1264. https://doi.org/10.3390/app7121264

Pepe, A., Yang, Y., Manzo, M., & Lanari, R. (2015). Improved EMCF-SBAS processing chain based on advanced techniques for the noise-filtering and selection of small baseline multi-look DInSAR interferograms. *IEEE Transactions on Geoscience and Remote Sensing*, *53*(8), 4394–4417. https://doi.org/10.1109/TGRS.2015.2396875

Perfettini, H., & Avouac, J. P. (2004). Postseismic relaxation driven by brittle creep: A possible mechanism to reconcile geodetic measurements and the decay rate of aftershocks, application to the Chi-Chi earthquake, Taiwan. *Journal of Geophysical Research: Solid Earth*, *109*(B2). https://doi.org/10.1029/2003jb002488

Perkins, J. P., Ward, K. M., de Silva, S. L., Zandt, G., Beck, S. L., & Finnegan, N. J. (2016). Surface uplift in the central Andes driven by growth of the Altiplano Puna Magma Body. *Nature Communications*, *7*(1). https://doi.org/10.1038/ncomms13185

Pi, X. (2015). Ionospheric effects on Spaceborne Synthetic Aperture Radar and a new capability of imaging the ionosphere from space. *Space Weather*, *13*(11), 737–741. https://doi.org/10.1002/2015sw001281

Poland, M., Bürgmann, R., Dzurisin, D., Lisowski, M., Masterlark, T., Owen, S., & Fink, J. (2006). Constraints on the mechanism of long-term, steady subsidence at Medicine Lake Volcano, Northern California, from GPS, leveling, and InSAR. *Journal of Volcanology and Geothermal Research*, *150*(1–3), 55–78. https://doi.org/10.1016/j.jvolgeores.2005.07.007

Poland, M. P., & Zebker, H. A. (2022). Volcano geodesy using InSAR in 2020: The past and next decades. *Bulletin of Volcanology*, *84*(3), 27. https://doi.org/10.1007/s00445-022-01531-1

Potin, P., Rosich, B., Miranda, N., Grimont, P., Shurmer, I., O'Connell, A., Krassenburg, M., & Gratadour, J. B. (2018). Sentinel-1 constellation mission operations status. *IGARSS 2018 - 2018 IEEE International Geoscience and Remote Sensing Symposium*. https://doi.org/10.1109/igarss.2018.8517743

Prejean, S. G., & Hill, D. P. (2018). The influence of tectonic environment on dynamic earthquake triggering: A review and case study on Alaskan volcanoes. *Tectonophysics*, *745*, 293–304. https://doi.org/10.1016/j.tecto.2018.08.007

Pritchard, M. E., Biggs, J., Wauthier, C., Sansosti, E., Arnold, D. W., Delgado, F., Ebmeier, S. K., Henderson, S. T., Stephens, K., Cooper, C., Wnuk, K., Amelung, F., Aguilar, V., Mothes, P., Macedo, O., Lara, L. E., Poland, M. P., & Zoffoli, S. (2018). Towards coordinated regional multi-satellite Insar Volcano Observations: Results from the Latin America Pilot Project. *Journal of Applied Volcanology*, *7*(1), 5. https://doi.org/10.1186/s13617-018-0074-0

Pritchard, M. E., Henderson, S. T., Jay, J. A., Soler, V., Krzesni, D. A., Button, N. E., Welch, M. D., Semple, A. G., Glass, B., Sunagua, M., Minaya, E., Amigo, A., & Clavero, J. (2014). Reconnaissance earthquake studies at nine volcanic areas of the central Andes with coincident satellite thermal and InSAR observations. *Journal of Volcanology and Geothermal Research*, *280*, 90–103. https://doi.org/10.1016/j.jvolgeores.2014.05.004

Pritchard, M. E., Jay, J. A., Aron, F., Henderson, S. T., & Lara, L. E. (2013). Subsidence at southern Andes volcanoes induced by the 2010 Maule, Chile earthquake. *Nature Geoscience*, *6*(8), 632–636. https://doi.org/10.1038/ngeo1855

Pritchard, M. E., Mather, T. A., McNutt, S. R., Delgado, F. J., & Reath, K. (2019). Thoughts on the criteria to determine the origin of volcanic unrest as magmatic or non-magmatic. *Philosophical Transactions of the Royal Society A: Mathematical, Physical and Engineering Sciences*, *377*(2139), 20180008. https://doi.org/10.1098/rsta.2018.0008

Pritchard, M. E., & Simons, M. (2002). A satellite geodetic survey of large-scale deformation of volcanic centres in the central Andes. *Nature*, *418*(6894), 167–171. https://doi.org/10.1038/nature00872

Pritchard, M. E., & Simons, M. (2004a). An InSAR-based survey of volcanic deformation in the central Andes. *Geochemistry, Geophysics, Geosystems*, *5*(2), Q02002. https://doi.org/10.1029/2003GC000610

Pritchard, M. E., & Simons, M. (2004b). An InSAR-based survey of volcanic deformation in the southern Andes. *Geophysical Research Letters*, *31*(15), L15610. https://doi.org/10.1029/2004GL020545

Purcell, V., Reddin, E., Ebmeier, S., González, P. J., Watson, A., Morishita, Y., & Elliott, J. (2022). Nearly Three Centuries of Lava Flow Subsidence at Timanfaya, Lanzarote. *Geochemistry, Geophysics, Geosystems*, *23*(10). https://doi.org/10.1029/2022gc010576

Qian, Y., Chen, X., Luo, H., Wei, S., Wang, T., Zhang, Z., & Luo, X. (2019). An Extremely Shallow Mw4.1 Thrust Earthquake in the Eastern Sichuan Basin (China) Likely Triggered by Unloading During Infrastructure Construction. *Geophysical Research Letters*, *46*(23), 13775–13784. https://doi.org/10.1029/2019gl085199

Ranero, C. R., Morgan, J. P., McIntosh, K., & Reichert, C. (2003). Bending-related faulting and mantle serpentinization at the Middle America Trench. *Nature*, *425*(6956), 367–373. https://doi.org/10.1038/nature01961

Reath, K., Pritchard, M., Poland, M., Delgado, F., Carn, S., Coppola, D., Andrews, B., Ebmeier, S. K., Rumpf, E., Henderson, S., Baker, S., Lundgren, P., Wright, R., Biggs, J., Lopez, T., Wauthier, C., Moruzzi, S., Alcott, A., Wessels, R., & ... Bagnardi, M. (2019). Thermal, deformation, and degassing remote sensing time series (CE 2000–2017) at the 47 most active volcanoes in Latin America: Implications for volcanic systems. *Journal of Geophysical Research: Solid Earth*, *124*(1), 195–218. https://doi.org/10.1029/2018JB016199

Recent crustal deformation in west-central south america (doctoral dissertation). (2003). California Institute of Technology. https://resolver.caltech.edu/CaltechETD:etd-06022003-105512

Remy, D., Froger, J. L., Perfettini, H., Bonvalot, S., Gabalda, G., Albino, F., Cayol, V., Legrand, D., & De, M. (2014). Persistent uplift of the Lazufre volcanic complex (Central Andes): New insights from PCAIM inversion of InSAR time series and GPS Data. *Geochemistry, Geophysics, Geosystems*, *15*(9), 3591–3611. https://doi.org/10.1002/2014GC005370

Richards-Dinger, K. B., & Shearer, P. M. (2000). Earthquake locations in Southern California obtained using source-specific station terms. *Journal of Geophysical Research: Solid Earth*, *105*(B5), 10939–10960. https://doi.org/10.1029/2000jb900014

Richter, N., Salzer, J. T., de Zeeuw-van Dalfsen, E., Perissin, D., & Walter, T. R. (2018). Constraints on the geomorphological evolution of the nested summit craters of Láscar volcano from high spatio-temporal resolution TerraSAR-X interferometry. *Bulletin of Volcanology*, *80*(3). https://doi.org/10.1007/s00445-018-1195-3

Rignot, E., Echelmeyer, K., & Krabill, W. (2001). Penetration depth of interferometric synthetic-aperture radar signals in snow and Ice. *Geophysical Research Letters*, *28*(18), 3501–3504. https://doi.org/10.1029/2000gl012484

Rodi, W. (2006). Grid-search event location with non-Gaussian Error Models. *Physics of the Earth and Planetary Interiors*, *158*(1), 55–66. https://doi.org/10.1016/j.pepi.2006.03.010

Rosen, P. A., Gurrola, E., Sacco, G. F., & Zebker, H. (2012). The insar scientific computing environment. *9th European Conference on Synthetic Aperture Radar*, 730–733.

Rott, H. (2009). Advances in interferometric synthetic aperture radar (InSAR) in Earth System Science. *Progress in Physical Geography: Earth and Environment*, *33*(6), 769–791. https://doi.org/10.1177/0309133309350263

Rucci, A., Ferretti, A., Monti Guarnieri, A., & Rocca, F. (2012). Sentinel 1 SAR Interferometry Applications: The outlook for sub millimeter measurements. *Remote Sensing of Environment*, *120*, 156–163. https://doi.org/10.1016/j.rse.2011.09.030

Ruch, J., & Walter, T. R. (2010). Relationship between the InSAR-measured uplift, the structural framework, and the present-day stress field at Lazufre Volcanic area, Central Andes. *Tectonophysics*, *492*(1–4), 133–140. https://doi.org/10.1016/j.tecto.2010.06.003

Ruch, J., Warren, J. K., Risacher, F., Walter, T. R., & Lanari, R. (2012). Salt Lake Deformation detected from space. *Earth and Planetary Science Letters*, *331–332*, 120–127. https://doi.org/10.1016/j.epsl.2012.03.009

Ryder, I., Parsons, B., Wright, T. J., & Funning, G. J. (2007). Post-seismic motion following the 1997 Manyi (Tibet) earthquake: Insar observations and modelling. *Geophysical Journal International*, *169*(3), 1009–1027. https://doi.org/10.1111/j.1365-246x.2006.03312.x

Salvi, S., Stramondo, S., Funning, G. J., Ferretti, A., Sarti, F., & Mouratidis, A. (2012). The Sentinel-1 mission for the improvement of the scientific understanding and the operational monitoring of the seismic cycle. *Remote Sensing of Environment*, *120*, 164–174. https://doi.org/10.1016/j.rse.2011.09.029

Samiei-Esfahany, S., Martins, J. E., Van Leijen, F., & Hanssen, R. F. (2016). Phase Estimation for Distributed Scatterers in InSAR Stacks Using Integer Least Squares Estimation. *IEEE Transactions on Geoscience and Remote Sensing*, *54*(10), 5671–5687. https://doi.org/10.1109/TGRS.2016.2566604

Schmidt, M. W., & Poli, S. (1998). Experimentally based water budgets for dehydrating slabs and consequences for arc magma generation. *Earth and Planetary Science Letters*, *163*(1-4), 361–379. https://doi.org/10.1016/S0012-821X(98)00142-3

Scholz, C. (2002). *The mechanics of earthquakes and faulting* (2nd). Cambridge University Press. https://doi.org/10.1017/CBO9780511818516

Scott, C. P., Lohman, R. B., & Jordan, T. E. (2017). InSAR constraints on soil moisture evolution after the March 2015 extreme precipitation event in Chile. *Scientific Reports*, *7*(1), 4903. https://doi.org/10.1038/s41598-017-05123-4

Sentinel-1 Observation Scenario. (2023). European Space Agency. Retrieved July 1, 2023, from https://sentinels.copernicus.eu/web/sentinel/missions/sentinel-1/observation-scenario

Seropian, G., Kennedy, B. M., Walter, T. R., Ichihara, M., & Jolly, A. D. (2021). A review framework of how earthquakes trigger volcanic eruptions. *Nature Communications*, *12*(1), 1004. https://doi.org/10.1038/s41467-021-21166-8

Shearer, P. M. (1997). Improving local earthquake locations using the L1 norm and waveform cross correlation: Application to the whittier narrows, California, aftershock sequence. *Journal of Geophysical Research: Solid Earth*, *102*(B4), 8269–8283. https://doi.org/10.1029/96jb03228

Shearer, P. M. (2019). *Introduction to seismology* (1st). Cambridge University Press. https://doi.org/10.1017/9781316877111

Shen, L., Hooper, A., & Elliott, J. (2019). A Spatially Varying Scaling Method for InSAR Tropospheric Corrections Using a High-Resolution Weather Model. *Journal of Geophysical Research: Solid Earth*, *124*(4), 4051–4068. https://doi.org/10.1029/2018JB016189

Shirzaei, M., & Walter, T. R. (2011). Estimating the effect of satellite orbital error using wavelet-based robust regression applied to InSAR deformation data. *IEEE transactions on geoscience and remote sensing*, *49*(11), 4600–4605. https://doi.org/10.1109/tgrs.2011.2143419

Singh, S. K., Reinoso, E., Arroyo, D., Ordaz, M., Cruz-Atienza, V., Pérez-Campos, X., Iglesias, A., & Hjörleifsdóttir, V. (2018). Deadly intraslab Mexico earthquake of 19 September 2017 (MW 7.1): Ground Motion and damage pattern in Mexico City. *Seismological Research Letters*, *89*(6), 2193–2203. https://doi.org/10.1785/0220180159

Sippl, C., Schurr, B., Asch, G., & Kummerow, J. (2018). Seismicity structure of the northern Chile forearc from ¿ 100,000 double-difference relocated hypocenters. *Journal of Geophysical Research: Solid Earth*, *123*(5), 4063–4087. https://doi.org/10.1002/2017jb015384

Ślezak, K., Díaz, D., Vargas, J. A., Cordell, D., Reyes-Cordova, F., & Segovia, M. J. (2021). Magnetotelluric image of the Chilean subduction zone in the Salar de Atacama Region (23°-24°S): Insights into factors controlling the distribution of volcanic arc magmatism. *Physics of the Earth and Planetary Interiors*, *318*, 106765. https://doi.org/10.1016/j.pepi.2021.106765

Solari, L., Del Soldato, M., Raspini, F., Barra, A., Bianchini, S., Confuorto, P., Casagli, N., & Crosetto, M. (2020). Review of satellite interferometry for landslide detection in Italy. *Remote Sensing*, *12*(8), 1351. https://doi.org/10.3390/rs12081351

Sousa, J. J., Hooper, A. J., Hanssen, R. F., Bastos, L. C., & Ruiz, A. M. (2011). Persistent Scatterer InSAR: A comparison of methodologies based on a model of temporal deformation vs. spatial correlation selection criteria. *Remote Sensing of Environment*, *115*(10), 2652–2663. https://doi.org/10.1016/j.rse.2011.05.021

Stebel, K., Amigo, A., Thomas, H., & Prata, A. J. (2014). First estimates of fumarolic SO2 fluxes from Putana volcano, Chile, using an ultraviolet imaging camera. *Journal of Volcanology and Geothermal Research*, *300*, 112–120. https://doi.org/10.1016/j.jvolgeores.2014.12.021

Steblov, G. M., Ekström, G., Kogan, M. G., Freymueller, J. T., Titkov, N. N., Vasilenko, N. F., & Kondratyev, M. N. (2014). First geodetic observations of a deep earthquake: The

2013 Sea of Okhotsk Mw 8.3, 611 km-deep, event. *Geophysical Research Letters*, *41*(11), 3826–3832. https://doi.org/10.1002/2014GL060003

Stechern, A., Just, T., Holtz, F., Blume-Oeste, M., & Namur, O. (2017). Decoding magma plumbing and geochemical evolution beneath the Lastarria volcanic complex (Northern Chile)—Evidence for multiple magma storage regions. *Journal of Volcanology and Geothermal Research*, *338*, 25–45. https://doi.org/10.1016/j.jvolgeores.2017.03.018

Stein, S., Geller, R. J., & Liu, M. (2012). Why earthquake hazard maps often fail and what to do about it. *Tectonophysics*, *562–563*, 1–25. https://doi.org/10.1016/j.tecto.2012.06.047

Stephenson, O. L., Liu, Y.-K., Yunjun, Z., Simons, M., Rosen, P., & Xu, X. (2022). The impact of plate motions on long-wavelength InSAR-derived velocity fields. *Geophysical Research Letters*, *49*, e2022GL099835. https://doi.org/10.1002/essoar.10511538.1

Stramondo, S., Moro, M., Tolomei, C., Cinti, F. R., & Doumaz, F. (2005). InSAR surface displacement field and fault modelling for the 2003 bam earthquake (southeastern Iran). *Journal of Geodynamics*, *40*(2–3), 347–353. https://doi.org/10.1016/j.jog.2005.07.013

Strasser, F. O., Arango, M. C., & Bommer, J. J. (2010). Scaling of the source dimensions of interface and intraslab subduction-zone earthquakes with moment magnitude. *Seismological Research Letters*, *81*(6), 941–950. https://doi.org/10.1785/gssrl.81.6.941

Styron, R., & Pagani, M. (2020). The GEM Global Active Faults Database. *Earthquake Spectra*, *36*, 160–180. https://doi.org/10.1177/8755293020944182

Takada, Y., & Fukushima, Y. (2013). Volcanic subsidence triggered by the 2011 Tohoku earthquake in Japan. *Nature Geoscience*, *6*(8), 637–641. https://doi.org/10.1038/ngeo1857

Thielmann, M., Rozel, A., Kaus, B. J. P., & Ricard, Y. (2015). Intermediate-depth earthquake generation and shear zone formation caused by grain size reduction and shear heating. *Geology*, *43*(9), 791–794. https://doi.org/10.1130/g36864.1

Thingbaijam, K. K. S., Mai, P. M., & Goda, K. (2017). New Empirical Earthquake Source-Scaling Laws. *Bulletin of the Seismological Society of America*, *107*(5), 2225–2246. https://doi.org/10.1785/0120170017

Tobita, M. (2016). Combined logarithmic and exponential function model for fitting postseismic GNSS time series after 2011 Tohoku-Oki earthquake. Geodesy. *Earth, Planets and Space*, *68*(1). https://doi.org/10.1186/s40623-016-0422-4

Tomás, R., Li, Z., Lopez-Sanchez, J. M., Liu, P., & Singleton, A. (2016). Using wavelet tools to analyse seasonal variations from InSAR Time-series data: A case study of the Huangtupo landslide. *Landslides*, *13*(3), 437–450. https://doi.org/10.1007/s10346-015-0589-y

Tralli, D. M., Blom, R. G., Zlotnicki, V., Donnellan, A., & Evans, D. L. (2005). Satellite Remote Sensing of earthquake, Volcano, Flood, landslide and coastal inundation hazards. *ISPRS Journal of Photogrammetry and Remote Sensing*, *59*(4), 185–198. https://doi.org/10.1016/j.isprsjprs.2005.02.002

Traversa, P., & Grasso, J. R. (2010). How is volcano seismicity different from tectonic seismicity? *Bulletin of the Seismological Society of America*, *100*(4), 1755–1769. https://doi.org/10.1785/0120090214

Twardzik, C., Vergnolle, M., Sladen, A., & Avallone, A. (2019). Unravelling the contribution of early postseismic deformation using sub-daily GNSS positioning. *Scientific Reports*, *9*(1), 1–12. https://doi.org/10.1038/s41598-019-39038-z

Vallée, M., Xie, Y., Grandin, R., Villegas-Lanza, J. C., Nocquet, J.-M., Vaca, S., Meng, L., Ampuero, J. P., Mothes, P., Jarrin, P., Sierra Farfán, C., & Rolandone, F. (2023). Self-reactivated rupture during the 2019 Mw= 8 northern Peru intraslab earthquake. *Earth and Planetary Science Letters*, *601*, 117886. https://doi.org/10.1016/j.epsl.2022.117886

van Zyl, J. J. (2001). The shuttle radar topography mission (SRTM): A breakthrough in remote sensing of topography. *Acta Astronautica*, *48*(5–12), 559–565. https://doi.org/10.1016/s0094-5765(01)00020-0

Vasyura-Bathke, H., Dettmer, J., Steinberg, A., Heimann, S., Isken, M. P., Zielke, O., Mai, P. M., Sudhaus, H., & Jónsson, S. (2020). The bayesian earthquake analysis tool. *Seismological Research Letters*, *91*(2), 1003–1018. https://doi.org/10.1785/0220190075

Wadge, G., Francis, P. W., & Ramirez, C. F. (1995). The Socompa collapse and avalanche event. *Journal of Volcanology and Geothermal Research*, *66*(1–4), 309–336. https://doi.org/10.1016/0377-0273(94)00083-s

Walter, T. R., & Motagh, M. (2014). Deflation and inflation of a large magma body beneath Uturuncu Volcano, Bolivia? Insights from InSAR data, surface lineaments and stress modelling. *Geophysical Journal International*, *198*(1), 462–473. https://doi.org/10.1093/gji/ggu080

Wang, L., Gao, H., Feng, G., & Xu, W. (2018). Source parameters and triggering links of the earthquake sequence in central Italy from 2009 to 2016 analyzed with GPS and InSAR Data. *Tectonophysics*, *744*, 285–295. https://doi.org/10.1016/j.tecto.2018.07.013

Ward, K. M., Delph, J. R., Zandt, G., Beck, S. L., & Ducea, M. N. (2017). Magmatic evolution of a Cordilleran flare-up and its role in the creation of silicic crust. *Scientific Reports*, *7*(1), 1–8. https://doi.org/10.1038/s41598-017-09015-5

Ward, K. M., Zandt, G., Beck, S. L., Christensen, D. H., & McFarlin, H. (2014). Seismic imaging of the magmatic underpinnings beneath the Altiplano-Puna volcanic complex from the joint inversion of surface wave dispersion and receiver functions. *Earth and Planetary Science Letters*, *404*, 43–53. https://doi.org/10.1016/j.epsl.2014.07.022

Webster, R., & Oliver, M. A. (2007). *Geostatistics for environmental scientists* (2nd). John Wiley; Sons. https://doi.org/10.1002/9780470517277

Wegmuller, U., Werner, C., Strozzi, T., & Wiesmann, A. (2006). Ionospheric electron concentration effects on SAR and INSAR. *2006 IEEE International Symposium on Geoscience and Remote Sensing*, 3731–3734. https://doi.org/10.1109/igarss.2006.956

Wei, M., & Sandwell, D. T. (2010). Decorrelation of L-band and C-band interferometry over vegetated areas in California. *IEEE Transactions on Geoscience and Remote Sensing*, *48*(7), 2942–2952. https://doi.org/10.1109/TGRS.2010.2043442

Wei, S. S., Wiens, D. A., van Keken, P. E., & Cai, C. (2017). Slab temperature controls on the Tonga double seismic zone and slab mantle dehydration. *Science advances*, *3*(1), e1601755. https://doi.org/10.1126/sciadv.1601755

Wessel, P., Smith, W. H. F., Scharroo, R., Luis, J., & Wobbe, F. (2013). Generic Mapping Tools: Improved version released. *Eos, Transactions American Geophysical Union*, *94*(45), 409–410. https://doi.org/10.1002/2013EO450001

Weston, J., Ferreira, A. M. G., & Funning, G. J. (2012). Systematic comparisons of earthquake source models determined using InSAR and seismic data. *Tectonophysics*, *532–535*, 61–81. https://doi.org/10.1016/j.tecto.2012.02.001

White, G. F. (2019). Natural hazards research. *Directions in Geography*, 193–216. https://doi.org/10.4324/9780429273292-9

Wilson, G., Wilson, T. M., Deligne, N. I., & Cole, J. W. (2014). Volcanic hazard impacts to critical infrastructure: A Review. *Journal of Volcanology and Geothermal Research*, *286*, 148–182. https://doi.org/10.1016/j.jvolgeores.2014.08.030

Wiseman, K., Banerjee, P., Bürgmann, R., Sieh, K., Dreger, D. S., & Hermawan, I. (2012). Source model of the 2009 Mw 7.6 Padang intraslab earthquake and its effect on the Sunda megathrust. *Geophysical Journal International*, *190*(3), 1710–1722. https://doi.org/10.1111/j.1365-246x.2012.05600.x

Wittmann, W., Sigmundsson, F., Dumont, S., & Lavallée, Y. (2017). Post-emplacement cooling and contraction of lava flows: InSAR Observations and a thermal model for lava fields at Hekla Volcano, Iceland. *Journal of Geophysical Research: Solid Earth*, *122*(2), 946–965. https://doi.org/10.1002/2016jb013444

Wu, K., Ji, C., Luo, L., & Wang, X. (2020). Simulation study of moon-based InSAR observation for Solid Earth Tides. *Remote Sensing*, *12*(1), 123. https://doi.org/10.3390/rs12010123

Xu, X., & Sandwell, D. T. (2019). Toward absolute phase change recovery with InSAR: Correcting for earth tides and phase unwrapping ambiguities. *IEEE Transactions on Geoscience and Remote Sensing*, *58*(1), 726–733. https://doi.org/10.1109/tgrs.2019.2940207

Xu, X., Sandwell, D. T., Klein, E., & Bock, Y. (2021). Integrated Sentinel-1 InSAR and GNSS time-series along the San Andreas Fault system. *Journal of Geophysical Research: Solid Earth*, *126*(11), e2021JB022579. https://doi.org/10.1002/essoar.10507566.1

Xue, F., Lv, X., Dou, F., & Yun, Y. (2020). A review of time-series interferometric SAR techniques: A tutorial for surface deformation analysis. *IEEE Geoscience and Remote Sensing Magazine*, *8*(1), 22–42. https://doi.org/10.1109/mgrs.2019.2956165

Yang, X. M., Davis, P. M., & Dieterich, J. H. (1988). Deformation from inflation of a dipping finite prolate spheroid in an elastic half-space as a model for volcanic stressing. *Journal of Geophysical Research*, *93*(B5), 4249–4257. https://doi.org/10.1029/JB093iB05p04249

Yu, C., Li, Z., Penna, N. T., & Crippa, P. (2018). Generic Atmospheric Correction Model for Interferometric Synthetic Aperture Radar Observations. *Journal of Geophysical Research: Solid Earth*, *123*(10), 9202–9222. https://doi.org/10.1029/2017JB015305

Yu, H., Lan, Y., Yuan, Z., Xu, J., & Lee, H. (2019). Phase unwrapping in InSAR: A review. *IEEE Geoscience and Remote Sensing Magazine*, *7*(1), 40–58. https://doi.org/10.1109/mgrs.2018.2873644

Yun, S., Segall, P., & Zebker, H. (2006). Constraints on magma chamber geometry at Sierra Negra Volcano, Galápagos Islands, based on InSAR observations. *Journal of Volcanology and geothermal research*, *150*(1-3), 232–243. https://doi.org/10.1016/j.jvolgeores.2005.07.009

Yunjun, Z., Amelung, F., & Aoki, Y. (2021). Imaging the Hydrothermal System of Kirishima Volcanic Complex With L-Band InSAR Time Series. *Geophysical Research Letters*, *48*(11), e2021GL092879. https://doi.org/10.1029/2021GL092879

Yunjun, Z., Fattahi, H., & Amelung, F. (2019). Small baseline InSAR time series analysis: Unwrapping error correction and noise reduction. *Computers and Geosciences*, *133*, 104331. https://doi.org/10.1016/j.cageo.2019.104331

Zebker, H. (2021). Accuracy of a model-free algorithm for Temporal InSAR tropospheric correction. *Remote Sensing*, *13*(3), 409. https://doi.org/10.3390/rs13030409

Zebker, H. A., Hensley, S., Shanker, P., & Wortham, C. (2010). Geodetically accurate InSAR Data Processor. *IEEE Transactions on Geoscience and Remote Sensing*, *48*(12), 4309–4321. https://doi.org/10.1109/tgrs.2010.2051333

Zebker, H. A., Rosen, P. A., & Hensley, S. (1997). Atmospheric effects in interferometric synthetic aperture radar surface deformation and topographic maps. *Journal of geophysical research: solid earth*, *102*(B4), 7547–7563. https://doi.org/https://doi.org/10.1029/96JB03804

Zhan, Z. (2020). Mechanisms and implications of deep earthquakes. *Annual Review of Earth and Planetary Sciences*, *48*(1), 147–174. https://doi.org/10.1146/annurev-earth-053018-060314

Zhang, B., Ding, X., Amelung, F., Wang, C., Xu, W., Zhu, W., Shimada, M., Zhang, Q., & Baba, T. (2021). Impact of ionosphere on InSAR observation and coseismic slip inversion: Improved slip model for the 2010 Maule, Chile, earthquake. *Remote Sensing of Environment*, *267*, 112733. https://doi.org/10.1016/j.rse.2021.112733

Zhao, C., & Lu, Z. (2018). Remote Sensing of landslides—A review. *Remote Sensing*, *10*(2), 279. https://doi.org/10.3390/rs10020279

Zheng, Y., Fattahi, H., Agram, P., Simons, M., & Rosen, P. (2022). On closure phase and systematic bias in multilooked SAR interferometry. *IEEE Transactions on Geoscience and Remote Sensing*, *60*, 1–11. https://doi.org/10.1109/tgrs.2022.3167648

Zhou, L., Yu, H., Lan, Y., & xing mengdao, m. (2021). Artificial Intelligence In Interferometric Synthetic Aperture Radar Phase Unwrapping: A Review. *IEEE Geoscience and Remote Sensing Magazine*, *9*(2), 10–28. https://doi.org/10.1109/MGRS.2021.3065811

Zhu, B., Li, J., & Tang, W. (2017). Correcting InSAR topographically correlated tropospheric delays using a power law model based on ERA-Interim reanalysis. *Remote Sensing*, *9*(8), 765. https://doi.org/10.3390/rs9080765

Zhu, K., Zhang, X., Sun, Q., Wang, H., & Hu, J. (2022). Characterizing spatiotemporal patterns of land deformation in the Santa Ana Basin, Los Angeles, from InSAR time series and independent component analysis. *Remote Sensing*, *14*(11), 2624. https://doi.org/10.3390/rs14112624

Zinke, R., Hollingsworth, J., & Dolan, J. F. (2014). Surface slip and off-fault deformation patterns in the 2013 Mw 7.7 Balochistan, Pakistan earthquake: Implications for controls on the distribution of near-surface coseismic slip. *Geochemistry, Geophysics, Geosystems*, *15*(12), 5034–5050. https://doi.org/10.1002/2014GC005538

Zobin, V. M. (2017). *Fundamentals of volcanic seismology* (3rd). Introduction to Volcanic Seismology. https://doi.org/10.1016/b978-0-444-63631-7.00003-0

Appendix A

Improving the Resolving Power of InSAR for Earthquakes Using Time Series: A Case Study in Iran

Introduction

This is supporting information for chapter 3.

Content

Text S1 to S4

Figures S1 to S12

Tables S1 to S2

Additional Supporting Information

Text S1. Stacking strategy

Here we use the stacking method proposed by Luo et al., 2021. Suppose there are M images ($i = 1, 2, \ldots, M$) before and N images ($j = 1, 2, \ldots, N$) after an earthquake event time. Then

the unwrapped stacked phase ψ_s which contains the coseismic deformation is obtained by

$$\psi_s = \frac{1}{N}\sum_{j=1}^{N}\psi_{Mj} - \frac{1}{M-1}\sum_{i=1}^{M-1}\psi_{Mi}$$

Since there are several earthquakes that happened close in time in our study, we may use the observations that happened between events both as pre and post observations for different events. For the M_w 6.3 earthquake, we use 10 pre and 10 post observations to avoid too much of the post-seismic impact of the mainshock. For the M_w 6.0 and M_w 5.6 earthquakes, we use the data between the events time (as pre or post observations) and similar time window on either side to do stacking (see Table A.2 for more details).

Text S2. Calculation of standard error (SE)

The SEs are calculated by the mean of multiple linear regression. Suppose a linear equation likes the following form:

$$\mathbf{y=Ax}$$

then the least square solution and the root mean square error (RMSE) are obtained:

$$\mathbf{x} = (\mathbf{A'A})^{-1}\mathbf{A'y}$$

$$RMSE = \frac{1}{n}(\mathbf{y} - \hat{\mathbf{y}})^2$$

where n is the observation number and $\hat{y}$is the predicted values. So, the SE values of each parameter are acquired by:

$$SE = RMSE * diag(\sqrt{(\mathbf{A'A})^{-1}})$$

And the margin of error (uncertainty, or confidence interval) is obtained by multiplying a constant value to SE through t test as follows:

$$x_i \pm t_{\alpha/2,DF} * SE_i$$

where α means a $100 * (1 - \alpha)$ percent confidence interval, DF is the degrees of freedom which equals to $(n - k - 1)$, k is the number of unknown parameters.

Text S3. Details of Maximum Likelihood Approach

We use a maximum likelihood inversion to solve the non-linear **Equation 2** and determine the postseismic time τ. In this inversion, we assume the errors are multivariate Gaussian with zero mean, which means the likelihood function is calculated as follows:

$$p(\mathbf{d}|\mathbf{m}) = (2\pi)^{-\frac{N}{2}}((|\sum_{d}|)^{-\frac{1}{2}} \exp\{-\frac{1}{2}(\mathbf{d\text{-}Gm})^{T}(|\sum_{d}|)^{-1}(\mathbf{d\text{-}Gm})\}$$

where $p(\mathbf{d}|\mathbf{m})$ is the likelihood function of $\mathbf{m}$ given $\mathbf{d}$ based on residuals between the data and the model ($\mathbf{G}$) prediction of the observations, N is the number of epochs on time series, and $(|\sum_{d}|)^{-1}$ is the inverse of the variance-covariance matrix. We set $(|\sum_{d}|)^{-1}$ to the identity matrix as we assume each epoch is independent and we weight them equally. We apply a Markov chain Monte Carlo method using the Metropolis-Hastings iterative algorithm to find the maximum likelihood value for the model parameters.

Text S4. Details of GBIS Inversion

When using the GBIS software to do earthquake modelling with the Bayesian approach, we assume the errors are multivariate Gaussian with zero mean and use same likelihood function in Text S3. We characterize the errors in InSAR data by experimentally estimating variance and covariance in each independent dataset (Figure A.6). We assume a uniform prior probability for all source parameters (logarithmic for nonnegative parameters) between reasonable bounds, and they are independent to each other. GBIS applies a Markov chain Monte Carlo method using the Metropolis-Hastings iterative algorithm and will automictically adjust the step size for optimal run times. We run 10^6 iterations and burn-in the first 20% iterations when doing earthquake modelling. All these details regarding GBIS can be found in Bagnardi and Hooper, 2018.

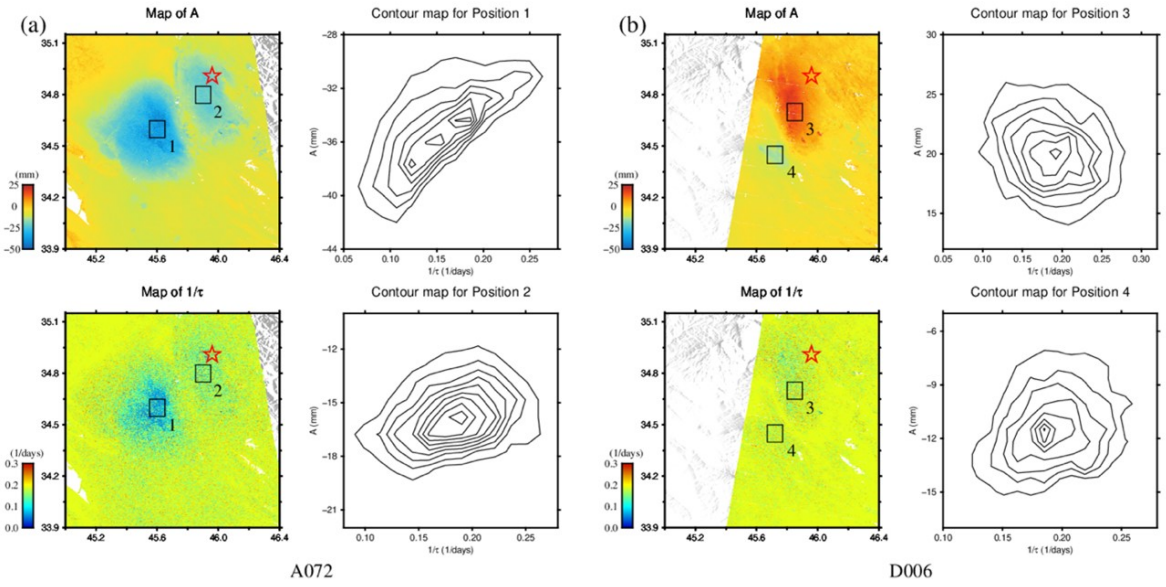

Figure A.1: Tradeoff between postseismic parameters for amplitude A and $1/\tau$ time constant of the maximum likelihood inversion results of Equation 3.2 following the 12 November 2017, M_w 7.3 Ezgeleh-Sarpolzahab earthquake. We assume a uniform prior distribution of the parameters (-50-50 for A and 0-0.5 for $1/\tau$), and the initial values for A and $1/\tau$ are 0 mm and 0.2 day^{-1}, respectively. Red star is the epicentre of the large M_w 7.3 earthquake from the USGS catalog. (a) Map of A and $1/\tau$ for track A072, and the contour map of the peak postseismic deformation area marked by black rectangles. (b) Same as (a) but for track D006. We average the value of $1/\tau$ in these rectangle areas and use this mean value (0.18 day^{-1}, equivalent to ∼6 days for τ) to transform Equation 3.2 into a linear problem.

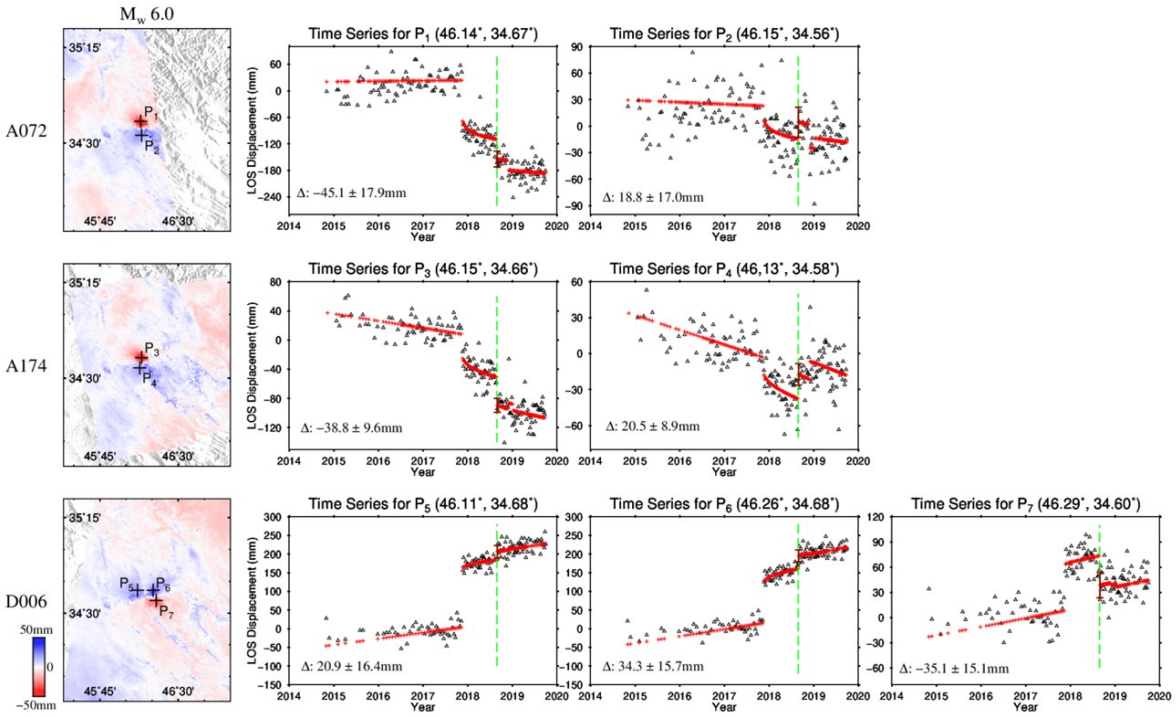

Figure A.2: Time series fitting of peak displacement pixels for the M_w 6.0 earthquake on three different tracks. Green vertical dashed lines represent the event time (25 August 2018). Red plus symbols show the fitted results. The values of fitted coseismic offsets and their 95% confidence interval (CI) are shown at the lower-left corner, and marked by the error bars along with the fitted data. Earthquake focal mechanisms are from the USGS solution.

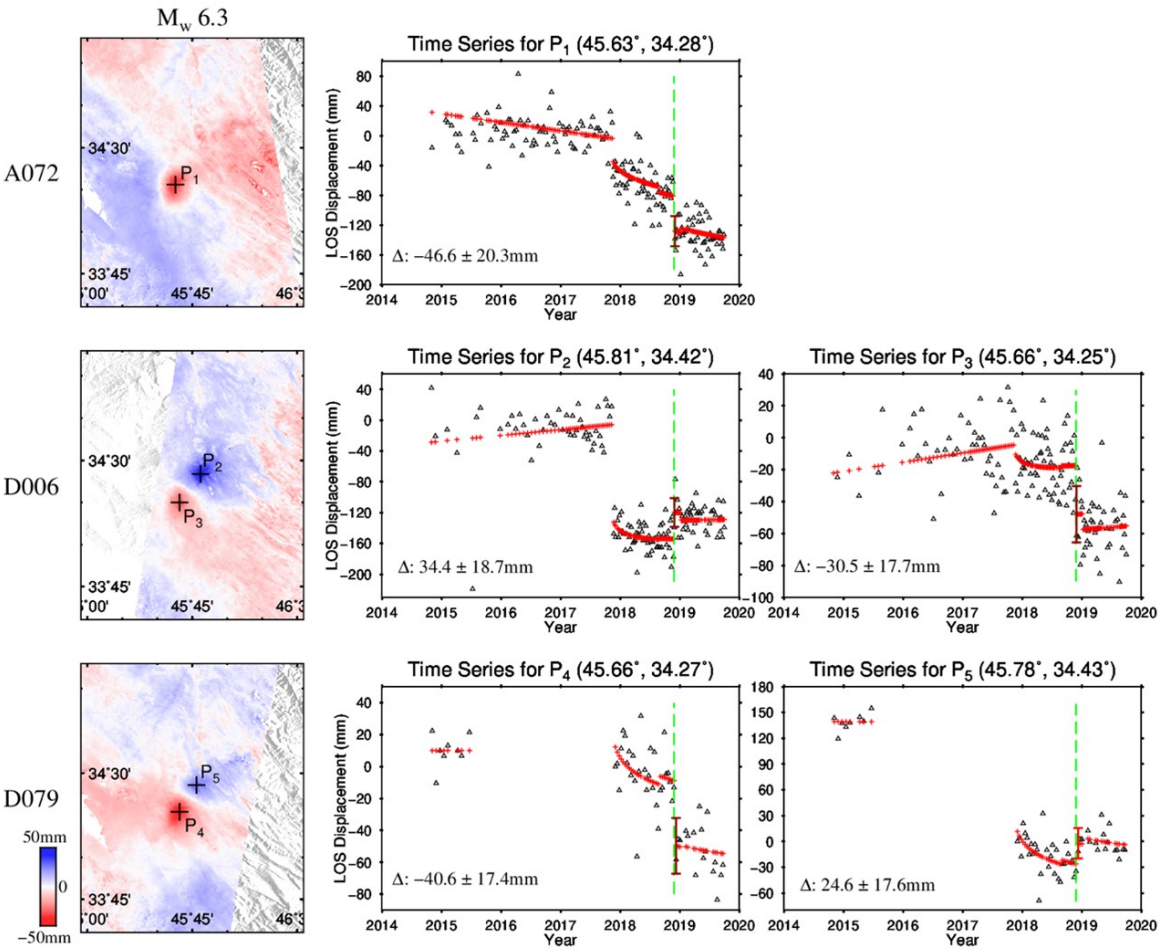

Figure A.3: Same as Figure A.2 but for the M_w 6.3 earthquake (25 November 2018). In addition, due to the long observation gap in track D079 (no acquisition from July 2015 to Oct 2017 over this area), we cannot estimate the long-term linear deformation rate robustly by Equation 3.2, with the existence of postseismic deformation of the large M_w 7.3 earthquake. Therefore, we do not fit the linear deformation term and set its value to zero for this track.

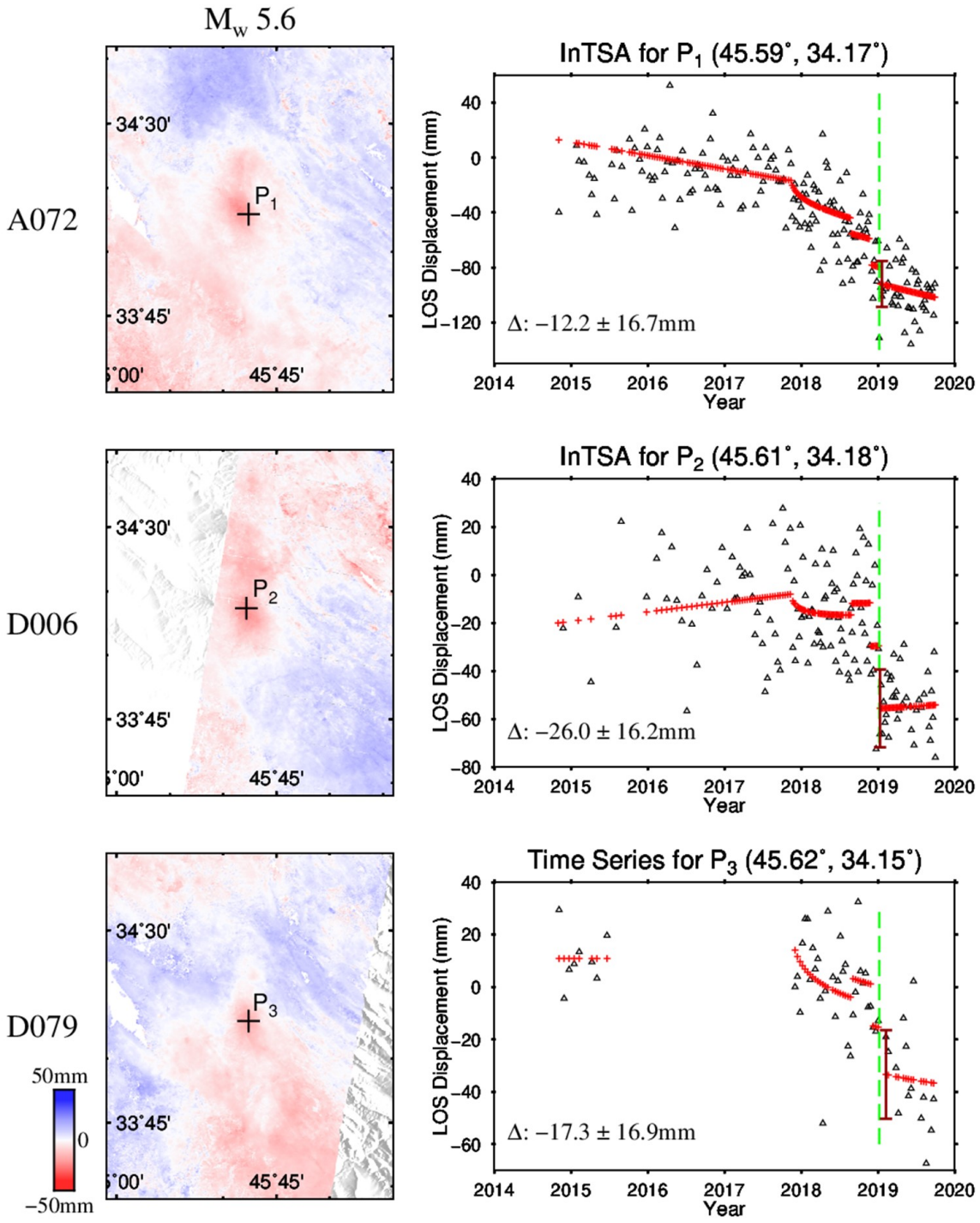

Figure A.4: Same as Figure A.2 but for the M_w 5.6 earthquake (06 January 2019).

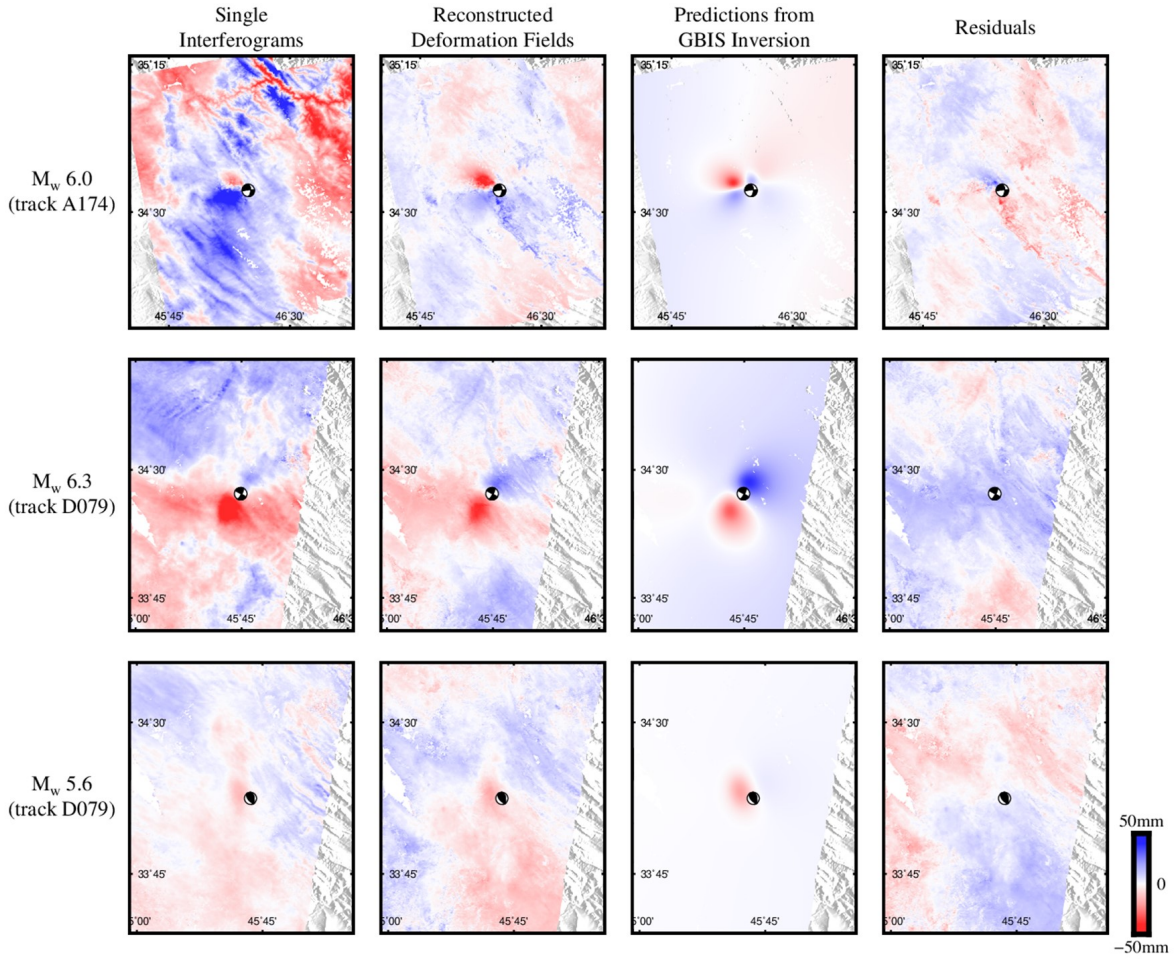

Figure A.5: Comparison between the single (the shortest temporal one) interferograms and the reconstructed coseismic deformation fields for other track observations. Along with the results shown in Figure 3.3, each earthquake is covered by three tracks and we use all these overlapping reconstructed deformation fields to do the earthquake modelling with the GBIS software.

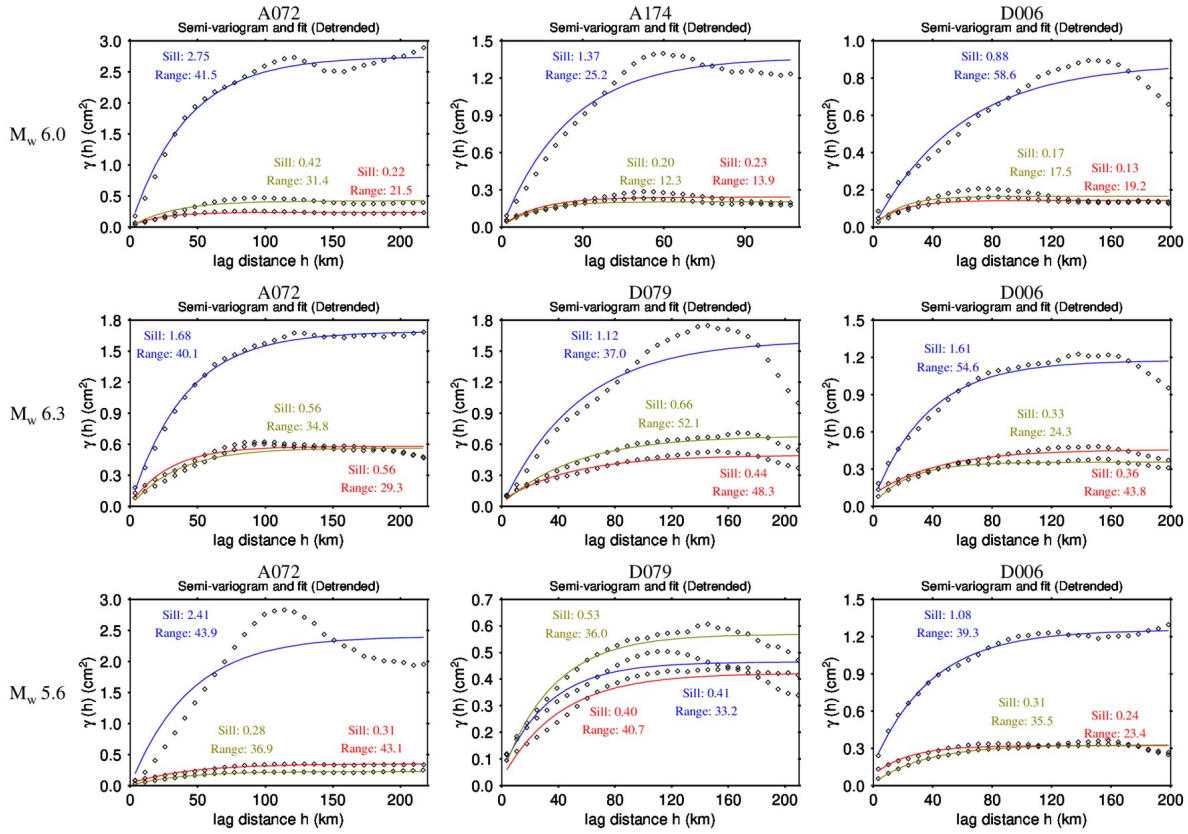

Figure A.6: Semi-variogram fitting for all three earthquakes using the GBIS software. Errors in the InSAR data can be simulated using an exponential function fitted to the isotropic experimental semi-variogram (Webster and Oliver, 2007), and the lower sill value of the fitted result indicates the higher the signal-to-noise ratio (SNR). We mask out the area showing surface deformation and remove a linear ramp from the data before the fitting. The black circles, blue lines (along with blue texts), green lines (along with green texts), and red lines (along with red texts) represent the semi-variogram, the fitted result for single coseismic interferograms, stacked deformation fields, and the reconstructed coseismic deformation fields, respectively. Overall, the reconstructed coseismic deformation fields achieve similar sill values as the stacked ones, and both greatly improve the SNR compared to the single interferograms.

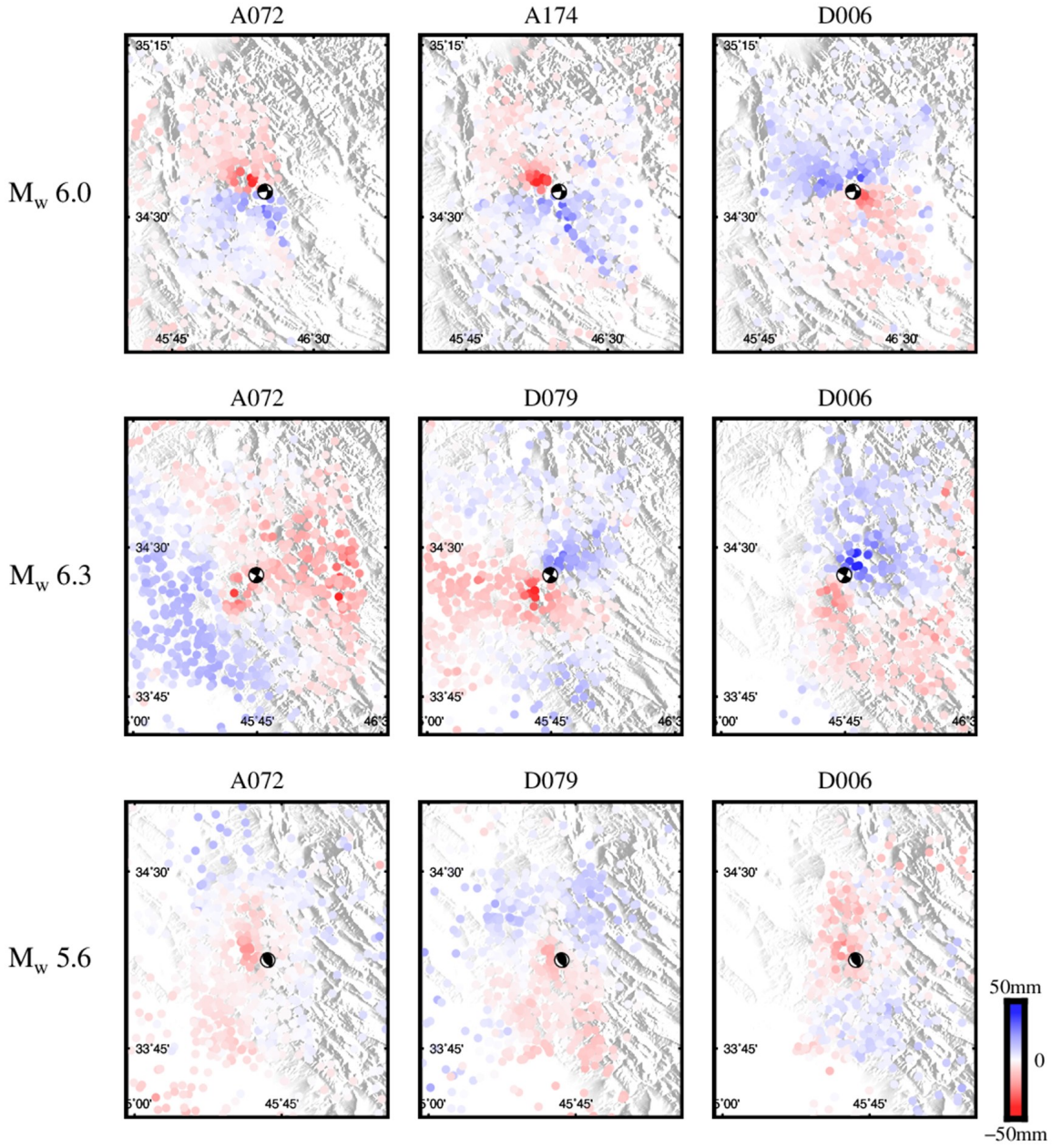

Figure A.7: Downsampled reconstructed deformation fields for different earthquakes and tracks, with ∼500 pixels in the near field, and later are used for GBIS inversion.

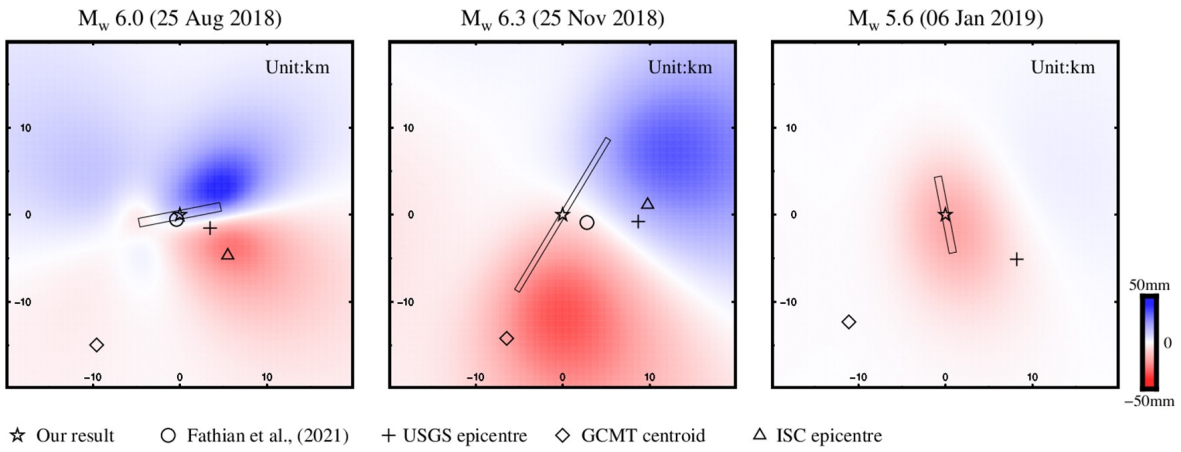

Figure A.8: Relative earthquake location from different sources. The coseismic displacements are forward modelling according to the fault parameters from GBIS inversion, using our reconstructed deformation fields. The black rectangles represent the projection of fault plane on Earth surface. Black star, circle, plus, diamond, and triangle are the fault centroid location from our reconstructed deformation fields, fault centroid location from Fathian et al., 2021, epicentre from USGS catalog, centroid from Global Centroid-Moment-Tensor (GCMT) catalog, and epicentre from International Seismological Centre catalog, respectively. Note that the M_w 5.6 event is not modelled by Fathian et al., 2021 and the epicentre of this event for the ISC was not yet available by the time paper published.

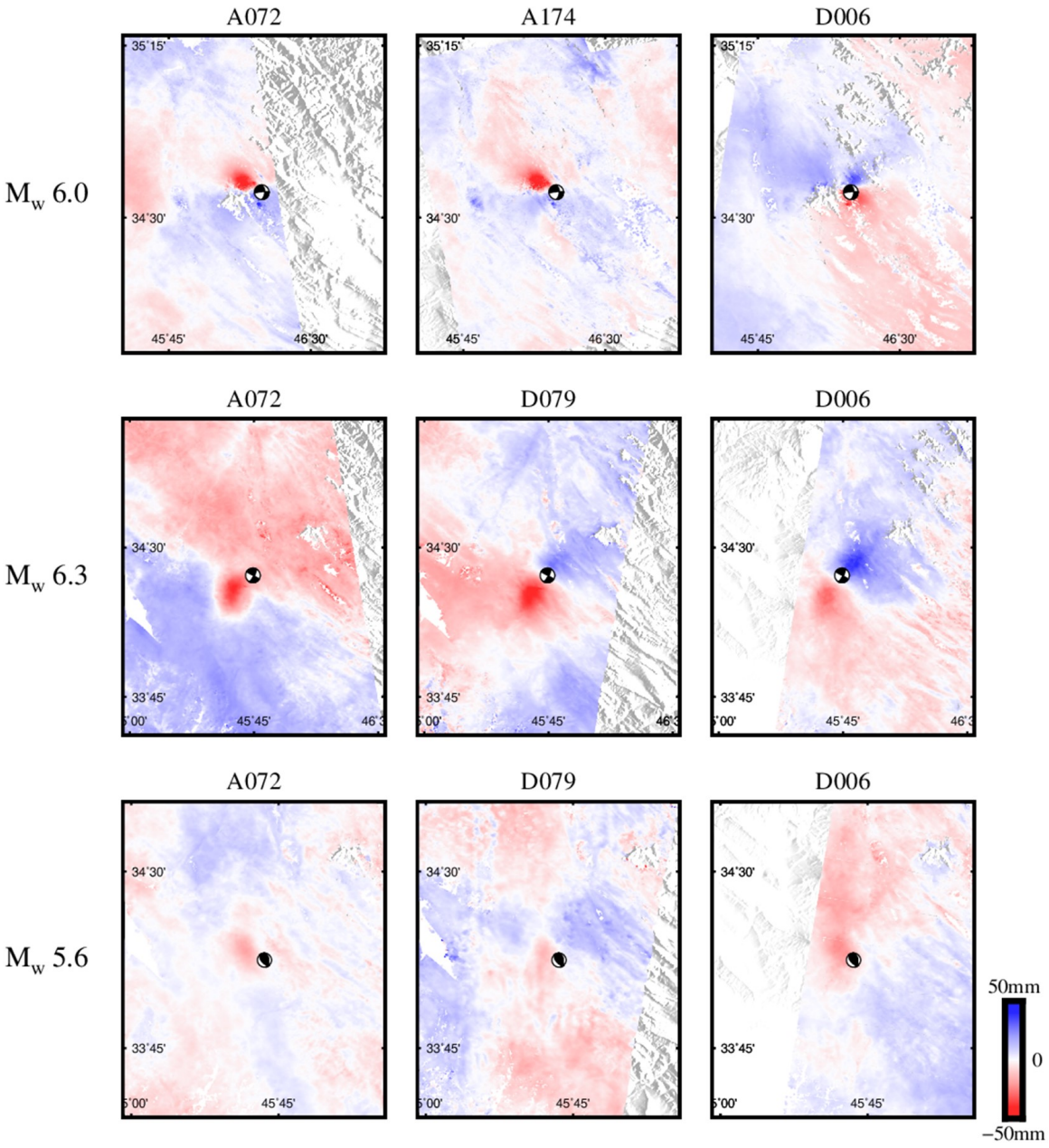

Figure A.9: Stacked deformation fields for the three study cases on different tracks with GACOS correction applied. All these deformation fields are used for the subsequent GBIS inversion.

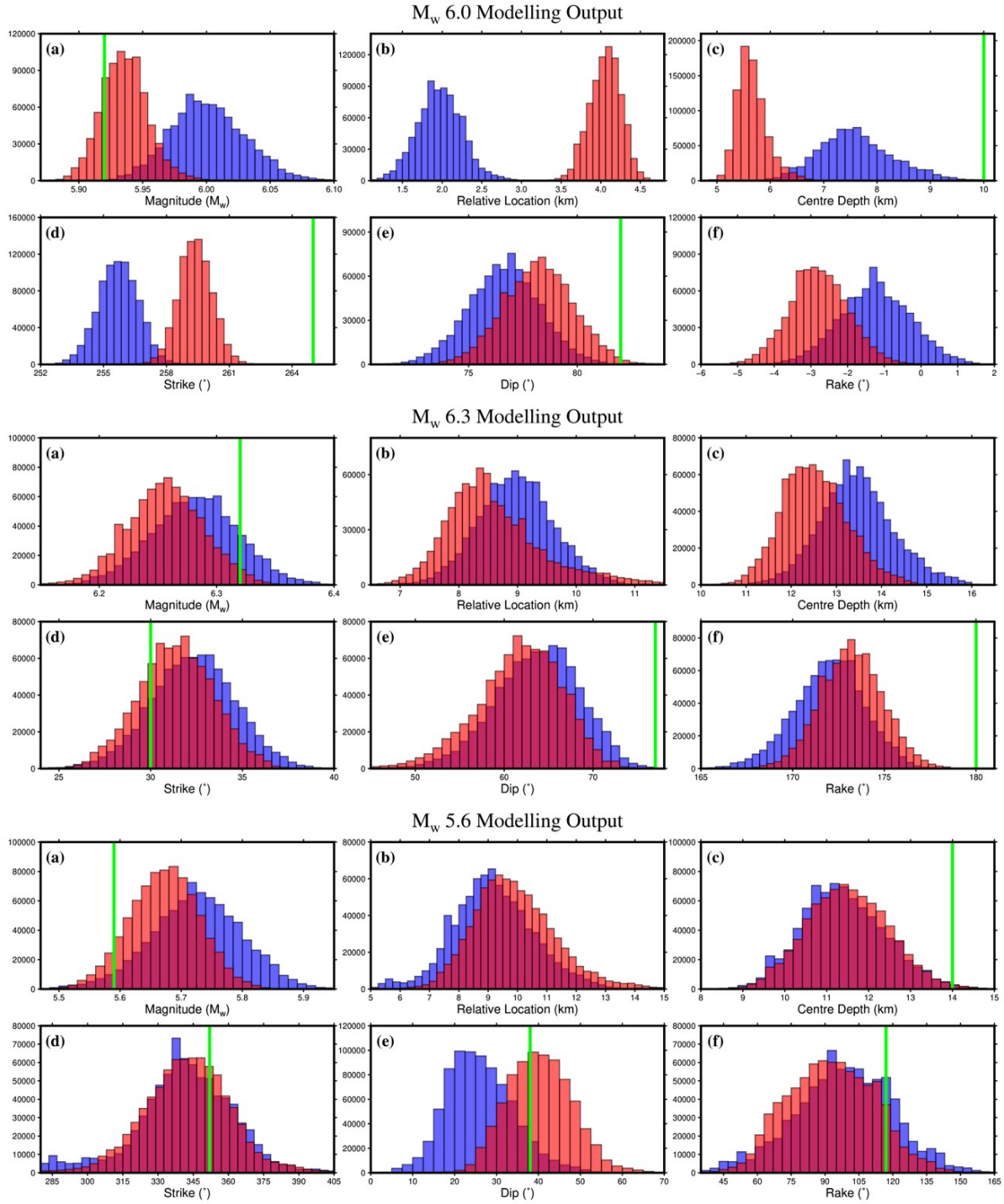

Figure A.10: Modelling outputs for selected fault parameters, same as Figure 3.4 but for the reconstructed and stacked deformation fields. Red and blue bins represent the distributions from the reconstructed and the stacked deformation, respectively. Green lines are the USGS solutions. (a) Earthquake moment magnitude. (b) Relative location, the horizontal distance between the InSAR derived source location and the epicentre from USGS (not indicated by green lines as zero reference value). (c-f) Fault plane centre depth, Strike, Dip and Rake values.

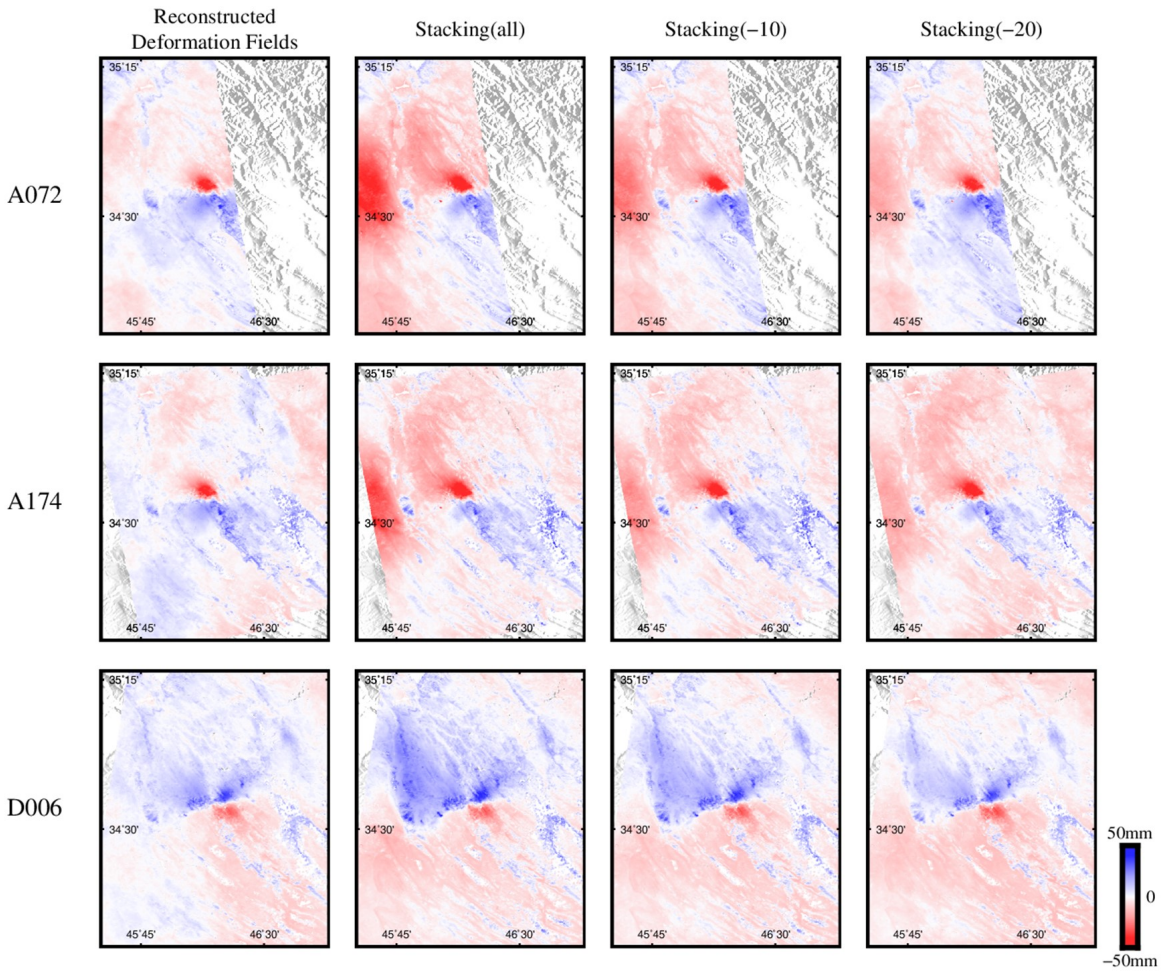

Figure A.11: The impact of unmodelled post-seismic deformation from the 12 November 2017, M_w 7.3 Ezgeleh-Sarpolzahab mainshock on the stacking result for the subsequent M_w 6.0 earthquake. Here we simulate the stacking process using time series data rather than the real long temporal interferograms. From left to right: the reconstructed deformation fields by our approach, the stacked deformation fields using all epochs, the result from dropping the first 10 epochs, and finally the result from dropping the first 20 epochs closest in time to the mainshock. Although the real stacked deformation fields might be slightly different from the simulation shown here, we consider it is clear that post-seismic deformation can greatly bias the stacking results considering the post-seismic deformation pattern shown in Figure A.1.

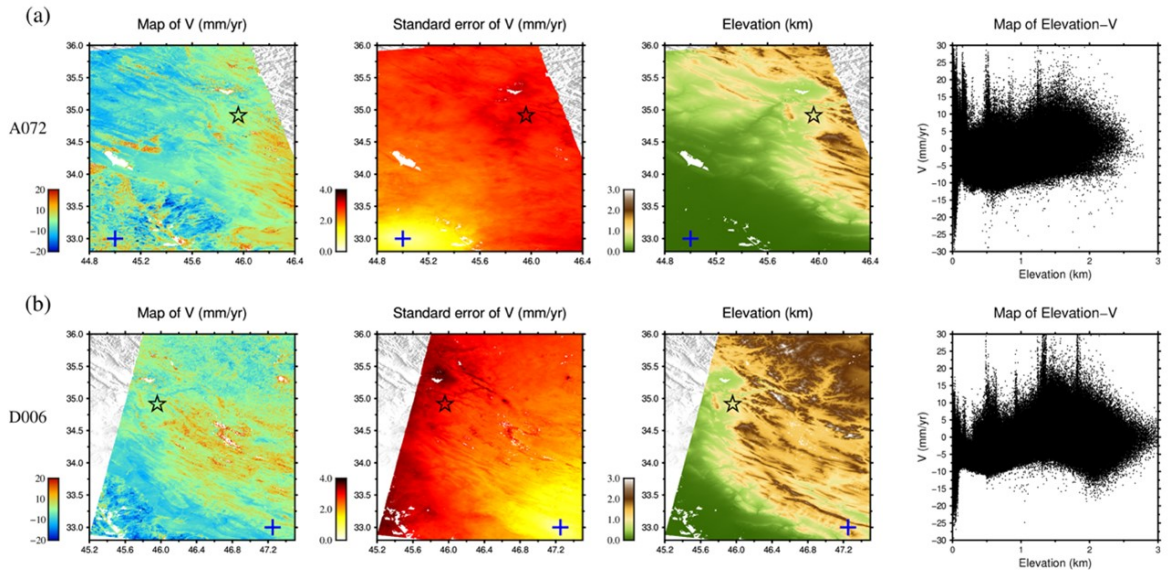

Figure A.12: Maps of estimated long-term linear rates. Black star is the epicentre of the M_w 7.3 earthquake from USGS catalog, and blue plus symbol is the reference point. (a) Data from track A072. From left to right: map of velocity, standard error of velocity, elevation, and elevation-velocity for all pixels. (b) Same as (a) but for track D006.

		Magnitude (Mw)	Moment (10^{17} Nm)	Centre Depth (km)	Upper Depth (km)	Relative Location (km)	Strike (degree)	Dip (degree)	Rake (degree)
M_w 6.0 (25 Aug 2018)	USGS	5.99 ± 0.07	12.1	10.0 ± 1.8	-	± 6.0	265	82	-31
	GCMT	6.0	12.7	16.0	-	-	268	86	-17
	Fathian et al., 2021	5.89	8.6	-	1.5 ± 1.2	4.0	267 ± 12	78 ± 9	2 ± 11
	Reconstructed Deformation Fields	5.92	9.7	5.4	4.5	4.2	259	78	-3
		5.90-5.97	9.0-11.5	4.8-6.9	3.4-5.1	3.7-4.4	258-261	75-81	-4-(-1)
	Stacked Deformation Fields	6.00	12.5	7.5	3.1	1.8	255	75	-1
		5.95-6.06	10.5-15.6	5.5-12.0	2.7-3.7	1.4-2.6	254-258	73-80	-3-1
	Single Interferograms	5.86	7.9	5.6	4.5	4.7	271	78	3
		5.79-5.96	6.2-11.0	4.6-12.0	2.8-5.5	4.0-5.1	268-275	70-85	-1-6
M_w 6.3 (25 Nov 2018)	USGS	6.32 ± 0.06	38.2	18.0 ± 1.8	-	± 5.7	30	77	180
	GCMT	6.3	35.2	23.2	-	-	30	79	173
	Fathian et al., 2021	6.28	33.1	-	7.6 ± 1.2	5.9	34 ± 4	63 ± 7	170 ± 4
	Reconstructed Deformation Fields	6.27	31.6	12.6	12.1	8.2	31	61	174
		6.19-6.32	24.5-38.1	10.0-15.9	9.5-13.2	7.3-10.7	27-35	51-70	170-177
	Stacked Deformation Fields	6.29	33.8	13.3	12.7	9.0	32	62	171
		6.20-6.35	25.8-42.7	10.7-17.8	11.2-14.6	7.7-10.3	27-37	53-72	168-176
	Single Interferograms	6.28	33.0	11.7	11.1	7.5	35	66	172
		6.19-6.37	24.1-45.7	8.9-18.4	8.9-12.9	6.5-10.1	27-39	56-77	166-176
M_w 5.6 (06 Jan 2019)	USGS	5.59 ± 0.06	3.1	14.0 ± 1.8	-	± 5.6	352	38	117
	GCMT	5.7	4.9	17.3	-	-	351	30	124
	Reconstructed Deformation Fields	5.68	4.1	11.0	9.9	9.2	343	39	98
		5.56-5.79	2.7-6.1	7.5-16.2	8.8-12.7	7.6-13.3	306-380	27-56	64-127
	Stacked Deformation Fields	5.67	4.1	11.0	10.7	9.6	356	25	116
		5.57-5.79	2.8-6.1	8.0-15.9	9.1-13.0	6.4-12.3	290-380	12-44	52-140
	Single Interferograms	5.68	4.1	11.4	11.9	12.6	362	19	121
		5.57-5.87	2.9-7.9	7.4-19.1	8.4-13.8	6.4-14.1	303-389	7-51	63-149

Table A.1: Earthquake modelling comparison. When using the GBIS software, we apply a uniform downsampling method and use the fault parameters from the USGS solutions (W-phase Moment Tensor) as initial values (with a search range wider than the output distribution). We ensure a search range wider than the initial output distribution. For each earthquake, the fault parameters from different seismological catalogues (with uncertainties are given from the USGS origin hypocentre depth, location, and magnitude), InSAR derived results from recent study (for M_w 6.3 and M_w 6.0 earthquakes, Fathian et al., 2021, derived from the reconstructed deformation fields, stacked deformation fields, and the single (shortest temporal baseline) interferograms (optimal solution and 95% confidence interval) are given. The relative location means the location uncertainties in the case of the USGS as provided in the catalog solution, or the horizontal distance between the InSAR derived source location and the epicentre from USGS. The rigidity value used for moment calculation in all studies is 32 GPa.

	A072	A174	D006	D079
M_w 6.0 (25 Aug 2018)	20 27 Jun 2018 to 19 Oct 2018	20 28 Jun 2018 to 20 Oct 2018	20 17 Jun 2018 to 27 Oct 2018	-
M_w 6.3 (25 Nov 2018)	14 13 Oct 2018 to 05 Jan 2019	- 	14 15 Oct 2018 to 01 Jan 2019	7 20 Oct 2018 to 31 Dec 2018
M_w 5.6 (06 Jan 2019)	14 30 Oct 2018 to 22 Feb 2019	- 	14 26 Nov 2018 to 12 Feb 2019	6 07 Dec 2018 to 25 Mar 2019

Table A.2: Number of epochs and spanning date used for stacking. For each earthquake, the numbers of epochs in each track and the spanning date are given.

Appendix B

From Space to Slab: Probing the 112 km Deep M_w 6.8 2020 Intraslab Earthquake, Northern Chile, Using Geodetic and Seismological Observations

Introduction

This is supporting information for chapter 4.

Content

Figures S1 to S31

Tables S1 to S2

Additional Supporting Information

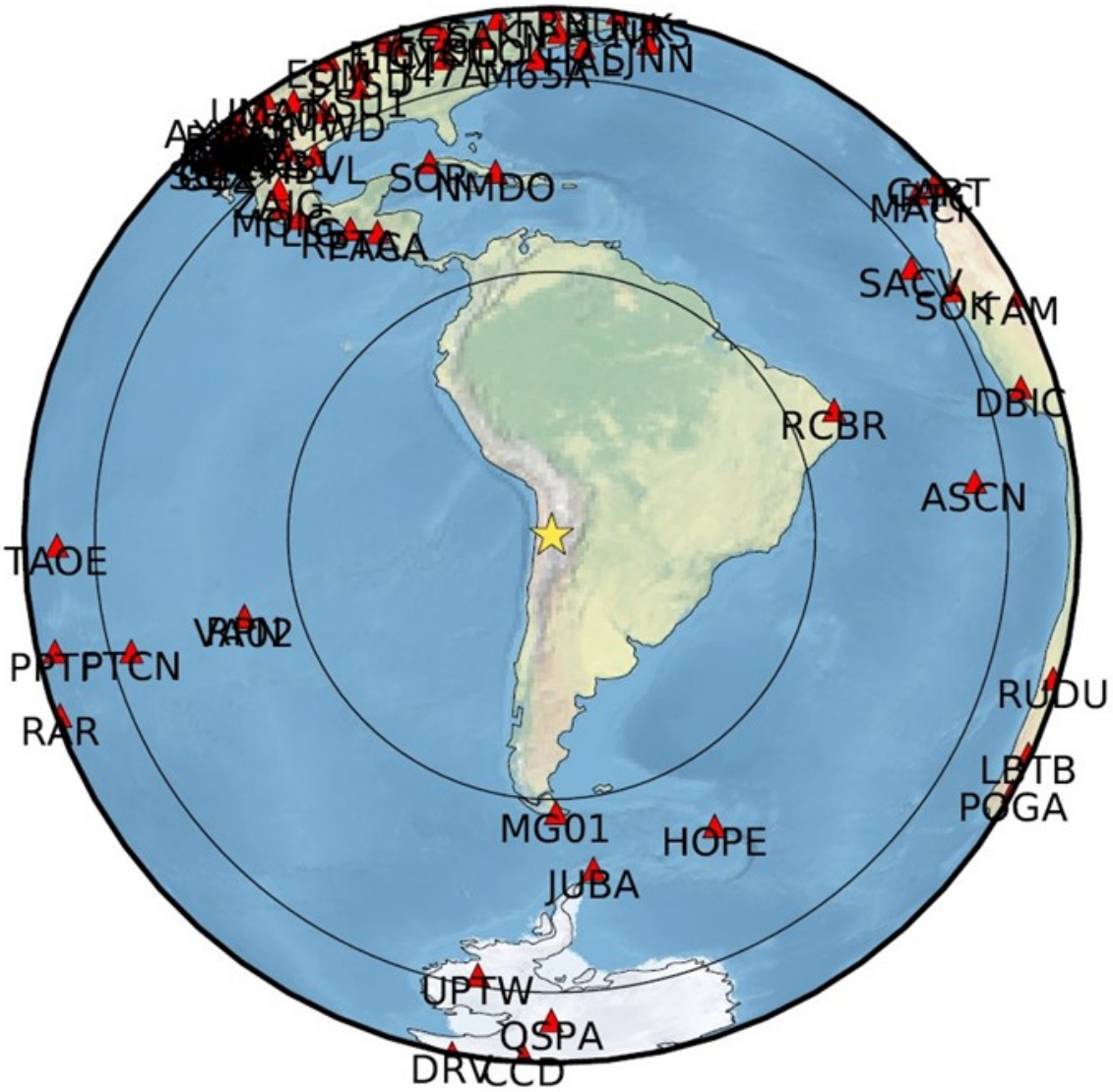

Figure B.1: The station map of used P waves dataset in global view. The epicentre of the earthquake is indicated by the star.

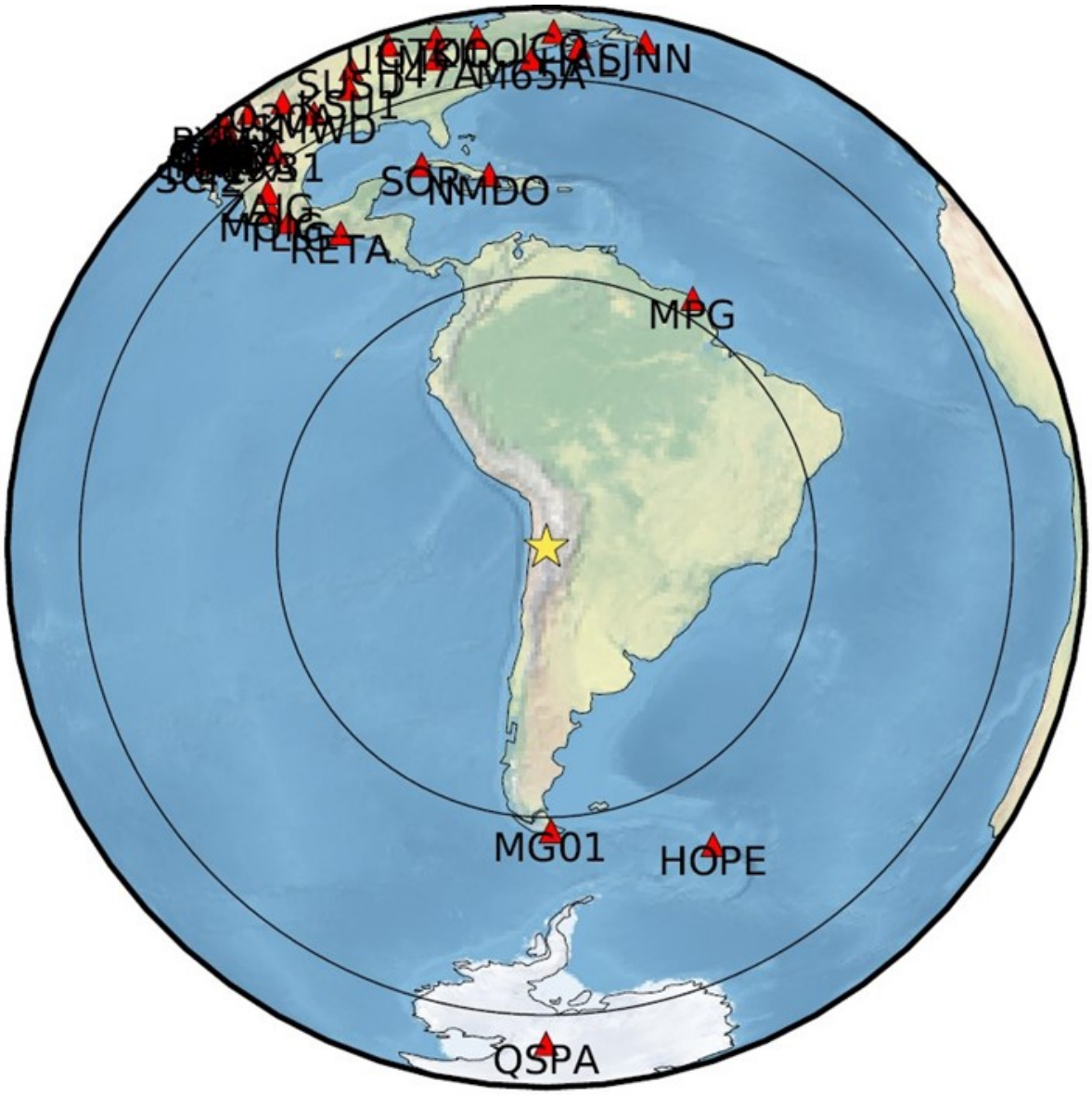

Figure B.2: Same as Figure B.1 but for the S waves datasets.

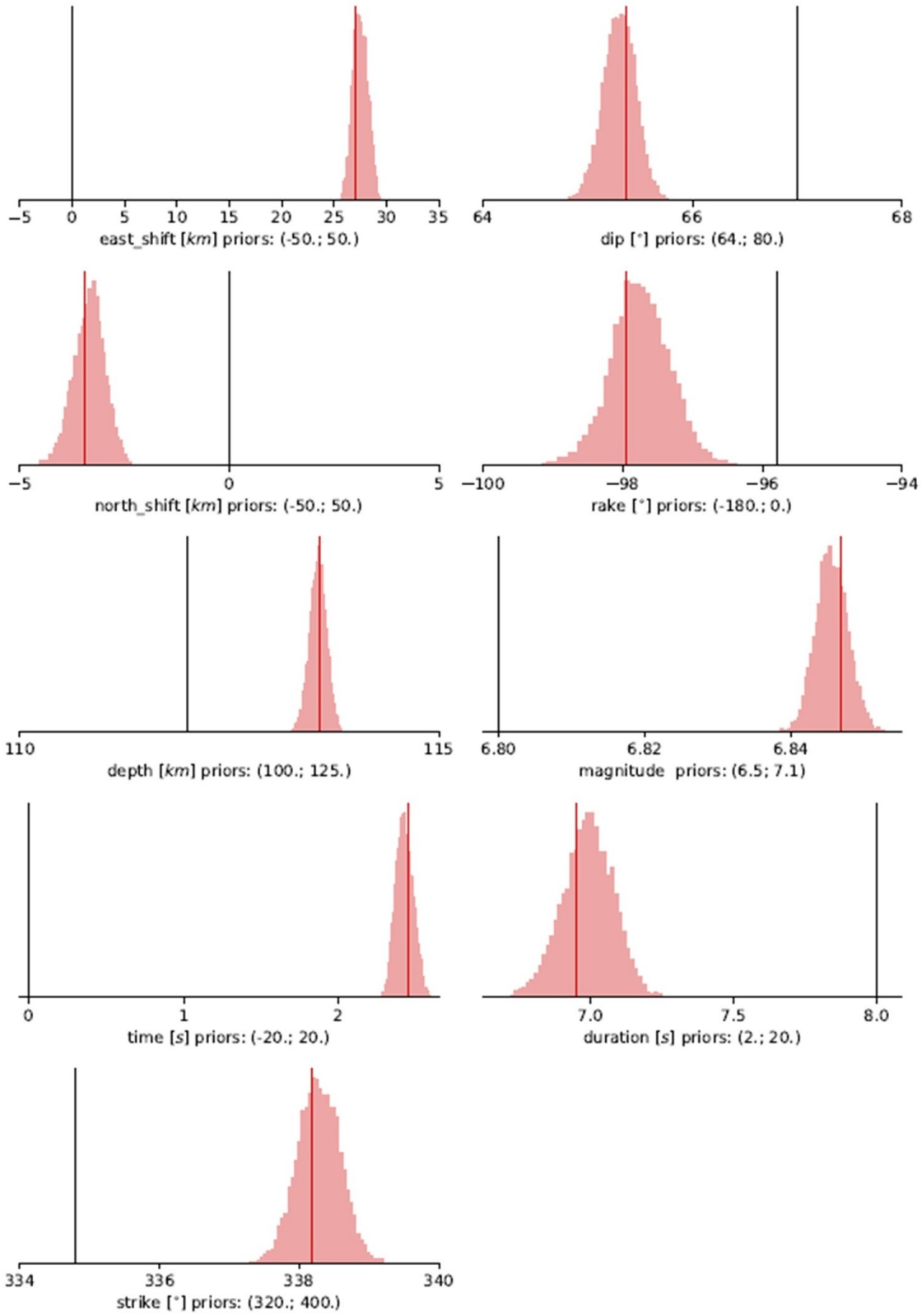

Figure B.3: The posterior distributions of source parameters of the seismic inversion (use seismological stations data only). Red and black vertical lines indicate the optimal solutions from the model, and the prior values used as initial guess from the USGS, respectively.

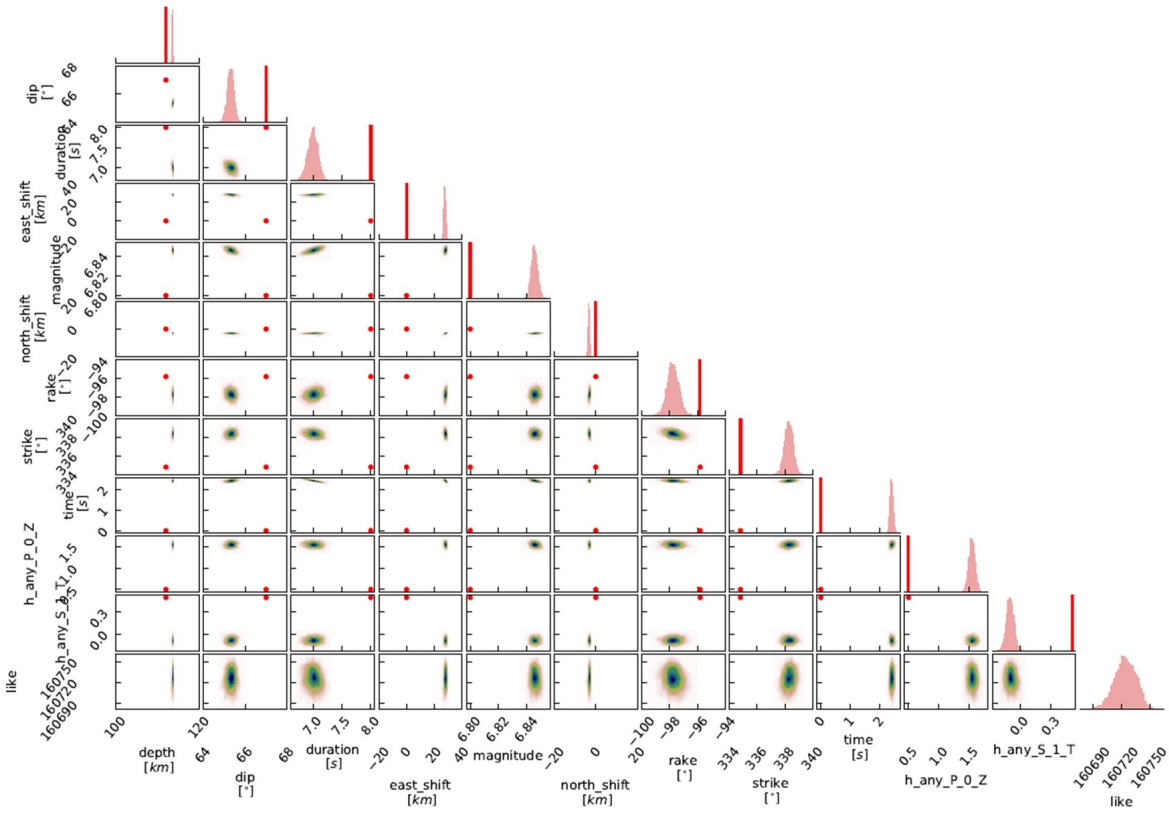

Figure B.4: Correlation histogram of the source parameters from the seismic inversion, which shows the posterior distributions and trade-offs between different parameters during the inversion (red dot and line depict the maximum likelihood solution).

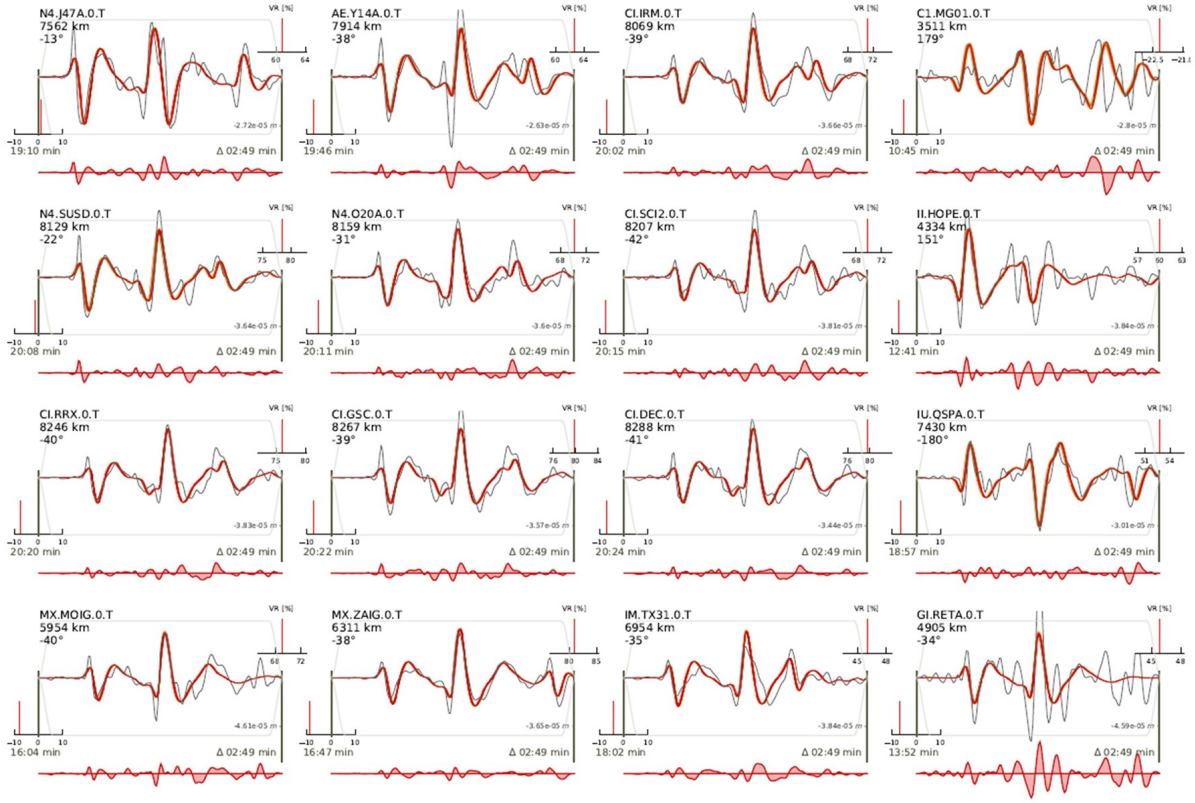

Figure B.5: Seismic waveform, and their fitting of some stations from vertical (Z) components, when performing seismic inversion.

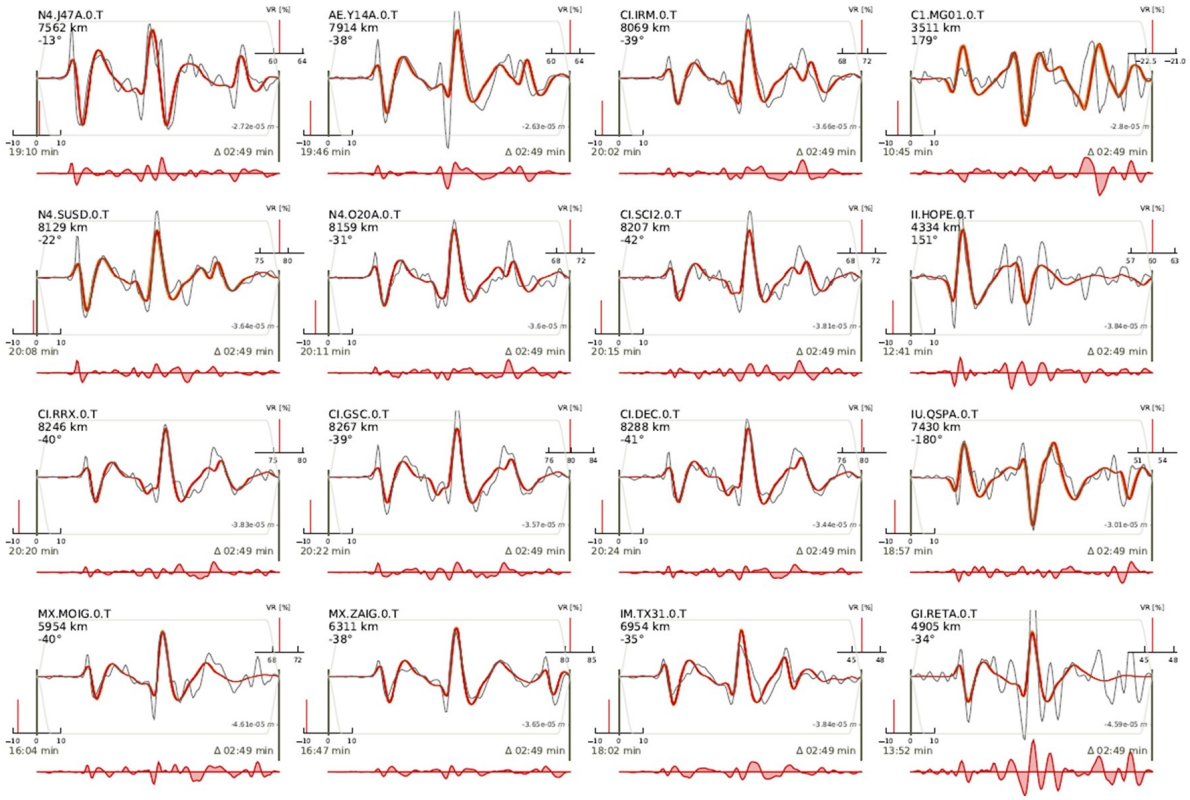

Figure B.6: Seismic waveform, and their fitting of some stations from (transverse) T components, when performing seismic inversion.

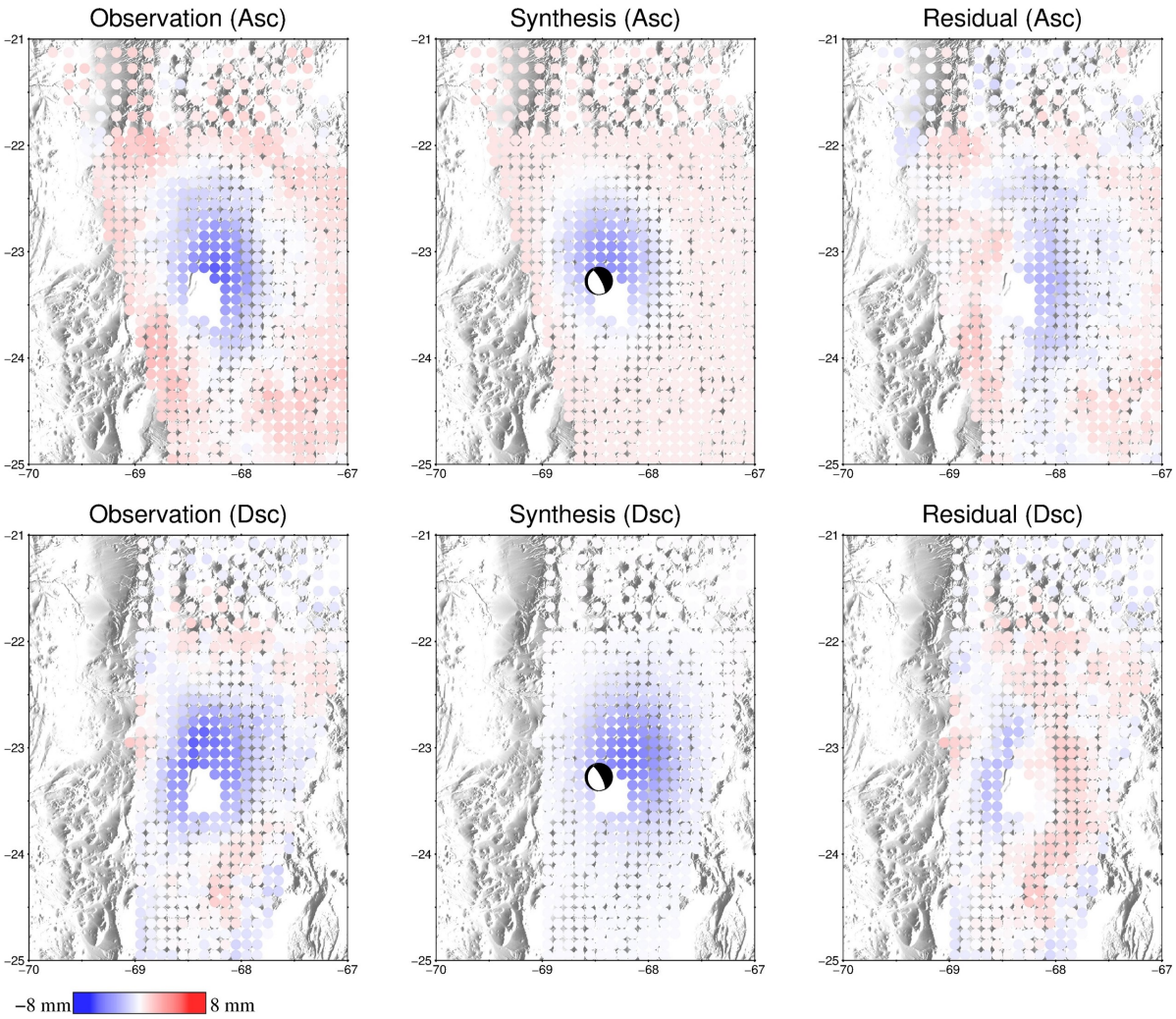

Figure B.7: Geodetic inversion using InSAR data only (derived from sICA) on layered half-space. Focal mechanisms indicate the location of epicentre.

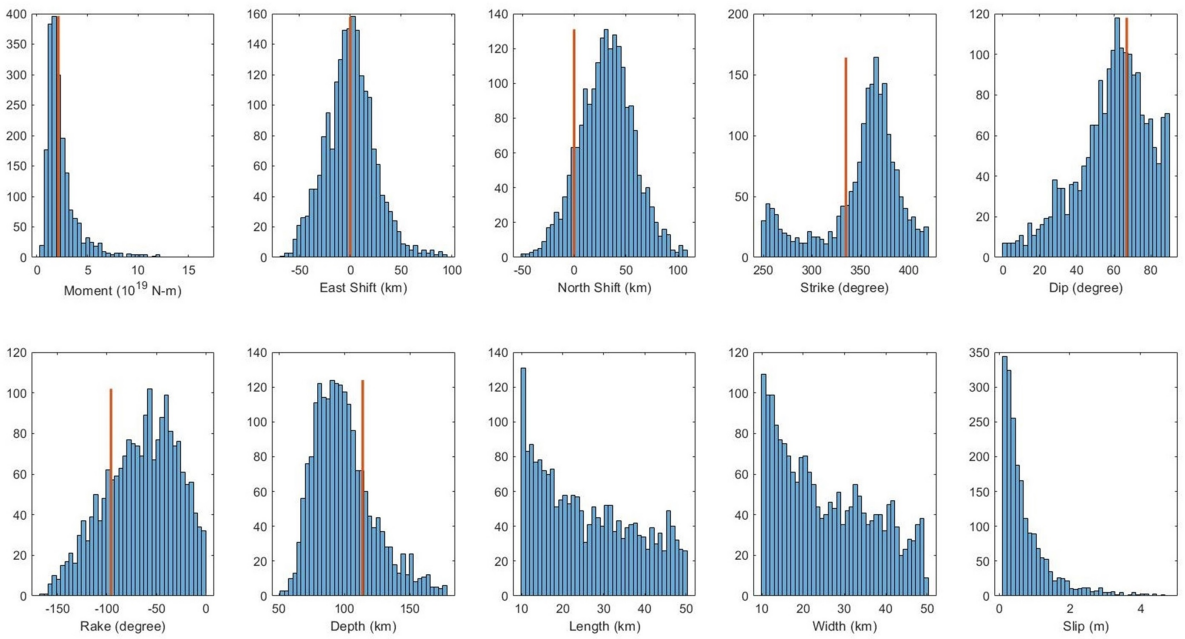

Figure B.8: The posterior distribution of source parameters, using InSAR data only (derived from sICA) on layered half-space. The red lines indicate the bodywave solution from the USGS for comparison.

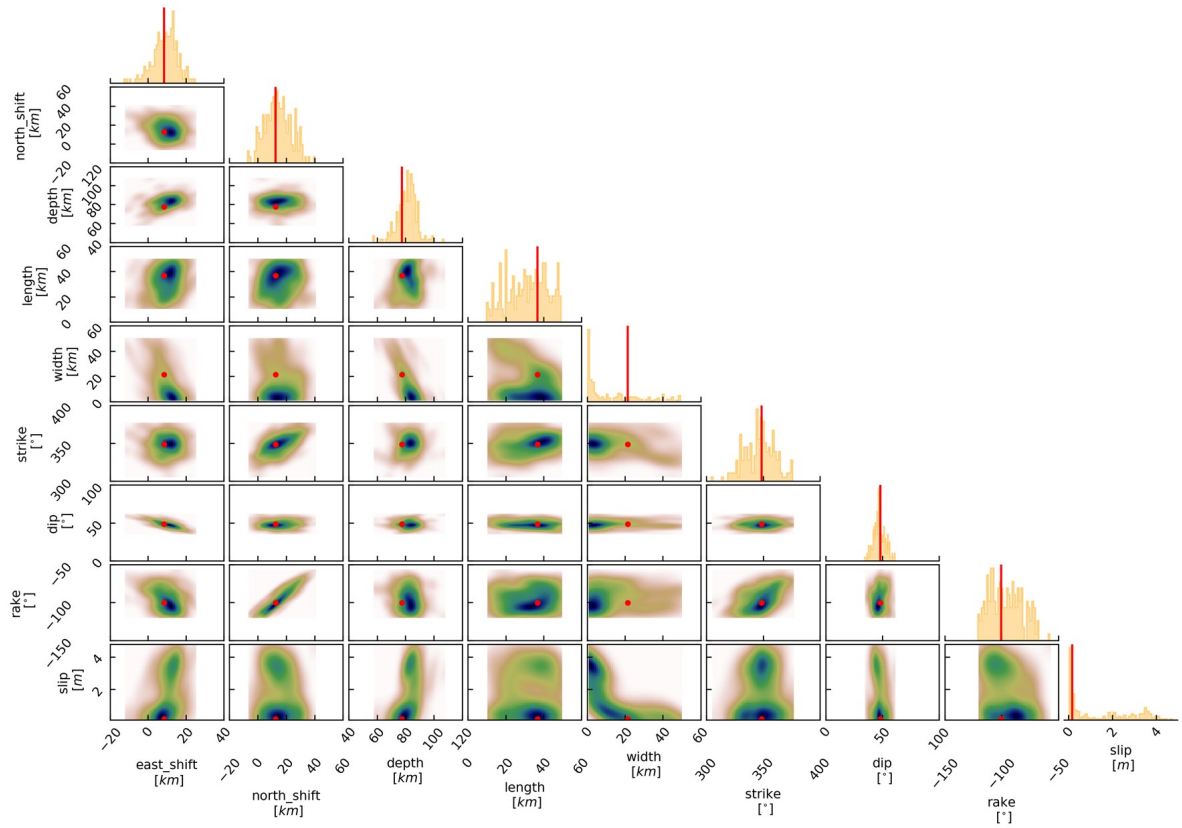

Figure B.9: Correlation histogram of some selected parameters from the geodetic inversion (using InSAR data only derived from sICA on layered half-space), which shows the posterior distributions and trade-offs between different parameters during the inversion (red dot and line depict the maximum likelihood solution).

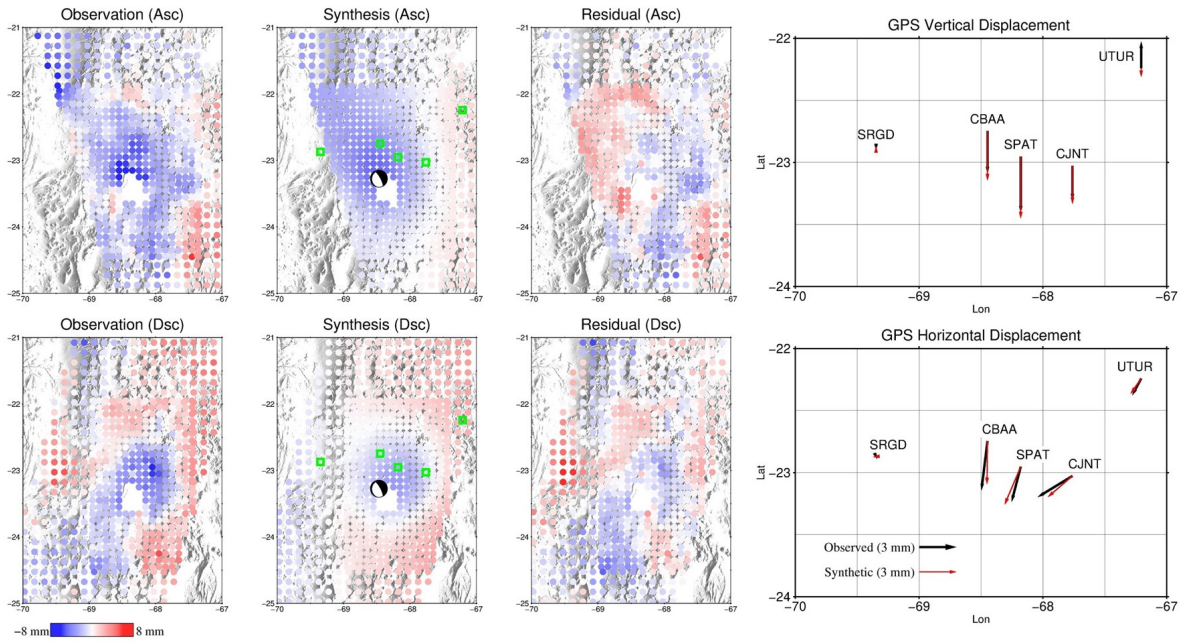

Figure B.10: Geodetic inversion using InSAR data (derived from parameterized fitting) and GPS on layered half-space. Focal mechanism and green boxes indicate the epicentre and the location of the GPS stations, respectively.

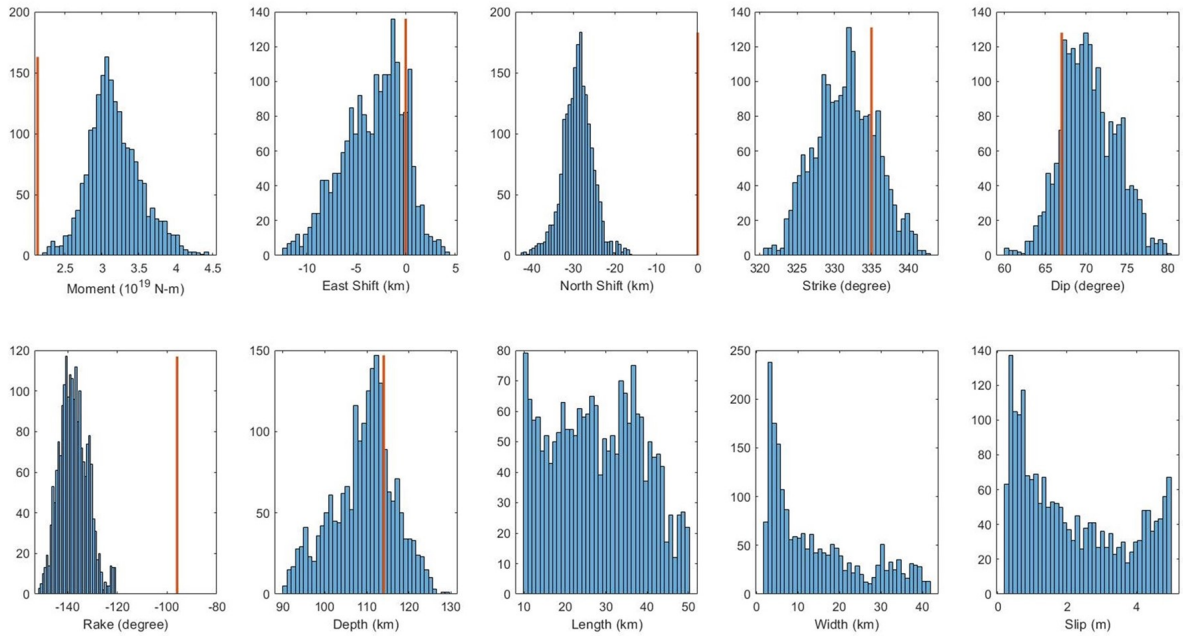

Figure B.11: The posterior distribution of source parameters, using InSAR (derived from parameterized fitting) and GPS data on layered half-space. The red lines indicate the bodywave solution from the USGS for comparison.

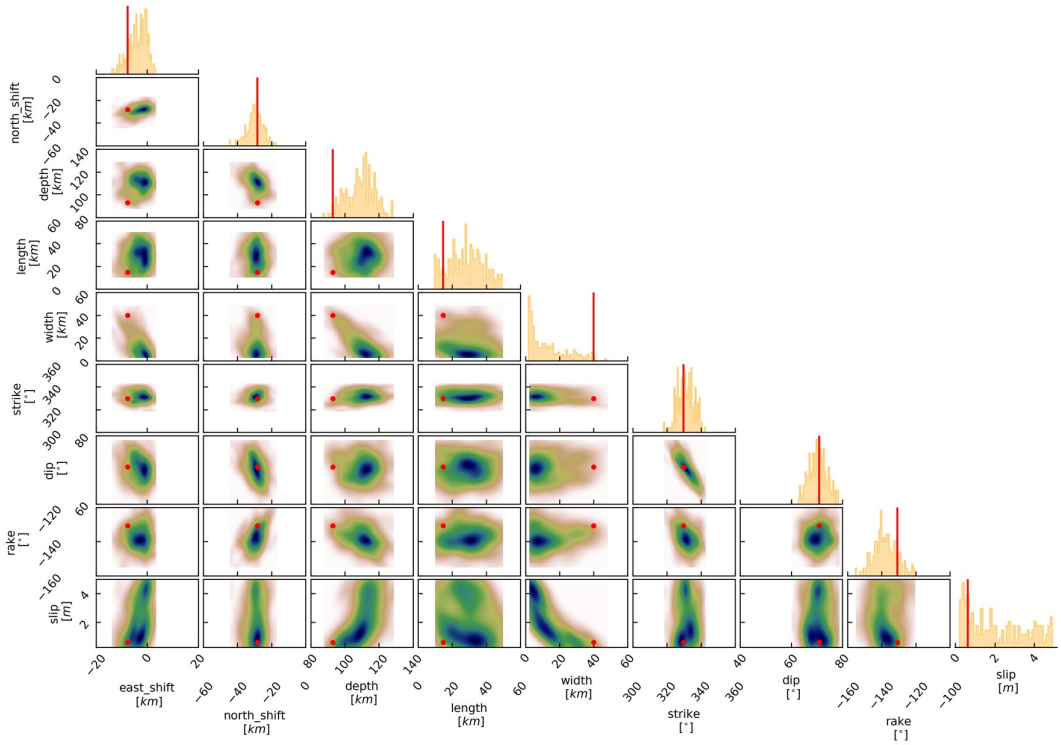

Figure B.12: Correlation histogram of some selected parameters from the geodetic inversion (using InSAR data derived from parameterized fitting and GPS data on layered half-space), which shows the posterior distributions and trade-offs between different parameters during the inversion (red dot and line depict the maximum likelihood solution).

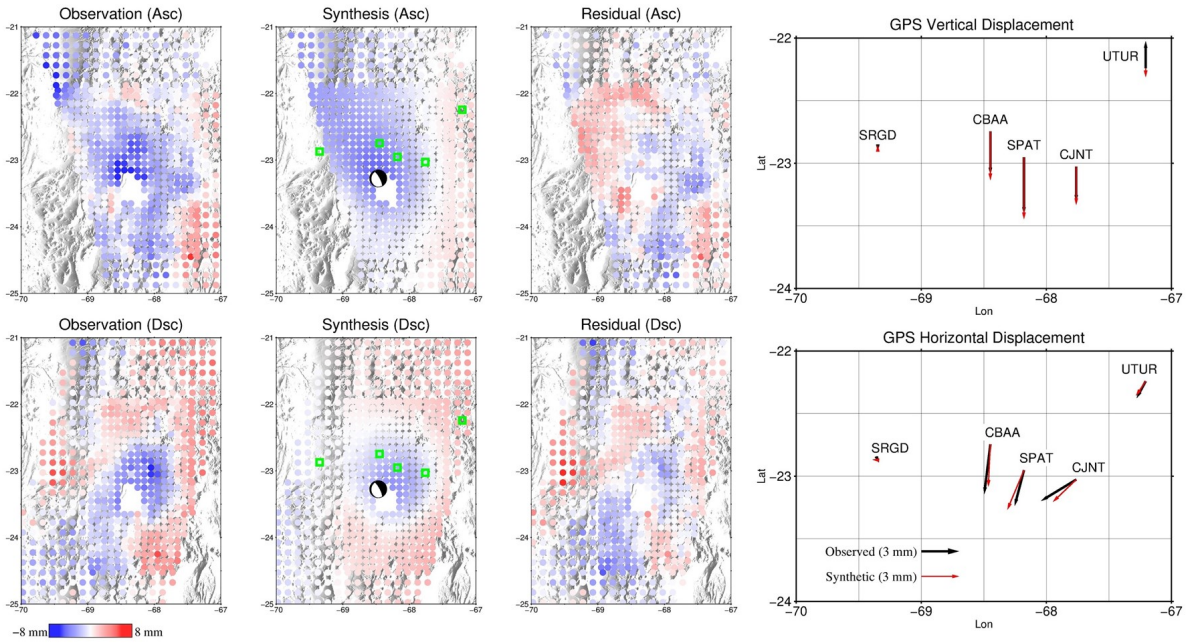

Figure B.13: Geodetic inversion using InSAR data (derived from parameterized fitting) and GPS on uniform half-space. Focal mechanism and green boxes indicate the epicentre and the location of the GPS stations, respectively.

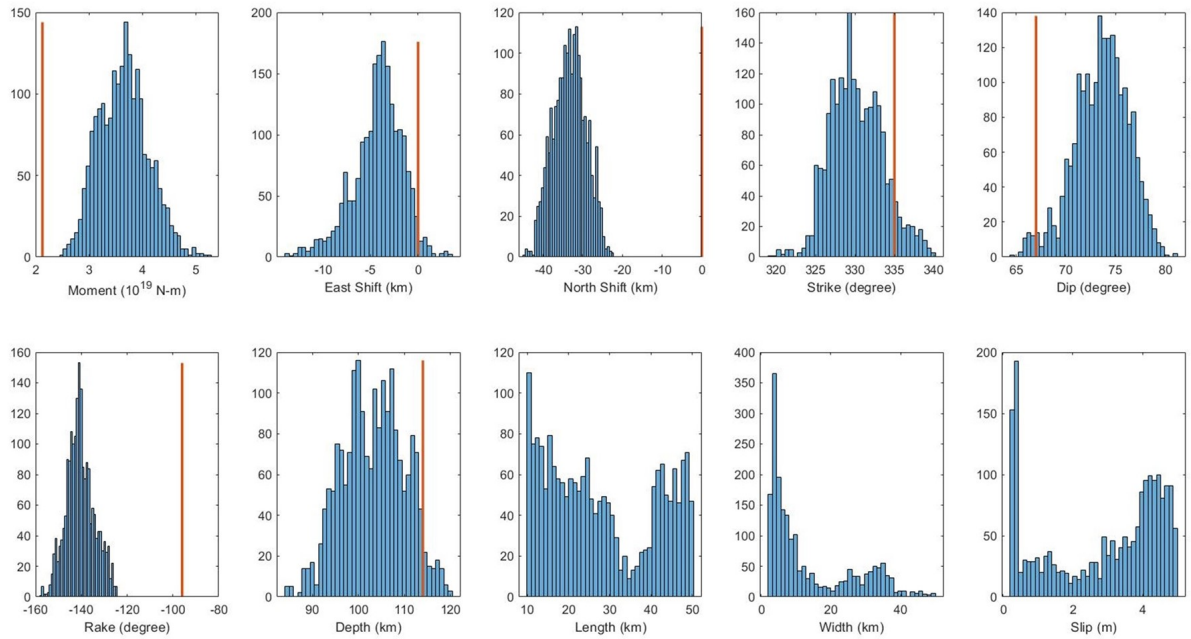

Figure B.14: The posterior distribution of source parameters, using InSAR (derived from parameterized fitting) and GPS data on uniform half-space. The red lines indicate the bodywave solution from the USGS for comparison.

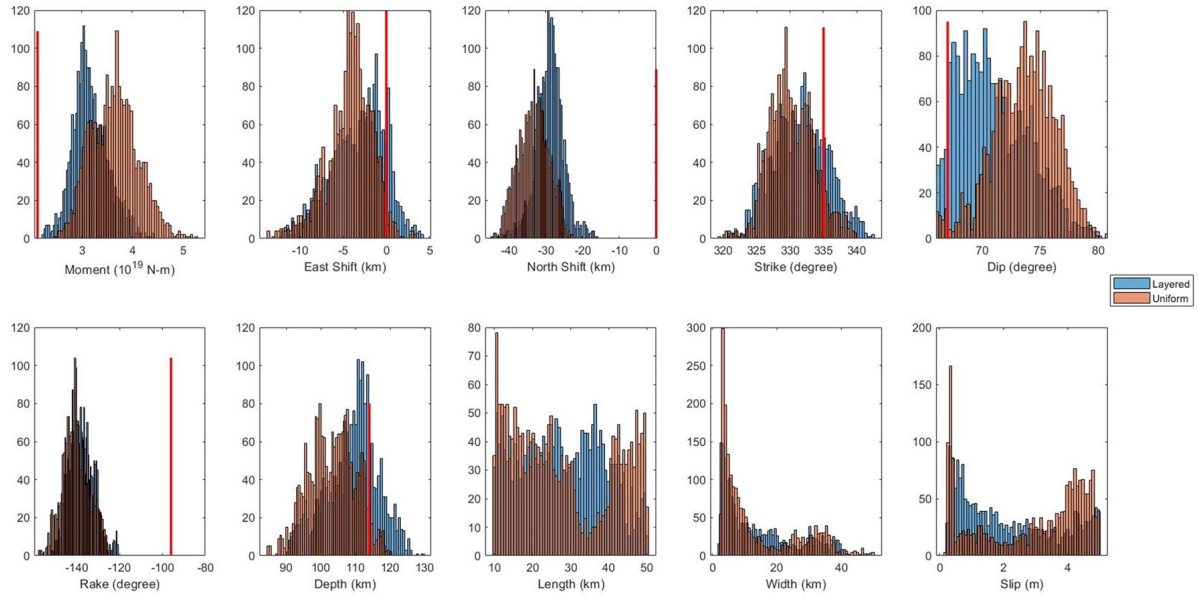

Figure B.15: The comparison of posterior distributions between the layered (Figure B.11) and uniform half-space (Figure B.14), using InSAR data derived from parameterized fitting and GPS.

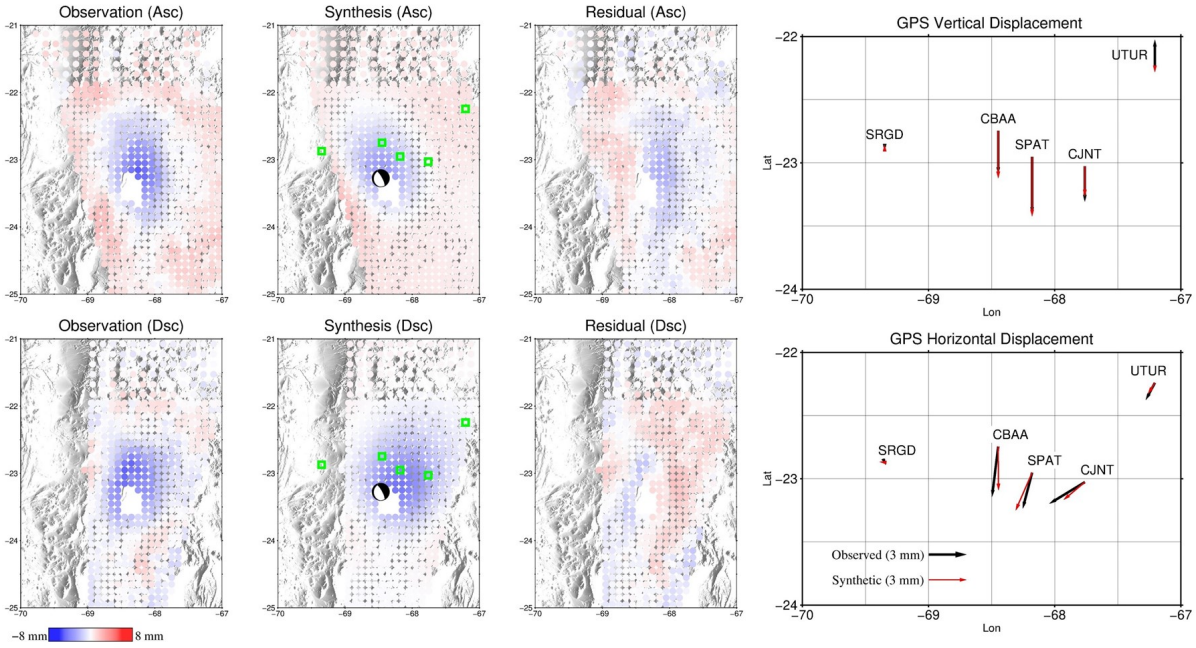

Figure B.16: Geodetic inversion using InSAR data (derived from sICA) and GPS on layered half-space. Focal mechanism and green boxes indicate the epicentre and the location of the GPS stations, respectively.

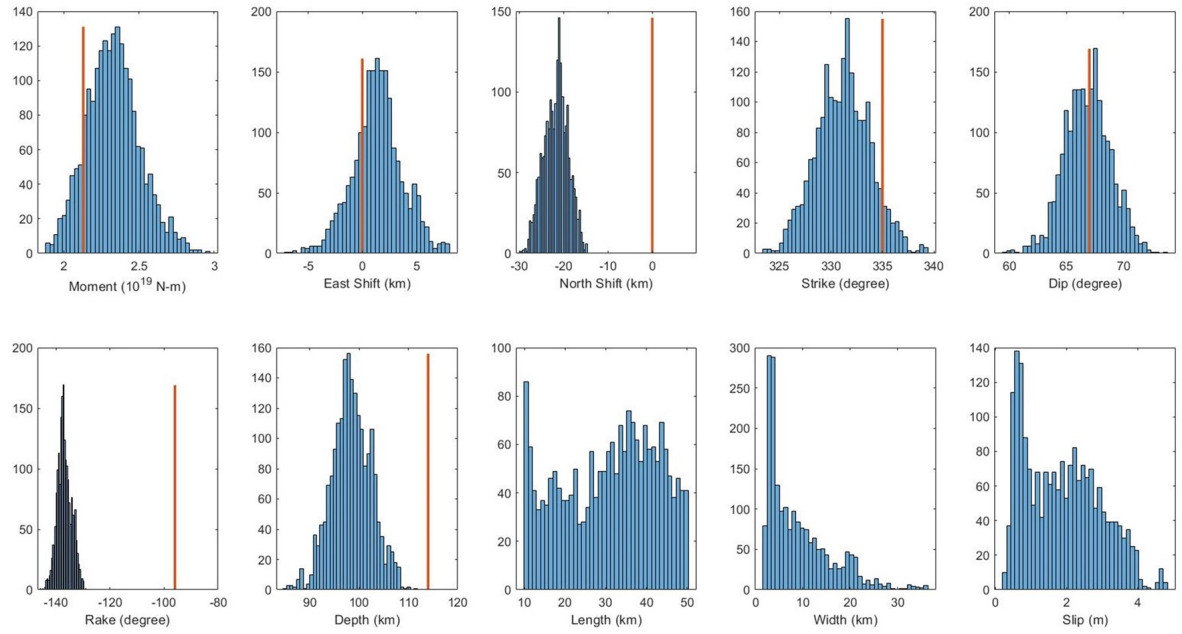

Figure B.17: The posterior distribution of source parameters, using InSAR (derived from sICA) and GPS data on layered half-space. The red lines indicate the bodywave solution from the USGS for comparison.

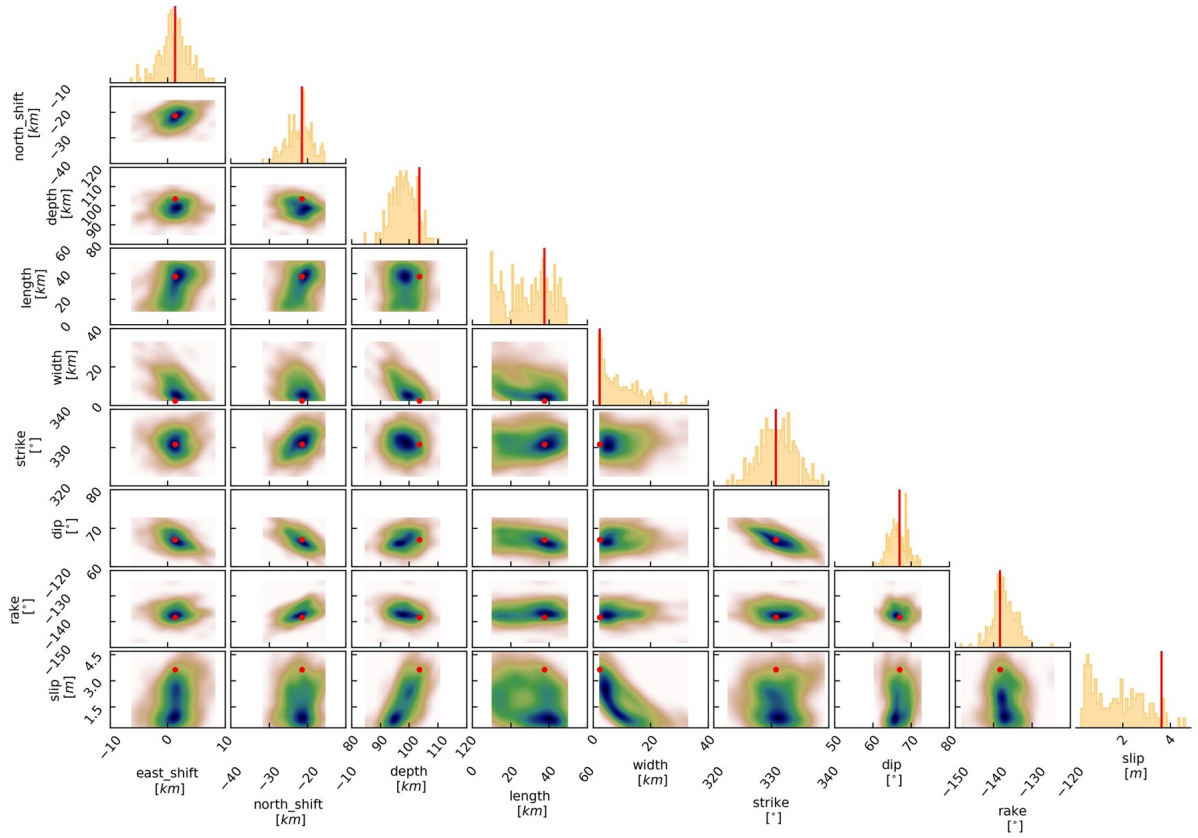

Figure B.18: Correlation histogram of some selected parameters from the geodetic inversion (using InSAR data derived from sICA and GPS data on layered half-space), which shows the posterior distributions and trade-offs between different parameters during the inversion (red dot and line depict the maximum likelihood solution).

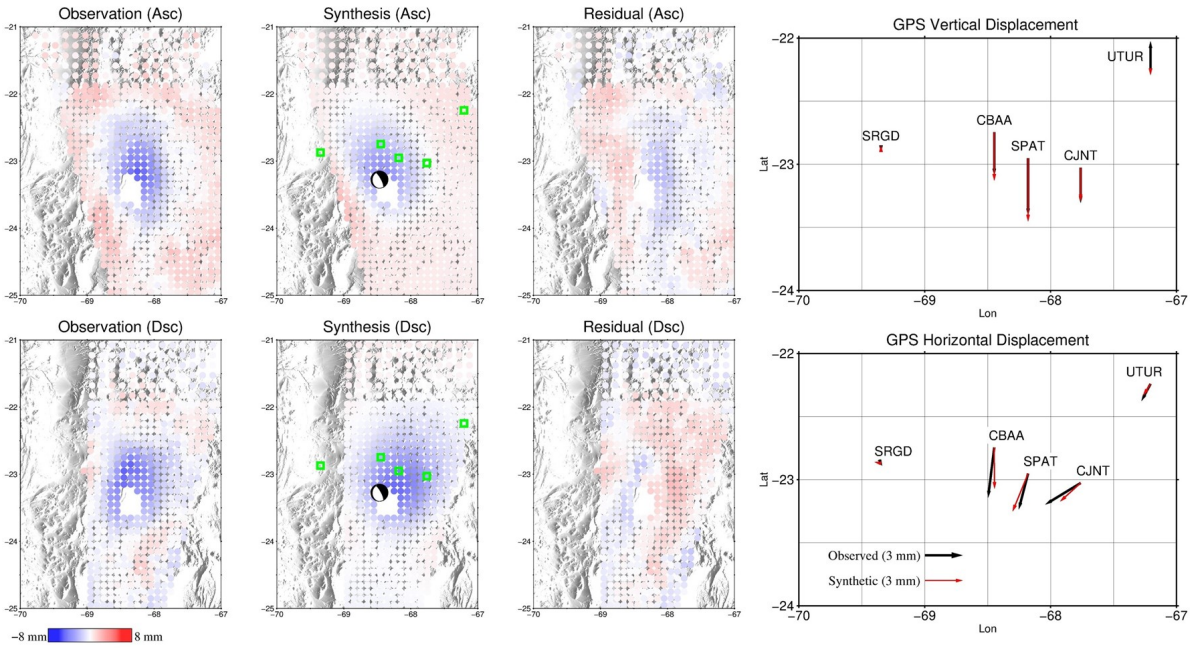

Figure B.19: Geodetic inversion using InSAR data (derived from sICA) and GPS on uniform half-space. Focal mechanism and green boxes indicate the epicentre and the location of the GPS stations, respectively.

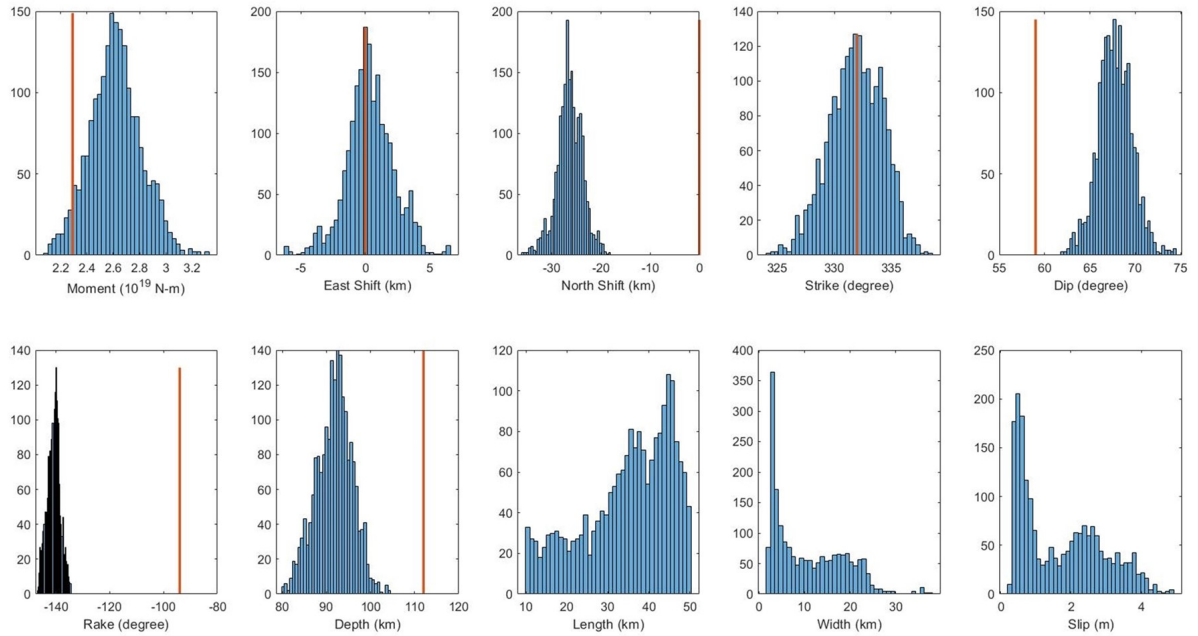

Figure B.20: The posterior distribution of source parameters, using InSAR (derived from sICA) and GPS data on uniform half-space. The red lines indicate the bodywave solution from the USGS for comparison.

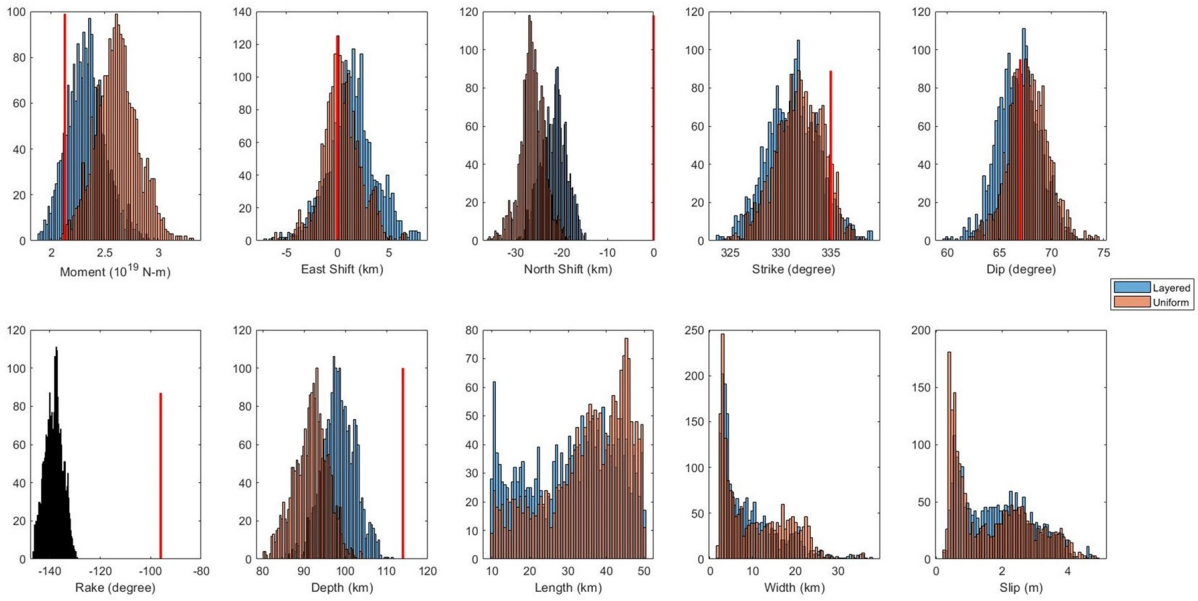

Figure B.21: The comparison of posterior distributions between the layered (Figure B.17) and uniform half-space (Figure B.20), using InSAR derived from sICA and GPS data.

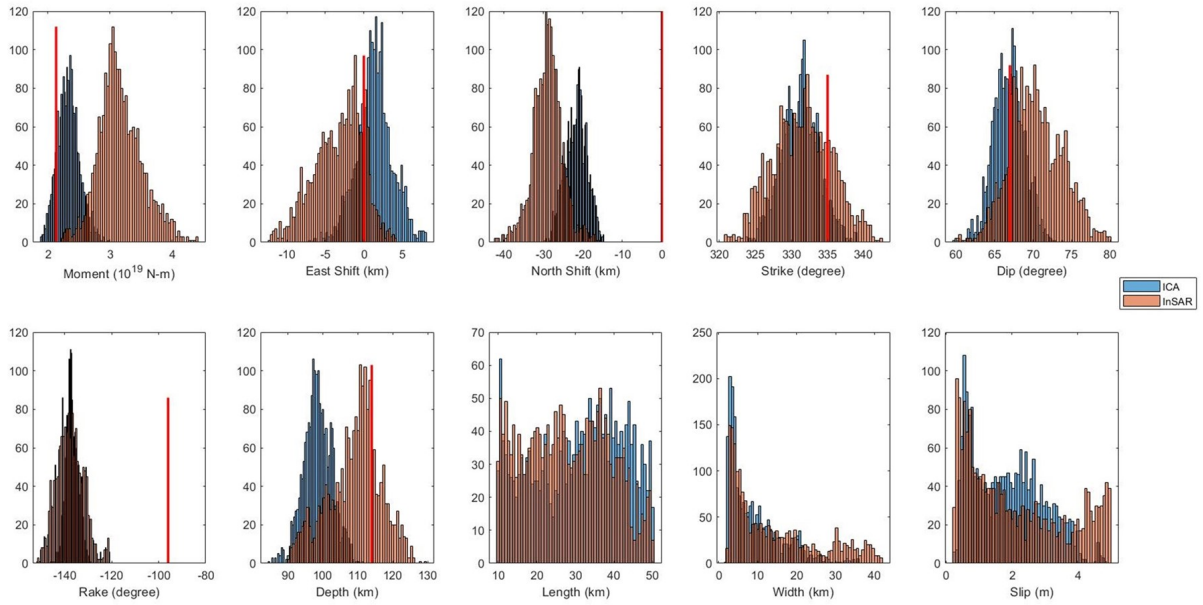

Figure B.22: The geodetic inversion (InSAR and GPS) comparison of posterior distributions between using the InSAR data derived from ICA (Figure S17) and parameterized fitting (Figure S11), on layered half-space.

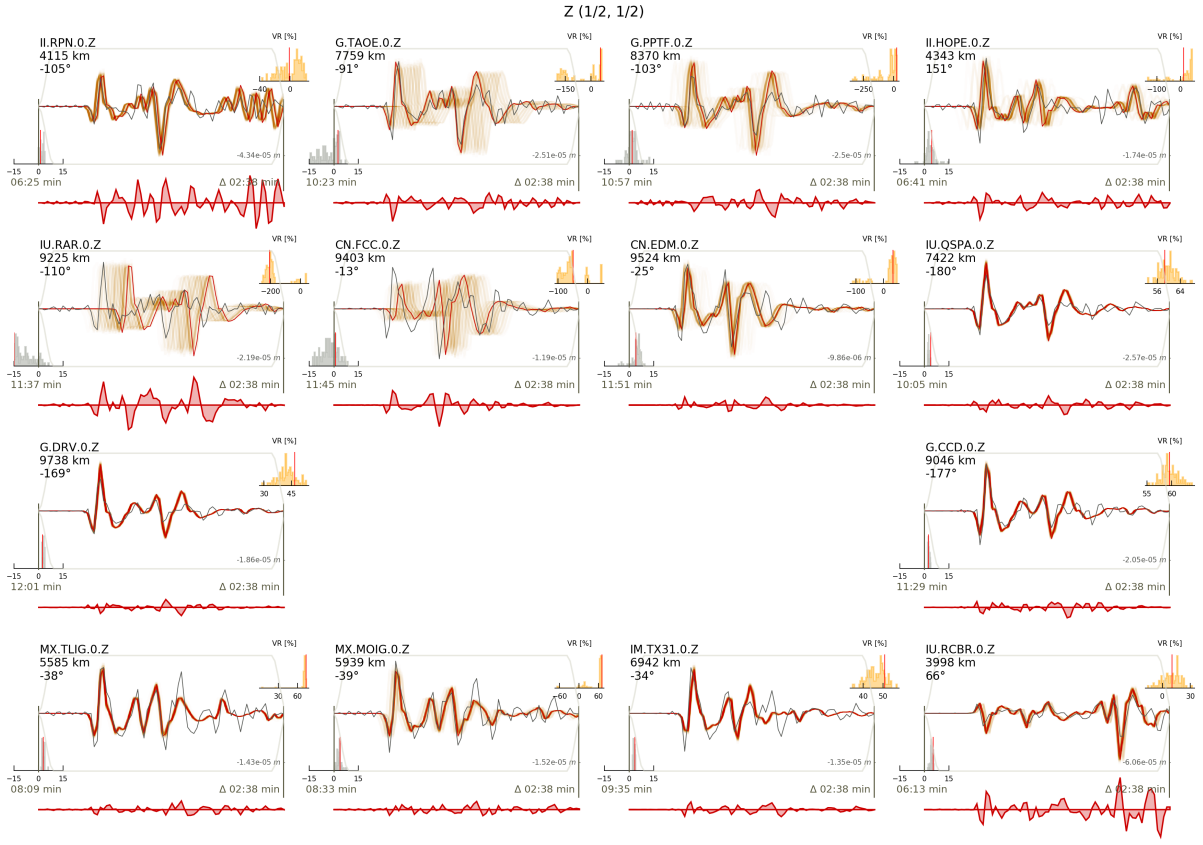

Figure B.23: Seismic waveform, and their fitting of some stations from vertical (Z) components, when performing joint inversion using InSAR (derived from sICA), GPS, and seismology (part of stations) on layered half-space.

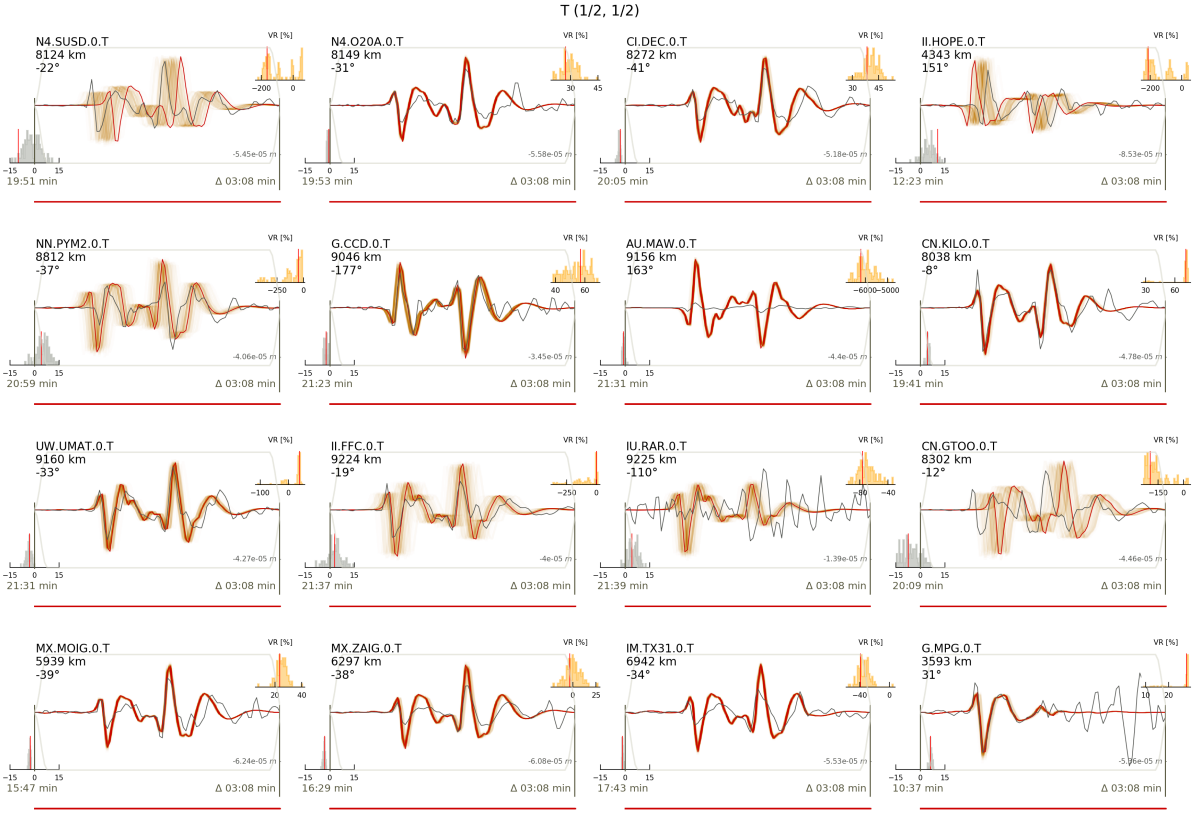

Figure B.24: Seismic waveform, and their fitting of some stations from (transverse) T components, when performing joint inversion using InSAR (derived from sICA), GPS, and seismology (part of stations) on layered half-space.

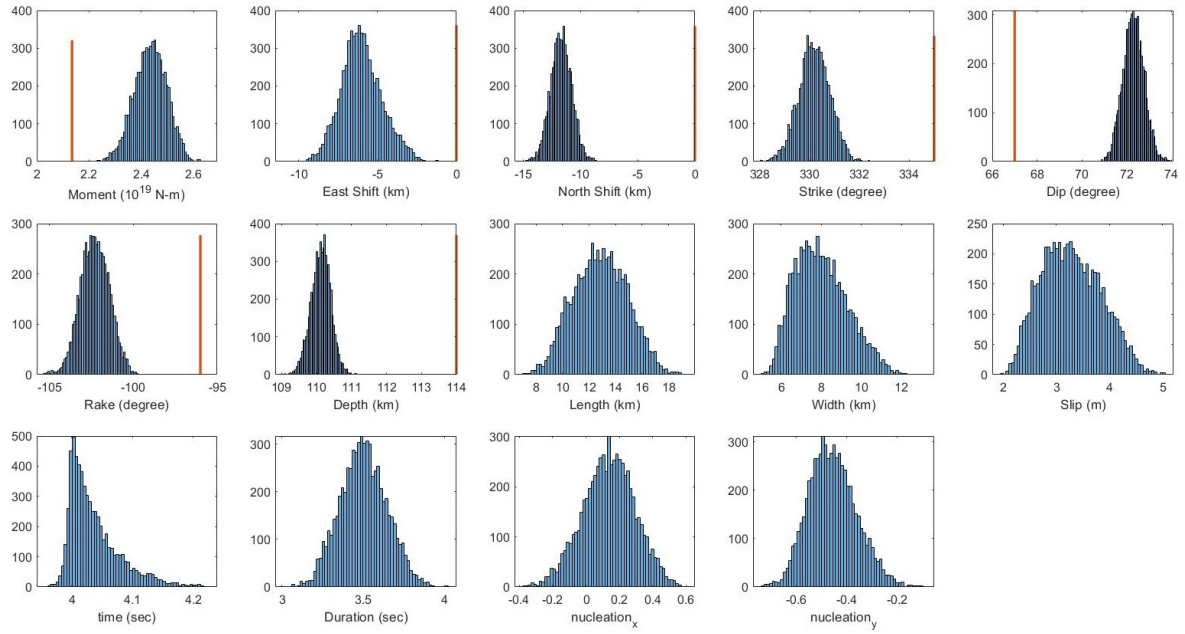

Figure B.25: The posterior distribution of source parameters, using InSAR (derived from sICA), GPS, and seismological data on layered half-space for another focal plane. The red lines indicate the bodywave solution from the USGS for comparison.

	Magnitude (M_w)	Centroid Depth (km)	Strike1(°)	Dip1(°)	Rake1(°)	Strike2(°)	Dip2(°)	Rake2(°)
USGS	6.8	114	335	67	-96	169	24	-77
GCMT	6.8	108	333	60	-91	155	30	-88
GFZ	6.8	95	328	60	-99	167	31	-73
Seismic Inversion	6.8	113	338	65	-97	-	-	-
Geodetic Inversion	6.8	98	331	69	-137	-	-	-
Joint Inversion	6.8	111	330	75	-101	192	19	-51

Table B.1: Summary of the earthquake information from different catalogues and inversion results. The geodetic inversion uses the InSAR (derived from sICA) and GPS dataset on a layered elastic half-space, the seismic inversion uses data from seismological stations only, and the joint inversion using all the dataset.

		Average Standard deviation (mm)	Average Sill values (mm^2)	Average RMSE for time series fitting (mm)
Ascending	ifg	6.54	1.40e3	17.49
	ifg-ion	6.21 (5.11%)	1.40e3 (-0.12%)	14.25 (18.49%)
	ifg-tropo	4.34 (33.70%)	0.51e3 (64.60%)	10.20 (41.64%)
	ifg-ion-tropo	2.86 (56.20%)	0.18e3 (87.38%)	8.10 (53.67%)
Descending	ifg	5.90	1.00e3	18.26
	ifg-ion	3.42 (42.04%)	0.34e3 (66.86%)	8.42 (53.89%)
	ifg-tropo	6.20 (-4.96%)	1.1e3 (-10.59%)	17.85 (2.25%)
	ifg-ion-tropo	3.92 (33.47%)	0.44e3 (57.14%)	8.27 (54.71%)

Table B.2: Quality of data improvements after tropospheric (GACOS) and ionospheric (split spectrum) correction on ascending and descending tracks, respectively. It reports the average standard deviation (of interferograms), the average sill values obtained by an exponential function fitted to the isotropic experimental semi-variogram (Webster and Oliver, 2007) to indicate the noise level, and the average Root Mean Square Error (RMSE) for time series fitting using Equation 4.2, on original interferograms (ifg), the interferograms with ionospheric correction (ifg-ion), the interferograms with tropospheric correction (ifg-tropo), and the interferograms with both ionospheric and tropospheric corrections (ifg-ion-tropo). The percentage numbers in the brackets represent the relative changes to the original interferograms (ifg).

Appendix C

First onset of unrest captured at Socompa: A Recent Geodetic Survey at Central Andean volcanoes in Northern Chile

Introduction

This is supporting information for chapter 5.

Content

Text S1 to S6

Figures S1 to S12

Tables S1 to S2

Additional Supporting Information

Text S1. InSAR processing details

We use the LiCSAR processing chain (which is based on GAMMA) to form interferograms with multilooking (4 in azimuth and 20 in range), but no further spatial filtering, using Sentinel-1 Interferometric Wide (IW) swath mode Single Look Complex (SLC) images and the Digital Elevation Model (DEM) from the Shuttle Radar Topography Mission (SRTM) 1 arcsec. We form interferogram networks by connecting each image to 10 subsequent acquisitions (6-60 days temporal interferogram, assuming revisiting time is 6 days). We then use the StaMPS software to perform time series analysis, which includes a) resampling pixels to 500 m resolution to reduce data volume, b) application of GACOS correction for tropospheric artefacts using the TRAIN software (Bekaert et al., 2015), c) unwrapping iteratively to reduce unwrapping errors by checking for phase consistency (Hussain et al., 2016), and finally d) generating time series data using only longer temporal interferograms (48-60 days) for the small baseline subset inversion to reduce the potential impact of the fading signal (Ansari et al., 2020;Maghsoudi et al., 2022; Purcell et al., 2022).

Text S2. Salar Deformation

The salar regions, principally the Salar de Atacama and Salar de, appear to show very different behaviours on either side of the onset time (Figure 5.2). However, we find it is mainly due to the misfit to Equation 1 since there no significant linear velocity changes occurred in salars.

However, we do find that there is an obvious InSAR phase change in the west of Salar de Atacama and southwest of Salar de Arizaro region, from early to middle 2019 (Figure C.12). Since the deforming area matches well with the salar boundaries on both ascending and descending tracks (data are unfiltered) and some small salars in this region have been reported to be deforming in the 1990s and 2003-2008 ("Recent crustal deformation in west-central South America (Doctoral dissertation)", 2003; Ruch et al., 2012), these patterns indicate real signals instead of artifacts that propagate in the processing chain. This deformation might be related to the extraction of lithium brines (extraction plants have been built in this area), and large groundwater movements (extractions, recharge or caused by tides) in the salar regions during this period ("Recent crustal deformation in west-central South America (Doctoral dissertation)", 2003; Liu et al., 2019).

Text S3. GPS time series fitting using the Markov Chain Monte Carlo approach

We apply the Markov Chain Monte Carlo (MCMC) method using the Metropolis-Hastings iterative algorithm to find the maximum likelihood values for the parameters of the trajectory model (2), and then determine the precise onset time of the Socompa uplift. During this inversion, we assume the errors are multivariate Gaussian with zero means, which means the likelihood function is calculated as follows:

$$p(\mathbf{d}|\mathbf{m}) = (2\pi)^{-\frac{N}{2}}((|\sum_{d}|)^{-\frac{1}{2}} \exp\{-\frac{1}{2}(\mathbf{d\text{-}Gm})^{T}(|\sum_{d}|)^{-1}(\mathbf{d\text{-}Gm})\}$$

where $p(\mathbf{d}|\mathbf{m})$ is the likelihood function of $\mathbf{m}$ given $\mathbf{d}$ based on residuals between the data and the model ($\mathbf{G}$) prediction of the observations, N is the number of epochs on time series, and $(|\sum_d|)^{-1}$ is the inverse of the variance-covariance matrix. We use the values of standard errors and the correlation between three components in the GPS file to construct the covariance matrix.

Text S4. GPS vector decomposition

We can decompose any vectors in a two-dimensional space into two orthogonal vectors. Considering the GPS horizontal displacement, we have the conventional orthogonal coordinates of the North and East components, to indicate the GPS position. It is also possible to decompose an arbitrary GPS observation into another orthogonal coordinate system instead of the North-East one. As the figure shown here, we could decompose the vector V_3, an arbitrary observation, into the V_1 (displacement parallel to the direction of seasonal motion), and V_2 (displacement perpendicular to the direction of seasonal motion) coordinates.

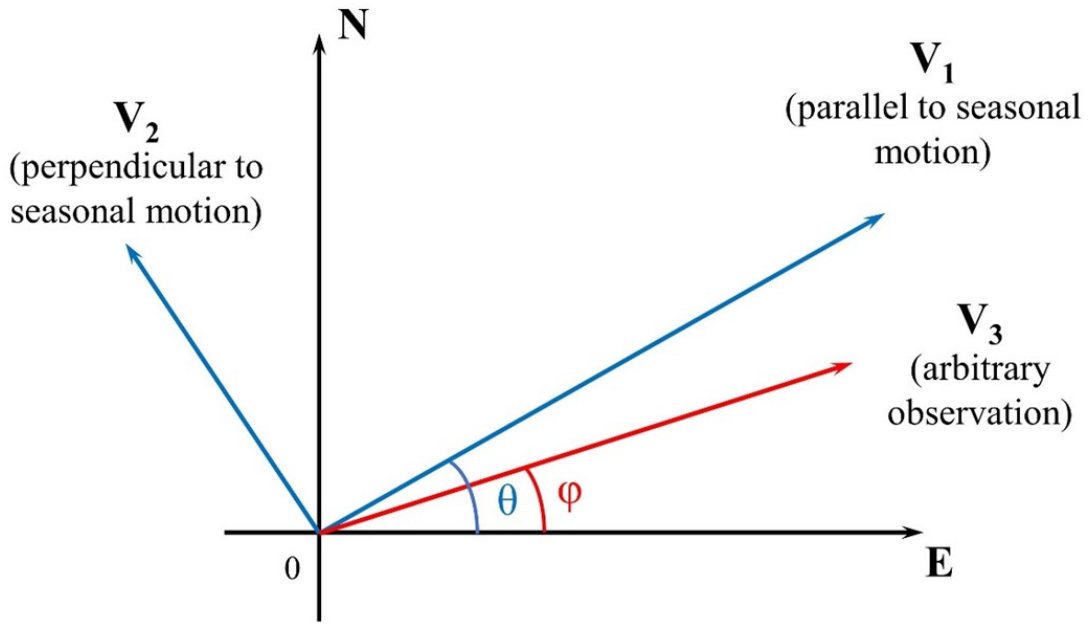

After the decomposition, we have

$$\delta_1 = \mid \boldsymbol{V_3} \mid \cos(\theta - \phi)$$

$$\delta_2 = \mid \boldsymbol{V_3} \mid \sin(\theta - \phi)$$

where δ_1 and δ_2 represent the displacement parallel and perpendicular to the direction of seasonal motion, respectively, θ is the angle between $\boldsymbol{V_1}$ and $\mathbf{E}$, and ϕ is the angle between $\boldsymbol{V_3}$ and $\boldsymbol{E}$.

Since the direction of seasonal displacement varies throughout the year, to determine the angle θ, we calculate the seasonal direction at time t using the following equation:

$$\theta(t) = \arctan\left(\frac{\mid \boldsymbol{N}(t) \mid}{\mid \boldsymbol{E}(t) \mid}\right.$$

As the first three years of the horizontal GPS time series of the SOCM site are dominated by seasonal signals, we first calculate θ for each day in the first three years, then average the results of the three years, and finally get the value of θ on each day throughout a year. After obtaining the seasonal direction, we then decompose the horizontal GPS time series into the displacement parallel and perpendicular to the direction of seasonal motion.

Text S5. Calculation of Reduced chi squared ($\chi 2$)

The reduced chi squared ($\chi 2$) is used to evaluate the goodness of fit. Here we calculate the values of ($\chi 2$) to indicate which source models fit the data best, using the following formula:

$$\chi^2 = \frac{(R_a^T \sum_a^{-1} R_a + R_d^T \sum_d^{-1} R_d + R_G^T \sum_G^{-1} R_G)}{(N_a + N_d + N_G - N_{parm})}$$

where R_a, R_d, and R_G are the residuals, $\sum_a^{-1}$, $\sum_d^{-1}$, and $\sum_G^{-1}$ are the inverse of covariance matrix, N_a, N_d, and N_G are the number of observations for InSAR ascending data, InSAR descending data, and GPS data, respectively. N_{parm} is the number of source parameters (including the parameters for estimating the ramp for InSAR dataset). The values of χ^2 and N_{parm} for the source models we used are 0.42 and 15 for pCDM, 0.43 and 14 for Yang, 0.48 and 14 for Okada, and 0.65 and 10 for Mogi, respectively.

Text S6. Tying InSAR and GNSS observation

Here we use all available continuous GPS sites from the database of the Nevada Geodetic Laboratory (Figure C.10). We adopt the linear velocity calculated by the Nevada Geodetic Laboratory, using South America Plate as the reference frame.

We first derive the InSAR velocity map from the time series data, and average the values of the pixels surrounding the GPS sites (a circle with a radius of 3 km centred on it, ∼120 pixels) as the corresponding velocity value of InSAR data. We then remove a spatial linear ramp in the east and north direction from the InSAR velocity map to minimize the relative difference between InSAR and GNSS, on ascending and descending respectively. Finally, based on this deramped InSAR velocity map and assuming no deformation signals on the north component, we can obtain the uplifting velocity of any pixels that are covered by both tracks by decomposing the InSAR velocity map into the east-west and vertical direction by solving the following formula:

$$\begin{bmatrix} U_{asc} & E_{asc} \\ U_{dsc} & E_{dsc} \end{bmatrix} \begin{bmatrix} V_U \\ V_E \end{bmatrix} = \begin{bmatrix} V_{asc} \\ V_{dsc} \end{bmatrix}$$

where U and E are the up and east components of the line of sight (LOS) vector, respectively.

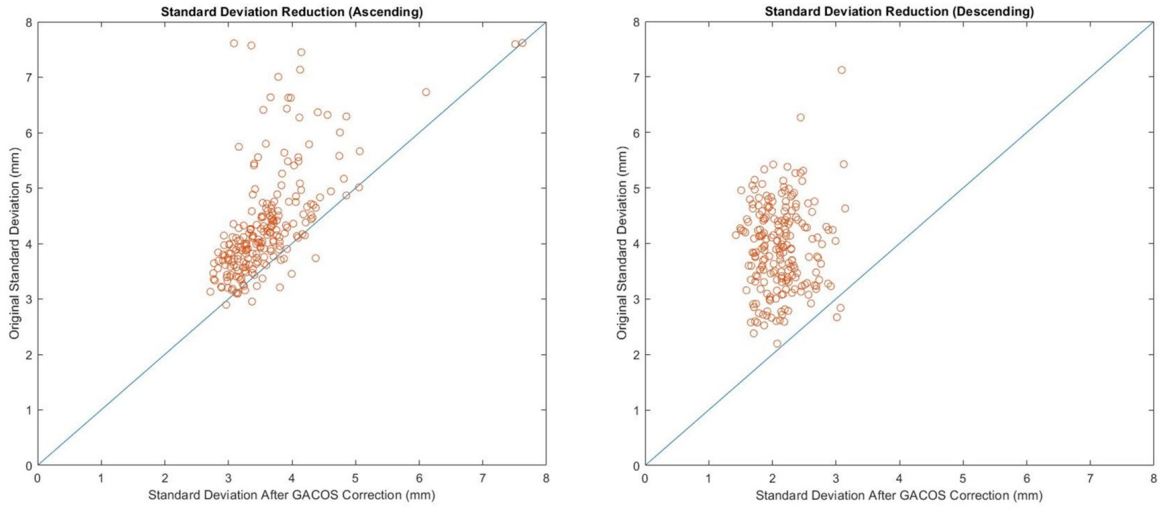

Figure C.1: Standard deviation reduction of interferograms after the GACOS correction on ascending and descending track data, respectively. The red dots represent each epoch on time series, and the blue line is the identity line where any dots above it means an improvement after the GACOS correction. Here the average standard error reductions are 16.9% and 45.7% for ascending and descending, respectively.

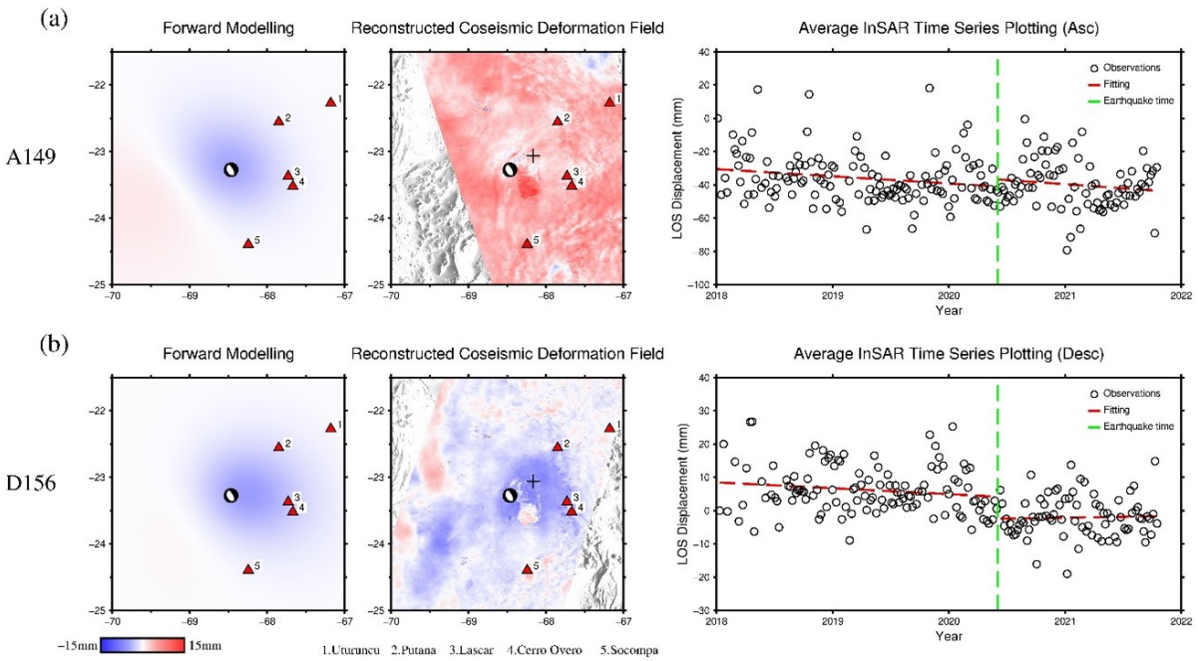

Figure C.2: Coseismic deformation field of the M_w 6.8 earthquake reconstruction by InSAR time series fitting. (a) Data of ascending track. From left to right, the forward modelling from the USGS solution (strike: 332°, Dip: 59°, Rake: -94°, centroid depth: 112 km, Moment: 2.29×10^{19} N-m), the reconstructed coseismic deformation field, and the average InSAR time series of peak displacement pixels. (b) Same as (a) but for the descending track. For the forward modelling, we assume a uniform dislocation embedded in an isotropic elastic half-space, faults are equal in width and length, the slip-to-length ratio is set to 1.5×10^{-5} for this interplate earthquake, and the rigidity value used here for moment calculation is 75 GPa. The epicentre of the earthquake is indicated by the black focal mechanism, and volcanoes are marked by red triangles. On the reconstructed coseismic deformation field, the location of peak displacement pixels is marked by a plus symbol. The red patch close to the southeastern point of the epicentre marked (which is observed on both tracks) indicates the shape of Salar de Atacama, and has different behaviour in the time series. In all figures, positive values mean movements towards the satellite.

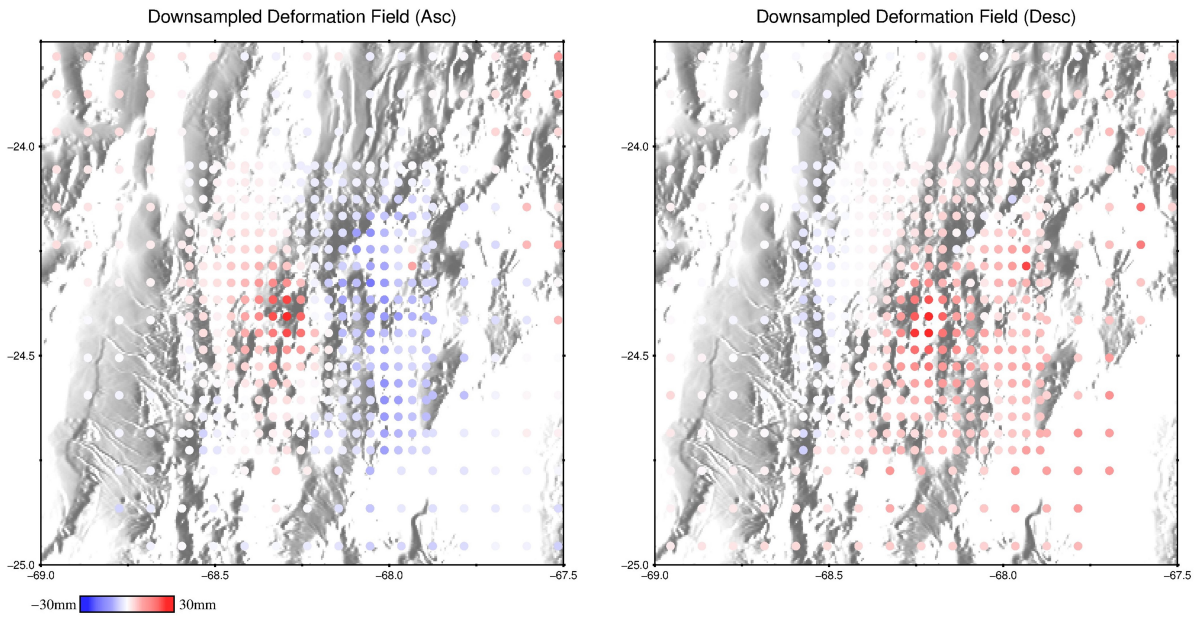

Figure C.3: Uniform downsampling of the reconstructed post-onset cumulative deformation fields for GBIS input. We use a larger pixel density over the Socompa deformation area (∼5 km in the near field and ∼10 km in the far field), resulting in 500 pixels on the ascending and 496 pixels on the descending tracks of data, respectively.

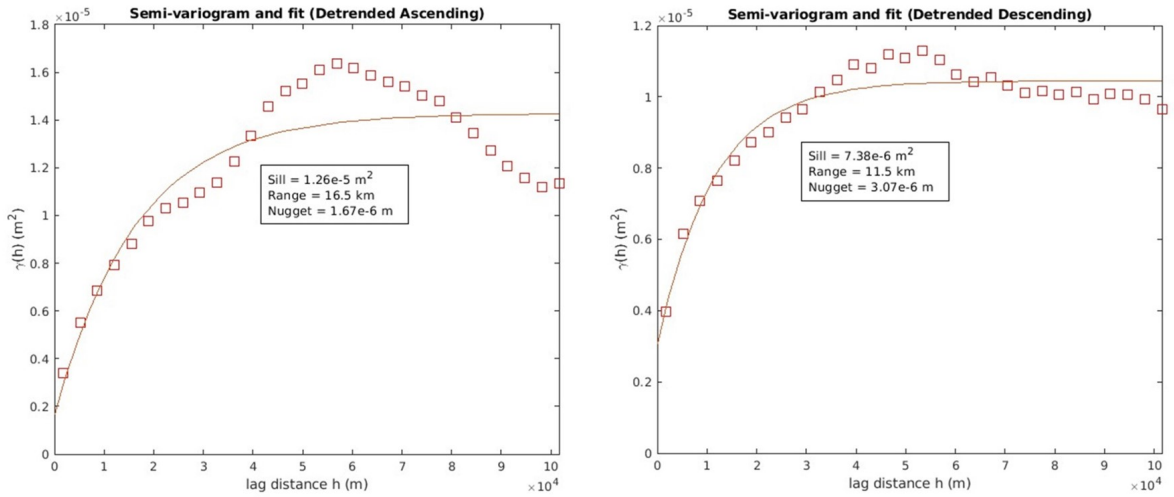

Figure C.4: Semi-variogram fitting for post-onset cumulative deformation fields on ascending and descending tracks using the GBIS software. Errors in the InSAR data can be simulated using an exponential function fitted to the isotropic experimental semi-variogram (Webster and Oliver, 2007), and the lower sill value of the fitted results indicates the higher the signal-to-noise ratio. We use this semi-variogram fitting to calculate the covariance matrix of the InSAR data during the inversion. While for the GPS data covariance matrix, it is obtained from the standard deviations by fitting the Equation 5.2 in the main text.

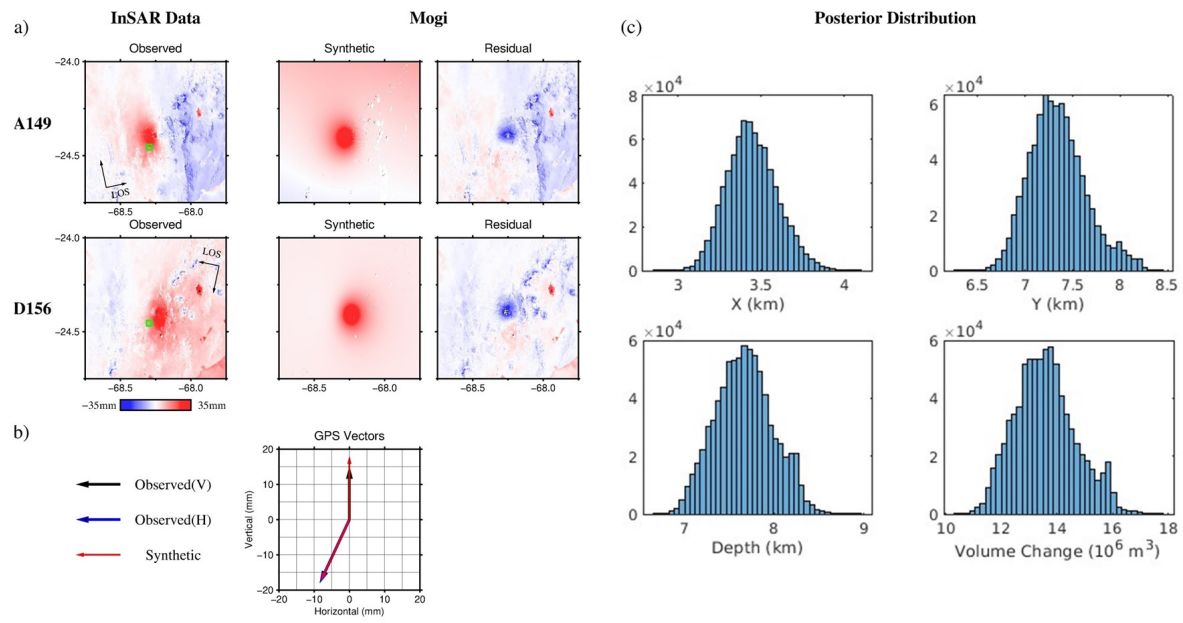

Figure C.5: Volcanic source model of Socompa cumulative uplift (Nov 2019 – Oct 2021) using the Mogi model. (a) Modelling results of InSAR observations. The green box indicates the location of the SOCM site. (b) Modelling results of GPS observations. The black vertical vector represents the up component of GPS deformation (∼15 mm), while the blue vector signified the horizontal deformation in the east and north directions (here moving ∼10 mm west and ∼20 mm south). (c) Posterior distributions for all parameters, where X, Y, and Depth indicate the source location reference to the SOCM site (northeast direction), and V represents the volume change (here $1.4{\times}10^7$ m^3).

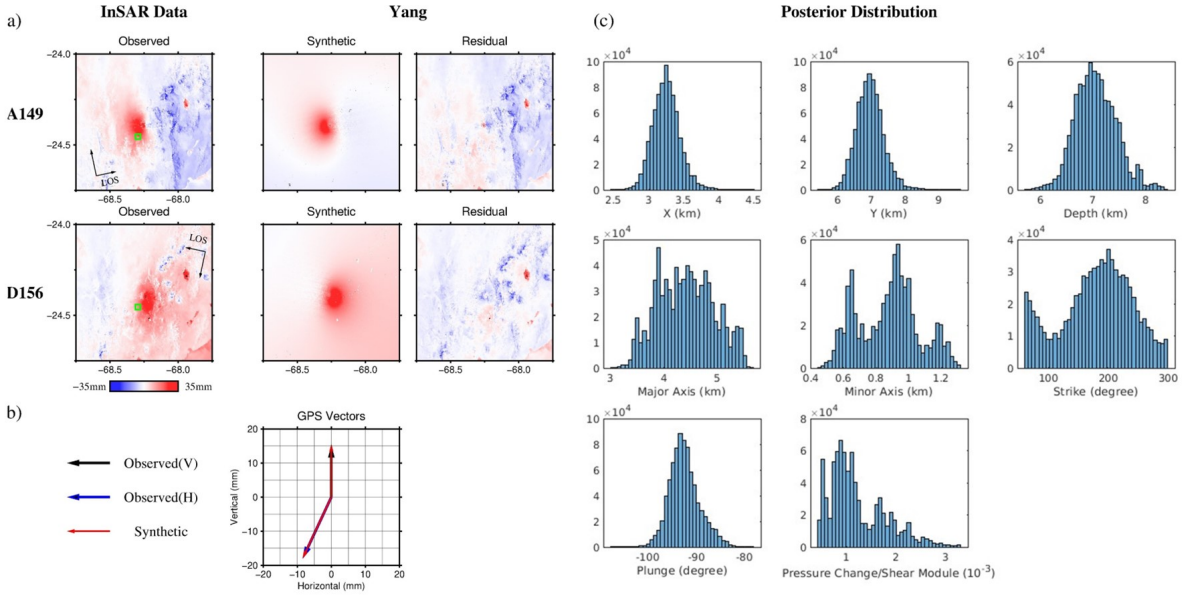

Figure C.6: Same as Figure C.5 but using the Yang model. (c) Semi-major and Semi-minor are the lengths of the two axes, Strike value is the angle of major semi-axis with respect to North, and the Plunge value is the inclination angle of major semi-axis with respect to horizontal. The volume change of the Yang model is $1.1{\times}10^7$ m^3.

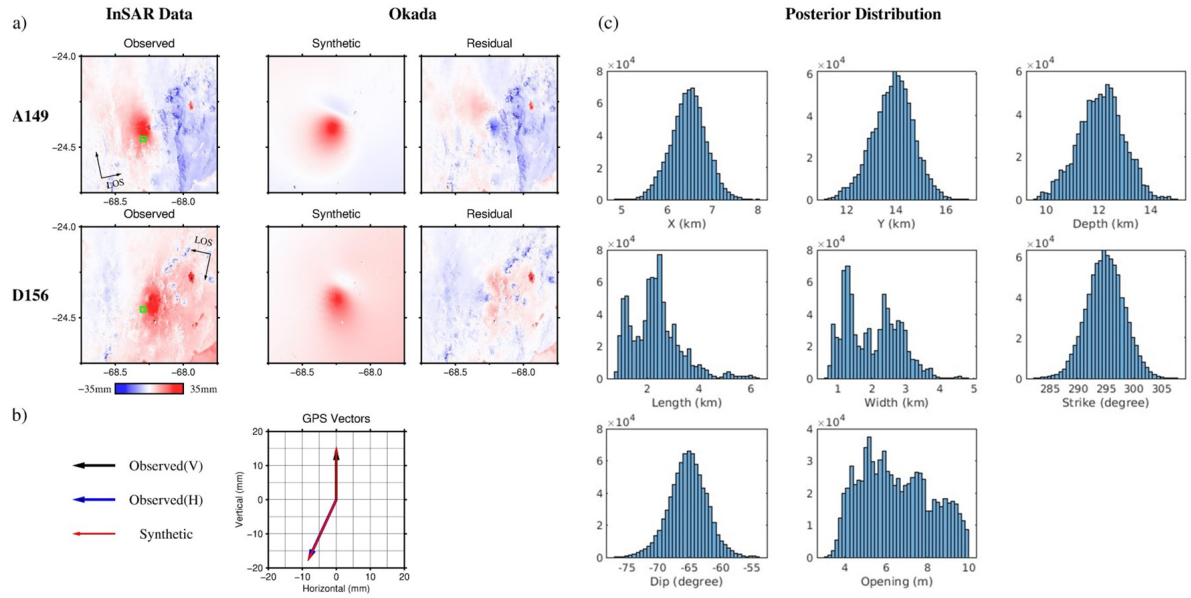

Figure C.7: Same as Figure C.5 but using the Okada model. The volume change of the Okada model is 2.4×10^7 m^3.

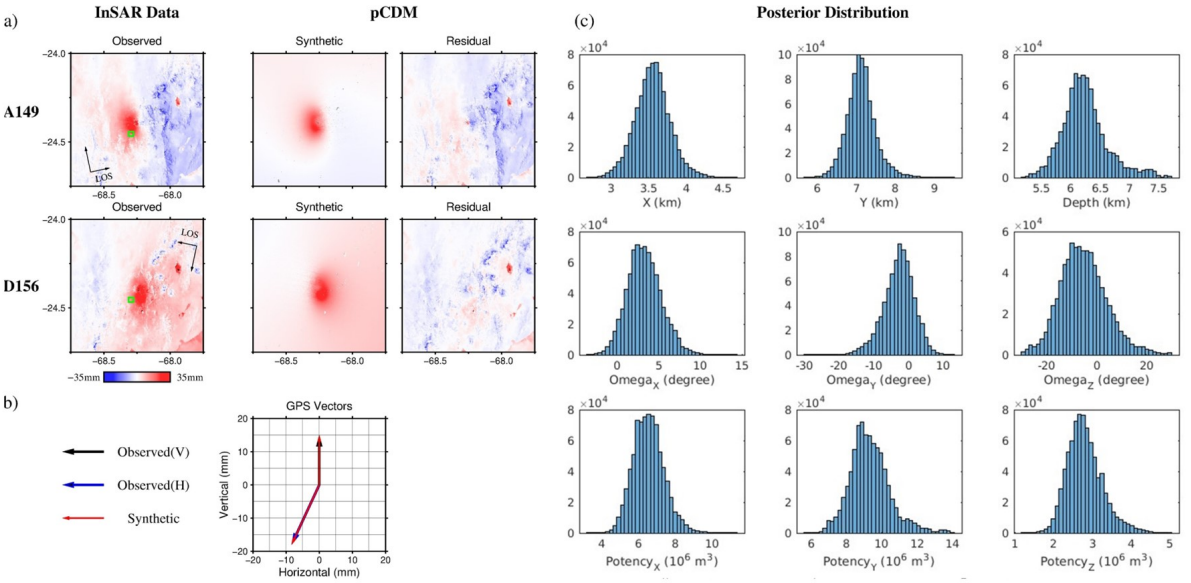

Figure C.8: Same as Figure C.5 but using the pCDM model. (c)$Omega_{X,Y,Z}$ are the rotation angles around three axes, and $Potency_{X,Y,Z}$ are the potencies of the point dislocations on three directions, respectively. Here the bimodal distribution of the rotation angles around the Z axes indicates similar values of potency in the X and Y direction. The total potency of the pCDM, which is defined as the product of dislocation surface area and opening and is a totally different concept from volume change, is 1.9×10^7 m^3 by summing the potency values in three directions.

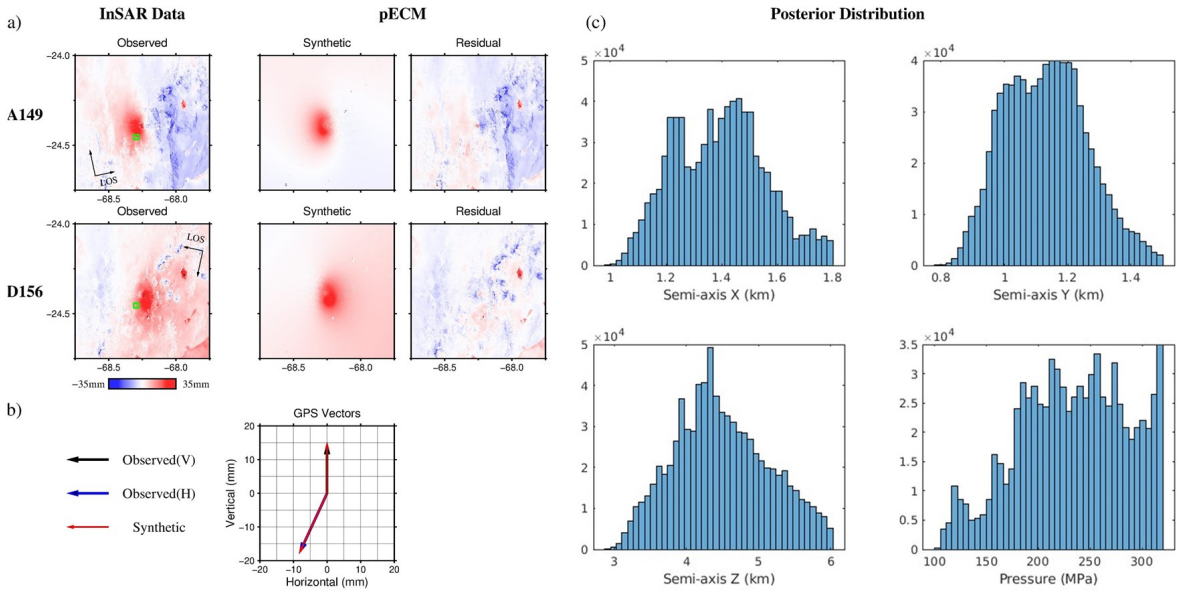

Figure C.9: Same as Figure C.5 but using the pECM model. We use the inferred source location and orientation from pCDM to perform the inversion. The total potency and volume change of the pECM are $\sim 2.0 \times 10^7$ m^3 and $\sim 1.1 \times 10^7$ m^3, respectively.

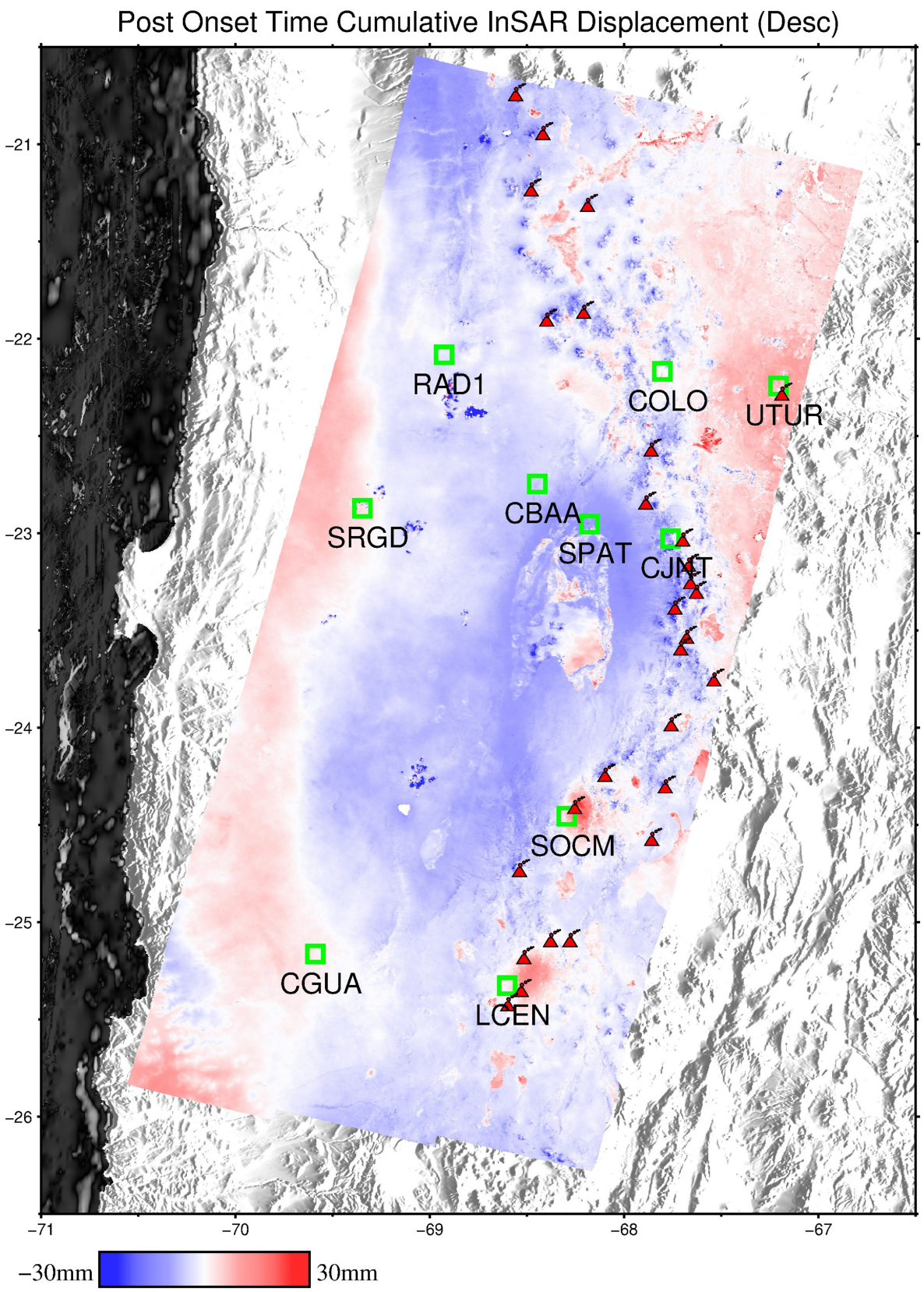

Figure C.10: The locations of continuous GPS sites that were used to tie InSAR data, using the descending post onset time cumulative deformation field and topography map as the background image. All GPS data are obtained from the database of the Nevada Geodetic Laboratory.

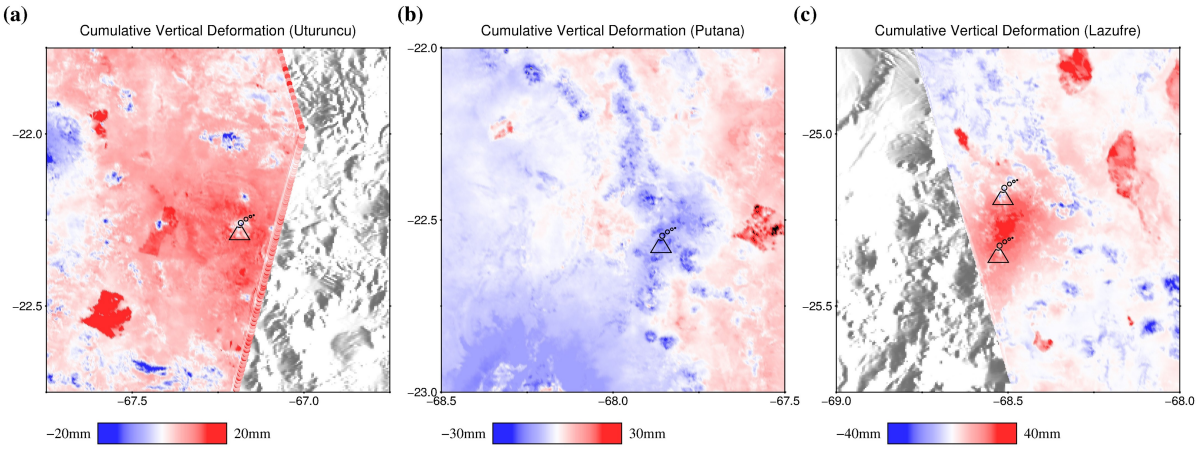

Figure C.11: The cumulative vertical deformations decomposed from ascending and descending track data (see Text S5 for more details). a) The cumulative deformation map near the Uturuncu volcano from Jan 2018 to Oct 2021. The summit of the volcano is marked by the black volcanic icon. b) Same as a) but for Putana volcano from Nov 2019 to Oct 2021. c) Same as a) but for Lazufre (Lastarria Azufre) volcano from Jan 2018 to Oct 2021.

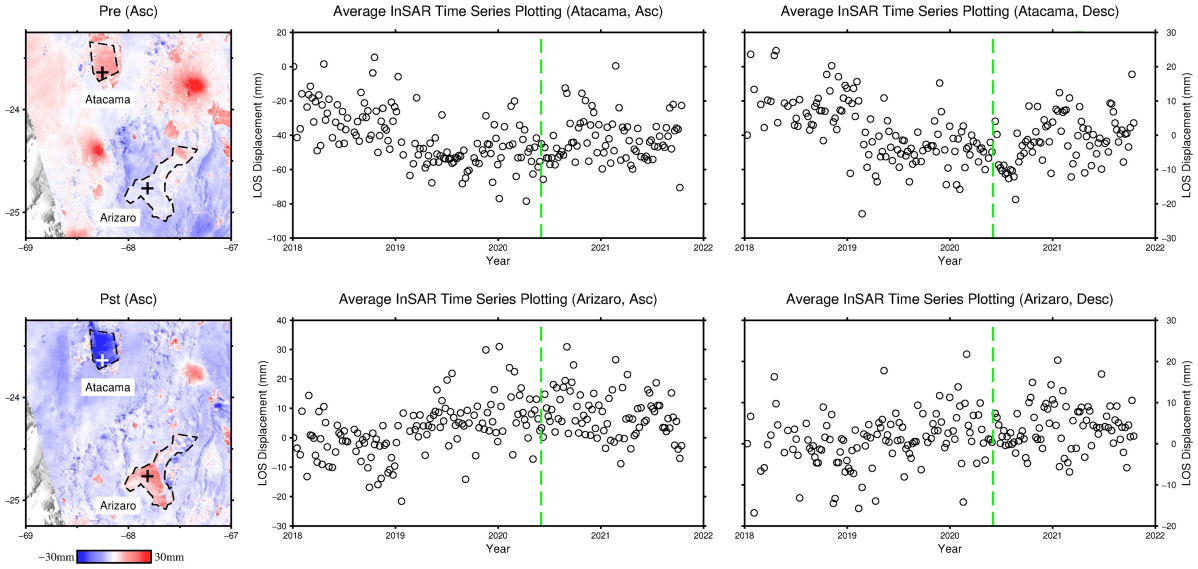

Figure C.12: Average InSAR time series over Salar de Arizaro and Atacama region on ascending and descending tracks data. Black dashed polygons, plus symbols, and green dashed lines indicate the approximate boundaries of Salar regions, the location of pixels plot on the time series panels, and the event time of earthquake M_w 6.8, respectively. It shows opposite surface displacements occurrence on Salar de Arizaro and Atacama at the beginning of 2019.

	Mogi	Yang	Okada	pCDM (pECM)
X (km)	3.43 3.17-3.76	3.30 2.90-3.66	6.52 5.68-7.22	3.65 3.09-4.05
Y (km)	7.39 6.83-8.03	6.91 6.22-7.84	13.9 12.1-15.4	7.21 6.44-7.97
Depth (km)	7.7 7.1-8.3	7.3 6.4-7.9	11.8 10.3-13.7	6.3 5.6-7.3
Volume Change ($\times 10^7$ m^3)	1.4 1.2-1.6	1.1 0.9-1.4	2.4 1.8-3.3	1.1 1.1-1.2

Table C.1: The comparison of some main parameters from different volcanic geodetic source modelling results. The optimal values and corresponding 95% confidence intervals are provided. Here X and Y represent the location reference to the SOCM station, where positive values mean towards north or east.

Volcano Name	Monitored or Not	Fumarolic Active	Geodesy Observation	Deformation mechanism and Source Depth	Key References
Uturuncu	N	Y	InSAR from ERS, ENVISAT, Sentinel-1 (1992-2018), GPS	Magmatic. Modelled by several source types, the typical depth is 15-30 km.	Fialko & Pearse, 2012 Henderson & Pritchard, 2017 Gottsmann et al., 2017 Lau et al., 2019 Barone et al., 2019
Putana	N	Y	InSAR from ERS and ENVISAT (1992-2011)	Hydrothermal. A shallow Mogi source at 1 km depth	Henderson & Pritchard, 2013
Lascar	Y	Y	InSAR from ERS, ENVISAT, and TerraSAR-X (1992-2000, 2012-2017), GPS	Complex deformation. A combination of ongoing crater evolution processes, including gravitational slumping, cooling and compaction of eruption products, as well as possible piston-like subsidence	Pritchard & Simons, 2002 Pavez et al., 2006 Richter et al., 2017
Cerro Overo	-	-	InSAR from ERS and ENVISAT (1992-2011)	Controlled by a single reversible mechanism involving fluid accumulation and loss within the crust at ~10 km depth	Henderson & Pritchard, 2013
Lastarria & Azufre	Y	Y	InSAR from ERS, ENVISAT, RADARSAT-2, TerraSAR-X, COSMO-SkyMed, and Sentinel-1 (1995-2016), GPS	Magmatic. Modelled by several source types, the typical depth is <10 km.	Pearse & Lundgren, 2013 Henderson et al., 2017 Díaz et al., 2015

Table C.2: Summary of volcanoes in our study area that have been reported to be deforming in the past few decades from previous studies. It shows whether the volcanoes have been monitored by ground observations. Here Cerro Overo presents a deformation area rather than a specific volcano and thus is not marked.